Exploring the selection of galaxy clusters and groups

Gilbank, David Geoffrey

Exploring the Selection of Galaxy Clusters and Groups

by David Geoffrey Gilbank

A thesis submitted to the University of Durham
in accordance with the regulations for
admittance to the Degree of Doctor of Philosophy.

Department of Physics
University of Durham
December 2001

Exploring the Selection of Galaxy Clusters and Groups

by David Geoffrey Gilbank

December 2001

Abstract

Data from a new, wide field, coincident optical and X-ray survey, the X-ray Dark Cluster Survey (XDCS) are presented. The aim was to conduct simultaneous and independent searches for clusters of galaxies in the optical and X-ray passbands. Optical cluster detection algorithms implemented on the data are detailed. This resulted in catalogues of 185 I-band selected, 290 colour selected and 15 X-ray selected systems, residing in $\sim$11deg^2 of optical + X-ray imaging. The relationship between optical (L_E) and X-ray luminosity (L_X) was examined and found to exhibit significant scatter. This study highlights the higher efficiency and resolution of optical colour selection compared with other cluster detection methods.

Spectroscopic redshifts confirmed the reality of a subsample of systems which were found with the optical algorithms, but required to have no detectable X-ray emission. These systems show comparable optical luminosity to the most X-ray luminous clusters, but orders of magnitude lower X-ray emission. This is consistent with the large scatter seen in the L_X-L_E relation.

A near-infrared multicolour technique was explored and extended to search for high redshift ($z \gtrsim 1$) clusters. Finally, application of such techniques to forthcoming wide field near-infrared surveys was discussed and predictions for cluster finding in such surveys made.

Declaration

The work described in this thesis was undertaken between 1998 and 2001 whilst the author was a research student under the supervision of Dr. Richard Bower in the Department of Physics at the University of Durham. This work has not been submitted for any other degree at the University of Durham or at any other University.

Portions of this work have appeared in the following:

- Gilbank D. G., Bower R. G., Castander F. J., 2001, ASP Conference Series, **240**, 644.

Contents

List of Figures

List of Tables

Acknowledgements

Firstly I must thank my supervisor Richard Bower for his constant encouragement and guidance. His knowledge is surpassed only by his enthusiasm and optimism. Most importantly, he has provided me with a broad overview of all aspects of astronomy from spectrographs to Press-Schechter.

I would like to thank the other astronomers whose ideas, comments and work have helped me significantly: Francisco Castander for teaching me a methodical approach to observing and being the fastest measurer of X-ray data I know; Eric Bell for teaching me a thoroughly laid-back approach to observing and also pretty much everything I know about data reduction; Taddy Kodama for providing me with the population synthesis model colours which are central to this work; Bodo Ziegler; Alastair Edge; Vince Eke; Peter Draper, without whom my data would be very distorted and the sound on my laptop wouldn't work; Nigel Metcalfe; Alan Lotts for making computers work; Peder "Group Finder" Norberg for being considerably better at dot-to-dot than I; Ian Smail for code, discussion and a job; and most importantly Mike Balogh, who has given me practical advice, beer, and listened to more of my whinging than any human being should be forced to endure.

The people with whom I have shared offices deserve a mention: Katherine; Claire; Eric; Fiona; Kev; Amaya; Rich for his knowledge of spectroscopy and guitars; Dajana; Takashi; and Pasquale "I'm not one to complain" Mazzotta for correcting most of my *mis*understanding of X-ray astronomy. Thanks to the others who have made my time in Durham more enjoyable than it would have been otherwise - some of them young, some trendy, some astronomers: Harold; Graham (who is none of the above); Tom and John for coming to the pub when noone else would, and everyone else. Dave Jackson, as always, provided the best moral support known to Man, and Shep and Stu provided plenty of beer. Apologies to anyone I've forgotten, as I'm quite tired whilst writing this....

Without my family I would not be where I am today. So, Mum, Dad, Robin and Fiona, I thank you for everything. Steve and Julie have done more for me than I can put into words, so I won't even try. The Scarborough and District Astronomical Society also has a lot to answer for. Above all I thank June for love and support and correcting my marginal grasp of the English language.

"There are over four hundred pints in a hogshead." — The Hogshead.

I stood and stared; the sky was lit,
The sky was stars all over it,
I stood, I knew not why,
Without a wish, without a will,
I stood upon that silent hill
And stared into the sky until
My eyes were blind with stars and still
I stared into the sky.

"Song of Honour", Ralph Hodgson, 1913.

Chapter 1 | *Introduction*

1.1 The Development of Cosmology

From a dark site, away from the light pollution of modern cities, a misty banding of light is visible running across the night sky. It was named *The Milky Way* by the ancient Greeks, as they thought it resembled a river of milk. In the mid-Eighteenth Century, telescopes pointed at the sky revealed previously unseen misty patches which were christened *nebulae*. These nebulae exhibited different characters - some appeared featureless; others showed distinct spiral structure. Thomas Wright and Immanuel Kant suggested at the time that the spiral nebulae might be self-contained systems of stars which lay beyond our own system of stars.

In the early 20th century, Opik (1922) and Hubble (1925) showed that the spiral nebulae are indeed external to the Milky Way. It is now known that the Milky Way is itself a "spiral nebula" and that the "river of milk" is the integrated light from many stars that make up the spiral disk structure, seen from inside. Some of the non-spiral nebulae are stellar nurseries - clouds of dust and gas inside the Milky Way where stars are being born - and the term "nebula" is now generally reserved for these objects. The external systems were given the name "galaxies" (from the Greek for milk!), and it is these that are considered in this thesis.

Hubble (1936) developed a classification scheme for galaxies, based on their morphology. Below is shown Hubble's "Tuning Fork" diagram. He thought that galaxy morphologies represented a sequence, seen in different stages of evolution, and although this is now thought to be incorrect, the terminology persists, and thus ellipticals and lenticulars/S0s are "early-type" and spirals are "late-type" galaxies. For the discussion of colour-based techniques in §1.2, it is sufficient to note here that early-type galaxy populations are observed to be relatively red and late-type galaxies are relatively blue, at a given epoch; and that the observed colours redden with increasing distance from the observer.

With the discovery of external galaxies, the view of the universe shifted from that of a single large collection of stars (thought at the time to be tens of thousands of light years

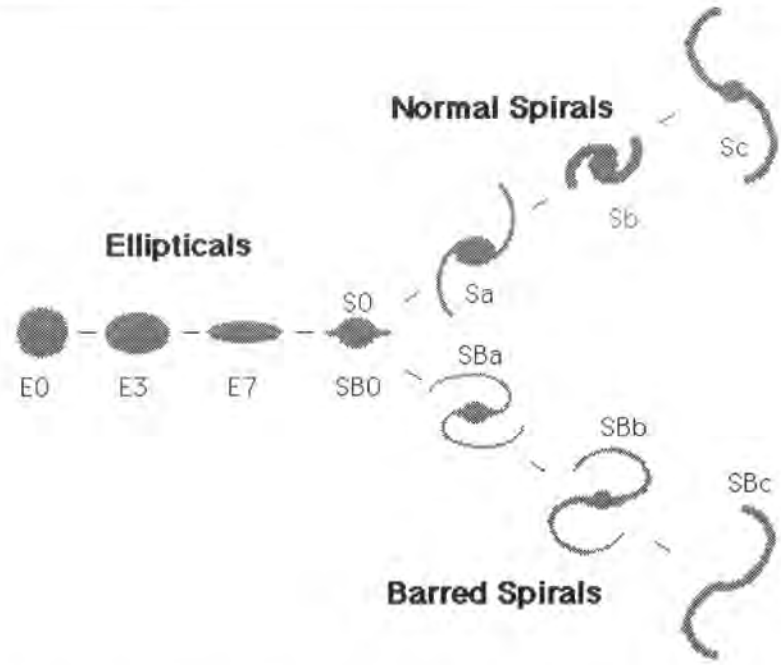

Figure 1.1: The Hubble Tuning Fork Diagram. The morphological sequence runs from left to right with ellipticals being classified as En where $n \approx 10(1 - b/a)$ (with a,b the major, minor axes); lenticulars (S0s); "normal" spirals (Sa,Sb,Sc), and barred spirals (SBa, SBb, SBc).

across) to that of a vast collection of such systems, the nearest of which were found to be millions of light years away. The finite speed of light means that, at these distances, we are seeing the objects as they were in the distant past (referred to as *lookback time*). A new science was needed to study this greatly enlarged world-view and cosmology was born.

Shortly before this was found, Einstein (1915) derived the field equations of General Relativity (GR). De Sitter (1917) derived a solution to the equations for a static universe, and Friedmann (1922) applied the field equations to homogeneous and isotropic models of the Universe. Robertson & Walker (1933) derived a spatial metric for such universes, using a geometric approach, independently of GR.

The next key cosmological discovery was made by Hubble (1929) when he discovered that the universe is expanding. Whilst making a systematic survey of galaxy velocities (by measuring the displacement of Doppler-shifted spectral lines), he found that, with few exceptions, the lines were observed at longer wavelengths than their counterparts at rest in a laboratory [1], ie. the galaxies are receding. Further, using Cepheids (pulsating variable

[1]This displacement is termed *redshift* and a galaxy's redshift, z, is given by $1 + z = \lambda_R/\lambda_E$ where λ_R

stars) to determine the distances to galaxies, he was able to find a linear relationship between distance and redshift. This is parameterised as Hubble's Law $v = H_0 d$ where v is the recessional velocity of the galaxy, d is its distance, and the constant of proportionality, ${H_0}^2$ is known as Hubble's constant (the present day value $t = t_0$ is referred to as H_0, whereas the general form of Hubble's parameter, H is actually a function of time).

With hindsight, perhaps the most surprising part of the discovery is the fact that it was not predicted. Indeed, Einstein had had to invoke an extra parameter (which he called "Λ" or the "cosmological constant") in order that the universe be prevented from expanding, and remain static. Upon hearing Hubble's discovery he removed Λ from his equations and called it the worst mistake of his career.

The Friedmann equations are summarised:

$$\frac{\ddot{a}}{a} = -\frac{4\pi G}{3}\left(\rho + \frac{3p}{c^2}\right) + \frac{\lambda}{3} \tag{1.1}$$

$$\left(\frac{\dot{a}}{a}\right)^2 = \frac{8\pi G\rho}{3} - \frac{kc^2}{a^2} + \frac{\lambda}{3} \tag{1.2}$$

$$d(\rho a^3) = -3\frac{p}{c^2}a^2 da \tag{1.3}$$

where a is the expansion parameter (and the dot notation denotes derivatives with respect to time) ρ is the density of the universe, c is the speed of light, p is the pressure of the fluid which is assumed to obey the equation of state $p = p(\rho)$, G is the gravitational constant, and k is a curvature parameter which is either $-1, 0, +1$ (see below).

It may be helpful to think of equation 1.2 in terms of densities

$$\Omega_\rho + \Omega_\Lambda + \Omega_k = 1 \tag{1.4}$$

where Ω_ρ is the matter density, as above; $\Omega_\Lambda = \Lambda = \lambda/3H^2$ is the contribution from the cosmological constant; and the curvature term contributes $\Omega_k = -k(c/aH)^2$.

In a $\lambda = 0$ model, equation 1.2 can be rewritten

$$\left(\frac{\dot{a}}{a_0}\right)^2 - \frac{8\pi}{3}G\rho\left(\frac{a}{a_o}\right)^2 = H_0^2\left(1 - \frac{\rho_0}{\rho_{0c}}\right) = H_0^2\left(1 - \Omega_0\right) = -\frac{kc^2}{a_0^2} \tag{1.5}$$

where the subscript 0 refers to the values of parameters at a reference time $t = t_0$. $H = \dot{a}/a$ and is the Hubble parameter; Ω is the density parameter in units of the critical density, ρ_c, and

is the wavelength of the received radiation and λ_E is the wavelength of the emitted radiation.

[2]quantities which depend on H_0 are usually expressed in terms of h, where $h = H_0/100$ kms^{-1} Mpc^{-1}

$$\rho_{0c} = \frac{3H_0^2}{8\pi G} \tag{1.6}$$

It can be seen from equation 1.5 that the value of the density parameter, Ω, determines the value of the curvature parameter, k. For $\rho < \rho_c$, $k = -1$, and the expansion velocity is always positive (the Universe is *open*); for $\rho > \rho_c$, $k = +1$, and the expansion at some time changes direction (the Universe is *closed*); for $\rho = \rho_c$, k=0, and the expansion rate $\rightarrow$0 as $t \rightarrow \infty$ (*critical Universe*). In the presence of a Λ term (as currently favoured in the best-fit cosmology of Ω_Λ ~0.7, Ω_M ~0.3 (see eg., de Bernardis et al. 2001, and references therein)), the fate of the Universe is undetermined.

If the universe is expanding now, then obvious questions are *has it always been expanding, and if so how did it begin?* Alpher & Herman (1948) predicted that if the universe began with a "primordial fireball" (now called "The Big Bang"), then this could be verified via relic background radiation. Supporting evidence was discovered by Penzias & Wilson (1965), in the form of the Cosmic Microwave Background (CMB) radiation, at a temperature of 3K. Alpher, Bethe, & Gamov (1948) also proposed a model of cosmological nucleosynthesis. Due to difficulties in explaining the abundance of helium in the universe (produced via fusion processes in stars) they suggested that some fraction of the helium was produced by hydrogen fusion in this primordial fireball. The study of light element abundances is an important, but technically complex area of cosmology. It has implications for the total density of baryonic material in the Universe (see later), and even predicts the number of neutrino types. Measurements of primordial abundances are complicated due to *astration*, the processing of primordial elements in stars (see, for example, Kolb & Turner 1990).

Another key discovery came with the measurement of rotation curves in spiral galaxies. Since these systems are rotationally supported, assuming stars are on circular orbits, simple Newtonian dynamics state that

$$\frac{v^2}{r} = \frac{GM(<r)}{r^2} \tag{1.7}$$

where v is the rotational velocity at a radius r, and $M(<r)$ is the mass enclosed within that radius.

Measurements of the rotation velocity as a function of radius showed that beyond the visible extent of the galaxy, instead of the velocity falling as described above, it remained constant. This implies that either the enclosed mass of the galaxy is still increasing

beyond where the starlight ends, or our theory of gravity is incorrect. This lead to the interpretation that a large fraction of the matter in the universe is invisible to conventional observational methods, or *dark*. The fraction of dark matter required increases with scale. For example, galaxies have mass to light ratios (M/L)$\sim$10, groups of galaxies have M/L$\sim$100 and clusters of galaxies have M/L$\sim$500 [3] (see §1.2). Modifications to Newtonian gravity in the limit of small accelerations have also been proposed (Milgrom 1983), but such theories are not widely accepted and are difficult to simulate.

Observational evidence for dark matter had been discovered 40 years earlier, but was not taken seriously at the time. Shapley (1933, 1934, 1935) made the first major survey of the distribution of galaxies. He saw that on large scales (seen in 2d data) galaxies are essentially distributed homogeneously, but on smaller scales there exist irregularities in the form of overdensities - groups, clusters and superclusters. The Coma cluster represents the richest nearby cluster of galaxies. It was studied by Zwicky (1933). He argued that since clusters of galaxies appeared to be smooth isolated systems, they should be in gravitational equilibrium. He thus assumed the Virial Theorem could be applied and compared the mass inferred from the light of the member galaxies' stars with the dynamical mass as measured by the velocity dispersion of the same galaxies.

For a gravitationally supported system in dynamic equilibrium, the Virial Theorem states that $2T + U = 0$ where T is the kinetic and U the potential energy of the system. Now,

$$T \approx \frac{1}{2} M_{cl} < v^2 > \tag{1.8}$$

where M_{cl} is the mass of the cluster, and $< v^2 >$ is the mean square velocity in three dimensions. The actual observable is the line-of-sight velocity dispersion, σ rather than its 3D equivalent. For an isotropic system $< v^2 >= 3\sigma^2$.

$$U \approx -\frac{GM_{cl}^2}{R_{cl}} \tag{1.9}$$

where R_{cl} is the radius of the cluster, and G is the gravitational constant.

Thus, the Virial Theorem reads,

$$M_{cl} \approx \frac{3\sigma^2 R_{cl}}{G} \tag{1.10}$$

[3]The division between these classes is not clear-cut, but in general: groups contain $\sim$10 galaxies, clusters $\sim$100-1000, and superclusters contain several clusters of galaxies. Galaxy associations containing fewer galaxies than a group are referred to as *the field*. Note: few galaxies are truly isolated.

Zwicky (1933) demonstrated that the sum of the mass traced by galaxy light was insufficient to make up the mass of the cluster measured from its dynamics by a factor of around a hundred. He thus concluded that some invisible mass (dark matter) must account for the difference. This mass discrepancy was paid little attention, until Kahn & Woltjer (1959) noticed a similar effect in the local group. The mass as determined from the velocity of our neighbour galaxy M31 is ten times more than the sum of the two masses as traced by starlight. This extended Zwicky's result from rich clusters to groups of galaxies. Results from Big Bang Nucleosynthesis (BBNS) models suggested that only a fraction of the total amount of dark matter is in the form of baryons.

With the field equations of GR as a framework, and observational data accumulating, various models for the growth of structure in the Universe developed in the 1970s. These models thus had to take into account the fact that a large fraction of the mass of the Universe was invisible, and its composition unknown, although its behaviour (ie. obeying the laws of gravity) was known. In such models, the Universe is treated as a smooth density field, at early times. Fluctuations occur in the field which grow with time. become unstable to gravitational collapse, turn around and condense into overdense structures. These eventually become the galaxies and large scale structure we see today. The linear solution for a perturbed, *static* fluid was first solved by Sir James Jeans (1928). He found that fluctuations grew exponentially with time. Using first order perturbation theory for an *expanding, flat, dust model universe*, for example, gives two modes of perturbation, one growing and one decaying (for details, see for example, Coles & Lucchin 1995), $\delta_+ \propto t^{2/3}$ and $\delta_- \propto t^{-1}$ (where $\delta_{+/-} = \delta\rho/\rho$ is the fractional density change of the perturbation. and t is time). In such a model, fluctuations grow more slowly than for the static case. Therefore, the expansion of the universe seriously retards the growth of such condensations. Fluctuations grow until such a time that the mass of the fluctuation exceeds that which can be supported by the random motions of the particles within it. The fluctuation then turns around and collapses.

Two main scenarios for structure growth were put forward in the 1970's. The first was put forward by Zel'Dovich and collaborators (eg, Zel'Dovich 1970), and suggested structure grew in a top-down fashion, with large structures forming first as large, flattened pancakes, and then fragmenting into smaller systems such as galaxies. This theory had several problems, the main one being that it predicted large scale fluctuations in the CMB, in excess of the observations. The second scenario advocated particularly by Peebles (1965,1972), hypothesised structure grew in a bottom-up manner, with small structures

forming first and coalescing to form larger structures. He further suggested that statistical randomness in an "incoherent dust" model induces the growth of larger instabilities with increasing time. Press & Schechter (1974) devised an analytic treatment based on these assumptions to describe the mass spectrum of these condensations. Their formula has the form $n(M,z) \propto \nu_M e^{-\nu_M^2/2}$ where $\nu_M \approx \delta_c/\sigma_M(z)$ and $\sigma_M(z)$ is the rms fractional mass fluctuation on the scale of mass M at a redshift z, and $\delta_c \approx 1.69$ is a numerical constant which is only a very weak function of epoch, cosmology and "non-sphericity". They tested their formalism against computer N-body simulations in which part of the expanding Universe is modelled as a box of N point masses (where N is a large number), interacting through their mutual gravity (they are, in this way, able to follow structure growth into the non-linear regime, inaccessible to first-order perturbation theory). Their simple expression has done remarkably well at describing the mass spectrum of objects obtained from numerical simulations for over twenty years, and it is only recently with the latest high resolution N-body simulations that the Press-Schechter theory has been shown to fail at the high and low mass ends. An improved (but closely related) analytic approach has been developed by Sheth & Tormen (1999) and a formula based on fits to large simulations has been proposed by Jenkins et al. (2001).

The mass function depends sensitively on Ω_m, more specifically on the combination $\sigma_8\Omega_m^\alpha$, where σ_8 is the rms fluctuation amplitude within a sphere of radius 8 h^{-1}Mpc, and $\alpha \simeq 0.4 - 0.5$ is weakly dependent on cosmological parameters, and the shape of the power spectrum (White, Efstathiou & Frenk 1993). Thus, measurements of the local mass function constrain this combination of parameters. Further, the degeneracy can be split by measurements of the mass function at different epochs.

1.1.1 The Significance of Galaxy Clusters

Clusters are the most massive virialised objects in the Universe. Since clusters form from extremely high peaks in the initial density field on scales of around $10h^{-1}$Mpc, they are sensitive to the amplitude of the power spectrum on these scales. Being massive makes them relatively easy to find out to large redshifts (see §1.2). Thus, observations of the cluster mass function out to large redshifts can place tight constraints on cosmological parameters (ie. Ω_m, σ_8, Λ). Measurements of cluster masses are described in more detail in §1.3.1.

Clusters also prove useful laboratories for studying galaxy formation and evolution. They comprise mainly elliptical galaxies, which are relatively simple systems in terms of

stellar populations. Star formation appears to have ended in elliptical galaxies at $z \gtrsim 1$ and the stars evolved passively ever since (see Chapter 5 for more details). Modelling of the stellar populations of galaxies has advanced tremendously in the last twenty or so years since the pioneering work of Tinsley in the late 1970s. Many codes now exist for constructing the spectral energy distributions (SEDs) of galaxies from a range of composite stellar populations (eg, Fioc & Rocca-Volmerange 1997, Bruzual & Charlot 1993, Kodama & Arimoto 1997). These stellar population synthesis (SPS) models start with some assumption for the distribution of masses of stars at their birth (the initial mass function - IMF) for a simple stellar population (SSP); new stars are born according to some given star-formation rate (SFR); and the stars evolve along tracks determined empirically from observations of local stars and resolved stellar populations in nearby external galaxies. These empirical models are combined with complex microphysics such as the opacities of stellar atmospheres. Usually a "closed-box" model for chemical evolution is employed in which elements produced in stars and expelled through stellar winds/ supernovae are recycled into the next generation of stars, and metallicity dependent properties of the next generation of stars are thus appropriately considered. In such a model, no metals leave or enter the system under consideration. With SPS codes, stellar populations can be constructed with a given age, star-formation history (SFH), IMF, etc. and then an SED output. This can be transformed to a desired redshift and convolved with standard broad-band filters to give observed colours in standard passbands. By varying parameters in the model, and making reasonable assumptions for other parameters, properties such as SFH of the galaxy can be deduced. More recently, nebular emission in star forming regions has been incorporated into models, allowing not just broad band colours, but also spectral emission lines to be incorporated into the SED (Fioc & Rocca-Volmerange 1997, Charlot & Longhetti 2001). There are many complications with such studies though, for example: the degeneracy between age and metallicity effects. The SED of a galaxy is almost unchanged if the metallicity (Z) and age of its stellar populations is changed by $\Delta Z/\Delta \mathrm{age} \sim 2/3$ (Worthey 1994). This degeneracy can be broken for certain combinations of spectral line indices or broad band colours.

In the last decade, SPS models have been combined with models for the growth of structure (either Press-Schechter formalisms or direct cosmological N-body simulations) to form semi-analytic models for galaxy formation and evolution (Cole et al. 1994, Kauffmann et al. 1996, Cole et al. 2000). These incorporate parameterisations of poorly-understood physics (eg. feedback effects from star-formation), which are tuned so that

the models attempt to reproduce local galaxy observables, in order to make predictions for observables at higher redshift.

If the hierarchical picture is correct, these models are crucial to interpreting evolutionary trends in clusters. The main difficulty in confronting the model with observational data is that it is incorrect to associate rich/ massive/ X-ray-luminous clusters in the local Universe with equally rich/ massive/ X-ray-luminous clusters at high-redshift. Since clusters grow through mergers/ accretion, the most massive clusters at z$\sim$1 have grown into systems more massive than anything in the local Universe by z$\sim$0 (eg, Kauffmann & Charlot 1998).

1.2 The History of Cluster Surveys

The first attempt at a large, homogeneous survey for galaxy clusters was conducted by Abell (1958). This was a phenomenal effort by one individual to identify overdensities of galaxies by visual inspection of Palomar Observatory Sky Survey (POSS) photographic plates. The survey yielded nearly 1700 clusters meeting Abell's criteria for magnitude and richness (compare this with the number of clusters previously known - only a few dozen, selected in a much more heterogenous way). Similar catalogues were constructed by Zwicky and collaborators (Zwicky, et al. 1961-1968). Abell's (1958) Northern catalogue was extended to the Southern hemisphere by Abell, Corwin & Olowin (1989), applying the same criteria. The total number of clusters in the final catalogue is in excess of 4000. Abell's (1958) original criteria were: *richness* - after statistical subtraction of foreground and background contamination at least 50 member galaxies must be no fainter then 2 magnitudes fainter than m_3 (where m_n is the magnitude of the n^{th} brightest cluster member); *compactness* - at least 50 members must be within a projected distance fixed in physical units. The Abell radius, R_A is $1.5h_{100}^{-1}$Mpc, and the relation used by Abell was $R_A = 1.7/z$ arcmin, where z is the cluster redshift estimated from the empirical relation between m_{10}-z (see Figure 9, Abell 1958); *distance* - clusters must be no more distant than $z = 0.2$ (set so that $m_3 + 2$ was visible to the limits of the POSS plates), and no closer than $z = 0.02$, so as to fit within the field of one POSS plate.

With the advent of space-based X-ray telescopes, such as UHURU, a new way to discover galaxy clusters was found. Spatially extended, thermal X-ray emission was detected and shown (through observations of X-ray emission lines of highly ionised iron at a temperature of 30-100 million K) to be due to the hot intracluster medium (ICM) - the

plasma trapped in a cluster's potential well (Mitchell et al. 1976, Serlemitsos et al. 1977). This provided a way to show that the cluster was a genuine physically bound system. The optical selection techniques such as Abell's lost favour. Their main disadvantage was that there was no way, at the selection stage, to distinguish between genuine clusters, and chance projections of less massive galaxy groups along the lines of sight. Extensive discussions of the contamination due to projection effects have been published (eg, Katgert et al 1996, Van Haarlem, Frenk, & White 1997). Observationally expensive spectroscopy was needed to obtain redshifts and confirm that the overdensities really existed in 3D.

The first (very shallow) X-ray selected samples (eg, Piccinotti et al 1982) suffered from confusion and incompleteness and most of the 30 discovered clusters lay at $z \lesssim 0.1$. The large beamsizes of early X-ray detectors meant that point sources (such as stars) could be misidentified as clusters (extended sources); and also that sources nearby on the sky could be confused. The first deep observations were made using the Einstein Observatory (Henry et al. 1982, Henry & Lavery 1984), but these were based on follow up of optically selected clusters, or serendipitous discoveries. This made quantifying the selection function very difficult. The survey of Edge et al. (1990) used the Ariel V all-sky survey with data from smaller beamsize instruments (Einstein and EXOSAT) to reduce confusion. This produced a true X-ray selected catalogue of 46 clusters to a flux limit of 1.7×10^{-11} erg cm^{-2}s^{-1}. The Einstein Extended Medium Sensitivity Survey (EMSS, Gioia et al. 1990) found 67 clusters in a smaller area, but down to a flux limit $\sim$100 times fainter, some at redshifts as large as $\sim$0.6. This survey was made using serendipitous detections of clusters in fields where a known cluster was not the target of the observation. Such methods should be treated with caution when estimating quantities such as the space density of clusters, though. The object of the observation could be, for example, an active galactic nucleus (AGN). Since AGN commonly inhabit cluster environments, the discovery of a cluster in such a field is not a truly random occurrence.

With a vast archive of deep X-ray data from pointed ROSAT observations, the most

N_{gals}	Class	N_{gals}	Class
30 - 49	0	130 - 199	3
50 - 79	1	200 - 299	4
80 - 129	2	300+	5

Table 1.1: Abell Richness Classification. N_{gals} is the number of galaxies statistically belonging to the cluster within an Abell radius (see text).

recent X-ray surveys such as RIXOS (Mason et al. 2000), WARPS (Jones et al. 1998), SHARC (Romer et al. 2000) and the 160 square degree survey (Vikhlinin et al. 1998) are able to cover wide areas (~10 - 100 degrees^2) to faint flux limits in such serendipitous searches.

Despite the revolutionary new X-ray techniques, four large optical photographic cluster surveys with follow up spectroscopy were undertaken in the late 1980s. The first two used visual inspection of photographic plates, and the second two utilised machines which automatically measured parameters of objects from photographic plates. Gunn, Hoessel & Oke (1986) found a total of 418 clusters for which they measured redshifts, in the range $0.15 < z < 0.92$. Their survey was conducted using a variety of telescopes, passbands, and photographic emulsions and clusters were selected "by hand" as overdensities. It should be noted that such a heterogenous survey is unsuitable for studies of the evolution of cluster galaxy populations. The authors comment that the main factor for identifying a cluster was its contrast with the background, which varies over different redshift intervals (the contrast generally decreasing with increasing redshift), but depending in a complicated way on the mean colour difference between the cluster and the field.

Couch et al. (1990) visually examined 55 high contrast film derivatives of prime focus AAT photographic plates taken in the J (b_J) and/or F (r_F) passbands to select clusters. They used a simple selection criterion - the enhancement over the mean background - defining the contrast, σ_{cl}, as $\sigma_{cl} = (N_{cl} - N_f)/\sigma_f$, where N_{cl} is the number of galaxies in the region centred on the density enhancement, down to the limit of the film; N_f the mean field count; and σ_f its variance determined from counts within similar areas, placed randomly on the film. The visual inspection process was tested exhaustively against simulated fields.

Using estimates for the local space density of clusters and applying their selection function, the number of F_r-band clusters found agreed well with predictions in which the number density does not evolve with cosmic epoch (no-evolution), but too many J_{b_J}-band[4] clusters were found. To try to assess whether this discrepancy is due to evolution or to higher spurious detection rates in the bluer passband, the authors obtained spectroscopy for a complete subsample of 11 fields, to a contrast limit of $\sigma_{cl} > 4.0$. Through a detailed study of a few high redshift clusters, they conclude that the J_{b_J}-band excess is due to either projection of foreground groups from spiral-rich groups, or to recent star-formation in the distant clusters. The spectroscopic sample was too small to assess the relative

[4]The subscript is used to avoid confusion with the 1.25μm J-band, referred to later in the thesis.

contribution of these effects.

The Automatic Plate Measuring (APM) machine cluster survey (Maddox 1988, Dalton et al. 1997), and the Edinburgh-Durham Cluster Catalogue (EDCC, Lumsden et al. 1992), were the first machine-based cluster catalogues. The EDCC covered an area of 1500 deg^2 centred on the South Galactic Pole, utilising COSMOS scans of 60 UK Schmidt survey plates, and was 95% complete to $b_J = 20.5$. The cluster selection was performed using a peak-finding algorithm to find local density enhancements. Comparison with the Abell catalogue showed that the EDCC is ~90% complete for Abell-type clusters, in addition to discovering many new clusters not in the Abell catalogue. They also concluded that the Abell magnitude system is biased toward bright magnitudes, and the Abell richness estimates are prone to larger uncertainties than Abell suggested. No richness limit was imposed, and the final catalogue comprised 737 systems from clusters to groups. The APM cluster catalogue was constructed using a percolation technique in which all pairs of galaxies closer than 0.7 times the mean galaxy separation are linked; all mutually linked galaxies are assigned to the same group; and the centroid of any group containing $\geq$20 galaxies is then taken to be the centre of a cluster candidate. The final catalogue comprised 957 candidate clusters over 4300 degrees^2. Spectroscopic confirmation was made of a subsample of 229 of these (Dalton et al. 1994).

With the advent of high quantum-efficiency, large format charged-coupled devices (CCDs) in the early 1990s, optical cluster studies are again becoming attractive. The first serious attempt at an automated optical CCD survey with a quantifiable selection function was carried out with the Palomar Distant Cluster Survey (PDCS, Postman et al. 1996). Their pioneering work involved assuming a model for the spatial and luminosity distribution of galaxies in a cluster and in the field, and filtering the data using these models as templates. Using a likelihood analysis of the data, with cluster richness and redshift as free parameters, the most likely cluster candidates could be extracted, and their redshifts estimated as a by-product of the process. This technique is known as the matched-filter (MF) and is discussed in more detail in Chapter 2. This method reduced spurious clusters due to projection effects compared with the more traditional techniques described above, but many still remained (discussed further below).

The MF need only be used on photometric data from a single passband, but with an additional filter other techniques are possible. Algorithms using colour selection have been proposed (eg, Gal et al. 2000, Gladders & Yee 2000). Gal et al. (2000) began a $z \lesssim 0.3$ cluster survey over 60 square degrees. This was intended to supercede the Abell

catalogue, using three-band photographic data calibrated with CCD photometry to the Gunn g,r,i system. They used mild colour cuts to reduce contamination due to field-like galaxies. Since elliptical galaxies are predominantly found in dense environments (the morphology-density relation, Dressler 1980), and exhibit only a narrow range of colours at a given redshift, in any environment, data can be filtered in colour to remove galaxies with colours incompatible with ellipticals. Once the data have been processed in this way, an adaptive kernel (Pisani 1996) spatially filters the data to select overdensities in such a way that no assumption for the shape of the cluster is required. They argue that this technique avoids bias due to assuming a spatial profile for the cluster, as many of their candidates are asymmetric; and that the Abell catalogue has a bias toward centrally concentrated clusters, especially those with dominant central (cD) galaxies. They show several convincing cluster candidates missed in the Abell catalogue, but spectroscopic confirmation has not yet been published.

Gladders & Yee (2000) took the colour selection a stage further, placing very strict colour cuts in two-colour data, to only search for overdensities of galaxies with colours consistent with elliptical galaxies at a given redshift (see Chapter 2). This works because in all known clusters for which multi-band photometry exists (regardless of how the cluster was selected), a tight relation exists between the colour and magnitude of its early-type galaxies (eg, Bower, Lucey & Ellis 1992, Visvanathan 1978). This relation is clearly visible over small spatial scales ($\sim$ the size of the cluster core), as early-type galaxies are predominantly found in the central regions of a cluster (Dressler 1980). This greatly reduces the projection effects of the single-passband methods; however, this raises the question of colour bias in the cluster sample. Richer clusters with a high fraction of red galaxies are much more easily detected than poorer clusters with a higher fraction of blue galaxies. Careful consideration must be made of the selection function if such a cluster sample is to be used to study galaxy evolution in clusters.

Cluster candidates found by the MF can be examined for the presence of a colour-magnitude relation (CMR) (eg, Olsen et al. 1999b). This would seem to be a good independent test of the reality of the cluster. The CMR also provides an accurate way of measuring the redshift of a cluster (eg, Stanford, Eisenhardt & Dickinson 1998). The advantage of using the CMR to measure the redshift, rather than fitting photometric redshifts to individual galaxies (discussed in Chapter 5), is that the colours of many galaxies at the same redshift are averaged for the estimate, rather than fitting on a galaxy-by-galaxy basis (which can still lead to quite high uncertainties even with four

or more photometric passbands (Bolzonella et al. 2000)). Using photometric redshifts of individual galaxies has also been proposed as a method to find high-redshift clusters (Kodama, Bell, & Bower 1999), but this is much less efficient than the CMR method, mainly for the reason just given.

The morphology-density relation has also been used in another way for cluster finding. Ostrander et al. (1998) took advantage of the Hubble Space Telescope (HST)'s exquisite resolution to morphologically select a sample of early-type galaxies with which to search for overdensities. This method has a similar success rate to the MF (~60-70%). Projection effects due to superpositions of poorer systems are similarly problematic, as the advantage of the colour (and hence redshift) information provided by the Gladders & Yee (2000) method is not utilised.

Several other recent cluster selection methods are worth noting. Variations of the single-passband techniques have been proposed (for example, Lidman & Peterson 1996, Kepner et al. 1999, Kawasaki et al. 1998, Kim et al. 1999, Lobo et al. 2000) including a counts-in-cells technique, replacing assumptions in the cluster models, using Voronoi tessellation as the density estimator, and incorporating photometric or spectroscopic redshifts. The C4 algorithm (Nichol et al. 2000), one of the cluster-finders used by the Sloan Digital Sky Survey (SDSS) collaboration (York et al. 2000) uses multi-colour photometry to look for neighbouring galaxies of similar colours, and also the ROSAT All-Sky Survey (RASS) (Voges 1993) data to look for coincident X-ray emission. The surface brightness fluctuation (SBF) method of Dalcanton (1996), Zaritsky et al. (1997) uses shallow imaging data with astronomical sources masked-out to look for enhancements due to clusters in the extragalactic background light. This is an interesting idea, but quite difficult to apply (for example, the data needs to be extremely well corrected for detector sensitivity variations, and there is the potential for confusion between distant clusters and nearby low surface-brightness galaxies), and it is not obvious that the selection function is easily quantifiable. That said, a large catalogue with many convincing cluster candidates selected in this way has recently been published (Gonzalez et al. 2001). The weak-lensing technique of Wittman et al. (2001) is an interesting and potentially very powerful method. Using only four band photometry of a "blank field", they measured ellipticities of galaxies in the field, and estimated their redshift distribution via a photometric redshift technique (Bolzonella et al. 2000). Using this information, a statistical weak shear signal was seen due to the gravitational field of a galaxy cluster within the region. The shear as a function of source redshift was used to measure the redshift of the cluster (lens) independently of

any photometric property of the cluster. Furthermore, the redshift and mass of the cluster were measured using spectroscopy and found to be in good agreement with the values obtained from the gravitationally measured values. This offers a promising method for selecting clusters by *mass* and allowing a direct measurement of the cluster mass function. With sufficient passbands providing the photometric redshifts, it should be possible to measure the mass in 3D (mass tomography) such as is planned with the VISTA survey [5]. The Sunyaev-Zeldovich (SZ, Sunyaev & Zeldovich 1972) effect offers another possibility to select clusters by mass. The CMB spectrum is distorted as CMB photons pass the hot ionised cluster gas of the ICM. This depends only on the optical depth to Compton Scattering and the temperature of the plasma (the relation between $T_X$and cluster mass is discussed in §1.3.1). For an example of the application of the SZ effect to cluster-finding, see Holder et al. (2000).

A final set of methods for searching for clusters involve targeted searches around objects which are thought to be indicators of overdense environments. These are usually radio-loud objects such as radio-loud galaxies and quasars (AGN), and will be discussed in later chapters.

1.3 The Relative Merits of Optical and X-ray Surveys

The drawbacks of optically-selected catalogues have been discussed above. To summarise, projection effects are a big problem - firstly because they cause the contrast between the cluster and the background galaxy distribution to be artificially increased (possibly leading to the cluster's incorrect inclusion in a catalogue), and secondly they complicate the study of cluster galaxy properties by adding excess galaxies into the cluster region which are not true members. However, it should be noted that the second point applies (probably to a lesser extent) to optical studies of clusters selected by any method, and that the effect can be reduced with spectroscopy of a large enough sample of galaxies in the cluster region.

The drawbacks of X-ray selection can be seen by considering the question *what makes a galaxy cluster visible in the X-ray?*

The X-ray luminosity of a cluster can be expressed as the sum of the X-ray luminosity from all the individual cluster galaxies and the contribution from the ICM

$$L_X = \Sigma L_{X\,gal} + \rho^2 V T^{1/2} \tag{1.11}$$

[5] http://www.vista.ac.uk/

where ρ,V, and T are the density, volume and temperature of the ICM, respectively. Thus, in order to be an efficient X-ray emitter, a cluster must contain a sufficient mass of gas. This gas must be heated to X-ray emitting temperatures (note: the cooling rate and hence the rate of X-ray production also depends on the metallicity of the ICM). The gas must be sufficiently centrally concentrated (ie. dense) to be observed; but not so much so that the emission is unresolved (since X-ray clusters are defined as extended sources). Projection effects of clusters along the line-of-sight are also possible in X-ray surveys, but much less likely (as clusters massive enough to emit in the X-ray have a low space density). A more common problem is contamination of the X-ray flux due to other sources, such as AGN (either within the cluster, or along the line of sight).

X-ray emission can also be affected by the presence of cooling flows (Fabian 1988). The centres of some clusters show evidence of cooler gas. X-ray surface brightness profiles imply high central gas densities and therefore short cooling times; and X-ray spectroscopic observations have shown cluster core temperatures factors of 10 lower than the cluster mean. Such a mechanism increases the emission-weighted luminosity of a cluster as, although the temperature is lowered, the density is increased, and the luminosity depends on density squared, but only the square root of temperature. This can also affect mass estimates from X-ray data, see §1.3.1.

Briel & Henry (1993) used the RASS to conduct a comparison with the Abell catalogue. This was the first attempt to compare clusters found via optical and X-ray selection at low redshift [6]. Briel & Henry (1993) took a complete (*wrt* the Abell catalogue) sample of 145 Abell clusters, with $\bar{z} = 0.17$. 46% of the clusters were detected at >99.7% significance down to a point source flux limit of $\approx 4.2 \times 10^{-13}$erg s^{-1}cm^{-2} in the 0.5 – 2.5 keV band. 80% of ARC$\geq$0 clusters and 86% of ARC$\geq$1 clusters are X-ray emitters with fluxes $> 1 \times 10^{-13}$erg s^{-1}cm^{-2}, and nearly 90% of Abell's clusters emit in the X-ray above some level. A strong correlation ($\geq$99.95% confidence) was found between X-ray luminosity and richness (taking into account both X-ray measurements and upper limits for non-detections) with an rms scatter of a factor of 2.5 in $L_X$for a given richness (Bower et al. 1994). It is interesting to note that at $z > 0.3$ [7], 6 out of the 7 clusters are detected. This implies that only the optically richest (and hence most X-ray luminous clusters)

[6] In this thesis, the arbitrary division of cluster redshift regimes into: *low* - $z \lesssim 0.1$; *intermediate* - $0.1 \lesssim z \lesssim 0.5$; *high* - $z \gtrsim 0.5$ is adopted.

[7] Although Abell's catalogue is restricted to $z \leq 0.2$, he published a supplemental "statistical" catalogue containing higher redshift clusters.

are selected in this redshift regime (by Abell's method). However, this study is unable to say if there are any X-ray emitting clusters missed by Abell. This question has been addressed to some extent by Neta Bahcall (unpublished) [8]. In a study using the Einstein Medium Sensitivity Survey (EMSS) all the 25 or 30 nearest Abell clusters (near enough that a richness class 0 system should be visible above the X-ray flux limit) of ARC$\geq$0 were detected as X-ray sources. Conversely, examining optical photographic plates at the position of extended X-ray sources showed many overdensities of ARC<0 but none which corresponded to ARC>1 systems. This suggests that locally there are no bright X-ray clusters which are optically poor systems, and that the richest optical systems are X-ray emitting clusters.

Prior to the recent large, deep, X-ray selected surveys based on data from the ROSAT archive (eg. Jones et al. 1998, Romer et al. 2000, Vikhlinin et al. 1998), since the most X-ray luminous clusters have a low space density and deep X-ray surveys are observationally expensive, the obvious first step is to follow up distant optically selected clusters with ROSAT. However, the correlation between optical richness and X-ray luminosity (the observables in each survey) is known to have considerable scatter even at low redshift. Thus the selection function in terms of X-ray luminosity of an optically selected survey does not have a sharp cut-off in L_X, but rather a gradual turnover (see Figure 2 of Bower et al. (1994) for an illustration). Bower et al. (1994) undertook ROSAT X-ray observations of optically selected clusters from the Couch et al. (1990) catalogue. From the 46 square degree contrast limited catalogue (described above), they took clusters with reliable spectroscopic follow up and X-ray data (taken to be a random subsample of the full catalogue) in the redshift range 0.15 to 0.66. The total sky coverage of this survey was 26.8 square degrees and contained 14 clusters. The X-ray luminosities of all but two of the clusters was found to be surprisingly weak - less than 5×10^{43}erg s^{-1}. This decrease with respect to the locally measured value was attributed to evolution in the XLF between z=0 and $\approx$0.4. The alternative is that if the XLF does not evolve between these redshifts, then the missing X-ray luminous clusters must be made up of optically poorer systems, missing from this sample.

Castander et al. (1994) used ROSAT to observe cluster candidates in the redshift range 0.7-0.9 from the Gunn, Hoessel & Oke (1986) optical cluster catalogue and also found surprisingly weak X-ray emission ($\approx10^{43}$erg s^{-1}). The heterogeneity of the Gunn, Hoessel & Oke (1986) sample was described above, but in an attempt to make the selection

[8] In a comment made in the discussion following M. J. Geller's talk at the 1990 STScI symposium.

function more quantifiable, Castander et al. (1994) selected a complete subsample of Gunn, Hoessel & Oke (1986) candidates by choosing the telescope+plate combination which yielded the most distant spectroscopically confirmed clusters. The total area of this sub-survey was 3.5 square degrees.

Nichol et al. (1994) also attempted X-ray observations of high-redshift cluster candidates, but in a less reproducible way. They used a combination of optically-selected cluster candidates and extended or wide-angle radio sources [9]. They found no bright X-ray clusters ($L_X \gtrsim 10^{45}$ erg s^{-1}), and similarly to Castander et al. (1994) found weak emission from the rich optical clusters.

In order to assess whether the optically rich, X-ray poor clusters of Bower et al. (1994) are genuinely massive clusters, or just chance superpositions along the line-of-sight, Bower et al. (1997) performed spectroscopy of the original sample to measure velocity dispersions. Around 10 redshifts were secured for cluster members, with which to determine the velocity dispersion. An attempt was made to preferentially select red galaxies (from the original plates) for spectroscopic observation. It is important to note the selection process, as blue cluster members typically have higher velocity dispersions than the cluster as a whole; whereas red members appear to be more representative (Carlberg et al. 1996). They found that, due to the low number of cluster members, the velocity dispersion estimates had relatively large uncertainties, but by stacking the clusters to make a composite example typical of this class of object, a more accurate estimate could be made. However, this method is particularly susceptible to artificial inflation of the velocity dispersion if the redshift of the cluster centre is not well-determined (thus, the stacked clusters will be shifted slightly in velocity prior to combination). The result was that the composite cluster had a velocity dispersion about a factor of two higher than is typical for a cluster of its X-ray luminosity. The authors suggest that the increased velocity dispersion is evidence that the cluster is not truly virialised and that the galaxy population sampled is still infalling, or that the clusters selected by the Couch et al. (1990) sample are due to projection effects due to filaments of galaxies aligned with the line-of-sight.

The MF method should somewhat reduce contamination over simple overdensity selection. So, the next step was to examine MF catalogues. Holden et al. (1997) measured fluxes/ limits for 31 (of the 79) PDCS candidates that lay in archival ROSAT PSPC data,

[9] Briefly, wide-angle radio sources are a signature of the pressure of a radio galaxy moving through an ICM - see Chapter 3

to a flux limit of 3×10^{-14} erg cm^{-2}s^{-1} in the 0.4-2.0 keV band, corresponding to a limit of $L_X \approx 5 \times 10^{43}$ erg s^{-1}, assuming the MF estimated redshifts are correct. They found 6 possible detections, all of which could be due to contamination and 3 of which probably are. Thus, PDCS clusters are not strong X-ray emitters, consistent with observations of other optically-selected clusters (Bower et al. 1994, Castander et al. 1994, Nichol et al. 1994). The X-ray luminosity - richness ($L_X - \Lambda_{cl}$) relation found by Briel & Henry (1993) was not seen, but this is not surprising given the large uncertainties in the estimated redshifts. The data is consistent with the hypothesis that the Abell and PDCS catalogues sample the same clusters but at different redshifts.

To assess the accuracy and completeness of Postman et al.'s (1996) MF method, Holden et al. (1999) undertook spectroscopy of a subset of 16 cluster candidates. The PDCS catalogue was resampled in such a way as to preferentially select low redshift, high richness clusters. Although few galaxies with similar redshifts were found in some candidate fields, they state that using their selection techniques, finding three galaxies within 1500 kms^{-1} of each other should only occur by chance ~3% of the time. This leads to a space density of PDCS clusters of $31.3^{+30.5}_{-17.1} \times 10^{-6} h^3 Mpc{-}3$ in the redshift range $0.1 < z < 0.35$. This is $\approx 5\times$ the space density of Abell clusters. Continuing this study with more redshifts per cluster, Holden et al. (2000) measured redshifts in 17 PDCS fields, and calculated velocity dispersions (albeit with few members for each cluster) for 11. They found 11/12 clusters were real (the remaining fields had too few redshifts to tell), and most PDCS clusters had velocity dispersions appropriate for clusters, although $\sim 1/3$ of these had richnesses of clusters with velocity dispersions appropriate for groups ($\sim$ 200 kms^{-1}). Re-evaluating the X-ray luminosity function (XLF) for the Holden et al. (1997) data with the new redshifts yields an XLF consistent with that found from X-ray selected cluster surveys. This they claim shows that optical MF surveys do not miss clusters which would be found in an X-ray selected survey. They conclude by saying that either the Abell catalogue is incomplete by a factor of 3 or 4 (which does not seem to be the case from X-ray selected surveys and modern automated optical surveys (eg, Gal et al. 2000)); or there is a mismatch between Abell's richness measurements and machine-based measurements. This should be addressed by surveys such as that begun by Gal et al. (2000).

1.3.1 Cluster Mass Estimates

The oldest technique for estimating a cluster's mass, that of velocity dispersion from spectroscopy, has been described above. Most spectroscopy of clusters relies on typically ≈10 - 20 redshifts per cluster to determine a velocity dispersion. There is a tendency to underestimate velocity dispersions using so few redshifts (Zabludoff & Mulchaey 1998); or overestimate the mass with a correctly-measured velocity dispersion, if the system is not in virial equilibrium. Several surveys such as the ESO Nearby Abell Cluster Survey (ENACS, Katgert et al 1996) and the Canadian Network for Observational Cosmology cluster survey (CNOC1, Carlberg et al. 1996) made use of multi-object spectroscopy to obtain large numbers of spectra per cluster (≈ 20-100, and ≈ 50-200, respectively), for accurate velocity dispersion estimates. With this many redshifts, unvirialised systems are normally visible from substructure in the redshift histogram.

Hydrodynamic simulations predict a tight relationship between a cluster's X-ray temperature (T_X) and its binding mass (although note that most of these simulations do not include accurate gas cooling or feedback). These simulations show that as a cluster collapses, the gas is shock-heated to the virial temperature and rapidly settles into hydrodynamic equilibrium with approximately isothermal structure (Evrard 1990, Cen & Ostriker 1994). T_X is a more difficult quantity to measure observationally than L_X, but these quantities are correlated. Using a self-similar model, Kaiser (1986) predicted the relation $L_X \propto T_X{}^2$. The observed relation is in fact more like $L_X \propto T_X{}^3$ (eg, White, Forman & Jones 1997), with significant intrinsic scatter (at the level of about 10-20%). This correlation appears to hold out to redshifts ~ 1 (Fairley et al. 2000), although the current best measurements were made with the ROSAT satellite, which means that the errors in fitting $T_X$are quite substantial. Improved measurements will come with observations of the highest redshift clusters using the new generation of X-ray satellites.

About 50% of the local cluster population shows evidence for ongoing mergers, making truly relaxed clusters quite rare. Mathieson & Evrard (2001) explored the effects of substructure in temperature measurements, using hydrodynamical simulations. By producing realistic mock data (for the Chandra satellite), and analysing it in the same way as the real data, they found that (surprisingly) the emission spectrum of a realistically complex ICM is nearly indistinguishable from an isothermal gas, and that spectral-fit temperatures are commonly 10-20% lower than mass-weighted temperatures (since, the mass-weighted temperature follows the virial relationship it is therefore the more accurate

indicator of virial mass). This bias, which must be corrected for in cluster mass estimates, is due to accreting small lumps of cool gas which merge into the ICM and produce an excess of soft X-rays. The spectrum is then biased toward cooler temperatures until these lumps equilibrate with the surrounding medium.

A large sample of X-ray selected clusters analysed with many different mass estimators is provided by the CNOC sample. Lewis et al. (1999) calculated X-ray mass estimates for 14 clusters in the range $0.14<z<0.55$. These were then compared with dynamical mass estimates from velocity dispersions measured by Carlberg et al. (1996). No systematic bias between these two methods was found across the sample, although individual clusters could have X-ray-to-dynamical mass estimates discrepant by factors of up to 2. Further, using gravitational lensing mass measurements from the literature, two more mass estimators can be included in the comparison - *strong* and *weak* gravitational lensing masses. (By examining the ellipticities of field galaxies in the region of a cluster, the weak tangential shearing effect of the cluster's gravitational potential on background galaxies can be examined. The mass profile of a cluster can thus be reconstructed (Kaiser & Squires 1993). When the mass density in the central regions of a cluster exceeds a critical value, background galaxies may be strongly lensed - appearing as giant arcs or multiple images of the same object.) In the CNOC sample, weak lensing masses appeared systematically higher than X-ray masses by factors of $\sim$50%. Strong lensing masses were more discrepant, by factors of about 2.5. Such comparisons are complicated by the fact that the different techniques probe the cluster mass within different radii. The bulk of X-ray emission comes from the central $\sim$100kpc, so X-ray masses must be extrapolated to larger radii, under some assumption of the mass profile, in order to obtain a total mass. The strong lensing measurements gave poorest agreement among the other methods. Lewis et al. (1999) suggested this might be due to the lack of redshift information for the lensed arcs; possible offset between the lensing and X-ray cluster centres; asymmetry or substructure within the cluster; or possibly the strong-lensing mass is high due to mass superposed along the line of sight (strong lenses may be preferentially found in clusters which have such intervening mass structures).

Weak-lensing measurements are generally in good agreement with the dynamical and X-ray mass estimates. The two former techniques typically probe scales larger than the central $\sim$100 kpc where the latter technique is most sensitive. In a similar study, Smail et al. (1997) compared the same mass estimators for a sample of 12 (mostly optically selected) distant clusters; but found that the dynamical masses were about 50% higher

than weak shear masses. They state that the overestimates of the velocity dispersion may be due to the inclusion of outliers, or unidentified substructure in the velocity histograms. Such a problem is likely not present in the CNOC sample, due to their large numbers of redshifts per cluster. It should also be noted that for weak-shear measurements, the redshift distribution of the background galaxies must be known, and that accurate ellipticities be measured for them (requiring small or well-characterised instrumental distortions).

In conclusion, the different techniques for mass estimation are likely reconcilable with improved datasets. High numbers of spectra are necessary for accurate velocity dispersion estimates; wider-field, more-sensitive X-ray telescopes (such as the recently launched *XMM-Newton* and *Chandra*) will allow better fitting/ modelling of X-ray profiles; and the new-generation of wide-field instruments (such as ESO's Wield Field Imager) built with minimal optical distortions will allow better measurement of weak shear fields on cosmic scales (Rhodes, Refregier, & Groth 2001).

1.4 Thesis Plan

The aim of this thesis is to directly compare competing methods of cluster detection on the same regions of sky. Of primary interest is the comparison between optical and X-ray selection, with particular reference to searching for the optically rich but X-ray faint clusters reported by Bower et al. (1994) and Bower et al. (1997).

To this end, Chapter 2 introduces the optical data which lie in regions of the deepest archival X-ray images. This will form the basis for the X-ray Dark Cluster Survey (XDCS). The optical cluster finding algorithms are described in this chapter, along with methods for measuring cluster optical richness.

Chapter 3 explains how these algorithms are used to construct final optical cluster catalogues. The method of X-ray cluster selection is explained, and X-ray selected cluster catalogues are presented. The optical and X-ray catalogues are then directly compared, along with estimates of the accuracy of redshifts derived from the optical methods. The relationship between optical richness and X-ray luminosity is explored. Finally, publically available radio data is used to illustrate two methods for the radio selection of clusters.

Chapter 4 presents spectroscopic observations of optical cluster candidates, specifically selected to be non-detections in the deepest X-ray images (ie. X-ray dark clusters). The significance of these clusters is then assessed from spectroscopic redshifts and the accuracy of the optical finders tested.

Chapter 5 examines the use of photometric redshifts from additional near-infrared (NIR) observations of X-ray dark clusters. The significance of optically selected X-ray dark clusters is examined by searching for galaxy overdensities in multicolour space, and a possible extension of the optical selection technique using multicolour data is commented on.

Chapter 6 uses deep NIR observations of colour-selected subfields from the main XDCS survey to attempt to push the high redshift limit of the selected clusters into the $z\sim1$ regime. Predictions for selection of high redshift clusters in forthcoming large NIR surveys are made.

Chapter 7 discusses conclusions of the work and describes the prospects for future work in the field.

Chapter 2

An Optical and X-ray Survey for Galaxy Clusters

2.1 Introduction

In order to try to understand the effect that the selection method has on the resulting cluster catalogue, a coincident optical and X-ray survey has been undertaken. This is referred to as the X-ray Dark Cluster Survey (XDCS), as the project is specifically aimed at searching for the optically rich but X-ray under-luminous clusters described in Bower et al. (1994), Bower et al. (1997). By imaging exactly the same regions of sky at optical and X-ray wavelengths, one can directly compare the clusters found by the different techniques.

The history of cluster detection and some of the many different possible methods were outlined in the previous chapter. This chapter describes the datasets used, the reduction of the optical data and the development of the cluster detection algorithms, tailored to this particular project. The optical cluster-finders are designed to make as few assumptions as possible about the shape and extent/ concentration of the galaxies within the cluster. In this way, if the *X-ray dark* clusters are due to irregular, unrelaxed systems, this survey will still be sensitive to them. The resultant catalogues are presented in Chapter 3.

The optical survey uses identical passbands over a similar area to a similar depth as the recent ESO Imaging Survey (EIS, da Costa et al. 1999) which was also utilised for cluster detection using various techniques (eg, Olsen et al. 1999a, Olsen et al. 1999b, Lobo et al. 2000). The EIS provides a useful comparison dataset; the main difference between it and the XDCS is that the former survey uses several large contiguous patches and so offers little overlap with X-ray data. Also XDCS is a northern hemisphere survey, and the EIS is based entirely in the southern hemisphere.

2.2 Sample Selection

X-ray observations are observationally expensive, thus archival data is the obvious choice. Essentially a random sample of deep X-ray fields was required. The ROSAT International X-ray/ Optical Survey (RIXOS)(Mason et al. 2000) provided an ideal source of such fields. The RIXOS sample was constructed from ROSAT Position Sensitive Proportional Counter (PSPC) fields which had exposure times of at least 8ks. This ensures that sources at the intended survey flux limit (for a point source) of 3×10^{-14} erg cm^{-2} s^{-1} (0.5-2.0 keV) lie significantly above the sensitivity threshold of every field. They also limited the choice of fields to those which have Galactic latitudes greater than 28° in either hemisphere, since RIXOS is primarily intended for extragalactic source studies.

Thus the sample comprises random fields pointed out of the plane of the Galaxy, so any clusters found will be *serendipitous*. The other advantage of this choice of fields is that by distributing the fields across the sky, rather than having a small contiguous patch, bias which may be introduced through variations in large scale structure is avoided.

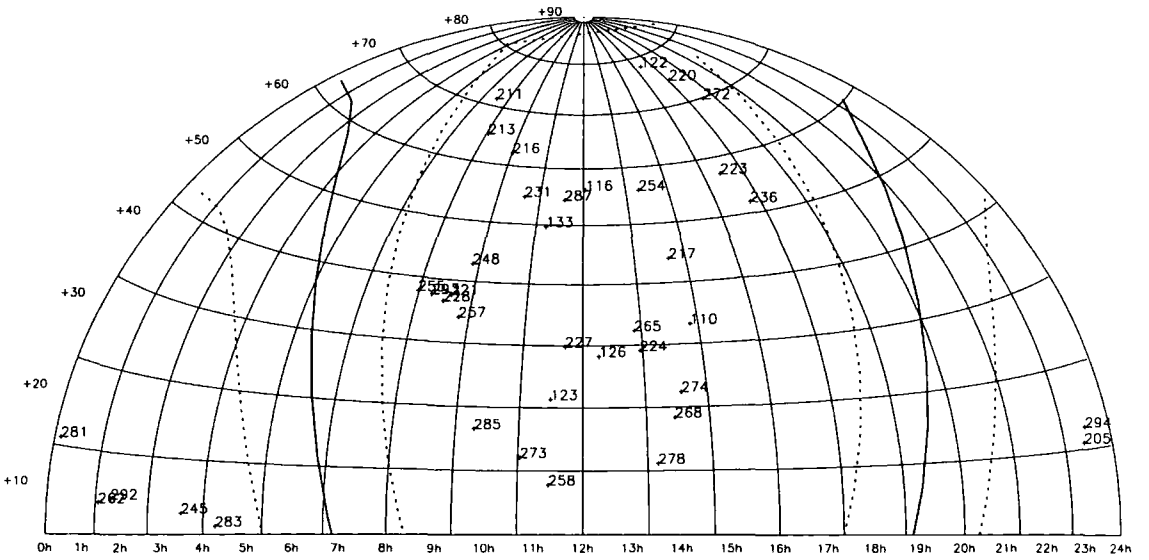

Figure 2.1: Distribution of XDCS fields on the sky (Aitoff projection). Fields are labelled with their IDs from the RIXOS survey. See also Appendix A. Solid line indicates position of the Plane of the Galaxy. Dotted lines indicate a Galactic Latitude of ±20 degrees.

2.3 Optical Observations and Data Reduction

2.3.1 Observing Strategy

Archival ROSAT PSPC fields were observed using the Wide Field Camera (WFC) on the Isaac Newton Telescope (INT), La Palma. The observations were carried out in two runs, in June 1998 and January 1999. Both runs appeared to be photometric, as can be seen from Figure 2.6. Also, the uniformity of the number counts, the median colours of field galaxies, and the repeatability of photometric measurements (Appendix B) in overlapping data were examined, and all suggested that the data was photometric.

The inner $\gtrsim$19 arc minutes of the PSPC fields were imaged to depths of V$\sim$24 and I$\sim$23. This is the region of the PSPC used for X-ray source identification in RIXOS, to ensure the best X-ray image quality and the most accurate source positions (Mason et al. 2000). For each band, two exposures were taken, rotating the camera through 180 degrees, and offsetting the centre of the pointing in order to ensure optimum coverage of the PSPC, as shown in figure 2.2. Hereafter, images taken with the camera rotator angle set to 360 degrees will be referred to as *A* images; and those with a rotator angle of 180 degrees *B* images. The log of observations is given in Appendix A. Each field was observed in the pattern AV-AI-BI-BV, or similar, to cut down possible systematic errors and improve observing efficiency.

The WFC comprises four thinned EEV (2048 $\times$ 4100) Charge-Coupled Device (CCD) chips, at the prime focus of the 2.5 metre INT. The science devices have 13.5 micron pixels (0.333"/pixel). Each covers an area of 22.8 arcmin x 11.4 arcmin on sky. The total sky coverage per exposure is 0.29 square degrees. A single exposure covers 76% of the ROSAT PSPC area. By using two exposures virtually the entire inner 38 arc minute diameter was covered: see Figure 2.2.

2.3.2 Reduction Method

CCD detectors take incoming photons from the sky and convert them to electrons, which are clocked as "counts" in the device. A number of instrumental signatures must be removed from the data prior to scientific analysis. Working in the notation of Gullixson (1992), these can be summarised as:

$$raw = [obj + sky \times (1 + fringe)] \times qe + zero \tag{2.1}$$

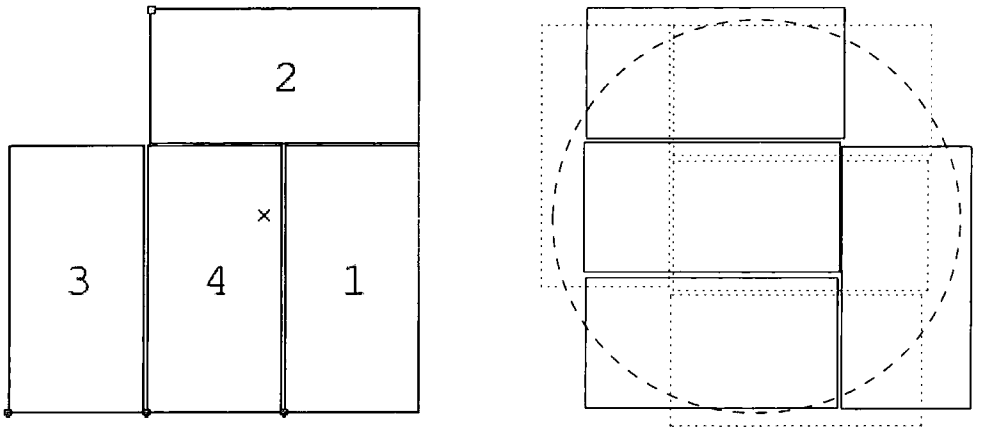

Figure 2.2: INT WFC Tiling Strategy. The circle represents the inner 19 arcmin radius of the PSPC field. Rectangles show the four CCDs of the WFC. The diagram illustrates how the field can be efficiently imaged in two pointings. The figure on the left shows the idealised layout of the WFC with the chips numbered. Heavy points in the corners show the origins of the chip coordinates. The cross shows the position of the optical centre of the camera. The diagram on the right shows the actual relative positions of the CCDs, with the correct tilts and offsets.

where *raw* and *object* represent the data counts as read from the instrument, and the counts from the astronomical object of interest, respectively. The additive *sky* term is not considered in this chapter, as sky variation in the optical is negligible, but this will become important in the chapters dealing with near-infrared observations. *fringe* must be considered for the I-band data and is explained in the defringing section. The "flatfield" or *qe* comprises not only the intrinsic quantum efficiency of each pixel, but also the extrinsic efficiency in converting photons to electrons, considering the way in which the detector is illuminated. The *zero* level term is a sum of *overscan* + *bias* terms for this data, discussed in the next section.

The data reduction was carried out with a custom-written pipeline for the project, using mostly standard `IRAF`[1] routines, and is detailed below.

[1]IRAF is distributed by the National Optical Astronomy Observatory which is operated by AURA Inc. under contract with the NSF.

Debiasing

CCD pixels have an artificial DC offset, or bias, added to prevent negative counts. It is necessary to remove this offset, and also any fixed pattern noise. In addition, an overscan region is generated by continuing to read out the CCD after all the charge has already been clocked. This appears as an extension in width of the chip, beyond its physical pixels, which is used to monitor the intrinsic bias level and rms noise of the electrons.

The images were first debiased by using bias frames taken at the beginning and end of each night. The individual zero-second exposures were first inspected for irregularities, such as electrical interference picked up from local sources. Such interference appeared as narrow banding across the frames. These frames (typically one or two were found each night) were rejected. The bias frames were then combined to make a master bias frame for each of the four CCDs. The data was then processed by subtracting the master bias frames from all the data frames and applying overscan strip correction in the `IRAF` task `ccdproc`.

Linearity Correction

At this point it was necessary to correct for the non-linear response of the WFC. The procedure is described in Appendix A. Briefly, if this is not corrected for, photometric measurements of the same object could be discrepant by as much as 0.1 magnitudes, depending on the detector count regime in which the object is observed. This can be corrected by applying a polynomial to the observed counts, bringing the residual error down to $\sim$0.005 magnitudes.

Flatfield Correction

In order to correct for intrinsic pixel-to-pixel sensitivity variations, and the different ways in which they are illuminated, it is necessary to expose the devices to a uniform source of illumination. At the beginning and end of each night, short exposures of "blank" (ie. devoid of bright stars) regions of sky ("twilight sky frames") were taken with both the V and the I filters. These were combined to give an essentially uniformly illuminated field. Using the sky itself also correctly reproduces the way in which the detectors are illuminated during science exposures, which would not necessarily be the case if, for example, lamps illuminating the dome were used to make the flatfield frames. Due to the large quantity of data from each night, it was decided that a better flatfield could

be made by combining the data itself, after filtering out the astronomical objects. On inspecting the data, the I-band images showed fringing, at the level of ≈3% of sky, so it was decided not to stack them to make a flatfield. This fringing dominates the night sky spectrum in the science observations, but its contribution is less in the twilight sky flats. Therefore, the I-band data were flatfielded using a master flatfield frame, comprising a combination of all available I-band twilight images for each night. The V-band data were flatfielded using a master flatfield from median combination of the V-band data frames, rejecting deviant pixels (astronomical objects at the high end, intermittent cold pixels at the low end) using the `avsigclip` routine. The accuracy of the flatfields was assessed by comparing the corresponding master flats from night-to-night within each run, dividing one frame by another and examining the deviation from unity of the result. This showed that the flats were consistent with each other to better than 1 percent. CCD 3 suffers from severe vignetting across one corner. The flatfielding process raises the mean counts across this region to be consistent with the mean counts of the whole chip, but due to the low intrinsic signal, the pixel-to-pixel variation is increased, and so this area is essentially unusable for object detection or photometry. A triangular region in the lower left of chip 3, where the pixels satisfy $x + y \leq 1200.00$, is therefore omitted from the catalogues (see §2.3.3).

I-band Data Defringing

I-band data taken with a thinned CCD suffers from fringing. This is an artifact introduced by OH emission lines at around 8000Å in the night sky, visible in the I-band and amplified via interference in the chip, as the thickness of the detector is of the order of the wavelength of the lines. The fringes are additive, but their broad structure is largely stable with time through the night. Therefore, all the I-band data for each chip were added together to make the four master fringe frames for each night. Although the shape of the lines is stable, the amplitude can vary considerably (although always at the level of a few percent of sky). Thus, a method was needed to scale the amplitude of the fringe mask to the amplitude of the fringes in each data frame, before subtraction. This was done with software kindly provided by Dr Mike Irwin. His algorithm works by subtracting the median counts from the fringe frame (to provide a crude but adequate sky subtraction), applying a scale factor to the fringe mask, subtracting the scaled fringe mask from the data frame and examining the histogram of counts in the data. By iterating the scale factor and minimising the median average deviation in the image histogram (caused by

the fringes), a zeroth-order correction for fringing may be achieved. This reduces the fringing to ~0.5 percent of sky, which is of the order of the residual non-linearity. Hence, a better fringe correction would not improve the photometric accuracy. However, the worst of the residual fringing can pose problems for object detection (see below).

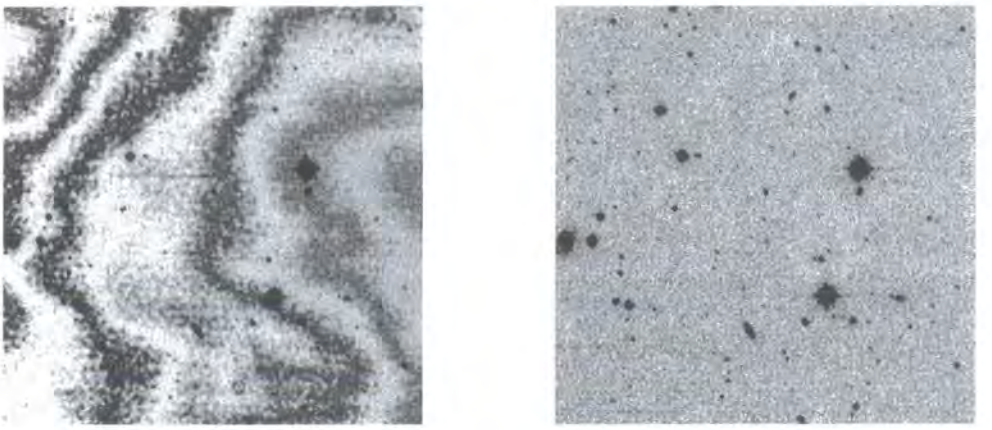

Figure 2.3: Typical I-band images before (left) and after (right) defringing. Images are 500 × 500 pixel subregions.

2.3.3 Object Detection and Classification

The `SExtractor` package (Bertin & Arnouts 1996) v2.2.1 was used to locate and classify objects in the optical data. First, it was necessary to obtain an estimate of the seeing in each frame. The reason for this is twofold: a) `SExtractor` 's star/ galaxy separation task requires a good estimate of the seeing, in order to distinguish between extended and point sources; b) it is necessary to match the point-spread functions of the two filters, to measure accurate galaxy colour, to ensure that the photometric aperture is sampling the same physical region of a galaxy in each band. In order to estimate the seeing, `SExtractor` was run with a high (10σ) detection threshold and a `CLASS_STAR` ≥ 0.99, so as to detect only the brightest stars. This " `CLASS_STAR` " parameter is derived from a neural network-based classification algorithm within `SExtractor` , which has "learnt" to classify objects from a training set. It performs well down to around 1 magnitude above the limiting magnitude, at which point there are too few photons in an object to accurately determine if it is resolved or not[2].

Saturated stars and cosmic rays were excluded by adding high and low cuts to the counts. Gaussian radial profiles were then fitted to the remaining objects and the median

[2]At this magnitude, galaxies already heavily outnumber stars. At I=21.0, the galaxies:stars ratio is around 4:1, and rises rapidly toward fainter magnitudes (N. Metcalfe, private communication).

value of the FWHM taken. Since the star/ galaxy classification is dependent on the input value of the seeing, it was deemed necessary to iterate this procedure to ensure that accurately classified point sources were used in the measurement of the seeing. Thus, the median and standard deviation of the FWHM measurements for each chip were recorded for each chip, `SExtractor` re-run using the new measurement of the FWHM as input, and the new distribution of FWHMs logged. Once this value had converged to within the standard deviation of the previous measurement, the median FWHM was logged. This automatic procedure agreed well with manual fitting to point sources for all 640 frames of the sample, except one (which gave an unreasonably high value), for which a manual measurement was used instead.

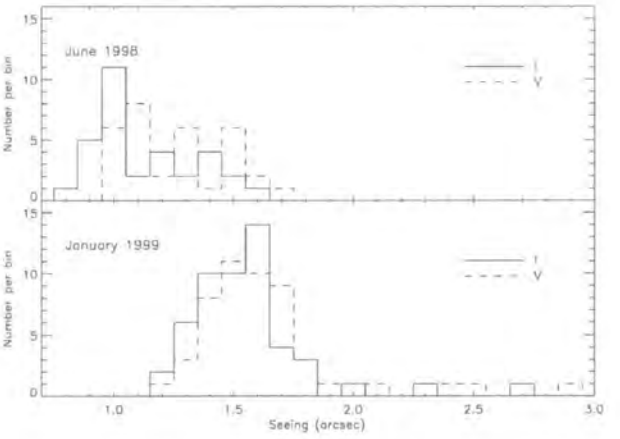

Figure 2.4: Distributions of seeing values for each XDCS run. The values are Gaussian FWHM fits to the brightest stellar sources in chip four, for each field. See text.

Object detection was performed on the V-band images. Also tried was combination of the V and I frames to make a deep V+I frame on which to perform object detection (similar to the method described by da Costa et al. (1999)[3]). This increased the number of detected objects by a small amount, adding an extra <3%. These objects were too faint or red to be detected using just the V frame. However, residual fringing from the I-band image dramatically increased the numbers of false detections, by a factor of $\gtrsim$ 300% in the most badly-fringed frames. Although the level of the remaining fringes is too small to affect the photometry (the photometric error is still dominated by the linearity correction at the bright end, and Poisson noise at the faint end), the background estimation method used by `SExtractor` cannot model the fringes. High residuals pass above the `SExtractor`

[3]The optimal method for improving object detection sensitivity through coaddition of multicolour data is the χ^2 image method of Szalay, Conolly, & Szokoly (1998).

detection threshold and are classified as extended objects. As this method could not be reliably used on all the data, its use was decided against.

For such a large quantity of data, it is not possible to visually inspect all the object detections/ classifications and remove artifacts such as cosmic rays, diffraction spikes, satellite trails, etc. So, these spurious objects (which are relatively few in number, eg. cosmic ray hits number ~100 per chip in a typical exposure), were ignored. Their impact is minimised through careful choice of `SExtractor` parameters, and the method of catalogue generation. Cosmic rays should not be a problem, due to the method of performing photometry. Cosmic ray hits in the I-band will be ignored (unless they fall on the location of astronomical objects) as the detection is performed in the V-band. V-band cosmic rays will have no counterpart in the I-band (again, unless they fall on astronomical objects), and so appear incredibly blue, and will not affect cluster detection.

After experimentation on a few frames and examination of the detected objects, it was decided to adopt 5 connected pixels of 1.0 × the rms of the amplitude of the background as a suitable threshold for detection. The choice of how `SExtractor` deblends its detected objects is a compromise between deblending too much and risking splitting up large objects, such as nearby galaxies, into too many smaller false objects; and not deblending enough and missing "touching" galaxies. A generous amount of deblending was opted for. `SExtractor` uses two parameters to control this: `DEBLEND_NTHRESH` and `DEBLEND_MINCONT`. The former controls the number of subthresholds into which each object can be divided (a value of 32 was chosen) and the latter, the minimum contrast between neighbouring regions before they are allowed to be deblended (0.001 was selected).

This choice meant that spurious detections were introduced due to repeated detection of diffraction spikes and objects in noisier regions, such as the haloes of bright stars and chip edges. Also, extended objects such as nearby galaxies were overly-deblended into cluster-like artefacts. However, if insufficient deblending was used, galaxies in the dense cores of clusters at small angular separations were missed, and the cluster signal greatly reduced. It was decided that the best approach was to use these `SExtractor` parameters, and remove spurious entries in the cluster candidate catalogues later, by visual inspection.

The x and y coordinates of objects in the V frame were logged and used to position the aperture for photometry. The object coordinates were used to align the I frames to the V frames using `imalign`. The frame with the better seeing was convolved to the same seeing as the corresponding frame in the other band using a standard Gaussian convolution (eg, Bracewell 1965), achieved using `gauss` in `IRAF`.

$$\sigma_{smooth} = \frac{\sqrt{FWHM^2_{higher} - FWHM^2_{lower}}}{2\sqrt{(2\ln 2)} \times pxscale} \tag{2.2}$$

where σ_{smooth} is the width of the Gaussian used to perform the smoothing; $FWHM_{higher}$ and $FWHM_{lower}$ are the values of the seeing (in arc seconds) of the frames with the higher and lower values of the seeing, respectively; $pxscale$ is the pixel scale of the instrument (to convert the seeing values into pixels); and the factor of $2\sqrt{(2\ln 2)}$ converts between FWHM and Gaussian sigmas.

A slightly different value for the seeing in each chip was measured. This was sufficient to account for the variation of the PSF as a function of location across the camera. No position-dependent variation was seen comparing photometry of objects observed in different parts of the camera. See Appendix B.

`SExtractor` was run in "dual image mode", which means object detection is performed in one image and photometric and shape parameters are measured from another frame. This was done in order to obtain `SExtractor` `MAG_BEST` magnitudes for I-band objects. The `MAG_BEST` magnitude is an approximation to a total magnitude based on an adaptive elliptical aperture magnitude. The second-order moments of the light distribution are used to define widths for a bivariate Gaussian, and then an elliptical aperture, some constant times this width is used as the aperture. This has been shown to contain a constant fraction of the flux from the star/ galaxy, independent of its magnitude (Bertin & Arnouts 1996, and references therein). This magnitude was compared with aperture photometry using large apertures for isolated objects in both bands. The median systematic offset was found to be around 0.03 magnitudes. Given the uncertainty in the absolute calibration of the photometry, it was decided to neglect this correction.

The `IRAF` task `phot` was used to perform aperture photometry, using an aperture of diameter 2.6 $\times$ the seeing, on the aligned, convolved V and I frames. Lilly, Cowie & Gardner (1991) found a similar value to be optimal for the measurement of faint galaxy colours. Using a diameter of 2.5 times the worst seeing FWHM, this was found to enclose about 90% of the light for stellar objects and about 80% for even the largest galaxies. Tests were performed to find the difference between using 2.6 times the seeing aperture for the best seeing data; versus convolving the best seeing data to the worst. Excellent agreement was found at the level of 0.04 magnitudes for typical galaxies. Thus, rather than degrading *all* the run 1 data to the run 2 conditions to place all aperture magnitudes on the same system; the 2.6$\times$seeing aperture method was used. Objects with a `SExtractor`

CLASS_STAR index of $\leq$0.90 were taken to be galaxies.

In addition, SExtractor produces internal FLAGS to warn of potential problems with extracted objects. Only detections with FLAGS<4 were retained. This means, blended objects and those with near neighbours are kept, but those with saturated pixels, or corrupted data (eg. due to boundary effects) are rejected.

It was decided at this stage not to try to combine the object catalogues from the A and B rotations into a single catalogue. Such a procedure is complicated when the instrumental distortions are not well-characterised (as was the case at the time - it took several months in conjunction with staff working on the Wide-Field Survey in Cambridge to provide even a first-pass instrumental solution, which has now been refined through the use of many fields). The presence of cosmic rays, diffraction spikes, and objects which were deblended differently in the two rotations proved problematic for cross-correlation algorithms. Furthermore, since the overlap in the two rotations is not complete (only $\sim$50%) a procedure such as only retaining A- and B-matched rotations would reduce in "patchy" catalogues with differing noise characteristics across the mosaic. Preserving two catalogues allows direct comparison of, for example, fits to colour-magnitude relations in the two catalogues (eg., Figure 3.5). Independent catalogues of overlapping observations were also produced for the first data release of the EIS (Nonino et al. 1999), due to similar complications in catalogue-matching, mentioned above.

2.3.4 Astrometry

The object catalogues from SExtractor comprise V and I instrumental colours, I-band "best" magnitudes, and x and y coordinates in terms of pixels on each chip. These chip coordinates can be converted into pixel coordinates for the whole camera by using the relative offsets and orientations of the chips. The equations given in Appendix B.2 were applied to convert to global pixel coordinates, with the origin at the centre of the WFC rotator.

All cluster detection routines are applied to these global chip coordinates, but for the purposes of matching up cluster candidates with those in the literature and the X-ray data, an approximate conversion to sky coordinates is applied. This is done by taking the R.A. and Dec of the telescope pointing from the header, and shifting this to the centre of the coordinate system.[4] The precision of the header coordinates was checked

[4]To ensure that a pair of A and B frames have similar global astrometric solutions, the centre of the B-frame was shifted "by hand" to that of the A-frame's coordinate system. This resulted in objects being

against DSS images for a number of frames. Overall, this translates to being able to assign positions of cluster candidates to an external accuracy of $\lesssim$ 10 arc seconds. This is certainly sufficient, given the angular extent of galaxy clusters on the sky, and there is no danger of confusing two different objects. For the purpose of follow-up spectroscopy (see Chapter 4) more accurate astrometry was performed on the individual candidates, using the `STARLINK` package, `astrom`.

2.3.5 Photometric Calibration

The photometric data were converted to the standard Cousins system used by Landolt (1992), as described below. A series of Landolt standard fields were taken every night. Due to the small size of the Selected Areas, relative to the field of view of the WFC, many standard stars fell on the central chip (chip four), and only a few on the other chips. Therefore the transformation equations are calculated using this central chip. The only differences between the chips are their gains and sensitivity to light in different passbands. These two effects translate into slightly different zeropoints in the transformation equation for each chip. Hence, calculating the zero point difference between each chip and chip four, and placing chip four on the Landolt system, will calibrate the other chips to the same system. The observing strategy of rotating and offsetting the fields means that every chip overlaps with at least one other chip for every pair of observations. Thus the data itself can be used to verify the internal calibration of the photometry. This also gives us a very good indication of the level of the random photometric errors. The method used to place chips one to three on the same system as chip four, and its accuracy is explained in Appendix B.

External calibration

The Landolt standards were used to calculate standard star solutions for every night. For each run, the best-fit solution was used to calculate the zero-point of chip four and the extinction term. The colour term was fit from the best night of both runs combined. The following values were measured.

matched between the frames to within a few pixels.

Table 2.1: Coefficients from Landolt Calibration

Run	Band	Zpt	Extinction	Colour term
June 1998	I	23.09	0.03	-0.05
June 1998	V	24.64	0.13	0.01
Jan 1999	I	24.20	0.00	-0.05
Jan 1999	V	24.93	0.10	0.01

Typical values for the extinction from La Palma are 0.12 in V and 0.08 in I (`http://www.ing.es`). The extinction correction is a small effect though, as most of the data were taken at the same airmass.

After calibration to Landolt's photometric system, a correction was made to account for reddening by foreground dust in the Milky Way. Since the RIXOS fields were selected to be in areas of low Galactic HI column density this correction was small (and roughly equal in the V- and I-bands) for all but a few fields (typically a few hundredths of a magnitude; but as much as two or three tenths in a few fields). Reddening measurements were taken from the dust maps of Schlegel, Finkbeiner & Davis (1998). For each WFC field, the RA and Dec of the field centre was used as the location in the dust maps, and the data were searched using the user-friendly IDL Code provided by the authors[5] to query the maps. Conversion from dust to Landolt V- and I-band extinction corrections was achieved using the transformation [6] quoted in the software.

The stability of the photometric zeropoint through the night, from standard star observations, is shown in Figure 2.6. The first run has few standard star observations in the middle of the night, but examination of number counts and median colours of field galaxies shows each night was stable. Nights 2 and 3 showed a slight zeropoint change at the very end, due to the thin cirrus which typically appears toward dawn; but were still stable for the remainder of the night. Since repeat observations of each field were made within the space of a few minutes (see observing logs, Appendix A), the zeropoint stability on very short timescales can be determined by looking at the reproducibility of the photometry of the same objects in the science frames. Even assuming a small amount of variable extinction, this will not affect colour measurements, as the extinction is likely to be grey. Reproducibility of magnitudes and colours are illustrated in Appendix B.

The V-band number counts are shown below and compared with literature counts, as a necessary but not sufficient test of the photometry. Counts were generated from `MAG_BEST` magnitudes in the V-band. These are in excellent agreement with those from the literature (taken from the EIS). The counts are $\approx 60\%$ complete at $V = 23.8$. The I-band counts are dealt with in more detail in §2.4.3. V-band total magnitudes are not used henceforth.

[5] from `http://astro.berkeley.edu/dust/`

[6] The dust maps were multiplied by a factor of 3.315 for the V-band and 1.940 for the I-band.

2.4 Cluster Detection

Two different cluster detection methods were applied to the optical data. Both use positional information to search for overdensities in the galaxy catalogues, but they do this in different ways. The first uses only the I-band photometry, and looks for overdensities of galaxies which appear to follow the luminosity function of a galaxy cluster; the second includes the V-band data and uses the V-I colour to search for colour-magnitude relations of early-type cluster galaxies.

2.4.1 Method 1: The Matched-Filter Algorithm

Background

The "matched-filter" (MF) was pioneered by Postman et al. (1996), and modified by several groups (including Kawasaki et al. 1998, Kepner et al. 1999, Lobo et al. 2000). Its principle is to assume that galaxy clusters follow some well-defined model, in both their spatial and luminosity distributions. ie. some universal radial profile is assumed for the distribution of galaxies in a cluster, which can be projected into 2D. In the same way, some universal luminosity function can be assumed for its member galaxies. High resolution N-body simulations suggest that the virialised objects follow a universal density profile (Navarro, Frenk & White 1997, NFW); observations show that cluster profiles

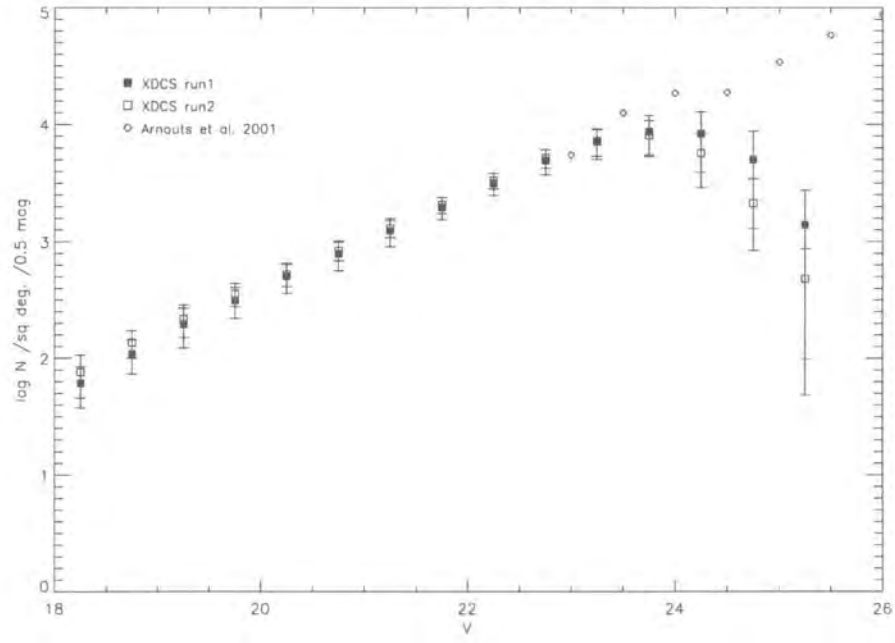

Figure 2.5: V-band number counts and comparison with literature counts.

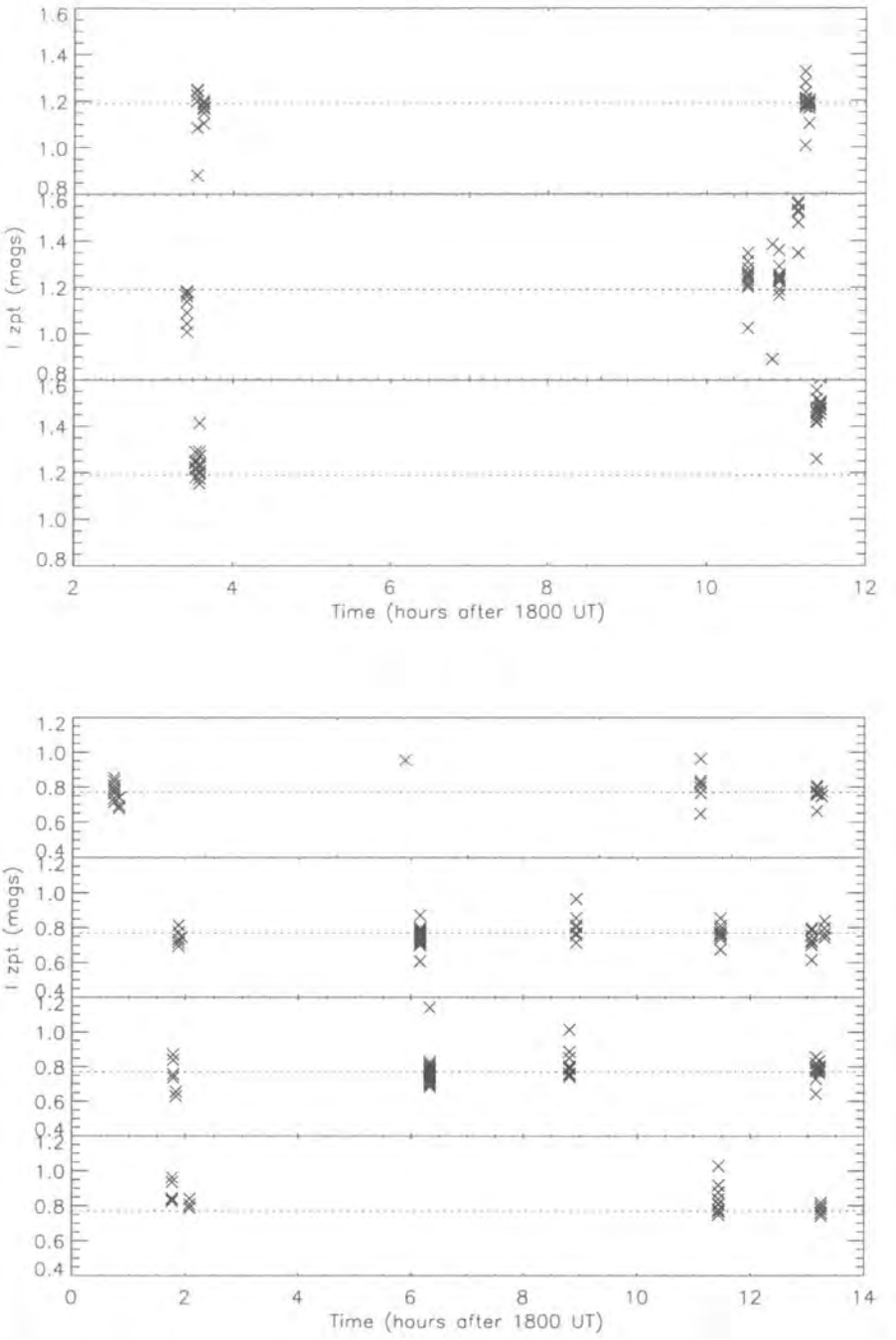

Figure 2.6: I-band zeropoint vs time, for each night, for all Landolt standards taken. No correction is made for extinction in this plot. The airmass of the observations varies between ~1.1 and 1.7. Since the extinction in the I-band is ~0.08, the maximum difference this can make is 0.05 mags. The value of the zeropoint at the start of each run is overplotted as a dashed line to guide the eye. Cirrus at the very end of the night is responsible for the slight zeropoint offset, during the first run, even though inspection of the data shows conditions were photometric throughout the night. The y-axis is the offset from the **phot** zeropoint of 25.0.

are compatible with such a profile, but also with simpler analytic fits (Carlberg, Yee & Ellingson 1997, Lubin & Postman 1996). The luminosity function of galaxies in clusters and the field is well-fitted by a Schechter function with mild luminosity evolution (Yee & Lopez-Cruz 1999), or mild luminosity and density evolution (Lin et al. 1999).

Now, this model can be scaled to any redshift. The observed radial profile scales with redshift according to the angular diameter distance, D, to the object, given by

$$D = (c/H_0)\{q_0 z + (q_0 - 1)[(2q_0 z + 1)^{1/2} - 1]/q_0^2(1+z)^2 \quad (2.3)$$

(eg. Coles & Lucchin 1995) where c is the velocity of light, H_0 is the Hubble constant, q_0 is the deceleration parameter, and z is the redshift). The observed luminosity distribution scales according to the distance modulus formula $m - M = 5\log(d_{Mpc}) + 25 + k + e$ with corrections for bandpass shifting due to the redshift of the source (k-correction, k) and evolutionary corrections of the stellar populations (e). m and M are the apparent and absolute magnitudes of the galaxy, and the luminosity distance, d, in Mpc is a factor of $(1+z)^2$ times the angular diameter distance, D. The only other free parameter the model needs is the *richness* of the cluster (ie. some parameterisation of the number of galaxies it contains). Thus, a model for the observed properties of a galaxy cluster of arbitrary richness and redshift is obtained. The only other aspect to be taken into account is the distribution of field galaxies. This model can be derived from the data itself. It is assumed they are randomly distributed in position - explicitly ignoring the correlation between the positions of pairs of galaxies (see §2.4.1). The contribution of cluster galaxies to the total number of galaxies in any dataset will be small, unless the survey consists of small fields targeted at clusters (which is obviously not the case for a cluster survey!). Hence, by studying the number density and luminosity distribution of the whole sample, a model for the field galaxies can be deduced. The luminosity function in the PDCS method had to be modelled by a power-law due to assumptions made in the derivation (see paper for details) which is generally a good fit to the data, depending on the magnitude range observed (eg, Metcalfe et al. 2000, Smail et al. 1995, see also Figure 2.15).

Now, astronomical data comprising positions and photometry can be searched for regions where the likelihood of the data fitting this cluster+field model is high. Since the cluster model is a function of richness and redshift, as a by-product of the detection process, a most likely richness and redshift for each cluster candidate is obtained as a by-product.

The Postman et al. (1996) algorithm made several approximations (detailed in their

paper) which have been removed and treated more fully by later workers. For example, their main approximation was to assume that the data (galaxies) could be binned in both position and magnitude in such a way that each bin had sufficient datapoints that their distribution was Gaussian. This was replaced by a more general treatment which assumed Poisson distribution of the data by Kawasaki et al. (1998). The other key assumption which has been followed by all subsequent works until Lobo et al. (2000) is that the models predict a unique combination of spatial and luminosity distributions at a given redshift. The drawback of this approach is that if a cluster is slightly larger or smaller in angular extent than predicted for its luminosity distribution, its signal is reduced and the probability of detection lessened. Lobo et al. (2000) circumvented this problem by choosing the combination of spatial and luminosity profiles which independently maximised the signal.

A New Matched-Filter Algorithm

The algorithm presented here is closest in spirit to the technique of Lobo et al. (2000), in that the assumptions for the distributions in radial profile and luminosity have been decoupled. This method offers many advantages for this project, the main one being that it is unnecessary to assume a characteristic physical size for the model cluster, *a priori*, which will obviously help if unvirialised systems have larger angular extent than virialised systems of the same richness and redshift (as may intuitively be expected). This also offers some computational rewards which will be explained below.

The assumptions for this model are:

- Field galaxies are distributed randomly over the sky (the two point galaxy-galaxy correlation function is explicitly ignored), and that their magnitude distribution has the same shape throughout the survey but changes slightly in normalisation, from field-to-field (see Figure 2.15).

All magnitudes in this section refer to the I-band. In principle any photometric passband can be used, but as red a band as possible is desired. This is due to the fact that the field galaxy counts steepen toward shorter wavelengths, so the contrast between the cluster and the field is greater at longer wavelengths (eg. power-law slopes of 0.28 and 0.40 were measured in the I- and V-bands, respectively, by Smail et al. 1995).

- Galaxy clusters appear as overdensities in this background distribution, and their visibility can be enhanced by filtering the galaxy catalogue with a Gaussian filter, the size of which is given by the typical sizes of galaxy clusters from the literature.
- Galaxy clusters follow a Schechter Luminosity Function (LF), with fixed faint-end

slope, and the normalisation is given by the amplitude of the overdensity (ie. the cluster's richness). The typical magnitude m* of the LF is a function of redshift.

The maximum-likelihood estimator, C, of Cash (1979) is then applied to the data.

Implementation

The algorithm is run on each mosaic separately. First, filtering of the spatial information is performed. The x and y positions of galaxies brighter than magnitude 22.5 are read in, and the mosaic is filtered with five Gaussian filters of different widths. The standard deviation of each filter is taken from Lobo et al. (2000). The widths will be referred to as W_n for the n^{th} filter (to avoid confusion with standard deviation σs, later), but are equivalent to the σ_{ang}s in their paper. The widths, W_1,...,W_5, range from ~0.35 to ~1.42 arcmins in steps of $\sqrt{2}$ - these represent the typical core-widths of clusters in the redshift range $\approx$ 0.2 to 1.0. A cut-off radius of 3 W_n is used. Unlike Lobo et al. (2000), instead of using a regular grid, the positions of the galaxies themselves are used as the grid to centre each of the Gaussian filters. This adaptive-grid method was also adopted by Kepner et al. (1999) and has the advantage that it ensures adequate resolution in the core of a cluster, and saves computational expense by performing few calculations where the galaxy density is low. For each spatial filter the mean and standard deviation of the filter amplitude is calculated (the amplitude follows a Gaussian distribution), and all five filters are normalised onto the same system (by subtracting the mean and dividing by the standard deviation).

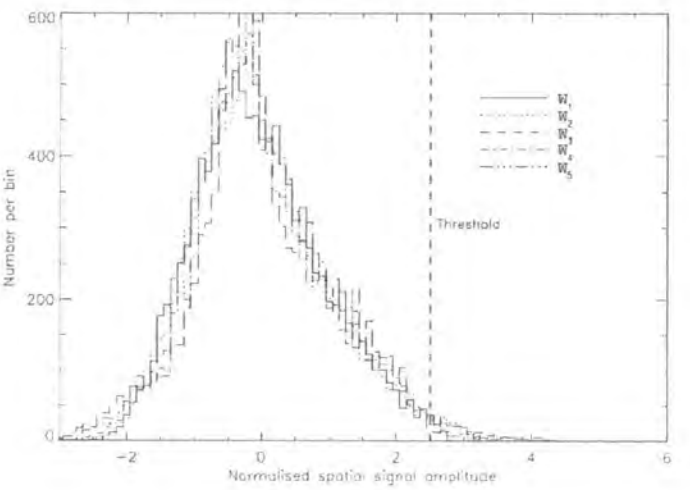

Figure 2.7: Distribution of normalised amplitudes from spatial filter. The distribution follows a Gaussian, with a high-end tail which contains cluster candidates.

Peaks are then found in each filter, by sorting the list of signal amplitudes, retaining the highest value, and then searching down the list, removing detections which fall within a radius W_n of the peak, and retaining the next highest value which does not. Values lower than a minimum threshold of 2.5 σ are immediately rejected.

The peaks from the five filters are then sorted and cross-correlated. So, if a peak is detected in more than one filter, the highest amplitude is retained and the duplicate detections removed. Two peaks are considered to be the same object if the distance between them is less than the mean of their scales (ie. $(W_n + W_n')/2$) (Lobo et al. 2000). This results in a single list of peaks, each with an associated scale (the filter width, W_n, in which the highest signal was detected).

A richness estimate of the candidate is now required, for use in the maximum-likelihood estimation. As a first pass estimate, the number of galaxies within a fixed angular radius was taken, for all candidates, regardless of its associated W_n. (The decision to use a fixed angular search cell is explained below.)

This number then has the number of background galaxies, scaled to the same area, subtracted from it. The background galaxy density is found by counting the number of galaxies in an annulus of radius $3 \times W_n$ to $15 \times W_n$. The W_n value is used to ensure the annulus is sufficiently far from the cluster core to avoid contamination with cluster members. The importance of using a local estimate of the background can be seen from looking at the field-to-field variations in the number counts in Figure 2.15. The local background number density is also used to re-normalise the expected number counts locally, for use in the maximum-likelihood calculation. The cumulative counts are used at I=20.5, two magnitudes brighter than the limiting magnitude, to ensure both a high number of objects and high completeness.

In estimating galaxy number densities, the geometry of the mosaic field needed to be taken into account. To compensate for border effects, where the detect cell starts to fall off the edge of the field, a weighting function was constructed, taking account of the fraction of the detect cell area lost. This requires caution though. Upweighting the signal from a few galaxies is likely to result in increased spurious detections, due to the uncertainty from using fewer galaxies. Thus a cut was made, rejecting candidates where the fraction of the area lost to borders is > 0.20.

The Cash C statistic (below) is then applied to the data within a radius of $2.5 \times W_1$. Most other MF algorithms use a search radius fixed in physical units at the estimated redshift of the cluster, and Lobo et al. (2000) use the radius which maximises the signal.

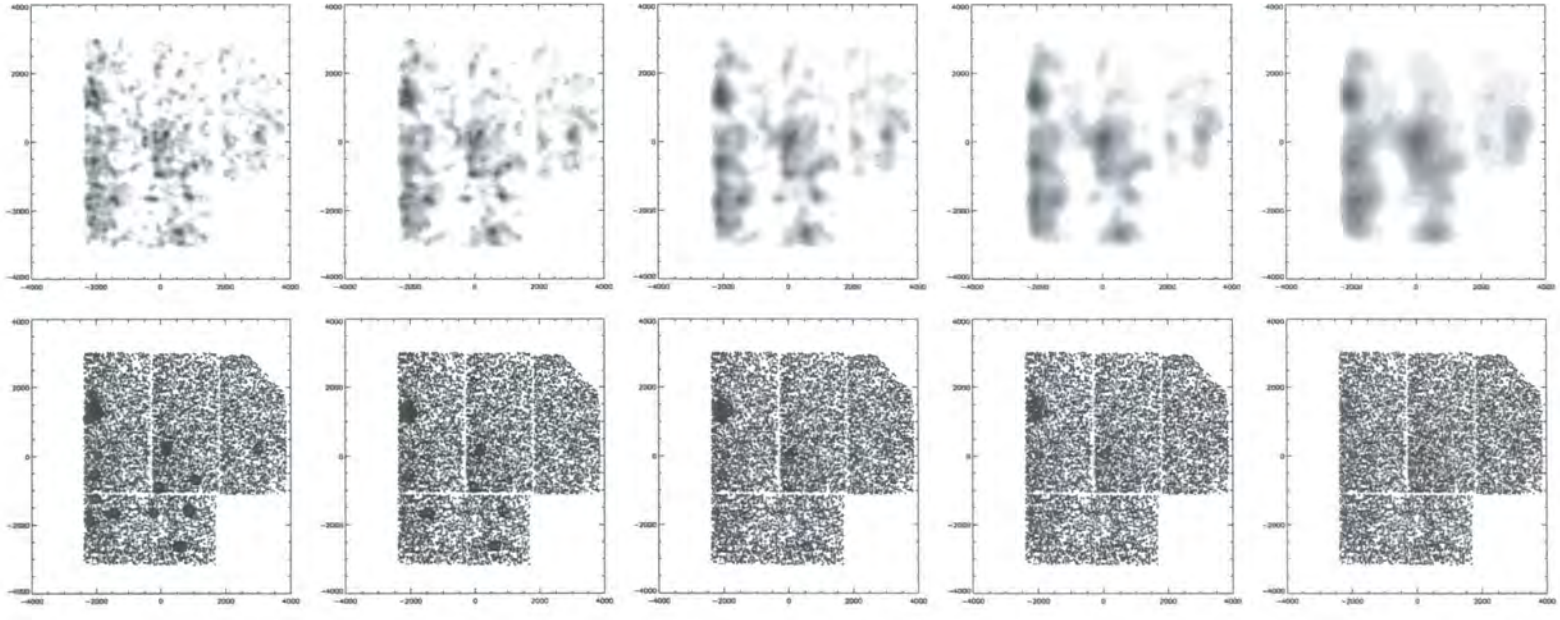

Figure 2.8: Illustration of filtering data with the five Gaussian spatial filters. Top row: normalised contour maps showing signal amplitude (filter width, given in text, increases from left to right). Contours are in intervals of 0.5σ, starting at -3.0σ. Bottom row: Circles highlight peaks >2.5σ in each filter after first-pass overlap removal (see text). Points show galaxies in WFC mosaic above I-band magnitude limit of the survey (22.5).

Early experimentation with simulated clusters showed that just using data within a fixed radius (of the smallest filter) was adequate and this is done for the sake of simplicity and computational speed. Since the same galaxies always enter the maximum-likelihood calculation, this makes the calculation much more stable. It also means that a fair estimate of the likelihood can be found by a simple application of the Cash statistic, without recourse to bootstrap resampling the detections to determine their significance, as needed by the Lobo et al. (2000) method.

The results are sorted in order of increasing C (decreasing likelihood), and overlapping detections are removed using a 2D friends-of-friends groupfinding algorithm (Huchra & Geller 1982). The groupfinder starts with the most significant point and searches within a fixed radius (the linking length) of it for another point. If a point is found, then the search is repeated within the same radius around this new point. The search continues, linking all points within the linking length of a neighbour, until no more points can be linked. Thus only the most significant candidate is retained and all linked neighbours are removed. This method was found to work better than just removing candidates within a fixed radius of each other, as this latter approach tended to either remove too many (unassociated) candidates (if the rejection radius was too large) or leave multiple detections of the same candidate around the periphery of a rich candidate. The friends-of-friends algorithm is a more natural method for associating related points. Through experimentation on fields with known clusters, a linking length of 500 pixels ($\sim$2.8 arcmin) appeared optimal. Finally, the distance between the highest likelihood point (the candidate centre) and the most distant point from it joined to the group was recorded. This distance is then used as a characteristic radius to estimate the extent of the group. This will be important later for matching up overlapping candidates.

Maximum-Likelihood Estimation

Cash (1979) originally developed the maximum-likelihood method for application to general Poissonian problems. The example given in his paper is the case of photon-counting experiments. Any real detector makes discrete measurements in a finite number of bins (N). If e_i is the expected number of counts in the i^{th} bin, at the end of the experiment there will be a finite number of counts, N_i in each of the bins. The probability P of obtaining the particular result, given the correct e_is, is just:

$$P = \prod_{i=1}^{N} \frac{e_i^{n_i} exp(-e_i)}{n_i!} \tag{2.4}$$

From this, the following statistic is generated:

$$C = -2 \ln P = -2 \sum_{i=1}^{N} (n_i \ln e_i - e_i - \ln n_i!) \tag{2.5}$$

Now, the e_is are functions of a set of parameters $x_1, ..., x_n$. One wishes to estimate the true set, $x_1^T, ..., x_n^T$, by using the data set. This is accomplished by finding the set of parameters $\hat{x}_1, ..., \hat{x}_n$ which maximise P.

Cash's (1979) method then involves taking the difference, ΔC, of two C equations, so any constant terms can be neglected, as they cancel, and just affect the normalisation of a single C.

$$C = 2 \sum_{i=1}^{N} (e_i - n_i \ln e_i) \tag{2.6}$$

or,

$$C = 2 \left(E - \sum_{i=1}^{n} \ln I_i \right) \tag{2.7}$$

where E represents the total expected counts, and in the limit of an infinitely fine grid, n_i is either 0 or 1, so the summation is now over the number of observed photons.

Replacing the photons with galaxies, e_i becomes the expected number of galaxies per unit area per unit luminosity. The number of galaxies can be broken up into cluster and field. Now, observing over a given area and luminosity range on the sky, $e_i = e_i(\theta, m; z_c)$ where θ is the angular radius of the search area, m is the galaxy magnitude, and z_c is the redshift of the cluster.

Thus the number expected within these spatial and luminosity ranges is:

$$e_i(\theta, m; z_c) d\Omega dm = [n_f(m) + n_c(\theta, m; z_c)] d\Omega dm \tag{2.8}$$

$d\Omega$ and dm are elements of solid angle and magnitude, respectively. $n_f(m)$[7] is the model for the field galaxy counts, as a function of magnitude. $n_c(\theta, m; z_c)$ is a model for the cluster contribution which requires some model for the spatial and luminosity

[7]In most MF algorithms this is modelled as a power-law, as is necessary in Postman et al.'s (1996) original implementation. However, there is no reason to assume this model in this maximum-likelihood approach, and so the background number counts are taken from the data, with a model for incompleteness, relative to literature counts, and a local normalisation (explained above). See Figure 2.15.

distribution of the cluster; which are themselves dependent on the cluster redshift. Λ is a parameterisation for the richness of the cluster, such that $n_c = \Lambda\phi_{cl}$, with Λ normalised by

$$\int_0^{m_{lim}} \Lambda\phi_{cl}(m)dm = 1 \tag{2.9}$$

The luminosity distribution, ϕ_{cl}, can be modelled by the Schechter function (Schechter 1976):

$$\phi_{cl}(m) = 0.92\phi^\star \exp\{-0.92(\alpha+1)(m-m^\star) - \exp[-0.92(m-m^\star)]\} \tag{2.10}$$

Now, the $\hat{x}_1, ..., \hat{x}_n$ one wishes to find are the cluster's typical luminosity, $m^\star$, and richness, Λ. In practice, one can determine Λ by measuring the excess number of galaxies in the search cell (see below), and so the most likely value of $m^\star$ can be sought. Matched-filters are usually used to provide redshift estimates of clusters, and each trial $m^\star$ value can be thought of as a matched-filter redshift estimate z_{MF}, using some relation between $M^\star$ and $m^\star$ (eg, Colless 1989). The predicted magnitude of a passively-evolving $M^\star$ elliptical, from the models of Kodama & Arimoto (1997) is used here, for consistency with the CMR method, explained in §2.4.2. Most implementations of the MF assume some radial profile for the model cluster fixed in metric coordinates (eg, Postman et al. 1996, Kepner et al. 1999). This then means that $d\Omega = d\Omega(z_{MF})$, where z_{MF} is the Matched-Filter redshift. Lobo et al. (2000) adopted the novel approach of decoupling the assumed radial profile from z_{MF}, and just used Gaussian profiles of several different widths. Here, this is taken a stage further and a fixed angular size of detect cell $d\Omega$ is used. One simply changes the parameterisation of radial shape and cluster richness to be contained within the Λ coefficient - which becomes the number of cluster galaxies within a fixed angular area. This is estimated from the number of excess galaxies over the local background value. Fixing $d\Omega$ makes the C statistic operationally easier, as the $\ln n_i!$ term in equation 2.5 becomes a constant and can be neglected.

$$C(m^\star, \Lambda) = 2\int_0^{m_{lim}} [\Lambda\phi_{cl}(m) + b(m)]\, d\Omega dm - 2\sum_{i=1}^{n} \ln\left\{[\Lambda\phi_{cl}(m_n^{data}) + b(m_n^{data})]d\Omega dm\right\} \tag{2.11}$$

The lower limit of the integral is replaced with I=16 in practice, as saturation sets in around this point, and there are so few galaxies this bright within the whole survey that number counts could not reliably be computed.

Simulations

In order to test the accuracy, completeness, and spurious detection rate of the cluster-finder, an extensive set of simulations was run. First, a cluster model is required. The fiducial cluster requires a model for the luminosity and spatial distribution of galaxies, since these are used by the detection algorithm. The spatial profile is given by the density profile of Navarro, Frenk & White (1997).

$$\frac{\rho}{\rho_{crit}} = \frac{\delta_c}{(r/r_s)(1+r/r_s)^2} \tag{2.12}$$

This is then projected into 2D using the formula:

$$\Sigma(x) = \frac{2\rho_s r_s}{x^2-1} f(x) \tag{2.13}$$

where $x = r/r_s$ and $f(x)$ is given by (Bartelmann 1996):

$$f(x) = \begin{cases} 1 - \frac{2}{\sqrt{x^2-1}} \arctan\sqrt{\frac{x-1}{x+1}} & (x > 1) \\ 1 - \frac{2}{\sqrt{1-x^2}} \operatorname{arctanh}\sqrt{1-\frac{x}{1+x}} & (x < 1) \\ 0 & (x = 1) \end{cases} \tag{2.14}$$

The luminosity profile is given by the same Schechter function used by the detection algorithm. The normalisation of the LF is varied, and the number of galaxies brighter than $m_3 + 2$ within an Abell radius counted to give the Abell Richness Class (ARC, see Table 1.2). Clusters from ARC 0 to 3 were simulated. The cluster models were generated in physical coordinates and then transformed to different redshifts. For the distribution of field galaxies, points were put down randomly over the field of the WFC mosaic. Each point then had a magnitude assigned to it, extracted from the observed number counts. The number of galaxies in each realisation was allowed to vary according to the range of surface densities seen in the data.

For each richness class of cluster, 100 realisations of cluster and field were produced at each redshift interval from z=0.2 - 1.0 in 0.2 steps. These mock fields were then passed to the detection algorithm. The results are plotted below.

The completeness was assessed from the same simulations. For every simulated cluster, the cluster was considered correctly recovered if a candidate centre lay within $2.5W_1$ of the simulated cluster centre, and its Cash C value lay below the threshold cutoff (explained below).

To assess the number of spurious candidates detected, the algorithm was run on simulated blank fields. Other authors (eg, Kepner et al. 1999, Postman et al. 1996, Lobo

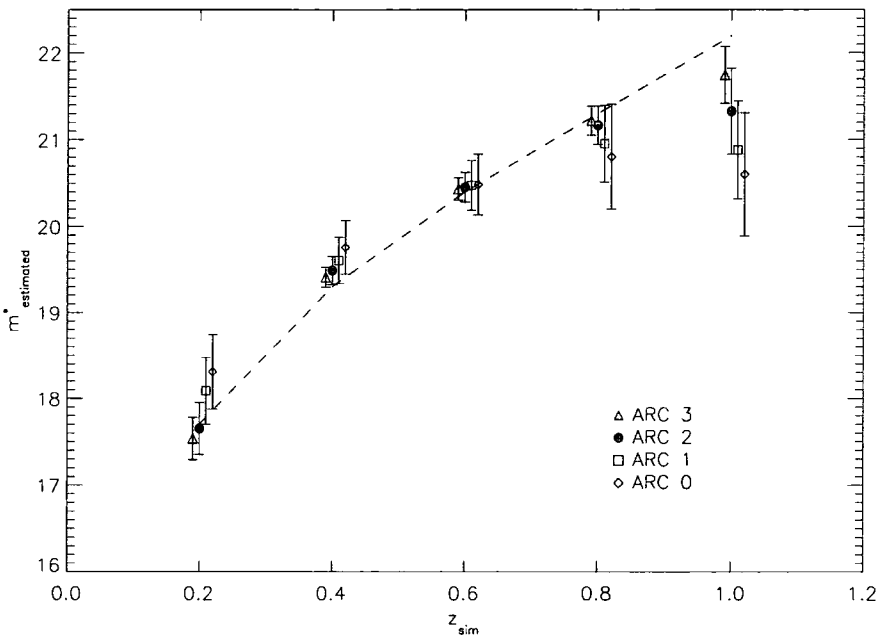

Figure 2.9: Matched-Filter Accuracy. Recovered estimate of $m^{\star}$ against simulated redshift. The dashed line shows the model used for the $m^{\star}$-z relation. Each point is the mean of 100 simulations. The points for the different richness classes are offset slightly in z_{sim}, in the plot, for clarity. Error bars are 1 σ standard deviation between all simulations.

et al. 2000) have used random realisations of their data to represent blank (ie. cluster-free) fields. However, this is likely to artificially suppress the false-positive rate, since the positions of galaxies on the sky are correlated. In order to account for the clustering, mock-fields were generated in such a way that the positions of points obeyed the observed two-point correlation function, $\omega(\theta)$ - a measure of the number of galaxies at a given angular separation θ - usually modelled as a power-law in θ (Davis & Peebles 1983). Such fields were generated using the iterative tree technique of Soneira & Peebles (1978). This was implemented using code kindly supplied by Dr Ian Smail. $\omega(\theta)$ is further discussed in §2.4.3.

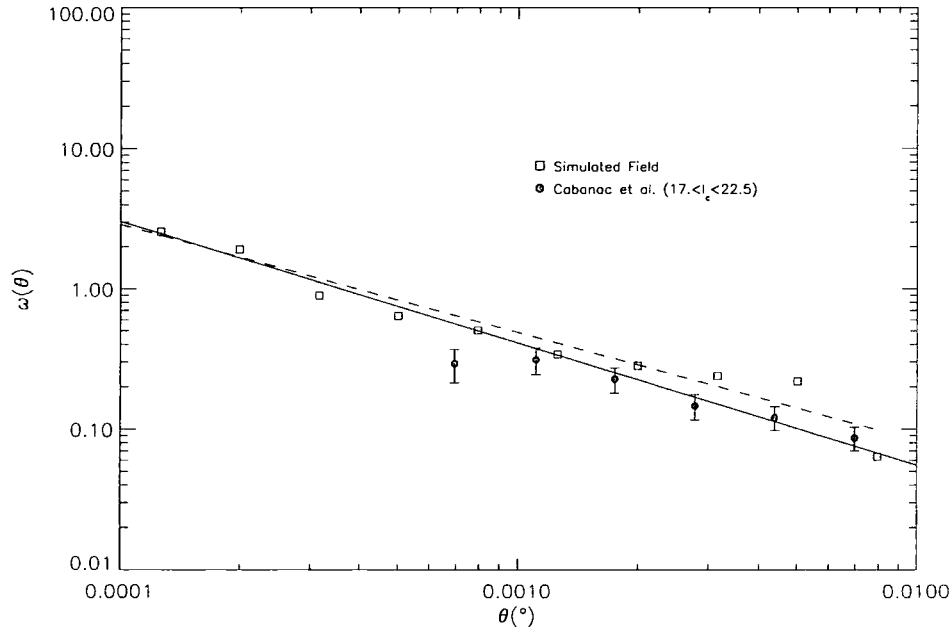

Figure 2.10: A correlated mock field. Square points are taken from one simulated field, and the dashed line is the best-fit using linear regression. The measured slope is -0.77. Filled circles are data from Cabanac et al. 2000, using all their observations in the magnitude range $17 < I_c < 22.5$, and the solid line is their best-fit.

The mock fields were constructed over square regions, slightly larger than the field of view of the WFC. The power-law slope is fixed in the code to be around -0.80, but it is not straightforward to set the amplitude of the correlation function using this technique, so the input parameters were varied incrementally until a reasonable fit (using Chi-by-eye) to observational data was achieved. The data were taken from Cabanac et al. (2000). Their observations were made in the same passband over the same magnitude range as the XDCS. 10 such fields were constructed with ~25000 points in each. This is a factor

of a few higher than the typical surface density of galaxies on a WFC field (down to the magnitude limit). This was done so that several realisations could be made of each field, and the number of points selected could be chosen to match that of the data (reproducing the field-to-field scatter, as seen in the number counts). Each point selected was then given a magnitude drawn randomly from a subsample of all XDCS fields selected so as not to contain any X-ray clusters (from the Vikhlinin et al. (1998) catalogue). The square region was then masked, using the weight-map described above, to reproduce the geometry of the WFC. 10 realisations of each of the 10 mock fields were created, and the 100 mock catalogues given as input to the MF algorithm. The threshold for the Cash C statistic was found by experimentation until a reasonable compromise was found between completeness and false-positive detection rate. The rates for the final threshold are plotted below. A value of $C_{thresh} = -155$ in the units set out in the previous section was chosen.

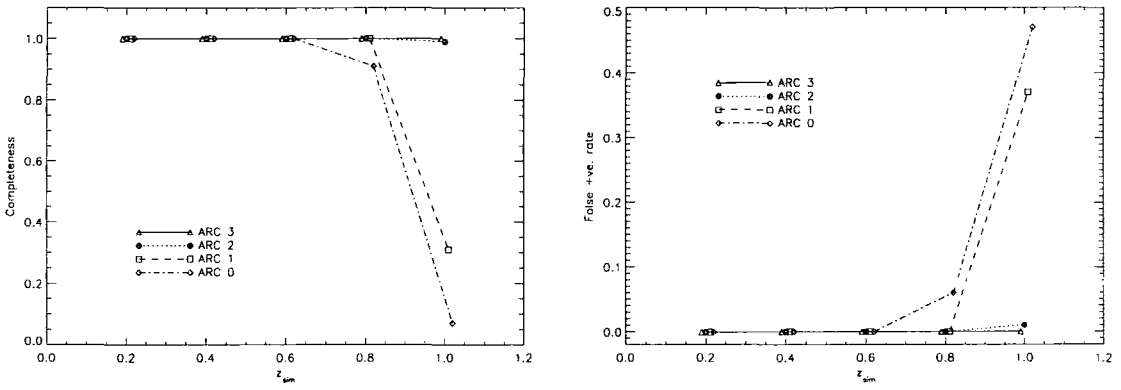

Figure 2.11: Matched-Filter Completeness (left). For the same simulations as in the above plot, the fraction of correctly-recovered clusters (see text) was calculated. Matched-Filter Spurious Detection Rate (right). As for adjacent plot, but now the points represent detections of cluster candidates in a blank but correlated field. See text for details.

To summarise, the matched-filter uses only the I-band galaxy positions and magnitudes to attempt to find systems with luminosity functions resembling those of galaxy clusters. This particular algorithm is designed to generously join points likely to belong to a given overdensity together to allow for the possibility of irregular, extended clusters, perhaps as yet unvirialised. The performance of this algorithm is compared with simulated data in Figures 2.9 and 2.11. Simulated clusters of various richnesses (given in Table 1.2) were simulated. The accuracy of the estimated redshifts is worst for the poorest clusters, but even for these it should be better than Δz=0.1 for redshifts less than about 0.7. Hereafter the accuracy decreases, as a large fraction of the galaxies drop below the

completeness limit of the survey. Again, for redshifts less than ~0.7, the MF algorithm should find all clusters of all richnesses (Figure 2.11). The fraction of false detections is essentially zero below this redshift and rises (most rapidly for poorer clusters) hereafter. Thus, this algorithm should essentially recover all clusters with negligible contamination below z~0.7.

2.4.2 Method 2: The CMR Algorithm

The CMR finder used is based on the Cluster Red Sequence (CRS) algorithm of Gladders & Yee (2000). Their method is directly applicable to the XDCS data set, as they tested the algorithm on V- and I_c-band data of the CNOC2 field redshift survey (Yee et al. 2000). The CNOC2 survey comprises four fields of similar area and depth to each of the XDCS fields, although the area of XDCS is an order of magnitude larger. The algorithm works by first filtering the data leaving only those which are compatible with galaxies belonging to a model colour slice in colour-magnitude space. Then the method proceeds in a similar manner to the previous methods - convolving the data points with a kernel and performing density estimation. However, there is now the added complication that the overdensity finding has to be done in 3D.

Model CMRs

The passive-evolution models of Kodama & Arimoto (1997), with the cosmology $H_0 = 64$ kms^{-1} Mpc^{-1}, and q_0=0.1, and a formation redshift of $z_f = 4.4$, were used. These models reproduce the evolution of the CMR for clusters to $z \gtrsim 1$ (Kodama et al. 1998). A redshift is selected and the model colours as a function of magnitude for this redshift extracted. A colour slice of width compatible with the scatter in the CMR is taken around this line The slices are selected in colour space and constructed in such a way that each overlaps by half the width of the next slice, in order to ensure that cluster CMRs are not lost between adjacent slices. This leads to irregular redshift spacing (shown below). Slices were chosen between $V - I_c = 1.4$ and $V - I_c = 2.7$. Bluer than this limit and the 4000Å break passes below the limit of the V-band filter, and redder than this limit and the colour errors become unreasonably large. The model slices used are shown below.

Each of the 24 slices shown above is confronted with the x,y-position, colour, colour-error and total I_c magnitude data in turn. Each galaxy is then given a weight which is the likelihood that for the given V - I_c, $\Delta(V - I_c)$, `MAG_BEST` (I_c), the galaxy belongs to the model CMR slice (errors in the I_c magnitude are ignored as the CMRs are virtually

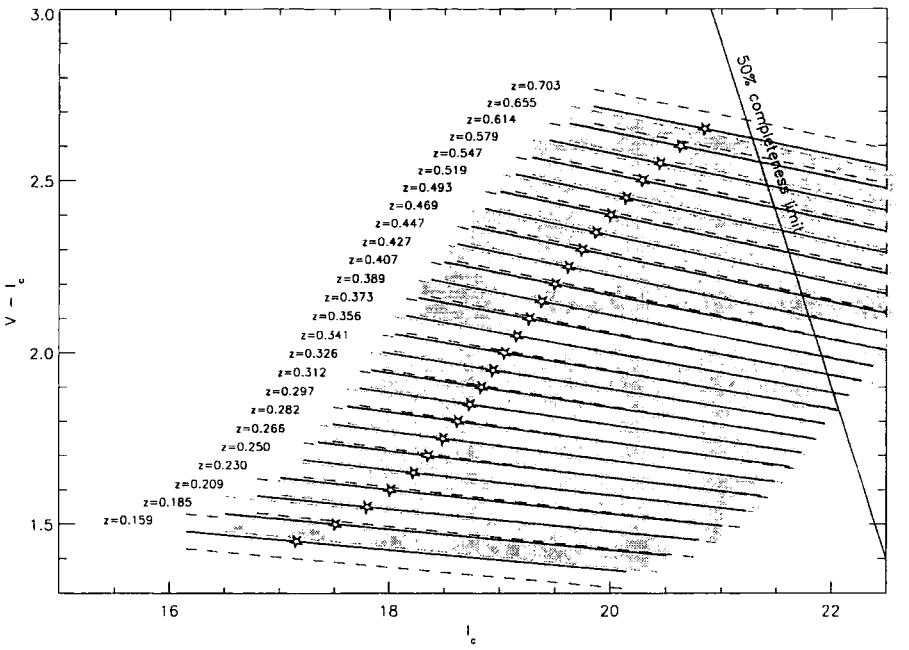

Figure 2.12: Model colour slices used in the CMR finder. Thick lines show the CMR at the redshift given to the left; stars illustrate the position of M*; and dashed lines show the 1σ scatter in the CMR, bounding the slice. Colour slices run from M*-1 to M*+3 (to a limiting magnitude of $I_c = 22.5$). Alternate slices are shaded differently for clarity. The 50% completeness limit of the photometry is also shown.

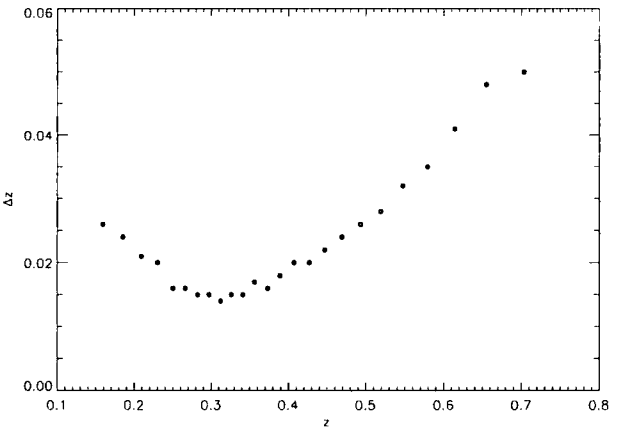

Figure 2.13: The redshift resolution of the CMR-finder. The binwidth in redshift of the model slices (spaced constantly in colour), is shown as a function of redshift. This illustrates that the method offers greatest sensitivity at $z \sim 0.3$, and the binwidths increase rapidly above $z \sim 0.5$. Also increasing colour errors and incompleteness lead to increasing uncertainty in redshift estimation, at the high end.

horizontal). This weight shall be termed the *colour weight.* In practice, many galaxies are so far from the colour slice that their colour weights can safely be set to zero, thus galaxies with colour weights of less than 0.1 (ie. 10 *per cent* probability of belonging to the CMR slice) are ignored. This is done for computational efficiency.

As mentioned above, the aim is to run kernel density estimation on the data, using colour-based weights to amplify the signal from cluster galaxies. Now, as can be seen from the number counts, the numbers of galaxies at faint magnitudes grows rapidly. Thus, if just the colour weights were used, spurious detections would be caused simply due to some fields containing large numbers of faint objects (many of which would have the same colour as the CMR slice). Put simply, brighter (and rarer) galaxies are more powerful diagnostics of cluster members. Hence, it is necessary to also apply *magnitude weights* to weight brighter objects more heavily, within each colour slice. The form of this weighting function was determined by Gladders & Yee (2000) for the CNOC2 data. This function is the probability that a galaxy of a given magnitude is a cluster galaxy. It could be derived from theoretical models - but requires the cluster galaxy LF; the space density of clusters and its evolution; and the field galaxy counts - but it is simpler to deduce internally from the data. Gladders & Yee (2000) show that whether they assume 2% or 20% of all their galaxies lie in clusters, the fit to the weighting function only differs in linear slope by a factor of 1.5 (although there is considerable scatter about the relation). Bearing this in mind, the function chosen here is a fit by eye to the result in their Figure 5).

$$P(M) = \begin{cases} 0.55 & (M^\star - 1 < M < M^\star) \\ -0.08(M - M*) + 0.55 & (M^\star < M < M^\star + 3) \end{cases} \tag{2.15}$$

Once colour weights have been assigned, each galaxy is given a *total weight* for each colour slice which is just the product of the colour weight and the magnitude weight. The next step is to smooth the data with a kernel and estimate the density of the weighted points. In a change from the previous method, a regular grid is chosen. This makes several later stages computationally easier. A grid fixed in physical size (for the above cosmology) is constructed with the pixels spaced in intervals of 0.125 h^{-1}Mpc. The kernel chosen also differs from the Gaussian kernel used in the above methods. Gladders & Yee (2000) chose to use an exponential kernel of the form $k(r) = Ae^{(-1.965r)}$ where A is a normalising constant [8] and r is the physical distance between galaxies at the redshift of

[8] although this is unnecessary, as a further normalisation step is carried out later in the algorithm, and so A is ignored here.

the colour slice, in units of $0.33h^{-1}$Mpc. They chose this kernel as it approaches the shape of the NFW profile at intermediate radii (for the value of -1.965 chosen) and is constant provided that r is given in units of the NFW scale radius (a value of $0.33h^{-1}$Mpc is suggested by the CNOC1 survey (Carlberg et al. 1996)).

Thus, running the above algorithm results in a series of grid points distributed over the field of view, each with an associated signal resulting from the convolution of the exponential kernel with the total weights. These signal amplitudes will be referred to as δ_{ij}s in the notation of Gladders & Yee (2000). Each colour (redshift) slice contains a different number of grid points (as the angular size of the field is fixed, but the physical scale at the redshift of the slice decreases with increasing redshift), and a different distribution of δ_{ij}s. The distribution changes as the fixed physical size kernel changes apparent size, and the mean density of objects differs between redshift slices. Thus, the δ_{ij}s need transforming into some standard measure of significance, correctly normalised between the colour slices.

Several cluster detection algorithms (Gal et al. 2000, Lobo et al. 2000, Gladders & Yee 2000) have used bootstrap resampling techniques to assess the significance of detections, and this is also done here. As noted by Gladders & Yee (2000), a direct application of the bootstrap is likely to be incorrect (as the data contains clusters and is therefore not independently distributed). So, exclusion cuts of 10% of the data at the high-δ_{ij} and low-δ_{ij} (to preserve symmetry) ends are performed; and each data point (comprising an x,y-position, colour, colour-error, and magnitude) is sampled, with replacement, until the original number of datapoints have been extracted. The bootstrapped datapoints are then run through the algorithm resulting in a new distribution of bootstrapped δ_{ij}'s. Each WFC mosaic has one bootstrapped realisation of its data made, as the process is computationally expensive. The high-δ_{ij} tail (where the number of points is low) can be extrapolated well with a simple linear fit, rather than performing many more bootstrap resamplings. See the distributions illustrated in Figure 2.14, and cf. Figure 7 of Gladders & Yee (2000). The probability that a given δ_{ij} occurs at random can be found by comparing the number of δ_{ij}'s in a given range with the number in the same range in the clipped-bootstrap sample. $P(\delta_{ij}) = \frac{N(\delta_{bootstrap} \geq \delta_{ij})}{N(\delta_{bootstrap})}$. These can then be transformed into Gaussian sigma (denoted σ_{ij}) for convenience.

The final step in this process is to extract the significant peaks, and work out which peaks are associated (ie., part of the same cluster). The above σ_{ij}'s form a datacube in x,y,z space, where x,y are the physical metric coordinates and z is the redshift of each slice.

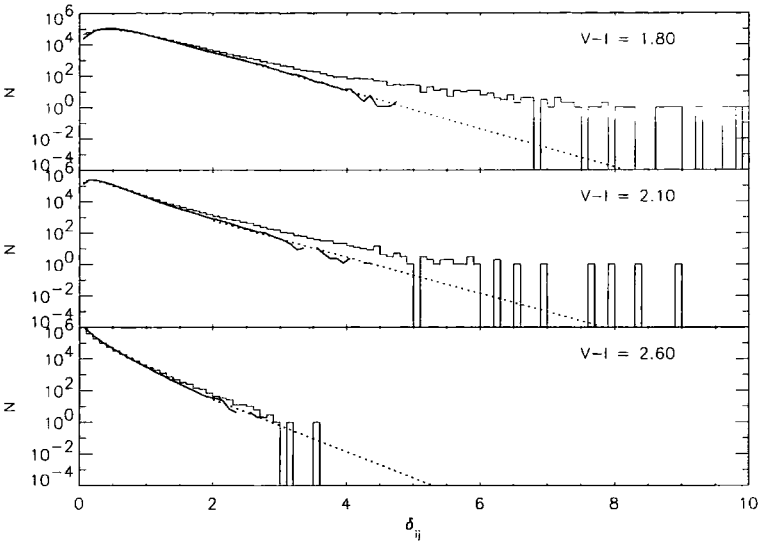

Figure 2.14: Histograms of δ_{ij} values for CMR-finder. Three different colour slices are illustrated. The solid histogram shows the binned values for the whole survey. The thick, solid line shows the values for the bootstrapped-thresholded data, and the dotted line is the power-law extrapolation to the bootstrap. See text.

Gladders & Yee (2000) used the clump-finding algorithm `clfind` of Williams, de Geus, & Blitz (1994) to extract significant associations from the data. A user-friendly version of this algorithm was downloaded from `http://www.astro.ufl.edu/~williams/clfind/` and run on the datacubes using the parameters detailed in Gladders & Yee (2000). Briefly, the algorithm is a 3D friends-of-friends group-finder which also contours the data at fixed intervals and looks for clumps in this 4D space. The code was originally used with temperature maps in radio data, but the temperature can be replaced with signal from the CMR-finder, and the method is identical. The highest peaks are identified first and traced down in contour levels, their friends above the minimum level being linked to them at each interval. Following this through, all points become joined into one clump as the lowest contour level approaches the noise within the data. From extensive simulations, Williams, de Geus, & Blitz (1994) recommend the data be contoured at intervals of twice the *rms* noise in the data. Gladders & Yee (2000) calculated this value to be $1.1\sigma_{ij}$. Tests were performed varying this value. The resulting groups found were practically identical, but using a value of $1.4\sigma_{ij}$ seemed a slightly better choice. Using a lower value split off clumps around the periphery of higher significance clumps (described in more detail below). The peaks were traced down to the lowest possible contour level ($1.1\sigma_{ij}$). This level resulted in a total catalogue of $\gtrsim$1000 candidates. This number was reduced

by setting a higher threshold later, by examining the repeatability of cluster detections in the overlapping data. A threshold of 4.8σ was found to result in a reasonable number ($\sim$200) of repeatable candidates, detected in the two independent images. This high value may suggest that the bootstrap estimate used may be an overestimate of the formal significance of candidates. However, since the relative significance is correct, just selecting a subsample of the most significant systems is a perfectly valid approach.

Thus a list of cluster candidates is extracted from the datacubes. One further stage is necessary to clean the resulting catalogues, as a number of candidates were found in close proximity to more significant candidates. These may be genuine groups infalling into larger clusters, or just spurious detections from increased noise around other candidates. Failure to remove these would result in the following problem: when measuring properties (such as richness, see below) of the detected systems, if a cluster and poor group are superposed along the same line, very close together on the sky, then the effect on the richness measurement of the richer system would be minimal; but the effect on the poorer system would be to catalogue another rich system (due to contamination from the richer cluster). Hence, a minimum distance in physical and redshift space was imposed to prevent these duplicate detections, and only the highest peak within two cutoff radii (ie. 8 times the NFW scale radius of $0.33h^{-1}$Mpc) and two redshift slices retained. An estimate of a characteristic radius for each group was made (as for the MF algorithm) by taking the maximum distance between the candidate centre and the 3σ contour.

2.4.3 Richness Measures

One of the simplest observables for a galaxy cluster, in optical data, is its richness. Richness measurements and correlations have been discussed briefly in Chapter 1. Different richness measures are discussed in detail below, and the results of the measures for cluster candidates are presented in Chapter 3.

The original richness classification of Abell has been shown to be subject to many biases (eg, Van Haarlem, Frenk, & White 1997, Katgert et al 1996). However, more recent estimates such as the B_{gc} parameter of Longair & Seldner (1979) and $N_{0.5}$ of Bahcall (1981) correlate well with cluster velocity dispersion (Yee & Lopez-Cruz 1999, Hill & Lilly 1991, for example).

The $N_{0.5}$ Measure

The $N_{0.5}$ parameter is an Abell-type richness measure, but with a more physically motivated basis. The main drawback of the Abell Richness Class (ARC) are that the counting radius is too large, and so the ARC is particularly sensitive to fluctuations in background density. Also, the discrete nature of ARCs can make them cumbersome for quantitative studies.

Bahcall (1981) suggested using the galaxy number density within 0.5 h^{-1}Mpc, and brighter than $m_3 + 2$ (where m_3 is the magnitude of the third brightest galaxy) as a measure of richness. A correlation exists between $N^c_{0.5}$ and cluster velocity dispersion, where $N^c_{0.5}$ is the value of $N_{0.5}$ corrected for the mean observed dependence of m_3 on cluster richness [9]. The relation is $N^c_{0.5} \approx 21(v_r/1000)^{1.2}$, where v_r is the cluster velocity dispersion in kms^{-1} . This is understood in terms of the Virial Theorem.

Hill & Lilly (1991) defined a similar $N_{0.5}$ measure for estimating the environments of radio galaxies. The authors chose to use the magnitude range $m_{rg} + 3$, where m_{rg} is the magnitude of the radio galaxy. They state that this approach has the advantages that the absolute magnitude of a radio galaxy has no strong dependence on environment; and that identifying the third brightest cluster galaxy at moderate redshifts is not robust due to the uncertainties in background subtraction. It is worth noting that $m_{rg} + 3$ is always brighter than $m_3 + 2$ (generally by about 0.4 mag in terms of metric apertures) and so will lead to a (conservative) underestimation of the cluster environment. Hill & Lilly (1991) also show both empirically and with a theoretical calculation, a relation between the correlation statistic B_{gg} and $N_{0.5}$, although the calibration at high redshift is open to question given the effects of evolution. The relation between typical bright cluster radio galaxies and the cluster characteristic magnitude, $m_{rg} = m^\star - 2.5$ (Hill & Lilly 1991) is used to calculate the magnitude range used. Thus, this calculation of $N_{0.5}$ uses the range $m_3 - 2.5$ to $m_3 + 0.5$.

The B_{gc} Measure

B_{gc} is explained in detail in Yee & Lopez-Cruz (1999). It has been used by several workers, primarily in studies of the environments of radio galaxies (for recent examples:

[9] This correction can be thought of in terms of the bias leading to the "Scott Effect". Scott (1957) noted that one would expect the n^{th} brightest galaxy in a rich cluster to correspond to a brighter magnitude than the n^{th} brightest galaxy in a poor cluster. This difference corresponds approximately to the difference in the local normalisation of the luminosity function.

Andersen & Owen 1994, Miller et al. 1999). In outline, it is found from the amplitude of the 3D two-point correlation function. The 3D correlation function is difficult to measure; observationally easier is the angular correlation function, $\omega(\theta)$. This is simply a measure of the number of galaxies at a given angular separation. This can be approximated as a power law $\omega(\theta) = A_{gg}\theta^{1-\gamma}$ (Davis & Peebles 1983, for example), where A_{gg} is the angular galaxy-galaxy correlation amplitude. Now, fixing a reference point as the assumed centre of the cluster, one can measure the two-point angular galaxy-cluster correlation function. Its amplitude, A_{gc}, can be calculated by counting the excess number of galaxies (ie. background-subtracted), within some radius, θ, of the cluster centre ($N_{net} = N_{total} - N_{bgd}$). Assuming fixed γ, $A_{gc} = (N_{net}/N_{bgd})[(3-\gamma)/2]\theta^{\gamma-1}$.

B_{gc}, the spatial amplitude, can be estimated via deprojection of the angular correlation function, assuming spherical symmetry, as given in Longair & Seldner (1979):

$$B_{gc} = N_{bgd}\frac{D^{\gamma-3}A_{gc}}{I_\gamma \Psi[M(m_0,z)]} \tag{2.16}$$

where N_{bgd} is the background galaxy counts to apparent magnitude m_0 and $\Psi[M(m_0,z)]$ is the integrated LF of galaxies up to the absolute magnitude M, given by m_0 at the cluster redshift z. I_γ is an integration constant arising from the deprojection ($I_\gamma = 3.78$ for an assumed γ of 1.77). D is the angular diameter distance to z (Equation 2.3).

Yee & Lopez-Cruz (1999) discuss extensively the effects of different assumptions/ measurement limits on B_{gc}. The salient points are summarised here. If the assumption of a universal LF is not strictly correct, then the systematic uncertainty this introduces in B_{gc} is $\sim$ 10%. Changing the parameters of the LF (slope and normalisation) results in $\lesssim$ 20% differences in B_{gc} - if $M^\star$ is incorrect by as much as 0.5 mags, and if α is incorrect by as much as ± 0.3. B_{gc} is independent of the sampling area, provided γ has been correctly chosen. B_{gc} is insensitive to the sampling magnitude limit if m_{lim} lies on the flat part of the LF (between $M^\star$+1 and $M^\star$+2). The most important step is ensuring that the cluster LF and background galaxy counts are determined in a self-consistent manner.

The model LF is the same as that chosen for the cluster in the MF algorithm. Figure 2.15 illustrates how the model LF assumed for both the cluster and the field translates into field galaxy counts. The LF was integrated over 0.05 redshift bins from $z = 0.00$ to $z = 2.00$, with the volume element, dV, at each stage given by the formula below (where the symbols have there usual meanings, as used throughout this thesis):

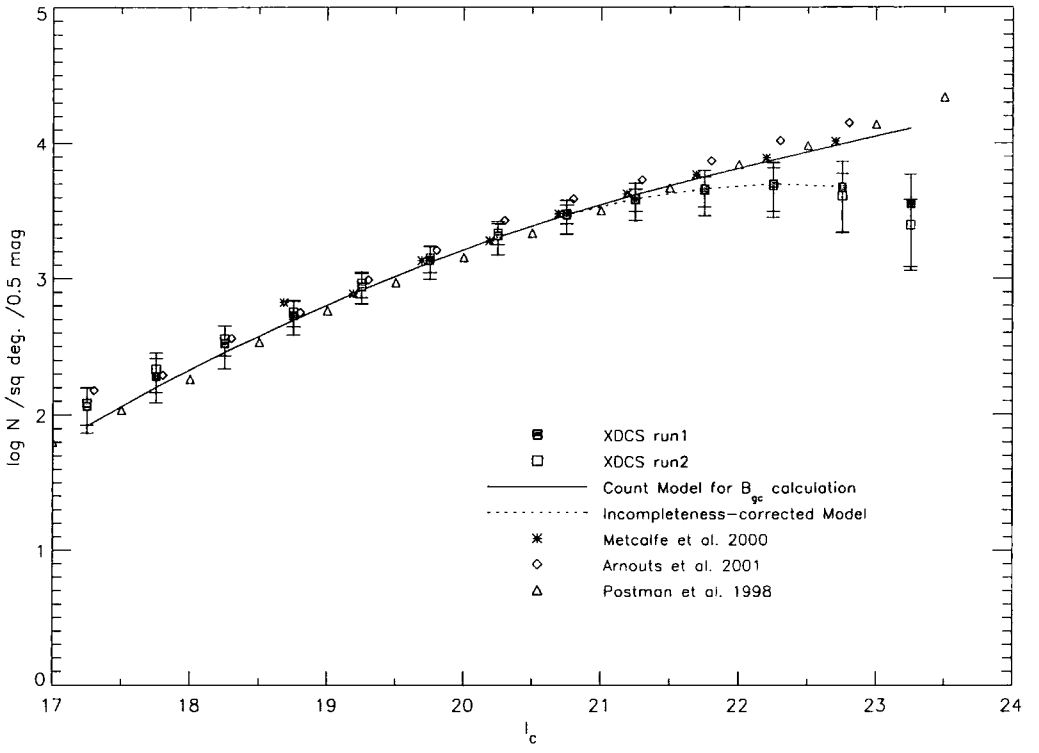

Figure 2.15: I-band galaxy counts for both XDCS runs and model counts used in derivation of B_{gc}. Error bars are standard deviation from field-to-field. Both runs are found to be in good agreement, suggesting that the photometry for XDCS is homogeneous. Overplotted is the completeness model (relative to Metcalfe et al. 2001) used to allow data to $I = 22.5$ to be used. Magnitudes are `SExtractor MAG_BEST` magnitudes. I-band counts from the literature are overplotted, and found to be in good agreement. The completeness is modelled by a single-sided Gaussian of width 1.90 mags, centred on I=20.86.

$$\frac{dV}{d\omega dz} = r_{char}^2(z)\frac{c}{H_0(1+z)(1+\Omega_0 z)^{1/2}} \tag{2.17}$$

and

$$r_{char}(z) = \frac{2c}{H_0(1+z)}\frac{\Omega_0 z + (\Omega_0 - 2)[(1+\Omega_0 z)^{1/2} - 1]}{\Omega_0^2} \tag{2.18}$$

for an open, non-accelerating Universe (eg. Coles & Lucchin 1995).

The normalisation, $\phi^\star$, was fit using a "chi-by-eye" technique, to give the best match to both XDCS runs. $\phi^\star = 0.0035\ h_{64}{}^3\mathrm{Mpc}^{-3}$ was found. This is consistent with the R-band value measured by Yee & Lopez-Cruz (1999), after correcting the number density to their cosmology. The completeness is modelled as XDCS counts/ literature counts (from Metcalfe et al. 2001) to $I_{lim} = 22.5$ (where the completeness falls to 70%). This factor is then applied to the expected counts for the B_{gc} calculation (as well as to the MF algorithm, earlier).

The uncertainty in the B_{gc} parameter is computed using the formula from Yee & Lopez-Cruz (1999):

$$\frac{\Delta B_{gc}}{B_{gc}} = \frac{(N_{net} + 1.3^2 N_{bgd})^{1/2}}{N_{net}} \tag{2.19}$$

The factor 1.3^2 accounts for the clustered (and so non-Poissonian) nature of the background counts (Yee & Green 1987).

The L_E Measure

The luminosity of galaxies on the CMR referred to as L_E (since the galaxies are primarily early-type), has been shown (for a limited sample, anyway) to correlate well with the X-ray temperature of the cluster (Smail et al. 1998). For a sample of the 10 most X-ray luminous clusters in the redshift range $z = 0.22 - 0.28$, Smail et al. (1998) investigated the homogeneity of the stellar populations of cluster early-type galaxies. One method they used was to compare mass of baryonic material locked up in stars in early-types (in the form of the luminosity of galaxies on the CMR) with the total mass of the cluster (using X-ray temperatures from the literature). They found a remarkably small scatter about this relation ($\approx$ 17% compared to the $\approx$30% when $L_X$is used instead of T_X). It should be noted that the sample spans a narrow range in redshift, and relatively narrow range in blue fraction (ie. few galaxies statistically belonging to the cluster are *not* red), and mass. A large sample to characterise an empirical relation between L_E and T_X(or

mass) over a larger range of parameter space does not currently exist in the literature. However, the evolution of cluster mass-to-light ratios for a sample of 4 X-ray selected clusters over a wide range ($0.22<z<0.83$) of redshift has been studied by Hoekstra et al. (2001). Using gravitational weak-shear measurements from HST images, they determined that the mass-to-light ratios in their sample evolve in a manner consistent purely with luminosity-evolution of the cluster early-type galaxies. Thus, inverting this argument, measuring the rest-frame luminosity of cluster early-type galaxies (corrected for passive evolution) could potentially provide an estimate of the total cluster mass. Again it should be emphasised that the datasets on which these correlations were based are small and so the scatter in the relation is not well known. Furthermore, all the data came from X-ray selected samples, so the scatter may be further increased once optically selected clusters are included.

For each cluster candidate, the colour slice from the CMR-finder in which the candidate was detected is selected. The galaxies within this colour slice, and within a radius of 0.45 Mpc (0.5 Mpc in Smail et al.'s (1998) cosmology) brighter than $M_V = -18.5+5\log h$ (Smail et al. 1998) were selected, and their apparent I-band magnitudes converted into rest-frame V luminosity, again using the stellar population synthesis models of Kodama & Arimoto (1997). This magnitude limit is approximately 1.5 magnitudes fainter than $L^\star$ at $z\sim0.3$. Background subtraction was carried out by calculating the number of galaxies in a surrounding annulus, scaled to the area of the cluster region, as above, and subtracting the corresponding luminosity, assuming these galaxies were at the same redshift as the cluster. The limits for the maximum and minimum luminosity were estimated by using all the galaxies whose photometric colour errors allowed them into or out of the colour slice, respectively, and summing their luminosities in the same way. This gives error estimates in excellent agreement with assuming the error is entirely due to the error in the estimated redshift (by taking the redshifts of the next highest and lowest colour slices and recalculating the luminosities).

2.5 Summary

This Chapter has described the optical data used in the X-ray Dark Cluster Survey (XDCS), a cluster survey carried out in archival ROSAT fields to ensure complete x-ray and optical overlap. The data reduction and construction of photometric catalogues for the 39 fields of 19 arcmin radius (providing a total survey area of around 12 $\deg^2$) have

been detailed. Two cluster detection algorithms have been described. The first using a modified version of a "matched-filter" algorithm to search for clusters in the I-band catalogues. The second using (an almost identical implementation of) Gladders & Yee's (2000) red-sequence cluster finder, to locate clusters in V and I-band data. Simulations to assess the performance of the former technique have been applied, and find that the algorithm should be complete for clusters of all richness classes below redshifts of about 0.7. Details of the performance of the latter technique are given in Gladders & Yee (2000). Finally, three techniques for measuring optical richness were described - a simple count of galaxies within a fixed physical radius (N_{05}), a more involved measure based on the deprojection of the correlation function (B_{gc}), and a measure of the total luminosity of (passively-evolved) galaxies on the colour-magnitude relation (L_E). It is worth emphasising here that potentially the only technique that can detect line-of-sight projections (described in Chapter 1) is the CMR-finder; and the only richness measure unaffected by these projections (except in the limit of very close systems where the CMRs touch, see Figure 2.13) is the L_E richness measure.

Chapter 3

Catalogues of Cluster Candidates

3.1 Introduction

In the previous chapter, two techniques for selecting clusters in optical passbands - the Matched Filter (MF) and the Colour-Magnitude Relation (CMR) finder - were presented, along with the Wide-Field Camera (WFC) dataset. These comprise the optical survey of the XDCS. The method with which these were used to construct and examine two cluster catalogues will now be detailed. The X-ray dataset and X-ray cluster selection will be outlined and a comparison between the different cluster selection techniques made.

3.2 Construction of Final Optical Catalogues

Both the MF and CMR finders were run on each WFC mosaic individually. Since each field possesses overlapping "A" and "B" data (Chapter 2), the next step is to combine the candidates from the A- and B-rotations, for each algorithm, into one catalogue. The MF technique is more straightforward, so this will be discussed first.

The MF catalogue was divided into two catalogues with different significance thresholds. The higher significance catalogue will be referred to simply as the MF catalogue, or the *final* MF catalogue, if it is necessary to emphasise the distinction between this and the lower-significance catalogue: referred to as the *full* MF catalogue. The full MF is that using the thresholding described in Chapter 2. The final MF catalogue was produced by imposing a stricter Cash C cut (a value of -280, this time). The completeness and spurious rates with this threshold are comparable to those plotted in Figure 2.11 for redshifts less than 0.7[1]. Also, candidates with a MF group radius (Chapter 2) of zero were rejected. Such objects occur when only a single galaxy (and none of its near neighbours)

[1]Using higher redshift candidates just increases the number of spurious detections, and the X-ray data are unlikely to probe enough volume to detect clusters at these redshifts.

lies above the Cash C threshold. This reduces the number of clusters detected to a more manageable number, $\lesssim$200, of higher confidence candidates, whilst the full MF catalogue allows the list of lower significance candidates to still be retained. This may prove useful later, if, for example in cross-comparisons between catalogues, a candidate is not found with high significance in the MF catalogue; then the full MF catalogue may be searched.

Next, I-band WFC thumbnail images were produced for all candidates in the MF catalogue. These were inspected to see if a candidate was found due to spurious objects (eg., satellite trails, haloes of bright stars). Those that were spurious were flagged and rejected from the catalogue. Finally, the MF catalogue comprising A- and B-rotation candidates was reduced to a single catalogue by searching for candidates which overlapped in the two rotations. Where this occurred, only the candidate with the larger group radius was retained. This was found to be more stable than selecting the highest peak Cash C value candidate, as the group radius is given by the extent of galaxies passing the Cash C cut; but the Cash C value noted for each candidate just comes from the galaxy with the highest individual value, in the candidate. This can be thought of as favouring a larger "total likelihood" over that of a "peak likelihood" for each cluster candidate.

The procedure for producing the CMR catalogue is slightly more involved. This is due to the "3D" aspect of finding clusters with this technique. Whereas the MF finder just selects overdensities and fits the most likely redshift to the clump; the CMR finder can, in principle, detect projections of groups along the line of sight. The same first steps as for the MF were followed: I-band thumbnails were generated, spurious candidates rejected, and a higher and lower significance catalogue generated. The final CMR catalogue had a threshold of 4.8σ imposed, as described in Chapter 2, whereas the full (lower significance) catalogue allowed candidates to be traced down to the lowest possible contour level with `clumpfind` (ie. 1.4σ). Candidates in the *same* rotation which showed more than one candidate overlapping (as defined by their group radii) were flagged as "projection" possibilities. This check was performed on an individual frame basis to avoid the possibility that a single candidate having a significantly different estimated redshift in the A- and B-rotations (eg. due to undetected photometric offset between the frames) would result in one candidate being artificially classed as a projected system. The final CMR catalogue was produced by combining the rotations as for the MF.

This provided the two main catalogues for the optical survey, the final MF catalogue and final CMR catalogue. These catalogues were then passed to the richness measuring algorithms described in Chapter 2. Finally, both catalogues were cropped to overlap with

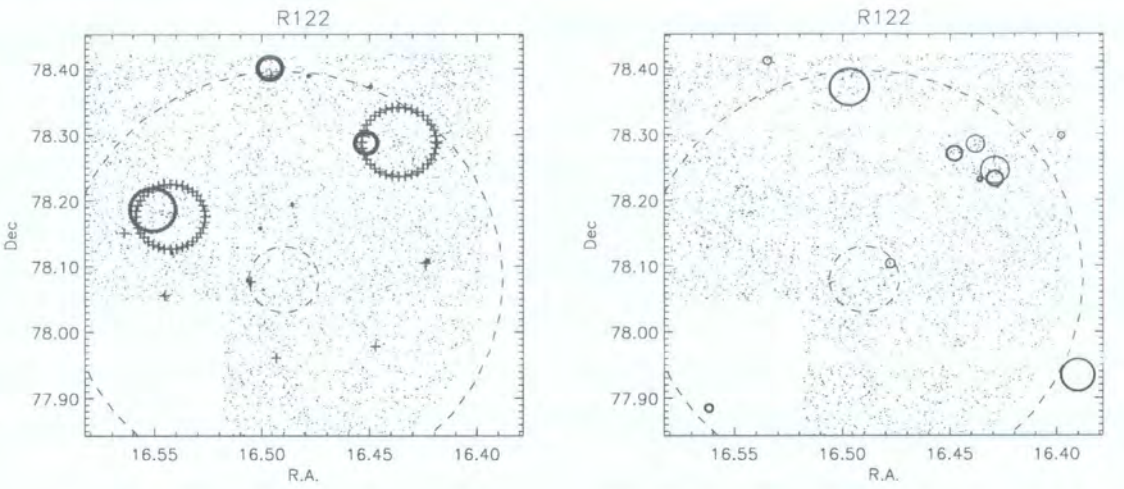

Figure 3.1: Full catalogues in one field for MF (left) and CMR (right) algorithms. Points show galaxies with I-band magnitudes brighter than 22.5 (for B-rotation only, for clarity). Dashed lines denote the limits of the PSPC field (19 arcmins: outer radius, 3 arcmins: inner radius). Cluster candidates are outlined by points marking their group radii (defined in text). Symbols are:
Left panel, MF candidates: filled circles - A-rotation; crosses - B-rotation.
Right panel, CMR candidates: thick lines - A-rotation; thin lines - B-rotation.
Those candidates which appear as single points have group radii of zero (see text).

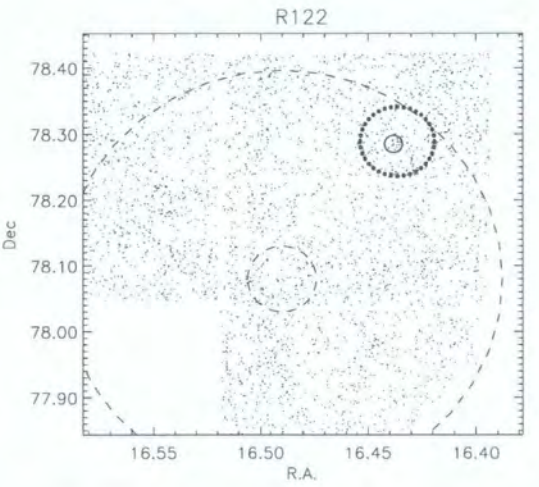

Figure 3.2: Final catalogues for this field. The thresholding described in the text has been applied. Dotted circle denotes MF candidate, solid line shows CMR candidate. Other symbols as for previous figure.

the X-ray data which is described below. To do this, only candidates within a certain annulus from the centre of the X-ray pointing were retained. The inner and outer radii of this annulus were 3 and 19 arcmins, respectively. At distances greater than this the X-ray data are not useful (due to degraded resolution and sensitivity - see below) and the inner region is excised to avoid objects associated with the target of the X-ray observation.

3.2.1 Final MF Catalogue

Table 3.1: Catalogue of MF candidates. Columns are : candidate ID (comprising algorithm type / Right Ascension / Declination (J2000)); RIXOS field ID; RA and Dec (decimal, J2000); value of the Cash C statistic; estimated M* (and the corresponding estimated redshift).

Candidate ID	RIXOS Field	α (J2000) [Hours]	δ (J2000) [Degrees]	Cash C Statistic	$M^\star_{est}$ (z_{est})
mfJ000923.4+104856	R281	0.1565	10.8156	-355.61	19.80(0.47)
mfJ000941.0+110502	R281	0.1614	11.0841	-317.17	18.70(0.31)
mfJ000945.0+104755	R281	0.1625	10.7986	-333.79	19.30(0.39)
mfJ000947.2+104314	R281	0.1631	10.7207	-303.71	19.40(0.41)
mfJ001036.5+104255	R281	0.1768	10.7153	-334.46	19.20(0.38)
mfJ001044.4+104942	R281	0.1790	10.8284	-310.87	18.40(0.26)
mfJ001057.0+105247	R281	0.1825	10.8798	-371.10	19.20(0.38)
mfJ001126.9+105358	R281	0.1908	10.8995	-365.34	18.90(0.34)
mfJ012427.7+034359	R262	1.4077	3.7332	-346.02	18.70(0.31)
mfJ012433.8+035816	R262	1.4094	3.9712	-322.80	18.10(0.22)
mfJ012445.4+033353	R262	1.4126	3.5649	-299.82	20.20(0.52)
mfJ012452.6+034424	R262	1.4146	3.7401	-336.97	19.70(0.45)
mfJ012515.2+035352	R262	1.4209	3.8978	-315.81	19.20(0.38)
mfJ012532.9+035935	R262	1.4258	3.9933	-353.92	20.00(0.49)
mfJ014229.2+043039	R292	1.7081	4.5110	-299.16	18.90(0.34)
mfJ014245.0+041521	R292	1.7125	4.2560	-306.10	19.10(0.37)
mfJ032741.4+023446	R245	3.4615	2.5796	-296.50	19.00(0.35)
mfJ032900.2+025637	R245	3.4834	2.9436	-308.10	18.40(0.26)

continued...

Candidate ID	RIXOS Field	α (J2000) [Hours]	δ (J2000) [Degrees]	Cash C Statistic	$M^{\star}_{est}$ (z_{est})
mfJ041702.0+011401	R283	4.2839	1.2338	-323.66	17.00(0.06)
mfJ041719.0+010132	R283	4.2886	1.0257	-337.62	19.00(0.35)
mfJ041752.8+010332	R283	4.2980	1.0590	-310.37	18.90(0.34)
mfJ071929.3+710923	R211	7.3248	71.1564	-321.78	18.20(0.24)
mfJ072014.6+713202	R211	7.3374	71.5340	-300.99	17.70(0.16)
mfJ072114.8+712241	R211	7.3541	71.3781	-293.61	18.90(0.34)
mfJ072409.0+710651	R211	7.4025	71.1142	-317.66	19.80(0.47)
mfJ075715.5+375159	R255	7.9543	37.8666	-387.78	18.90(0.34)
mfJ075716.6+374143	R255	7.9546	37.6953	-348.71	19.70(0.45)
mfJ075723.0+373750	R255	7.9564	37.6306	-336.24	19.70(0.45)
mfJ075731.0+380118	R255	7.9586	38.0217	-305.63	17.00(0.06)
mfJ075752.6+374348	R255	7.9646	37.7301	-328.97	18.10(0.22)
mfJ075937.7+374550	R255	7.9938	37.7641	-331.84	19.60(0.44)
mfJ075958.2+374909	R255	7.9995	37.8194	-343.09	19.50(0.42)
mfJ080241.6+651428	R213	8.0449	65.2411	-346.02	19.10(0.37)
mfJ080301.4+644747	R213	8.0504	64.7964	-295.08	19.30(0.39)
mfJ080312.6+645410	R213	8.0535	64.9028	-307.26	19.20(0.38)
mfJ080411.6+650956	R213	8.0699	65.1656	-306.23	19.60(0.44)
mfJ080504.6+644806	R213	8.0846	64.8018	-292.13	19.70(0.45)
mfJ080630.2+650331	R213	8.1084	65.0587	-293.87	19.00(0.35)
mfJ080645.0+645659	R213	8.1125	64.9499	-326.29	19.00(0.35)
mfJ081841.4+372128	R293	8.3115	37.3580	-335.08	19.40(0.41)
mfJ082003.1+371452	R293	8.3342	37.2478	-353.61	19.20(0.38)
mfJ082004.6+372650	R293	8.3346	37.4474	-323.54	19.20(0.38)
mfJ082005.6+373248	R293	8.3349	37.5467	-310.52	19.60(0.44)
mfJ082109.4+373141	R293	8.3526	37.5283	-311.45	19.10(0.37)
mfJ083750.9+362124	R228	8.6308	36.3569	-343.66	19.50(0.42)
mfJ083833.7+361535	R228	8.6427	36.2599	-355.23	19.90(0.48)
mfJ083833.7+362931	R228	8.6427	36.4921	-314.81	19.30(0.39)
mfJ083901.1+363746	R228	8.6503	36.6296	-366.14	19.80(0.47)
mfJ083901.4+362029	R228	8.6504	36.3414	-347.34	20.20(0.52)

continued...

Candidate ID	RIXOS Field	α (J2000) [Hours]	δ (J2000) [Degrees]	Cash C Statistic	$M^{\star}_{est}$ (z_{est})
mfJ083906.8+362709	R228	8.6519	36.4525	-365.05	20.20(0.52)
mfJ083945.0+362850	R228	8.6625	36.4807	-311.65	19.30(0.39)
mfJ084914.2+372710	R221	8.8206	37.4528	-299.70	18.80(0.32)
mfJ084914.5+373123	R221	8.8207	37.5232	-296.55	18.50(0.28)
mfJ084915.2+373440	R221	8.8209	37.5778	-297.14	19.50(0.42)
mfJ084937.2+374245	R221	8.8270	37.7125	-350.56	19.90(0.48)
mfJ090409.8+341315	R257	9.0694	34.2210	-333.51	18.60(0.29)
mfJ090533.0+342441	R257	9.0925	34.4114	-334.13	17.50(0.14)
mfJ090554.2+335743	R257	9.0984	33.9621	-297.34	20.10(0.51)
mfJ090618.7+341740	R257	9.1052	34.2946	-330.85	18.70(0.31)
mfJ090632.0+340224	R257	9.1089	34.0401	-361.74	20.70(0.60)
mfJ090634.9+340757	R257	9.1097	34.1326	-315.40	19.60(0.44)
mfJ090824.7+424548	R248	9.1402	42.7635	-418.61	20.20(0.52)
mfJ090933.1+430732	R248	9.1592	43.1256	-416.41	20.60(0.58)
mfJ090937.1+430159	R248	9.1603	43.0333	-394.63	20.00(0.49)
mfJ091049.4+425002	R248	9.1804	42.8341	-376.40	19.90(0.48)
mfJ091110.3+425647	R248	9.1862	42.9465	-396.39	20.50(0.57)
mfJ092018.2+621056	R216	9.3384	62.1824	-357.45	20.00(0.49)
mfJ092141.8+620246	R216	9.3616	62.0462	-362.37	18.90(0.34)
mfJ092142.1+622912	R216	9.3617	62.4867	-304.74	20.70(0.60)
mfJ092238.3+620438	R216	9.3773	62.0774	-385.69	20.00(0.49)
mfJ092246.2+621315	R216	9.3795	62.2210	-346.69	19.90(0.48)
mfJ092317.5+621506	R216	9.3882	62.2518	-296.85	19.20(0.38)
mfJ092330.8+620446	R216	9.3919	62.0796	-306.72	20.20(0.52)
mfJ092356.4+621450	R216	9.3990	62.2474	-310.45	18.70(0.31)
mfJ092402.5+622203	R216	9.4007	62.3675	-368.38	20.50(0.57)
mfJ094318.1+162011	R285	9.7217	16.3365	-302.48	19.80(0.47)
mfJ094355.9+164113	R285	9.7322	16.6871	-362.03	17.30(0.11)
mfJ100816.8+543715	R231	10.1380	54.6210	-330.95	17.00(0.06)
mfJ100934.6+543310	R231	10.1596	54.5530	-324.43	19.50(0.42)
mfJ100951.5+545815	R231	10.1643	54.9710	-338.33	19.40(0.41)

continued...

Candidate ID	RIXOS Field	α (J2000) [Hours]	δ (J2000) [Degrees]	Cash C Statistic	$M^{\star}_{est}$ (z_{est})
mfJ101050.9+543506	R231	10.1808	54.5850	-303.04	17.00(0.06)
mfJ101137.3+545036	R231	10.1937	54.8435	-332.23	18.50(0.28)
mfJ101204.0+544500	R231	10.2011	54.7502	-346.72	19.60(0.44)
mfJ104206.1+115827	R273	10.7017	11.9744	-339.19	19.40(0.41)
mfJ104219.8+121058	R273	10.7055	12.1828	-384.73	19.00(0.35)
mfJ104224.1+115119	R273	10.7067	11.8554	-306.20	20.80(0.61)
mfJ104239.2+120058	R273	10.7109	12.0162	-347.32	20.00(0.49)
mfJ104303.4+120040	R273	10.7176	12.0113	-332.00	20.60(0.58)
mfJ105617.5+493237	R133	10.9382	49.5438	-340.70	17.70(0.16)
mfJ105644.5+492642	R133	10.9457	49.4450	-312.01	19.70(0.45)
mfJ105732.0+492852	R133	10.9589	49.4812	-391.60	19.70(0.45)
mfJ105816.7+495014	R133	10.9713	49.8374	-380.48	20.30(0.54)
mfJ105836.8+494116	R133	10.9769	49.6879	-327.63	17.30(0.11)
mfJ111719.3+075841	R258	11.2887	7.9782	-344.10	19.60(0.44)
mfJ111726.2+074316	R258	11.2906	7.7213	-373.86	18.20(0.24)
mfJ111809.4+210622	R123	11.3026	21.1062	-403.82	18.60(0.29)
mfJ111824.1+074313	R258	11.3067	7.7204	-340.71	18.30(0.25)
mfJ111835.3+211600	R123	11.3098	21.2669	-335.17	20.40(0.55)
mfJ111903.0+212602	R123	11.3175	21.4341	-357.06	20.30(0.54)
mfJ111926.4+211734	R123	11.3240	21.2929	-307.67	20.00(0.49)
mfJ112000.2+211838	R123	11.3334	21.3107	-331.55	19.80(0.47)
mfJ112001.7+213103	R123	11.3338	21.5176	-341.73	18.90(0.34)
mfJ112337.0+541925	R287	11.3936	54.3236	-310.13	20.50(0.57)
mfJ112417.6+540915	R287	11.4049	54.1542	-370.79	20.00(0.49)
mfJ112512.0+542001	R287	11.4200	54.3336	-336.17	21.30(0.68)
mfJ112529.3+541701	R287	11.4248	54.2837	-319.39	20.80(0.61)
mfJ113531.2+300032	R227	11.5920	30.0091	-355.83	19.80(0.47)
mfJ113548.5+295531	R227	11.5968	29.9253	-385.90	20.30(0.54)
mfJ113611.9+295650	R227	11.6033	29.9474	-366.37	19.70(0.45)
mfJ113638.5+295500	R227	11.6107	29.9167	-376.31	21.10(0.65)
mfJ113721.4+294950	R227	11.6226	29.8306	-369.39	19.80(0.47)

continued...

Candidate ID	RIXOS Field	α (J2000) [Hours]	δ (J2000) [Degrees]	Cash C Statistic	$M^{\star}_{est}$ (z_{est})
mfJ113750.5+294824	R227	11.6307	29.8067	-382.70	20.20(0.52)
mfJ120304.3+555625	R116	12.0512	55.9405	-342.85	19.60(0.44)
mfJ120313.7+560711	R116	12.0538	56.1199	-335.93	18.40(0.26)
mfJ120422.8+560342	R116	12.0730	56.0617	-360.03	20.60(0.58)
mfJ120436.5+561801	R116	12.0768	56.3004	-352.25	20.30(0.54)
mfJ120504.2+555732	R116	12.0845	55.9591	-349.35	20.20(0.52)
mfJ120510.3+560551	R116	12.0862	56.0977	-321.85	19.60(0.44)
mfJ120516.8+560905	R116	12.0880	56.1516	-339.93	20.20(0.52)
mfJ120544.2+561914	R116	12.0956	56.3208	-452.19	20.70(0.60)
mfJ122106.8+281607	R126	12.3519	28.2688	-372.20	19.20(0.38)
mfJ122116.2+275828	R126	12.3545	27.9747	-349.45	20.40(0.55)
mfJ122139.2+282013	R126	12.3609	28.3371	-328.88	20.70(0.60)
mfJ122217.0+281646	R126	12.3714	28.2796	-345.87	19.20(0.38)
mfJ122232.9+281105	R126	12.3758	28.1849	-336.53	19.40(0.41)
mfJ130920.5+320909	R265	13.1557	32.1527	-400.21	19.90(0.48)
mfJ131020.6+320356	R265	13.1724	32.0656	-393.16	19.90(0.48)
mfJ131131.2+322905	R265	13.1920	32.4849	-492.20	19.60(0.44)
mfJ131554.7+290009	R224	13.2652	29.0025	-405.73	19.20(0.38)
mfJ131620.6+285315	R224	13.2724	28.8877	-364.94	20.60(0.58)
mfJ131623.9+285628	R224	13.2733	28.9411	-315.00	18.80(0.32)
mfJ131648.7+285236	R224	13.2802	28.8767	-353.95	19.10(0.37)
mfJ131729.8+285856	R224	13.2916	28.9824	-358.48	18.80(0.32)
mfJ133224.0+105056	R278	13.5400	10.8489	-430.99	19.70(0.45)
mfJ133314.4+105347	R278	13.5540	10.8966	-411.40	19.10(0.37)
mfJ134238.5+554801	R254	13.7107	55.8004	-314.39	19.80(0.47)
mfJ134300.8+554337	R254	13.7169	55.7272	-321.06	18.90(0.34)
mfJ134313.4+555952	R254	13.7204	55.9978	-398.15	19.10(0.37)
mfJ134419.7+560327	R254	13.7388	56.0577	-343.63	20.00(0.49)
mfJ135550.9+182936	R268	13.9308	18.4935	-377.38	19.50(0.42)
mfJ135625.1+181827	R268	13.9403	18.3077	-334.25	18.20(0.24)
mfJ135647.8+182410	R268	13.9466	18.4028	-352.11	18.80(0.32)

continued...

Candidate ID	RIXOS Field	α (J2000) [Hours]	δ (J2000) [Degrees]	Cash C Statistic	$M^{\star}_{est}$ (z_{est})
mfJ140516.8+221345	R274	14.0880	22.2293	-369.21	19.70(0.45)
mfJ140543.8+223056	R274	14.0955	22.5156	-391.51	19.60(0.44)
mfJ140602.5+221759	R274	14.1007	22.2998	-466.05	19.90(0.48)
mfJ140656.2+223113	R274	14.1156	22.5205	-354.36	20.00(0.49)
mfJ140717.0+223318	R274	14.1214	22.5551	-374.79	20.30(0.54)
mfJ141301.9+435346	R217	14.2172	43.8961	-378.66	19.70(0.45)
mfJ141328.9+435826	R217	14.2247	43.9740	-353.04	20.60(0.58)
mfJ141330.4+434729	R217	14.2251	43.7915	-358.02	19.50(0.42)
mfJ141501.4+435611	R217	14.2504	43.9364	-385.60	20.90(0.62)
mfJ141504.7+440313	R217	14.2513	44.0537	-378.75	19.90(0.48)
mfJ142754.0+330958	R110	14.4650	33.1663	-298.98	19.20(0.38)
mfJ142824.2+330538	R110	14.4734	33.0940	-318.18	17.00(0.06)
mfJ142902.4+325648	R110	14.4840	32.9469	-291.47	18.90(0.34)
mfJ162611.0+781719	R122	16.4364	78.2888	-307.87	19.60(0.44)
mfJ163300.7+572137	R223	16.5502	57.3603	-336.82	20.30(0.54)
mfJ163301.1+570015	R223	16.5503	57.0042	-320.04	18.10(0.22)
mfJ163320.2+571023	R223	16.5556	57.1732	-373.25	19.60(0.44)
mfJ163334.2+571457	R223	16.5595	57.2492	-340.58	19.30(0.39)
mfJ163342.5+565558	R223	16.5618	56.9329	-319.23	20.50(0.57)
mfJ163420.3+570405	R223	16.5723	57.0683	-339.83	19.30(0.39)
mfJ163529.0+570640	R223	16.5914	57.1112	-331.43	20.90(0.62)
mfJ163543.8+565536	R223	16.5955	56.9267	-329.47	19.80(0.47)
mfJ163558.9+570618	R223	16.5997	57.1052	-366.44	20.00(0.49)
mfJ163616.2+570709	R223	16.6045	57.1192	-331.49	19.70(0.45)
mfJ170007.2+513735	R236	17.0020	51.6265	-402.96	19.70(0.45)
mfJ170034.6+514249	R236	17.0096	51.7138	-324.81	19.90(0.48)
mfJ170100.8+513413	R236	17.0169	51.5703	-332.94	20.70(0.60)
mfJ170113.8+513205	R236	17.0205	51.5348	-361.14	19.30(0.39)
mfJ170124.6+515915	R236	17.0235	51.9876	-349.10	19.60(0.44)
mfJ170257.8+514935	R236	17.0494	51.8264	-375.95	19.60(0.44)
mfJ172321.8+744326	R220	17.3894	74.7241	-321.35	20.20(0.52)

continued...

Candidate ID	RIXOS Field	α (J2000) [Hours]	δ (J2000) [Degrees]	Cash C Statistic	$M^{\star}_{est}$ (z_{est})
mfJ172431.3+742613	R220	17.4087	74.4370	-342.65	20.10(0.51)
mfJ172531.8+743939	R220	17.4255	74.6610	-405.97	18.20(0.24)
mfJ172845.5+743945	R220	17.4793	74.6625	-345.28	19.90(0.48)
mfJ180430.0+695820	R272	18.0750	69.9723	-324.99	20.50(0.57)
mfJ180546.0+694813	R272	18.0961	69.8038	-321.20	19.90(0.48)
mfJ180601.1+700309	R272	18.1003	70.0525	-333.09	20.50(0.57)
mfJ180747.3+694836	R272	18.1298	69.8100	-329.27	20.90(0.62)
mfJ180910.8+700136	R272	18.1530	70.0267	-294.04	19.90(0.48)
mfJ231321.4+104251	R205	23.2226	10.7143	-336.23	20.10(0.51)
mfJ231838.2+122936	R294	23.3106	12.4935	-319.93	18.50(0.28)
mfJ231905.9+121919	R294	23.3183	12.3222	-306.09	18.90(0.34)
mfJ231954.5+123256	R294	23.3318	12.5489	-331.61	18.20(0.24)

3.2.2 Final CMR Catalogue

Table 3.2: Catalogue of CMR candidates. Columns are : candidate ID (comprising algorithm type / Right Ascension / Declination (J2000)); RIXOS field ID; RA and Dec (decimal, J2000); significance (σ); estimated redshift.

Candidate ID	RIXOS Field	α (J2000) [Hours]	δ (J2000) [Degrees]	σ	z_{est}
cmJ000953.6+105510	R281	0.1649	10.9196	5.45	0.28
cmJ001012.7+110052	R281	0.1702	11.0146	5.05	0.34
cmJ001059.9+105213	R281	0.1833	10.8705	5.25	0.39
cmJ001110.0+105608	R281	0.1861	10.9357	4.85	0.33
cmJ001119.0+111124	R281	0.1886	11.1902	5.05	0.30
cmJ001128.7+105457	R281	0.1913	10.9160	5.15	0.41
cmJ001133.7+110628	R281	0.1927	11.1080	4.85	0.16
cmJ012437.8+040022	R262	1.4105	4.0062	5.35	0.36
cmJ012442.8+034541	R262	1.4119	3.7614	5.25	0.28
cmJ012446.1+035152	R262	1.4128	3.8647	4.95	0.19
cmJ012455.8+034019	R262	1.4155	3.6720	4.95	0.37
cmJ032748.2+023319	R245	3.4634	2.5555	5.15	0.41
cmJ032821.0+023015	R245	3.4725	2.5043	5.25	0.41
cmJ032903.1+025640	R245	3.4842	2.9447	4.85	0.37
cmJ041604.8+010152	R283	4.2680	1.0311	5.15	0.16
cmJ041606.6+011730	R283	4.2685	1.2917	4.85	0.49
cmJ041629.6+011359	R283	4.2749	1.2333	4.95	0.27
cmJ041703.8+011324	R283	4.2844	1.2234	6.85	0.30
cmJ041721.1+005437	R283	4.2892	0.9103	4.85	0.23
cmJ041730.5+005852	R283	4.2918	0.9813	5.15	0.45
cmJ041744.2+010508	R283	4.2956	1.0857	5.25	0.37
cmJ071935.8+710947	R211	7.3266	71.1632	5.05	0.55
cmJ072103.2+710918	R211	7.3509	71.1551	5.95	0.19
cmJ072229.6+712435	R211	7.3749	71.4098	5.15	0.16
cmJ072345.2+712742	R211	7.3959	71.4618	5.25	0.16

continued...

Candidate ID	RIXOS Field	α (J2000) [Hours]	δ (J2000) [Degrees]	σ	z_{est}
cmJ072503.0+712129	R211	7.4175	71.3583	4.95	0.28
cmJ075712.2+375132	R255	7.9534	37.8590	5.55	0.23
cmJ075724.1+374055	R255	7.9567	37.6820	4.85	0.47
cmJ075739.6+380222	R255	7.9610	38.0397	5.15	0.41
cmJ075842.6+375111	R255	7.9785	37.8533	5.35	0.16
cmJ075843.0+375112	R255	7.9786	37.8534	5.25	0.16
cmJ075904.9+375009	R255	7.9847	37.8360	4.85	0.45
cmJ080146.2+645711	R213	8.0295	64.9532	4.95	0.49
cmJ080248.5+651409	R213	8.0468	65.2359	5.55	0.31
cmJ080306.8+650140	R213	8.0519	65.0278	4.85	0.43
cmJ080339.2+645714	R213	8.0609	64.9541	5.45	0.34
cmJ080352.6+651009	R213	8.0646	65.1694	5.55	0.28
cmJ080516.8+644419	R213	8.0880	64.7387	5.35	0.16
cmJ080606.5+650854	R213	8.1018	65.1485	4.95	0.19
cmJ080617.3+650209	R213	8.1048	65.0359	5.55	0.28
cmJ081840.0+372630	R293	8.3111	37.4419	5.85	0.28
cmJ081854.4+372054	R293	8.3151	37.3484	5.25	0.27
cmJ081943.7+371516	R293	8.3288	37.2546	4.85	0.33
cmJ082002.0+371513	R293	8.3339	37.2537	5.45	0.45
cmJ082006.4+372713	R293	8.3351	37.4538	5.65	0.47
cmJ082015.4+373158	R293	8.3376	37.5328	5.15	0.39
cmJ082040.2+372434	R293	8.3445	37.4097	5.35	0.47
cmJ082058.2+373709	R293	8.3495	37.6193	5.05	0.30
cmJ083750.5+361803	R228	8.6307	36.3009	6.25	0.33
cmJ083801.0+361637	R228	8.6336	36.2771	5.35	0.39
cmJ083816.1+362637	R228	8.6378	36.4437	5.15	0.36
cmJ083824.0+363542	R228	8.6400	36.5952	4.95	0.58
cmJ083824.4+363221	R228	8.6401	36.5393	5.05	0.49
cmJ083900.4+363803	R228	8.6501	36.6344	4.95	0.49
cmJ083904.7+362057	R228	8.6513	36.3492	5.45	0.27
cmJ083910.1+362831	R228	8.6528	36.4754	4.95	0.21

continued...

Candidate ID	RIXOS Field	α (J2000) [Hours]	δ (J2000) [Degrees]	σ	z_{est}
cmJ083924.1+364829	R228	8.6567	36.8081	4.95	0.49
cmJ084719.3+373701	R221	8.7887	37.6170	4.85	0.33
cmJ084755.0+375458	R221	8.7986	37.9163	5.35	0.19
cmJ084807.6+375624	R221	8.8021	37.9401	5.35	0.30
cmJ084852.2+374601	R221	8.8145	37.7671	5.35	0.33
cmJ084908.8+373036	R221	8.8191	37.5100	5.95	0.19
cmJ084929.6+374844	R221	8.8249	37.8124	5.65	0.30
cmJ090409.8+341315	R257	9.0694	34.2210	5.45	0.33
cmJ090423.2+341051	R257	9.0731	34.1810	4.95	0.39
cmJ090510.3+342151	R257	9.0862	34.3643	6.25	0.27
cmJ090511.8+335926	R257	9.0866	33.9907	4.85	0.21
cmJ090517.5+340055	R257	9.0882	34.0154	4.85	0.34
cmJ090549.9+335410	R257	9.0972	33.9030	5.05	0.43
cmJ090616.6+341717	R257	9.1046	34.2882	5.35	0.33
cmJ090616.9+340949	R257	9.1047	34.1638	4.85	0.25
cmJ090632.0+340519	R257	9.1089	34.0887	4.95	0.34
cmJ090826.9+424255	R248	9.1408	42.7155	5.15	0.19
cmJ090907.9+424012	R248	9.1522	42.6700	5.55	0.16
cmJ090927.0+430125	R248	9.1575	43.0238	4.85	0.49
cmJ090954.0+430006	R248	9.1650	43.0019	5.55	0.30
cmJ090958.0+430409	R248	9.1661	43.0692	4.95	0.39
cmJ091004.8+424701	R248	9.1680	42.7836	4.85	0.25
cmJ091045.1+424955	R248	9.1792	42.8322	5.25	0.45
cmJ092053.5+621009	R216	9.3482	62.1693	5.35	0.28
cmJ092221.7+622833	R216	9.3727	62.4759	4.95	0.16
cmJ092319.7+621009	R216	9.3888	62.1693	5.75	0.27
cmJ092347.0+622413	R216	9.3964	62.4036	4.85	0.55
cmJ094255.4+163131	R285	9.7154	16.5255	5.05	0.19
cmJ094329.3+163916	R285	9.7248	16.6545	5.95	0.19
cmJ094356.6+163533	R285	9.7324	16.5926	5.45	0.28
cmJ100904.0+545750	R231	10.1511	54.9641	5.35	0.27

continued...

Candidate ID	RIXOS Field	α (J2000) [Hours]	δ (J2000) [Degrees]	σ	z_{est}
cmJ100909.7+545145	R231	10.1527	54.8627	5.15	0.47
cmJ100931.0+545724	R231	10.1586	54.9568	5.25	0.28
cmJ100933.8+550053	R231	10.1594	55.0148	5.05	0.43
cmJ101039.4+543506	R231	10.1776	54.5851	6.35	0.55
cmJ101052.0+543530	R231	10.1811	54.5918	4.85	0.47
cmJ101056.3+545319	R231	10.1823	54.8886	4.85	0.61
cmJ101134.1+545014	R231	10.1928	54.8374	6.15	0.33
cmJ101206.5+544516	R231	10.2018	54.7545	5.55	0.58
cmJ101207.6+545056	R231	10.2021	54.8489	4.95	0.41
cmJ104144.2+115622	R273	10.6956	11.9397	5.85	0.49
cmJ104206.8+115625	R273	10.7019	11.9403	4.85	0.36
cmJ104211.5+121919	R273	10.7032	12.3220	5.15	0.34
cmJ104220.2+121111	R273	10.7056	12.1866	5.35	0.30
cmJ104222.3+114639	R273	10.7062	11.7776	4.85	0.23
cmJ104241.4+120010	R273	10.7115	12.0028	4.95	0.23
cmJ104313.4+115722	R273	10.7204	11.9561	4.85	0.55
cmJ104341.2+120501	R273	10.7281	12.0836	4.85	0.43
cmJ105503.7+494704	R133	10.9177	49.7845	4.85	0.23
cmJ105532.5+494420	R133	10.9257	49.7390	4.85	0.41
cmJ105608.9+494255	R133	10.9358	49.7155	4.85	0.39
cmJ105639.5+494827	R133	10.9443	49.8077	5.15	0.41
cmJ105709.7+493215	R133	10.9527	49.5375	6.45	0.39
cmJ105734.6+492812	R133	10.9596	49.4700	5.05	0.37
cmJ105810.6+495348	R133	10.9696	49.8967	5.65	0.27
cmJ111726.2+074319	R258	11.2906	7.7221	7.25	0.37
cmJ111742.7+074147	R258	11.2952	7.6964	5.35	0.45
cmJ111757.5+074544	R258	11.2993	7.7623	4.95	0.30
cmJ111758.9+074402	R258	11.2997	7.7339	5.05	0.37
cmJ111804.3+211549	R123	11.3012	21.2636	4.95	0.58
cmJ111809.0+210654	R123	11.3025	21.1151	5.65	0.33
cmJ111835.6+074440	R258	11.3099	7.7447	4.85	0.45

continued...

Candidate ID	RIXOS Field	α (J2000) [Hours]	δ (J2000) [Degrees]	σ	z_{est}
cmJ111847.5+074720	R258	11.3132	7.7891	5.65	0.39
cmJ111914.5+074827	R258	11.3207	7.8075	5.05	0.55
cmJ111918.1+211339	R123	11.3217	21.2276	5.15	0.36
cmJ111919.2+212406	R123	11.3220	21.4017	4.85	0.16
cmJ111934.7+212716	R123	11.3263	21.4547	4.85	0.34
cmJ111939.7+212222	R123	11.3277	21.3730	4.95	0.39
cmJ112407.2+543624	R287	11.4020	54.6069	5.85	0.43
cmJ112509.1+543659	R287	11.4192	54.6165	5.35	0.39
cmJ113529.0+300022	R227	11.5914	30.0061	6.35	0.37
cmJ113546.7+294545	R227	11.5963	29.7625	5.65	0.39
cmJ113548.8+295640	R227	11.5969	29.9447	5.55	0.47
cmJ113607.9+294213	R227	11.6022	29.7038	5.25	0.33
cmJ113620.9+300338	R227	11.6058	30.0606	5.15	0.55
cmJ113622.3+295303	R227	11.6062	29.8842	4.85	0.19
cmJ113749.8+294753	R227	11.6305	29.7982	5.05	0.45
cmJ120341.0+555415	R116	12.0614	55.9043	4.85	0.49
cmJ120422.1+560354	R116	12.0728	56.0651	5.25	0.41
cmJ120441.2+560322	R116	12.0781	56.0563	4.85	0.23
cmJ120556.4+561133	R116	12.0990	56.1927	5.45	0.33
cmJ122110.8+275925	R126	12.3530	27.9904	4.85	0.16
cmJ122213.1+280841	R126	12.3703	28.1449	5.35	0.37
cmJ122217.0+281652	R126	12.3714	28.2812	5.45	0.23
cmJ122231.1+281104	R126	12.3753	28.1846	5.15	0.34
cmJ122234.0+282053	R126	12.3761	28.3482	4.85	0.55
cmJ130858.9+322155	R265	13.1497	32.3653	5.65	0.37
cmJ130911.2+321823	R265	13.1531	32.3065	5.95	0.58
cmJ130920.5+321014	R265	13.1557	32.1706	5.15	0.61
cmJ130951.1+320940	R265	13.1642	32.1611	5.15	0.33
cmJ130954.0+322137	R265	13.1650	32.3605	6.55	0.27
cmJ130955.4+322925	R265	13.1654	32.4905	5.05	0.49
cmJ131012.7+322654	R265	13.1702	32.4484	5.35	0.58

continued...

Candidate ID	RIXOS Field	α (J2000) [Hours]	δ (J2000) [Degrees]	σ	z_{est}
cmJ131017.8+320402	R265	13.1716	32.0674	5.55	0.39
cmJ131030.0+321151	R265	13.1750	32.1976	4.85	0.58
cmJ131032.2+320434	R265	13.1756	32.0763	4.85	0.33
cmJ131037.6+321707	R265	13.1771	32.2855	5.25	0.61
cmJ131047.6+322107	R265	13.1799	32.3520	4.95	0.47
cmJ131054.5+322817	R265	13.1818	32.4715	5.05	0.65
cmJ131102.4+321050	R265	13.1840	32.1808	5.45	0.52
cmJ131108.9+321755	R265	13.1858	32.2988	6.55	0.36
cmJ131111.0+322825	R265	13.1864	32.4736	6.95	0.21
cmJ131148.5+322803	R265	13.1968	32.4675	5.75	0.70
cmJ131527.7+285842	R224	13.2577	28.9784	4.85	0.49
cmJ131532.0+285539	R224	13.2589	28.9276	4.85	0.34
cmJ131536.4+290901	R224	13.2601	29.1505	4.85	0.37
cmJ131537.4+291813	R224	13.2604	29.3038	5.65	0.30
cmJ131557.6+290011	R224	13.2660	29.0033	5.35	0.58
cmJ131605.9+285459	R224	13.2683	28.9166	5.95	0.19
cmJ131612.7+291916	R224	13.2702	29.3211	5.45	0.30
cmJ131614.9+285934	R224	13.2708	28.9928	5.55	0.28
cmJ131629.3+292141	R224	13.2748	29.3616	5.05	0.58
cmJ131702.4+290650	R224	13.2840	29.1140	5.15	0.19
cmJ131711.8+291854	R224	13.2866	29.3151	5.25	0.21
cmJ131729.4+285832	R224	13.2915	28.9756	5.75	0.47
cmJ131739.1+291451	R224	13.2942	29.2477	5.05	0.33
cmJ133120.3+110015	R278	13.5223	11.0044	5.25	0.58
cmJ133132.5+110215	R278	13.5257	11.0375	5.05	0.37
cmJ133137.6+110640	R278	13.5271	11.1112	5.75	0.37
cmJ133202.8+110043	R278	13.5341	11.0120	5.10	0.70
cmJ133211.0+105052	R278	13.5364	10.8480	5.75	0.23
cmJ133211.4+111412	R278	13.5365	11.2367	4.85	0.21
cmJ133243.1+105123	R278	13.5453	10.8566	5.55	0.47
cmJ133255.7+105413	R278	13.5488	10.9036	4.95	0.70

continued...

Candidate ID	RIXOS Field	α (J2000) [Hours]	δ (J2000) [Degrees]	σ	z_{est}
cmJ133256.8+105915	R278	13.5491	10.9875	5.15	0.28
cmJ133311.2+105425	R278	13.5531	10.9072	4.85	0.36
cmJ134238.9+554738	R254	13.7108	55.7939	5.45	0.70
cmJ134259.0+554700	R254	13.7164	55.7834	5.05	0.58
cmJ134315.2+560004	R254	13.7209	56.0011	5.25	0.41
cmJ134320.3+555025	R254	13.7223	55.8405	4.85	0.37
cmJ134415.0+560506	R254	13.7375	56.0852	5.25	0.52
cmJ134524.1+553520	R254	13.7567	55.5889	4.95	0.70
cmJ134556.2+555523	R254	13.7656	55.9233	4.95	0.52
cmJ134628.6+555103	R254	13.7746	55.8509	5.55	0.70
cmJ135532.9+181437	R268	13.9258	18.2436	4.95	0.37
cmJ135541.2+183635	R268	13.9281	18.6098	5.85	0.55
cmJ135549.8+182000	R268	13.9305	18.3334	5.35	0.34
cmJ140521.1+223506	R274	14.0892	22.5851	4.85	0.43
cmJ140525.8+222638	R274	14.0905	22.4439	5.65	0.55
cmJ140538.8+223109	R274	14.0941	22.5193	5.25	0.52
cmJ140558.6+223329	R274	14.0996	22.5582	4.95	0.36
cmJ140610.1+221518	R274	14.1028	22.2552	5.10	0.70
cmJ140638.2+223316	R274	14.1106	22.5545	4.85	0.34
cmJ140654.7+222349	R274	14.1152	22.3971	5.05	0.39
cmJ140703.0+221533	R274	14.1175	22.2592	5.05	0.43
cmJ140719.2+223314	R274	14.1220	22.5540	4.85	0.52
cmJ140741.5+222604	R274	14.1282	22.4347	5.55	0.61
cmJ141236.4+435302	R217	14.2101	43.8841	5.05	0.49
cmJ141244.3+434719	R217	14.2123	43.7886	4.95	0.49
cmJ141248.2+440147	R217	14.2134	44.0298	5.15	0.43
cmJ141250.8+435816	R217	14.2141	43.9712	5.55	0.37
cmJ141305.2+435044	R217	14.2181	43.8457	6.15	0.39
cmJ141316.0+434801	R217	14.2211	43.8003	4.85	0.27
cmJ141318.8+440431	R217	14.2219	44.0754	6.45	0.49
cmJ141322.4+435706	R217	14.2229	43.9519	4.85	0.58

continued...

Candidate ID	RIXOS Field	α (J2000) [Hours]	δ (J2000) [Degrees]	σ	z_{est}
cmJ141327.5+435833	R217	14.2243	43.9759	5.05	0.30
cmJ141330.7+434607	R217	14.2252	43.7686	5.45	0.49
cmJ141336.8+435511	R217	14.2269	43.9199	4.85	0.70
cmJ141351.6+435231	R217	14.2310	43.8754	4.85	0.43
cmJ141411.4+440829	R217	14.2365	44.1415	4.95	0.39
cmJ141414.6+435433	R217	14.2374	43.9092	5.15	0.31
cmJ141417.2+441344	R217	14.2381	44.2291	5.05	0.65
cmJ141418.2+434655	R217	14.2384	43.7822	5.65	0.49
cmJ141423.6+440212	R217	14.2399	44.0368	5.15	0.49
cmJ141455.7+434748	R217	14.2488	43.7969	4.85	0.65
cmJ141504.3+440250	R217	14.2512	44.0474	6.05	0.37
cmJ142724.8+330935	R110	14.4569	33.1599	5.25	0.43
cmJ142740.7+330743	R110	14.4613	33.1287	4.95	0.70
cmJ142745.4+331221	R110	14.4626	33.2060	5.10	0.70
cmJ142750.0+330102	R110	14.4639	33.0173	4.85	0.41
cmJ142812.0+330736	R110	14.4700	33.1268	5.05	0.16
cmJ142827.1+331931	R110	14.4742	33.3255	5.55	0.45
cmJ142829.6+325611	R110	14.4749	32.9365	4.85	0.37
cmJ142829.6+331708	R110	14.4749	33.2856	4.85	0.58
cmJ142832.5+325801	R110	14.4757	32.9672	4.95	0.47
cmJ142835.4+331445	R110	14.4765	33.2460	5.25	0.37
cmJ142846.2+325529	R110	14.4795	32.9249	5.05	0.49
cmJ142858.8+330448	R110	14.4830	33.0801	4.95	0.33
cmJ142901.7+325702	R110	14.4838	32.9507	5.55	0.45
cmJ142910.7+330422	R110	14.4863	33.0729	5.15	0.58
cmJ142923.6+330806	R110	14.4899	33.1350	5.25	0.58
cmJ142927.6+325808	R110	14.4910	32.9690	5.25	0.61
cmJ142928.3+331825	R110	14.4912	33.3071	5.65	0.36
cmJ142940.9+330834	R110	14.4947	33.1428	4.85	0.52
cmJ142942.7+325642	R110	14.4952	32.9450	5.25	0.19
cmJ162617.5+781706	R122	16.4382	78.2851	4.85	0.55

continued...

Candidate ID	RIXOS Field	α (J2000) [Hours]	δ (J2000) [Degrees]	σ	z_{est}
cmJ163231.2+570253	R223	16.5420	57.0483	4.85	0.55
cmJ163246.0+565540	R223	16.5461	56.9280	5.05	0.36
cmJ163302.5+565559	R223	16.5507	56.9333	5.25	0.70
cmJ163303.2+571100	R223	16.5509	57.1835	6.35	0.19
cmJ163314.8+572153	R223	16.5541	57.3648	5.65	0.23
cmJ163320.5+572452	R223	16.5557	57.4147	5.25	0.36
cmJ163343.9+565558	R223	16.5622	56.9330	4.95	0.65
cmJ163431.4+571600	R223	16.5754	57.2668	5.25	0.25
cmJ163501.3+570440	R223	16.5837	57.0780	5.05	0.19
cmJ163526.5+565433	R223	16.5907	56.9093	5.85	0.19
cmJ163526.9+570024	R223	16.5908	57.0068	5.05	0.28
cmJ163538.4+572039	R223	16.5940	57.3444	4.95	0.49
cmJ163547.0+571310	R223	16.5964	57.2196	4.85	0.55
cmJ163611.9+570412	R223	16.6033	57.0702	5.55	0.31
cmJ163613.3+571337	R223	16.6037	57.2272	5.45	0.47
cmJ163619.1+570759	R223	16.6053	57.1331	4.95	0.37
cmJ165949.2+513724	R236	16.9970	51.6235	5.45	0.39
cmJ165957.1+514826	R236	16.9992	51.8073	5.15	0.49
cmJ170004.0+513745	R236	17.0011	51.6292	4.85	0.34
cmJ170048.6+515205	R236	17.0135	51.8681	6.25	0.45
cmJ170050.8+515850	R236	17.0141	51.9806	5.25	0.47
cmJ170108.4+515535	R236	17.0190	51.9264	5.05	0.36
cmJ170122.4+513432	R236	17.0229	51.5758	5.45	0.41
cmJ170126.4+515844	R236	17.0240	51.9789	5.15	0.49
cmJ170136.1+520750	R236	17.0267	52.1308	4.85	0.36
cmJ170136.8+514351	R236	17.0269	51.7309	5.75	0.39
cmJ170144.0+515212	R236	17.0289	51.8702	4.95	0.70
cmJ170154.5+520419	R236	17.0318	52.0722	5.15	0.27
cmJ170232.6+514922	R236	17.0424	51.8228	5.05	0.30
cmJ170244.2+515539	R236	17.0456	51.9277	5.55	0.31
cmJ170248.1+520148	R236	17.0467	52.0300	5.45	0.36

continued...

Candidate ID	RIXOS Field	α (J2000) [Hours]	δ (J2000) [Degrees]	σ	z_{est}
cmJ170258.9+514921	R236	17.0497	51.8227	6.25	0.47
cmJ172211.6+742922	R220	17.3699	74.4896	4.85	0.43
cmJ172333.0+744410	R220	17.3925	74.7362	6.05	0.21
cmJ172428.8+741905	R220	17.4080	74.3182	5.05	0.49
cmJ172502.6+741556	R220	17.4174	74.2656	5.05	0.43
cmJ172606.4+743924	R220	17.4351	74.6567	5.25	0.49
cmJ172814.2+744721	R220	17.4706	74.7894	4.85	0.55
cmJ172842.2+744522	R220	17.4784	74.7561	5.15	0.33
cmJ172907.4+743319	R220	17.4854	74.5555	5.05	0.47
cmJ172952.8+744251	R220	17.4980	74.7144	5.65	0.19
cmJ180707.7+693807	R272	18.1188	69.6354	5.75	0.19
cmJ231228.4+103143	R205	23.2079	10.5288	4.95	0.70
cmJ231257.2+103005	R205	23.2159	10.5015	5.25	0.70
cmJ231822.0+124547	R294	23.3061	12.7633	5.05	0.43
cmJ231850.0+124135	R294	23.3139	12.6932	5.10	0.70
cmJ231906.6+121905	R294	23.3185	12.3181	5.25	0.23
cmJ231951.2+123208	R294	23.3309	12.5356	5.05	0.37

Summary of Catalogues

In total, the final MF catalogue (constructed and trimmed to the PSPC field, as described above) contains 185 cluster candidates. The final CMR catalogue contains 290 candidates. The MF technique fits the most likely value of M* in the range $17.0 \leq I_C \leq 21.5$. The bright limit is imposed by there being few galaxies this bright in the field and at this redshift (z=0.15) the angular diameter of clusters becomes so large that the contrast of the cluster against the background is greatly reduced. The faint limit (corresponding to z=0.9) is set such that the limiting magnitude is one magnitude fainter than this M*, thus there are still many galaxies to which to fit a luminosity function. The CMR method is limited by the depth of the photometry in *both* bands (as illustrated in Figure 2.12), which leads to colour limits $1.45 \leq$ V-I ≤ 2.65 corresponding to $0.159 \leq z_{est} \leq 0.703$. In practice, the MF catalogue is cropped at the high redshift end to match the colour limits imposed by the

CMR method. At the low redshift end, only a few clusters lower than the limit imposed by the CMR method are found by the MF, so these are retained.

3.2.3 Internal Check of Redshift Estimates

To assess the accuracy with which an estimated redshift can be assigned, an internal check can be performed comparing the redshifts estimated for candidates using the A- versus the B-rotation data. Due to the way in which the object catalogues are generated (Chapter 2), different data are produced for the same region of sky using two independent observations. For example, the main difference between object catalogues for the two rotations was the star/ galaxy classification. Several objects classified as galaxies in one rotation were classified as stars in the other, and vice versa. The neural network classifier of `SExtractor` uses both the FWHM of a source and its ellipticity to decide the nature of each source. The effect of FWHM differences was minimised due to the way in which the data were taken (observing the same A- and B-rotation fields sequentially) so that, unless the seeing is changing on very short timescales, the FWHM of point sources should be the same for the two rotations. Inspection of objects which changed class between the two frames showed that a slightly different measure of ellipticity was the primary cause. Overall, the level of star/ galaxy misclassification should be around the few percent level. From the spectroscopic observations presented in Chapter 4, two of the 87 redshifts measured (for objects brighter than I$\approx$20, classified as galaxies) were due to stars, or around 2%. The contamination is likely to be higher for fainter objects, where a lower signal makes shape parameters more difficult to measure. To a lesser extent, the object catalogues between the two rotations differ due to cosmic rays, diffraction spikes, and differently deblended objects (as discussed in Chapter 2).

A comparison of estimated redshifts between the two independent observations allows the effect of all these factors to be taken into account. This is one of the primary motivations for treating the repeat observations separately. Candidates for the comparison were selected in the following manner. For the MF catalogue, the full catalogue was compared with the final catalogue. For each entry in the final catalogue, if a single candidate from each rotation was present in the full catalogue, within the final catalogue entry's group radius (to avoid possible confusion with multiple matches), then the candidate was selected. A similar procedure was followed for the CMR catalogue, with the added condition that the candidate must not be flagged as comprising projected groups (again to avoid confusion due to multiple matches). In both cases a limiting radius of one arc minute was

imposed for the match, to ensure a high level of confidence that the same candidate had been selected from the two datasets. The comparison of the estimated redshifts from each rotation, for each cluster detection algorithm is shown in Figure 3.3. Quantifying the bias and scatter in these relationships as from: $\delta z = (z_A - z_B)/(1 + z_A)$, the mean value is -0.004 for the MF and -0.014 for the CMR algorithm; the standard deviations are 0.097 and 0.081 respectively. This is somewhat misleading as the majority of the scatter from the CMR comes from a few outliers, and the majority of points show excellent agreement between the two independent observations. A large fraction of the outliers were detected in the final (z=0.70) colour slice in one rotation, and thus could easily be missed and associated with a less significant lower redshift clump in the corresponding rotation. The few other outliers can be understood in terms of marginal cases for projected systems. If each rotation detects two systems and the lower significance candidate is measured as being more significant in the overlapping rotation, and the lowest significance system falls below the threshold in both cases, then a catastrophic failure of the redshift estimate would occur. This only appears to be the case for seven of the systems in the plot, at z_{est} <0.69. The scatter in the MF estimate is intrinsically large. Neither estimate shows any significant bias between the two datasets.

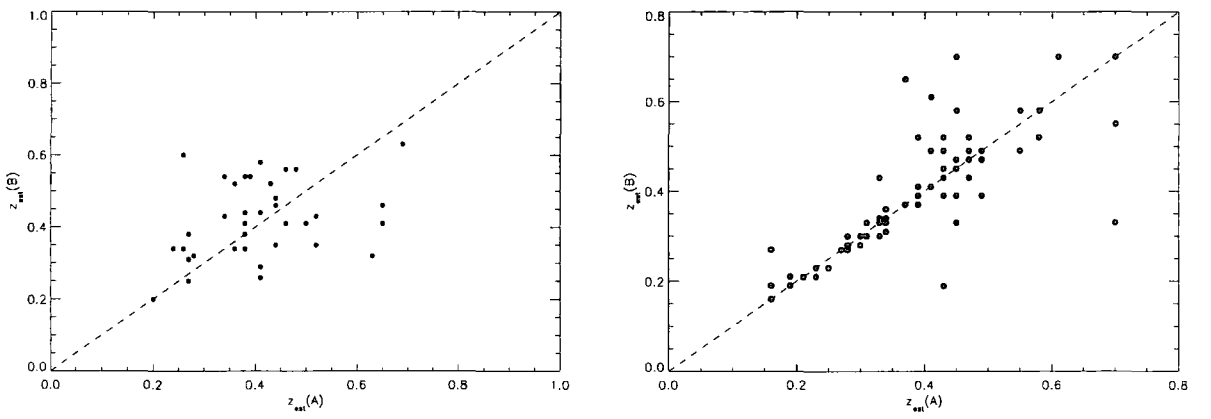

Figure 3.3: Comparison of estimated redshifts for the MF and CMR algorithms from the A versus B data. The left panel shows the MF estimated redshift in the B field versus the A field estimate of the same quantity. The right panel shows the A versus B estimated redshift for the CMR algorithm.

3.2.4 Comparison of MF Catalogue with CMR Catalogue

Now that both optical techniques have been compared with a spectroscopic sample, it can be seen that the estimated redshifts from the CMR technique offer greater precision than the MF estimated redshifts. Thus, a cross-comparison of the two techniques can be made, using the CMR catalogue as a reference. The final MF catalogue was cross-correlated with final CMR catalogue to determine cluster candidates in common. To avoid possible confusion from multiple associations of candidates, only MF candidates with a *single* CMR candidate within the former's radius were considered. If the candidates' centres were separated by more than two arc minutes, they were excluded. Thus, only secure "clean" matches are considered. Of the 185 final MF candidates, 62 show unique CMR matches (7 of these are flagged as line of sight group projections). A comparison between the estimated redshifts of these techniques is shown in Figure 3.4. The average bias and scatter (as defined earlier) in this relation is -0.066 and 0.106 respectively, although, inspection shows that this may equally be due to the MF redshift being randomly drawn from values between 0.3 and 0.5. This may be due to bias in the candidates selected for this comparison (those with "clean" matches between the CMR and MF candidates). A comparison of the MF estimated redshifts with those of spectroscopically determined redshifts (from the X-ray selected clusters in the next section) shows that the MF estimated redshift is not that bad.

A further comparison is to consider the MF candidates *not* matched with CMR candidates. This was done by comparing the full CMR catalogue with the final MF catalogue and searching for MF candidates with *no* CMR matches within their radii (or 2 arcmins). 41 of the final MF candidates show no CMR counterparts at any significance level. Under the assumption that *all* genuine clusters possess a CMR and that this technique will find them, this can be used as an approximation to the number of spurious MF detections. This gives a false detection rate of around 22%. This is in general agreement with estimates for other MF techniques of around 30% (eg. Holden et al. 1999). 22% is a lower limit, as some of the CMR matches are of low significance. Using the fraction of matched candidates flagged as projections (7 out of 62, above) compares well with the (spectroscopic) findings of Katgert et al (1996) that around 10% of Abell clusters comprise two or more significant clusters, projected along the line of sight.

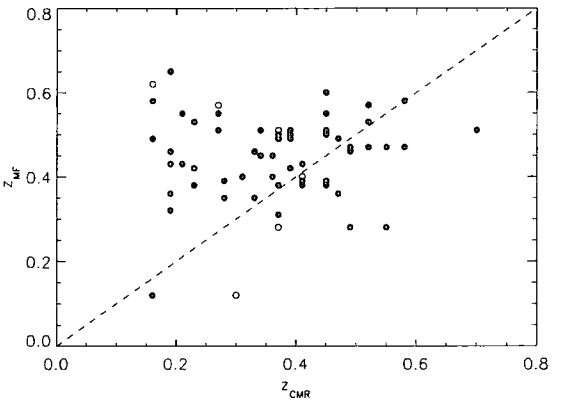

Figure 3.4: Comparison of MF and CMR estimated redshifts. Filled points are unique matches; open points are flagged as line of sight projections in the CMR catalogue. Dashed line is the one-to-one relation.

3.3 X-ray Selection of Galaxy Clusters

The X-ray data are archival images taken with the ROSAT Position Sensitive Proportional Counter (PSPC). Such observations are divided into two energy bands: "hard" (0.4−2.4keV) and "soft" (0.07−0.4 keV). The background flux is particularly high at energies below 0.5 keV and the sensitivity of ROSAT rapidly drops to zero above 2.0 keV. As a result, most X-ray cluster surveys use the hard band and cut its range down to 0.5−2.0 keV. All of the fields were taken from the RIXOS survey (Mason et al. 2000), which was an international campaign to follow up in the optical all X-ray sources in a sample of ROSAT PSPC fields above a point source flux limit of 3×10^{-14} erg cm^{-2} s^{-1} (0.5-2.0 keV). Thus, a sample of clusters discovered in the X-ray in these fields have already been selected and confirmed. However, the algorithm with which these were found was optimised for point source detection, and not for locating extended emission, as expected for clusters of galaxies. Thus the RIXOS cluster catalogue is incomplete. This resulted in a claim for a deficit of high redshift clusters in the RIXOS sample (Castander et al. 1995), when other investigators found no evolution in the abundance of clusters (eg., Nichol et al. 1997).

The currently favoured technique for the detection of faint, extended sources in X-ray data is the wavelet method. Sources are detected by convolving the data with a kernel to enhance the contrast between objects and the background, in the same way as described in Chapter 2 for the optical algorithms. The difference with the wavelet method is that this kernel consists of a positive core and a negative outer ring (such that its integral over the x,y plane is zero). This means that slowly varying backgrounds which can be approximated by linear functions are completely subtracted. Furthermore, a wavelet transform of the data reveals sources bounded by a ring of zero values; the diameter of the zero-rings gives a measure of the angular extent of the source. In practice, a range of kernel values is used (as was done with the Gaussian filtering of the MF method), and these can be used to infer the source radius. An instructive illustration of this technique is given in Figure 2 of Vikhlinin et al. (1998).

Given that several wide-field surveys have also made use of archival ROSAT data for the serendipitous discovery of clusters (eg. Jones et al. 1998, Romer et al. 2000, Vikhlinin et al. 1998), it is natural to check if any of these overlap with the fields selected for XDCS. Indeed 29 out of the 39 fields were used in the 160 square degree survey of Vikhlinin et al. (1998). This catalogue has the attractive feature that nearly all of the

200+ sources detected have been followed up in the optical, many possessing spectroscopic confirmation. Furthermore, their spurious detections are also recorded in their paper, so *all* X-ray detected cluster candidates can be examined, and not just the optically confirmed ones[2]. Of the remaining 10 fields, 7 were included in the Bright SHARC Survey (Romer et al. 2000). Both of these used wavelet detection algorithms in their construction. The SHARC catalogue has had a fairly bright ROSAT count-rate limit imposed (corresponding to a flux of approximately 10^{-13} erg s^{-1} cm^{-2} [3]) in order to reduce the numbers of clusters found, to make optical follow up achievable in a reasonable amount of time. Given this limit, 94 sources were found in 460 ROSAT fields. It is not too surprising, then, that in the seven fields overlapping with XDCS, no sources are found. The SHARC survey is not considered hereafter. The Vikhlinin et al. (1998) catalogue (VMF), on the other hand, contains 15 X-ray selected clusters in XDCS fields. This is the X-ray selected cluster survey with which the XDCS optical catalogues will be compared.

The ROSAT fields observed are given in Table 3.3. The VMF clusters in common fields are given in Table 3.4.

Table 3.3: List of ROSAT Fields in XDCS Columns give: RIXOS ID of field; name of the target of the original ROSAT pointing; RA, Dec; exposure time of field in RIXOS survey; overlapping X-ray cluster survey (V - VMF, S - SHARC); exposure time of the VMF or SHARC pointing (to give an indication of the depth to which they could have searched for X-ray emission).

RIXOS ID	Target	α (J2000) [hh:mm:ss.s]	δ (J2000) [dd:mm:ss]	T_{exp} (ks)	Overlapping Survey	T_{exp}(overlap) (ks)
R110	LHS 2924	14:28:43.17	+33:10:45.47	18.3	V	28.5
R116	NOWER2	12:03:60.00	+56:10:11.99	30.1	—	—
R122	Meaty	16:29:24.00	+78:04:48.01	38.5	S	34.4
R123	1116+215	11:19:4.80	+21:18:36.00	25.0	V	32.2
R126	ON 231	12:21:33.60	+28:13:48.00	10.4	V	12.5
R133	CY UMA	10:56:55.20	+49:42:0.00	9.4	V	7.9
R205	P100578	23:12:21.60	+10:46:48.00	10.3	S	9.8
R211	S5 0716+7	07:21:52.70	+71:20:23.99	21.0	S	17.3
R213	IRAS 0759	08:04:31.20	+65:00:0.00	8.4	V	6.4

continued on next page...

[2] 19 likely false detections, arising from concentrations of point sources, were recorded, but none of these occurs in the XDCS fields.

[3] or about an order of magnitude brighter than typical XDCS field limits.

RIXOS ID	Target	α (J2000) [hh:mm:ss.s]	δ (J2000) [dd:mm:ss]	T_{exp} (ks)	Overlapping Survey	T_{exp}(overlap) (ks)
R216	S4 0917+6	09:21:36.00	+62:15:35.99	19.5	V	15.9
R217	1411+442	14:13:48.00	+44:00:0.00	25.3	V	22.5
R220	RX J1726.	17:26:12.00	+74:31:11.99	10.6	V	8.1
R221	E0845+378	08:48:19.20	+37:40:11.99	12.4	V	10.0
R223	CM DRA	16:34:24.00	+57:09:0.01	47.5	V	37.3
R224	HZ43	13:16:24.00	+29:06:0.00	34.9	S	18.3
R227	GD140	11:36:33.51	+29:47:60.00	33.9	V	26.6
R228	GBS0839+3	08:38:47.90	+36:31:12.00	11.0	V	9.2
R231	Survey Fi	10:10:16.70	+54:45:0.00	16.8	V	14.4
R236	Q1700+515	17:01:23.90	+51:49:12.00	8.2	V	6.5
R245	H0323+022	03:28:25.82	+02:47:57.84	25.7	S	24.5
R248	3C216	09:09:33.50	+42:54:0.01	23.6	V	19.9
R254	MRK 273	13:44:43.10	+55:53:24.00	17.1	V	28.1
R255	0755+37	07:58:28.70	+37:47:24.00	16.0	S	15.5
R257	B2 0902+3	09:05:31.10	+34:07:48.00	14.5	V	26.5
R258	1115+080	11:18:16.70	+07:46:12.00	14.4	V	13.2
R262	520	01:24:33.50	+03:47:60.00	13.9	V	12.0
R265	B2 1308+3	13:10:28.70	+32:20:59.99	13.0	V	7.6
R268	MRK 463	13:56:2.30	+18:22:12.00	11.6	V	18.3
R272	3C 371	18:06:50.40	+69:49:12.00	10.5	S	8.0
R273	1040+123	10:42:45.51	+12:03:36.00	10.2	V	8.4
R274	1404+226	14:06:21.60	+22:23:60.00	10.1	V	6.7
R278	MKN 789	13:32:24.00	+11:06:36.00	9.6	V	9.1
R281	III ZW2	00:10:28.70	+10:58:12.00	9.1	V	16.8
R283	1H 0414+0	04:16:52.70	+01:05:24.00	9.0	—	—
R285	PSR 0940+	09:43:43.20	+16:31:12.00	9.0	V	8.1
R287	MKN 40	11:25:36.00	+54:22:48.00	8.8	V	7.7
R292	GLIESE 70	01:43:21.50	+04:19:48.00	8.7	V	5.4
R293	GD 90	08:19:47.90	+37:31:12.00	9.0	V	7.3
R294	KUV 2316+123	23:18:45.0	+12:36:00.00	9.5	—	—

3.4 Comparison of Optical and X-ray Selected Clusters

3.4.1 Introduction

The VMF X-ray selected clusters are listed in Table 3.4. A comparison between the RIXOS and VMF clusters is given in the table. 8 of the 15 VMF clusters were also discovered by RIXOS; no RIXOS clusters were missed by VMF. Trends in the selection were searched for by comparing fluxes, core radii and surface brightnesses of the matched and unmatched clusters. None was found. The differences are likely to be due to more subtle differences between the selection algorithms. The method used to determine the VMF redshift is also included in the table. Vikhlinin et al. (1998) used several methods to "confirm" their X-ray cluster candidates and it is pertinent to comment on these here. Aside from the traditional method of requiring an overdensity of galaxies in the optical, they included another possible criterion which was that if an elliptical galaxy not included in the NGC catalogue lay at the peak of the X-ray emission then this should be considered confirmation.

This latter point was designed to include "poor clusters and groups which fail to produce a significant excess of galaxies over the background". The authors state that it also helps to identify "fossil groups" in which galaxies have merged to form a single cD (Ponman et al. 1994, Jones, Ponman, & Forbes 2000). Such systems appear to be as X-ray luminous as other bright groups or poor clusters, but with a high percentage of the optical luminosity arising from the dominant giant elliptical. The second brightest group member is a factor of 10 fainter than the brightest (resulting in a gap of 2.5 magnitudes in the LF). A few examples of such systems have been identified, but insufficient to constrain the space density of such systems.

Optical follow up was obtained either from second generation Digitized Sky Survey (DSS-II) plates, or R-band (or sometimes B-, V-, or I-) CCD imaging on 1m class telescopes. Long-slit spectroscopy was also obtained for some candidates, usually for 2 - 3 galaxies per cluster, and always including the brightest galaxy.

VMF ID	RIXOS Field	α(J2000) [hh:mm:ss.s]	δ(J2000) [dd:mm:ss]	F_X 10^{-14} erg s^{-1} cm^{-2}	δF_X 10^{-14} erg s^{-1}	z	RIXOS Cluster?	Redshift Type
11	R262	01:24:35.1	+04:00:49	7.5	2.2	0.27	n	p
62	R221	08:49:11.1	+37:31:25	14.7	3.0	0.240	y	s
69	R248	09:10:39.7	+42:48:41	8.3	2.0	—	n	—
73	R285	09:43:32.2	+16:40:02	23.1	3.7	0.256	y	s
74	R285	09:43:44.7	+16:44:20	21.2	4.1	0.180	y	s
84	R231	10:10:14.7	+54:30:18	21.0	2.9	0.045	n	s
86	R231	10:11:26.0	+54:50:08	20.0	5.1	0.294	y	s
94	R133	10:56:12.6	+49:33:11	12.9	1.9	0.199	y	s
97	R258	11:17:26.1	+07:43:35	6.1	1.6	0.40	n	p
99	R123	11:19:43.5	+21:26:44	5.5	0.9	0.11	y	p
131	R265	13:09:55.6	+32:22:31	9.0	2.9	0.290	n	s
132	R265	13:11:12.8	+32:28:58	46.7	5.8	0.245	y	s
150	R254	13:43:29.0	+55:47:17	17.5	2.8	0.11	n	p
181	R223	16:33:40.0	+57:14:37	3.5	0.7	0.239	y	s
194	R220	17:29:01.9	+74:40:46	17.3	7.2	0.28	n	p

Table 3.4: VMF clusters in XDCS fields. Redshifts are given for all but one cluster. The type of redshift measured by VMF is given in the final column (p - photometric, s - spectroscopic); Clusters also found in the X-ray survey of RIXOS are indicated by a "y".

The comparison of the optical cluster candidates with the Vikhlinin et al. (1998) catalogue X-ray selected cluster catalogue will proceed as follows. Each panel of Figure 3.5 shows (from left to right) contours of PSPC count levels over DSS images, centred on the cluster position quoted in Vikhlinin et al. (1998). This is to show the position and spatial extent of the X-ray emission, and to show the optical imaging which was available to Vikhlinin et al. (1998) for initial identification of clusters. Next, I-band WFC images of the same areas are shown to illustrate the improvement in depth and image quality offered by the XDCS dataset. Colour-magnitude diagrams from the WFC data are also presented for these regions with model colour-magnitude relations overplotted, at the redshift given by VMF. For clusters where both A- and B-rotation data are available, the upper row of panels shows the A-data and the lower row the B-data. Note: the DSS image with PSPC contours is the same for each cluster, for both the upper and lower rows.

Finally, a detailed comparison with the two automated optical cluster finders will be presented.

To quantitatively compare the optically selected catalogues with the X-ray selected clusters, the following method is used. For each of the final MF and CMR catalogues, cross-correlation with the Vikhlinin et al. (1998) catalogue is performed, retaining the nearest match to each X-ray cluster. If the X-ray cluster lies within the optical candidate's group radius, it is considered matched (the only caveat is that a minimum radius of 1 arcmin and a maximum of 2 arcmin is adopted, to ignore excessively large or small group radii). These matches are tabulated in Table 3.5. For the X-ray clusters with no matches from this process, the full catalogues for each algorithm were checked, to see if a lower significance candidate is matched. Such matches are indicated in the table by parentheses. All matches were then inspected visually and special cases are commented on.

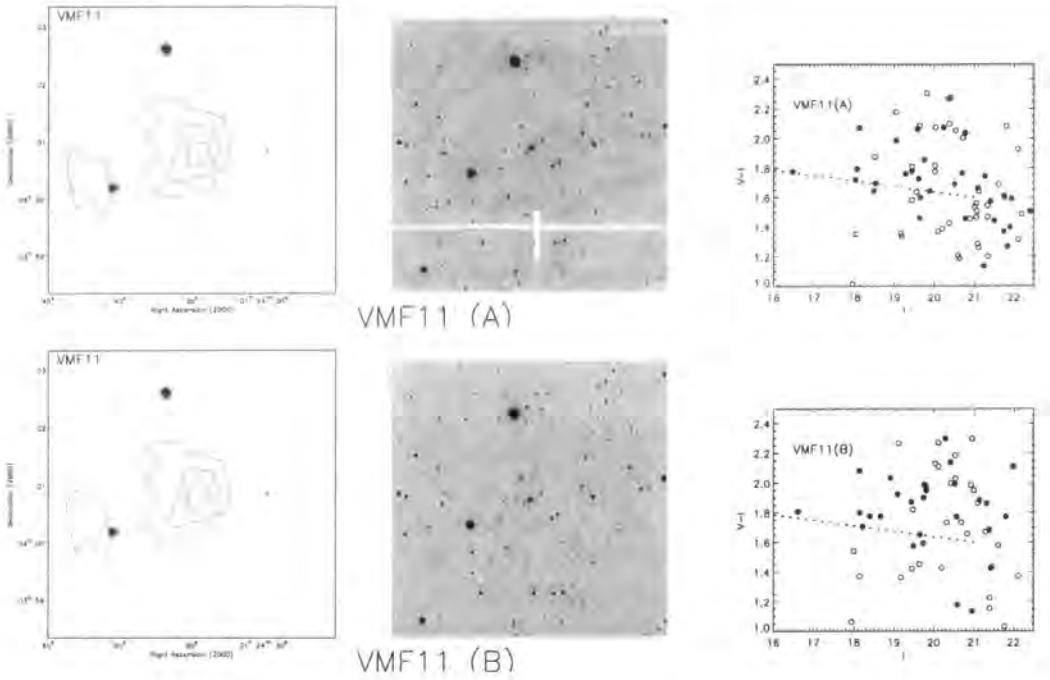

Figure 3.5: VMF11. Left panel: DSS image with PSPC contours overlaid (images are 5 arcmins on a side and PSPC contours have been smoothed to 30 arcsec - the approximate PSF. These contours do not correspond to any particular significance level, and are simply in units of X-ray count rate), centre panel: WFC I-band image of the same region, right panel: CMD centred on VMF position. Open symbols show galaxies drawn from 100 arcsec around VMF position, filled symbols are galaxies within 60 arcsec. Overplotted line shows CMR corresponding to VMF redshift (dashed line indicates VMF redshift is a photometric estimate). Upper row uses A-rotation WFC data, and lower row uses B-rotation data. Note: the DSS image is the same in both rows. The main reason for differences between the A- and B-rotation data in the CMDs is the fact that only approximate external astrometry was performed for the WFC data (Chapter 2). Thus, converting the VMF Right Ascension and Declination into WFC chip coordinates, results in a slightly different centre for each mosaic (at the level of around 10 arcsec). This causes some symbols from the inner region (filled points) in one rotation to become the outer region (open circles) in the other rotation, and vice versa, and also points to disappear from the plot. Furthermore, differences can be caused by proximity to a chip edge (causing points beyond the boundary in one rotation to disappear) and, to a lesser extent, objects deblended/ classified differently by `SExtractor` in the two rotations.

VMF11 is not found in the final MF catalogue, but it *is* found in the full MF catalogue, as it lies just below the Cash C threshold. This cluster is found in the final CMR catalogue. The associated MF and CMR candidates are listed in Table 3.5.

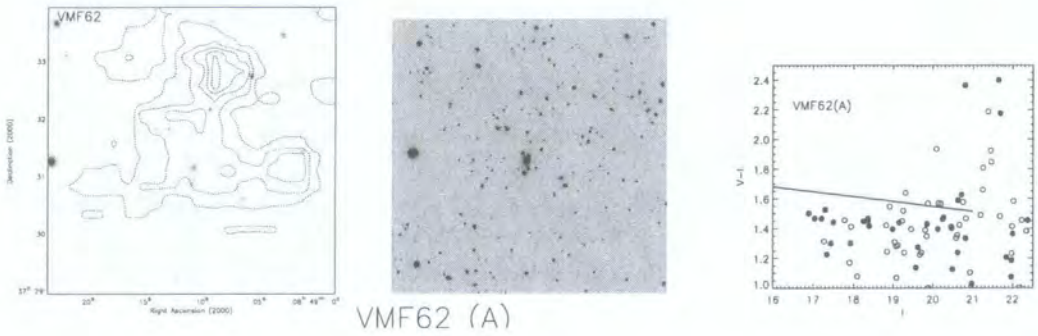

Figure 3.6: VMF62. Panels as for previous figure. This cluster is only visible in A-rotation data. Solid line on the CMD indicates that the VMF redshift was spectroscopically determined.

VMF62 is found in both the final MF and CMR catalogues.

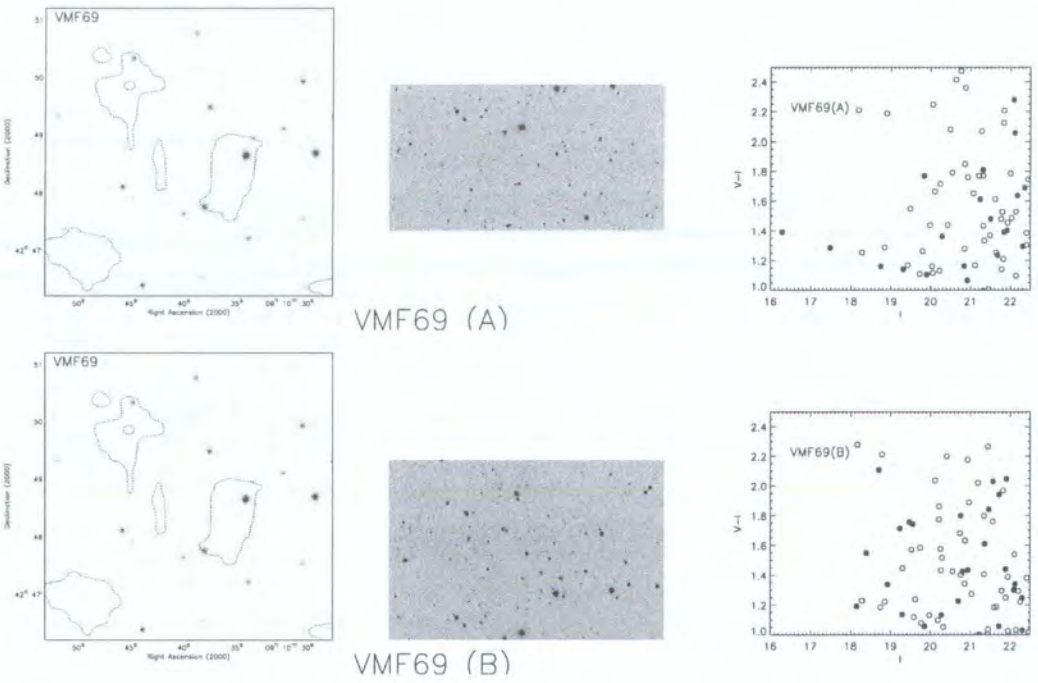

Figure 3.7: VMF69. Panels as for Figure 3.5. No redshift was assigned by VMF, due to uncertainty in identifying the brightest cluster galaxy.

VMF69 was found in the CMR catalogue. The nearest match in the MF catalogue lay within the candidate's estimated group radius, but further than 2 arcmins away. This association was treated cautiously, but visual inspection of the galaxy catalogue showed a large overdensity extending this far and thus the association seemed valid.

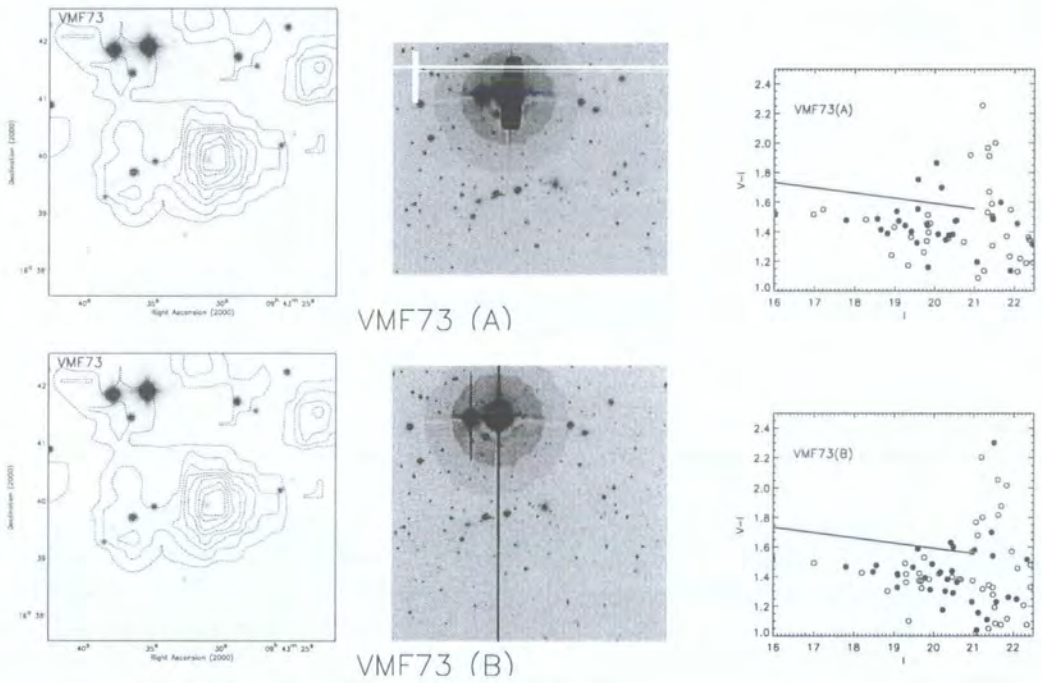

Figure 3.8: VMF73. Panels as for Figure 3.5.

VMF73 was found in the CMR catalogue. The nearest match in the MF catalogue lay outside the candidate's estimated group radius but within 2 arcmins. This association was treated cautiously, but visual inspection of the galaxy catalogue showed a large overdensity extending this far and thus the association seemed valid.

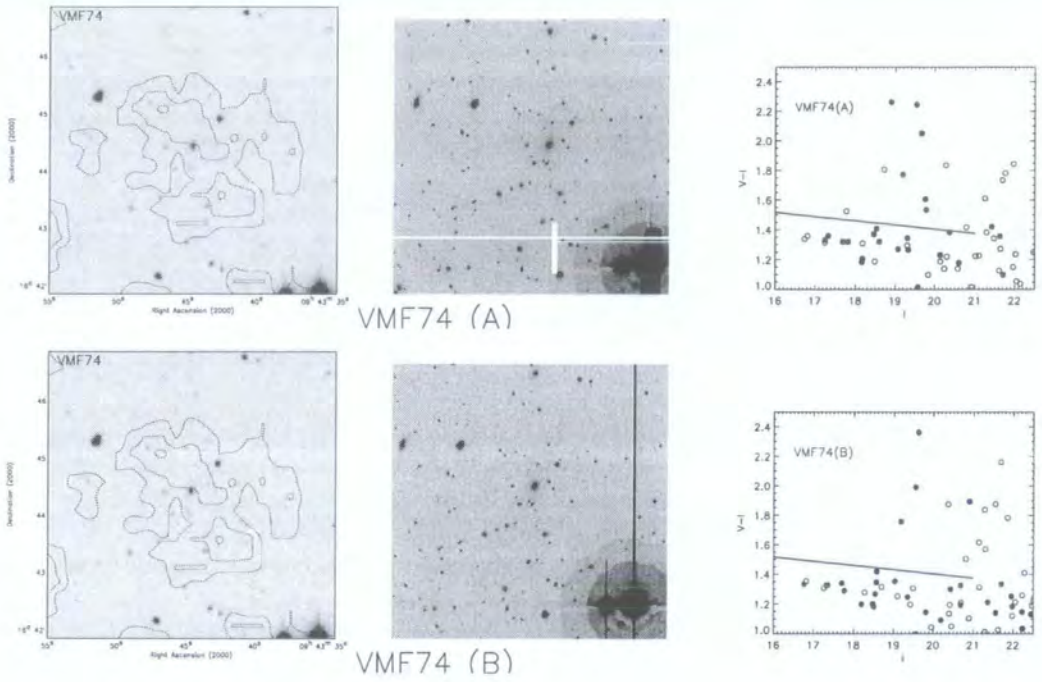

Figure 3.9: VMF74. Panels as for Figure 3.5.

VMF74 was found in the full MF catalogue, but not the higher significance final catalogue. This cluster was not found in the CMR catalogue as its CMR lies blueward of the bluest colour slice (V-I=1.45). ie. it is below the low redshift cutoff.

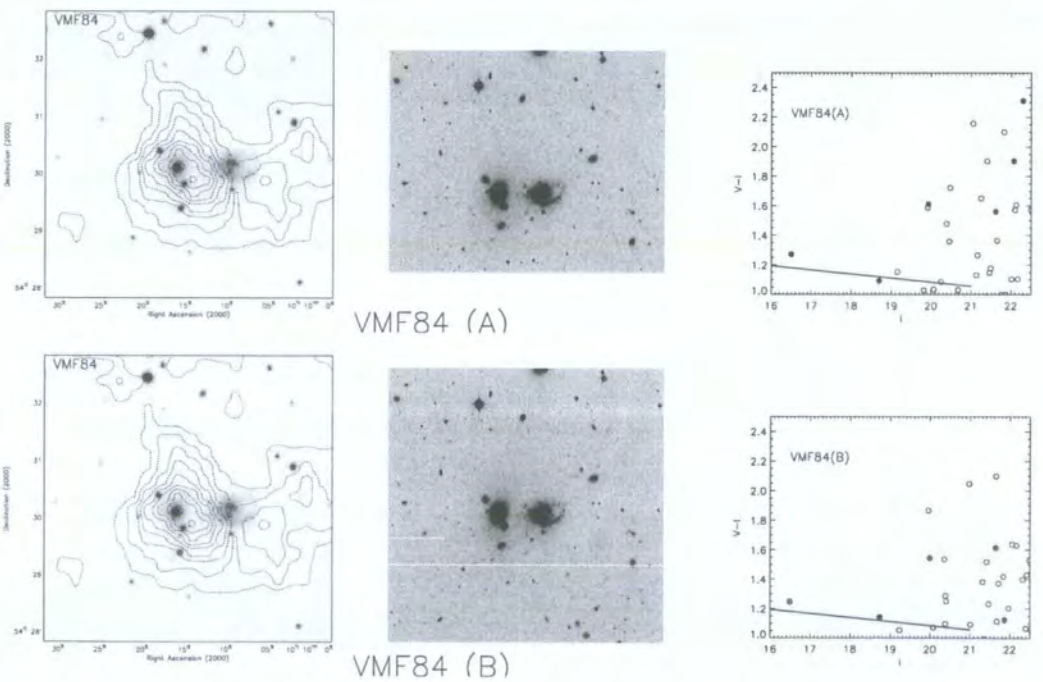

Figure 3.10: VMF84. Panels as for Figure 3.5.

VMF84 is undetected in both optical catalogues, as its redshift is just too low (z=0.045).

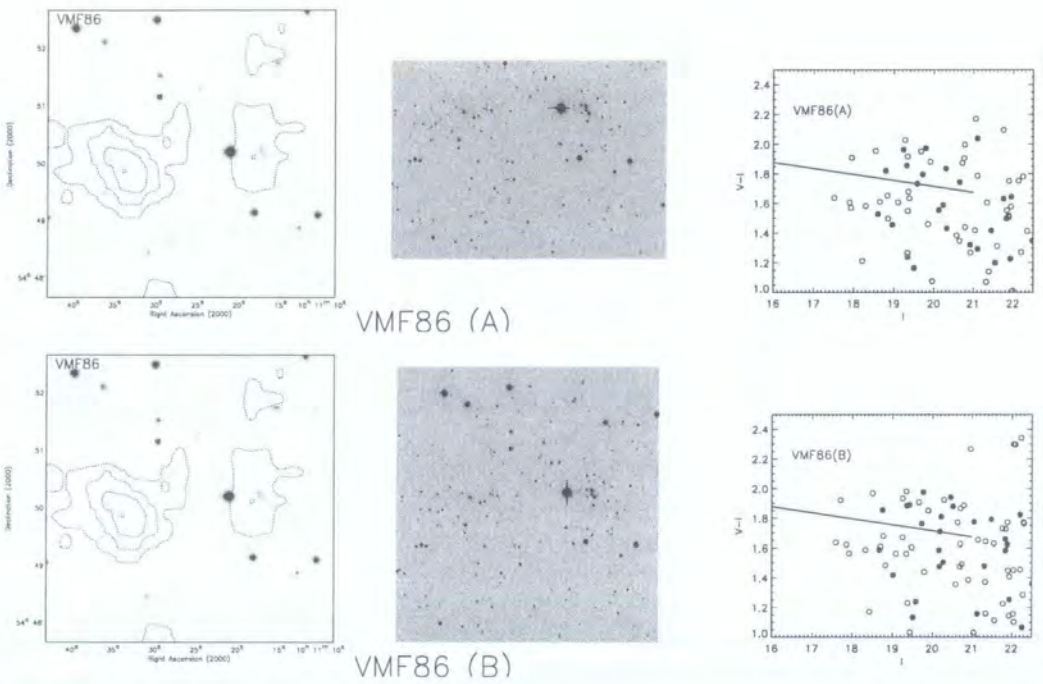

Figure 3.11: VMF86. Panels as for Figure 3.5.

VMF86 appears to show two clumps of X-ray emission, approximately 1 arcmin east and west of the VMF quoted centre. The DSS image seems to show overdensities of galaxies at the centres of these clumps. This is easily seen to be the case from the WFC images. The CMDs show two overdensities of points about 0.2 mags blueward and redward of the solid line (taken from VMF's quoted spectroscopic redshift). Thus, this appears to be, in fact, two distinct systems at very different redshifts. Indeed, this system was flagged by the CMR algorithm as being a system suffering from projection effects.

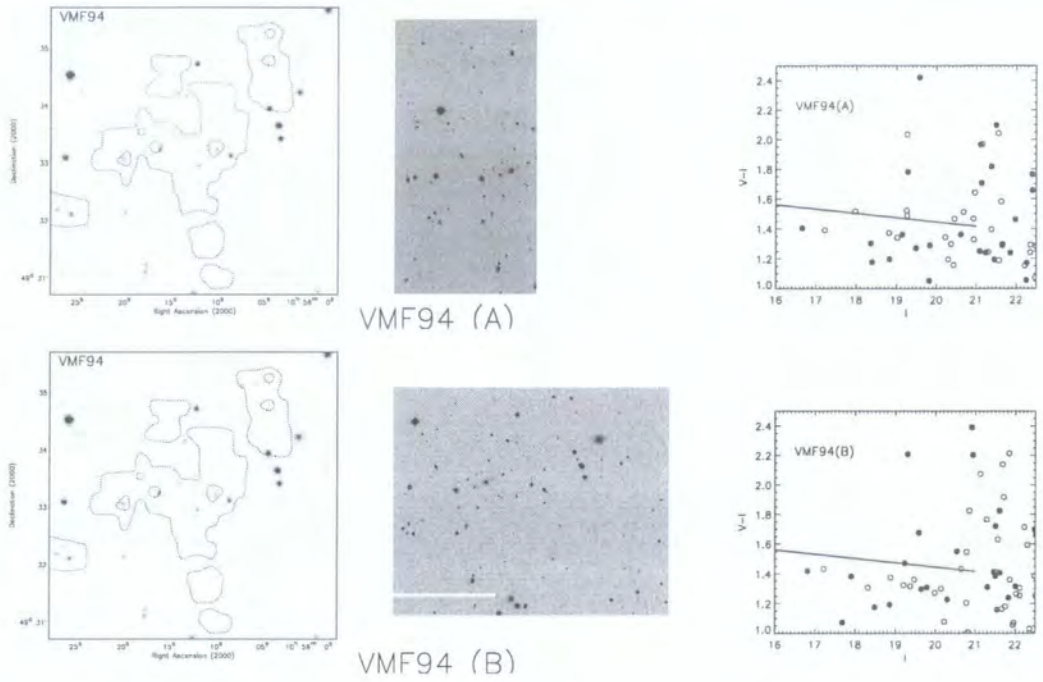

Figure 3.12: VMF94. Panels as for Figure 3.5.

VMF94 was found in the final MF catalogue, but not in the CMR catalogue as it lies blueward of the bluest colour slice.

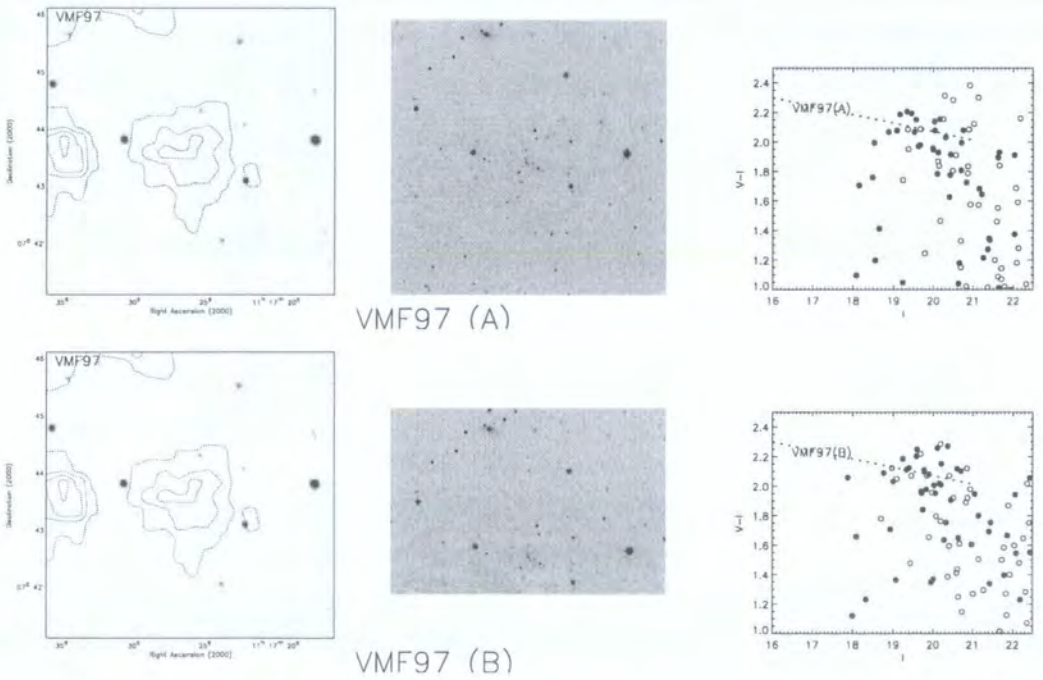

Figure 3.13: VMF97. Panels as for Figure 3.5.

VMF97 was found in both the final MF and CMR catalogues.

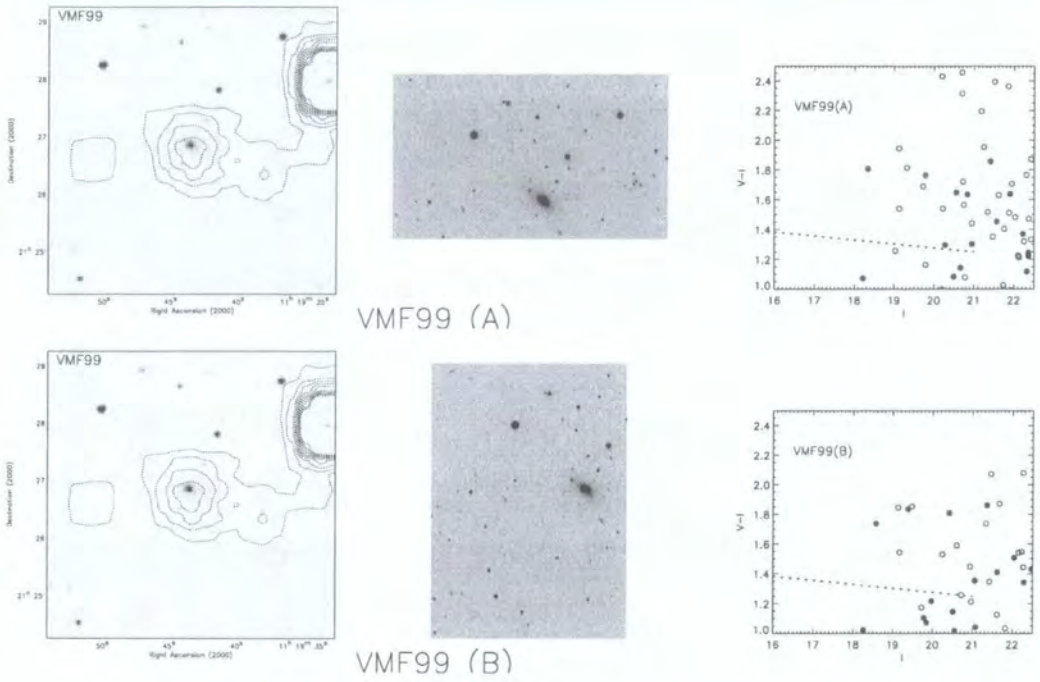

Figure 3.14: VMF99. Panels as for Figure 3.5.

VMF99 was not found in either optical catalogue, as it lies at too low redshift (z=0.11).

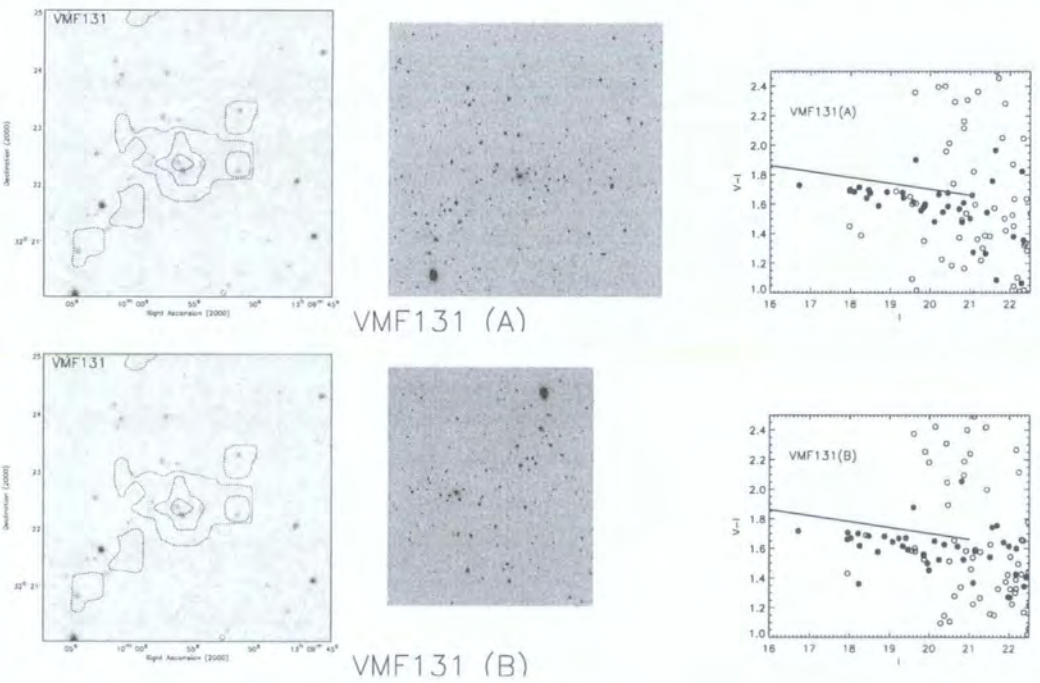

Figure 3.15: VMF131. Panels as for Figure 3.5.

VMF131 was found in the final CMR catalogue. In the MF catalogue, it was found outside the candidates associated group radius (at a distance of 1.9 arcmins), but again visual inspection suggests the association is valid.

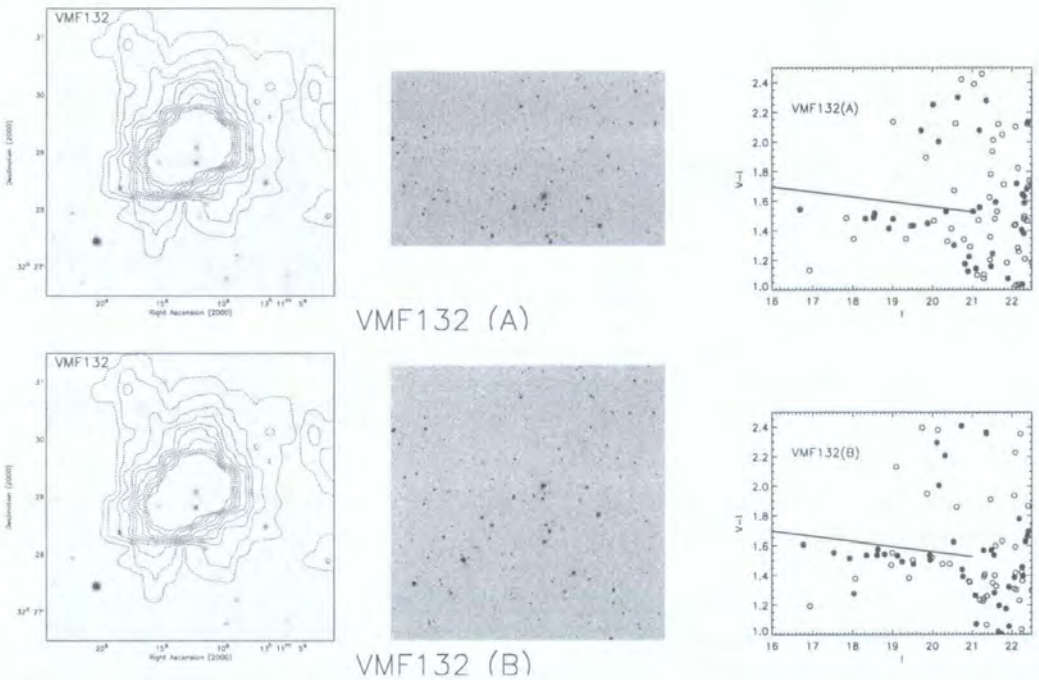

Figure 3.16: VMF132. Panels as for Figure 3.5.

VMF132 was not found in the final MF catalogue, but was found in the full catalogue, as it lay just below the significance threshold. This cluster was found in the final CMR catalogue, and it was also flagged as containing possible additional groups in projection. As well as the z_{CMR} =0.21 cluster, two potential groups are also detected at higher redshift (z_{CMR} =0.37 and 0.65). Their CMRs are not visible in the CMD as they lie just outside the field - the VMF cluster is very extended in the CMR catalogue (this agrees with visual inspection of the X-ray morphology).

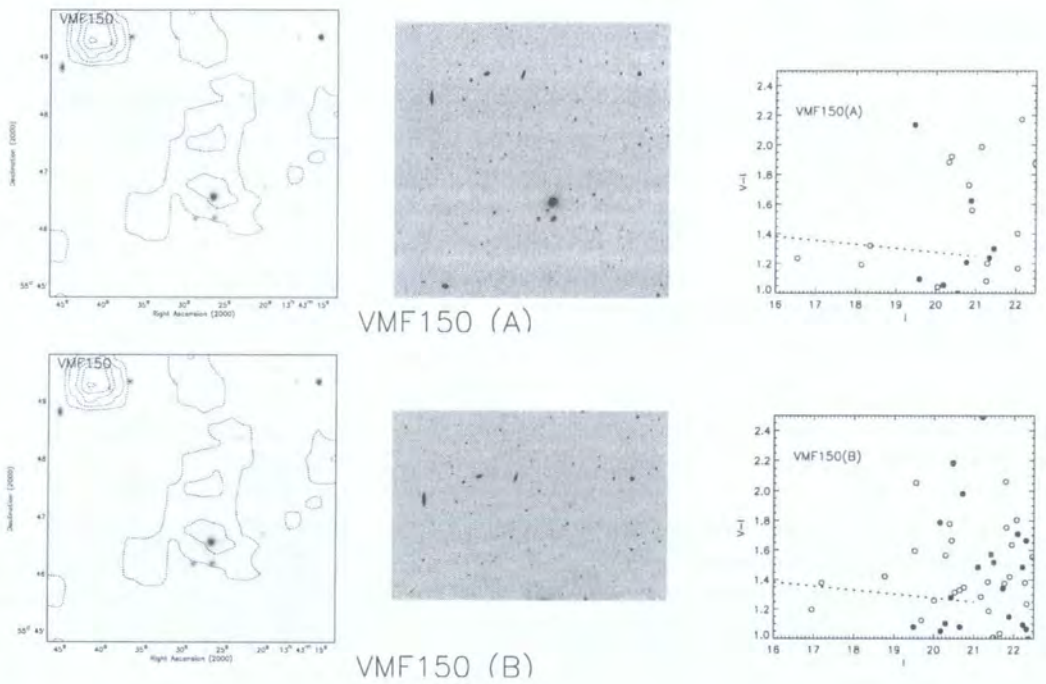

Figure 3.17: VMF150. Panels as for Figure 3.5.

VMF 150 was not detected by either optical technique. The field does not show an overdensity of galaxies, and it is possible that it was "confirmed" by Vikhlinin et al. (1998) on the "single, bright elliptical" criterion. Regardless of this, their estimated redshift (z=0.11) places this system below the lowest redshift limits of the optical algorithms.

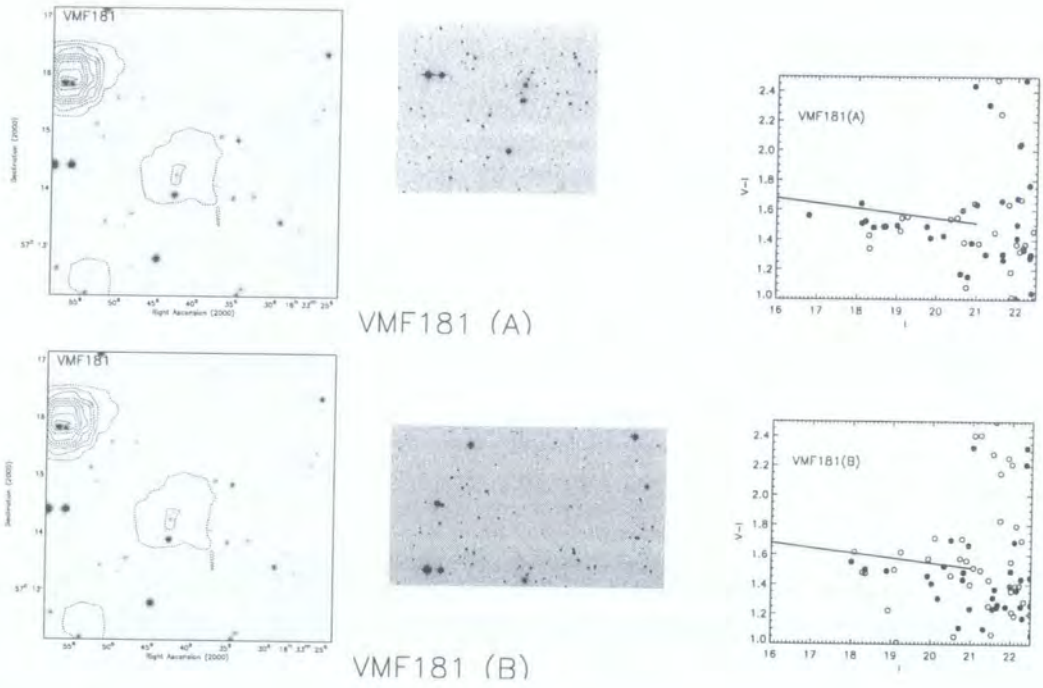

Figure 3.18: VMF181. Panels as for Figure 3.5.

VMF181 was found in the final MF catalogue, but not the final CMR catalogue. Inspection of the full CMR catalogue shows that the system is of high enough significance ($>6\sigma$) to appear in the final catalogue, were it not for the fact that this candidate is touching a neighbouring candidate of higher significance, and thus the former candidate was "cleaned" from the final catalogue.

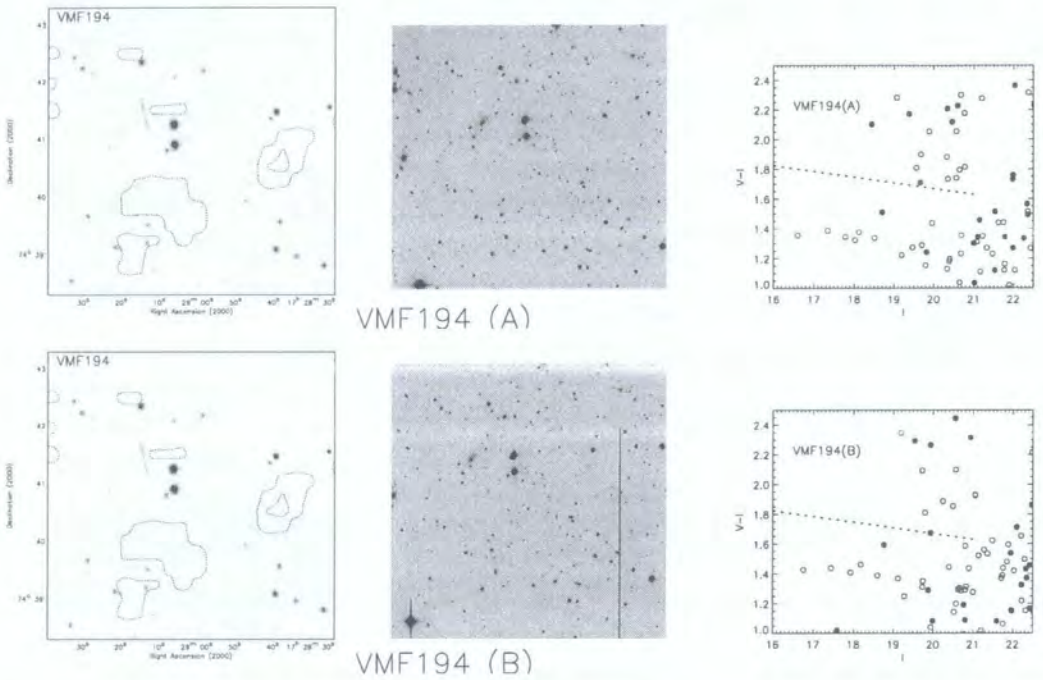

Figure 3.19: VMF194. Panels as for Figure 3.5.

VMF194 shows a distinctly diffuse X-ray morphology, with clumps of emission of the order of arcmins away from the VMF quoted centre. A match was found in the final MF catalogue, but a t quite a large distance (1.5 arcmins) from the VMF centre; a match was not found in the final CMR catalogue, but one was found in the full CMR catalogue (but at 3.5 arcmins away). This can be understood by examining the CMR and noticing that most of the points along the relation are unfilled, showing that the centre wrt red galaxies is at least 1 arcmin away. This field does not show an obvious overdensity of galaxies in the I-band image, suggesting it was confirmed on the single bright elliptical criterion. The position of a bright elliptical in VMF194 is not obvious. This candidate was only assigned a redshift based on an estimate of the magnitude of the brightest cluster galaxy, but the brightest object near the centre of the DSS field is clearly seen in the CCD images to be a star. The VMF photometric redshift is thus greatly overestimated.

VMF ID	MF candidate ID	z_{VMF}	Separation (arcmin)	z_{MF}	Δz	CMR candidate ID	offset (arcmin)	z_{CMR}	Δz
11	(mfJ012435.6+040107)	0.270	(0.328)	(0.422)	0.152	cmJ012437.8+040022	0.807	0.360	0.090
62	mfJ084914.5+373123	0.240	0.678	0.276	0.036	cmJ084908.8+373036	0.939	0.190	0.050
69	mfJ091049.4+425002	—	(2.246**)	0.484	—	cmJ091045.1+424955	1.596	0.450	—
73	mfJ094350.5+164034	0.256	(4.421*)	0.351	0.095	cmJ094329.3+163916	1.035	0.190	0.066
74	(mfJ094344.0+164500)	0.180	(0.691)	(0.293)	(0.113)	—	—	—	—
84	—	0.045	—	—	—	—	—	—	—
86	mfJ101137.3+545036	0.294	1.698	0.276	0.018	cmJ101134.1+545014 (p)	1.168	0.330	0.036
94	mfJ105617.5+493237	0.199	0.972	0.157	0.042	—	—	—	—
97	mfJ111726.2+074316	0.400	0.306	0.232	0.168	cmJ111726.2+074319	0.258	0.370	0.030
99	—	0.110	—	—	—	—	—	—	—
131	mfJ131001.9+322110	0.290	(1.889*)	0.437	0.147	cmJ130954.0+322137	0.949	0.270	0.020
132	(mfJ131113.2+322843)	0.245	(0.259)	(0.422)	(0.177)	cmJ131111.0+322825(p)	0.664	0.210	0.035
150	—	0.110	—	—	—	—	—	—	—
181	mfJ163334.2+571457	0.239	0.853	0.395	0.156	(cmJ163337.8+571328)	1.179	(0.210)	(0.029)
194	mfJ172845.5+743945	0.280	1.487	0.484	0.204	(cmJ172946.3+744238)	3.474	(0.190)	(0.090)

Table 3.5: The Nearest Optically selected Candidates to the VMF Clusters. For each X-ray selected cluster, the nearest matching MF and CMR candidate's details are given. Candidates in parentheses were not identified in the final catalogues.

* - candidate matched at a separation greater than its estimated radius.

** - candidate matched within its estimated radius, but greater than 2 arcmins.

(p) - candidate flagged as exhibiting projection along line-of-sight.

See text for details.

3.4.2 Summary of Optical Candidates Associated with X-ray Clusters

In terms of gross numbers, the final MF catalogue contains counterparts to 7 of the 15 X-ray selected clusters, and the final CMR catalogue contains 8 of the 15.

In the MF catalogue: VMF11 is not matched in the final catalogue, but is matched in the full catalogue (just below the Cash C threshold). VMF69 and 73 were both further than 2 arcmins away from the nearest candidates, but lay within the candidates' group radii. Thus, these were treated cautiously, but visual inspection showed large overdensities extending this far and thus the association of these objects seems valid. VMF74 and VMF132 were detected in the full catalogue, but did not make the higher significance cut of the final catalogue. VMF84 was undetected as its redshift is too low (0.045). VMF99 and 150 were also undetected. These fields do not show overdensities of galaxies, and the clusters were probably "confirmed" using the single luminous elliptical criterion. The redshifts given are also below the expected detection range (both have z=0.11). VMF131 has a match at a distance of 1.9 arcmins: this is outside the candidate's estimated radius of 0.5 arcmins, but again visual inspection suggests the association is valid. To summarise, if the three lowest redshift X-ray clusters (VMF84, 99, and 150) are excluded ($z \leq 0.11$), then the strict automated matching matches 6 of the 12 candidates. Visual matching suggests the recovery rate in the final MF catalogue should be 9/ 12. Lowering the significance threshold allows the remaining X-ray clusters to *all* be detected.

In the CMR catalogue: considering all except the 5 X-ray clusters at $z \leq 0.2$ (for the reasons described above), only two are not immediately matched. VMF181 is matched in the full catalogue and is of high enough significance ($>6\sigma$) to be in the final catalogue, but was "cleaned" from the catalogue as it had a neighbour of higher significance. VMF194 shows a counterpart some distance ($\approx$ 3.5 arcmin) from the X-ray cluster but, as noted above, the X-ray position seems to be at least an arc minute from a significant overdensity and CMR (the MF candidate at this position was only matched because it has a large associated radius).

One obvious effect revealed by the comparison is that all the model CMRs derived from spectroscopic redshifts result in a CMR redward of that which is observed in the WFC photometry. This systematic offset is at the level of V-I$\approx$0.1$-$0.2. This may arise from a slight systematic offset in the calibration of the V-I colour. Note that this effect will be exaggerated by using the redshift to predict the colour, as a slight difference in redshift translates to a much larger difference in colour (eg. Δz=0.03 translates into

a colour change of V-I≈0.1 magnitudes at these redshifts, cf. Figure 2.12). The VMF redshift may only be based on one redshift. Another possibility is inaccuracy in the model colours. Assuming a later epoch of formation results in bluer galaxy colours at a given redshift, as the stellar populations are younger. The models used in this thesis consider only one set of parameters for the model (and this assumes a formation redshift of 4.4). This was chosen as the models used are designed to reproduce the observed colours of early-type cluster galaxies at a given redshift (Kodama et al. 1998). However, the sample used to construct this model was too small (∼10 clusters) to examine cluster to cluster variation of the relation. The clusters selected were drawn from a heterogenous sample, so it is possible that an X-ray selected sample might show systematically bluer colours. A further possibility is a systematic offset between the calibration of the model colours and the calibration of the WFC photometry. Suffice it to note that estimated redshifts based on these V-I colours *may* systematically underestimate the redshift at a level of $\Delta z \sim 0.01$.

The CMR technique, furthermore, allows the possibility of distinguishing groups projected along the line of sight (the entries in Table 3.5 flagged with a "p"). VMF86 is identified as two systems (as suspected from the data, above): the most significant one at a redshift of 0.330 and another at 0.230. The quoted spectroscopic redshift of VMF is 0.294; this is within Δz=0.05 of the most significant candidate. VMF132 also shows two possible further groups, overlapping with the z_{CMR} =0.21 cluster, at higher redshift: z_{CMR}=0.37 and 0.65. Thus, to summarise, the CMR matches 8 of the 10 z>0.20 X-ray clusters immediately, and visual matching allows all 10 clusters to be matched. Another advantage of this method is that it is able to disentangle projection effects: correctly resolving structure (which is obvious visually in the CCD images) in one field, and suggesting higher redshift groups in another.

Next, the accuracy of the redshift estimates will be compared with Vikhlinin et al.'s (1998) redshifts.

Comparison of Estimated Redshifts with VMF Redshifts

The average bias in the redshift estimate, defined as $(z_{spec} - z_{phot})/(1 + z_{spec})$, is 0.067 with a standard deviation of 0.066 for the MF (using 8 spectroscopic redshifts from VMF); the average bias for the CMR technique is -0.022 with a standard deviation of 0.028 (from 6 VMF spectroscopic redshifts). The latter result compares very favourably with photometric redshifts (Chapter 5). Wittman et al. (2001) find an average bias of -0.027 with standard deviation of 0.059 for photometric redshifts over a similar range

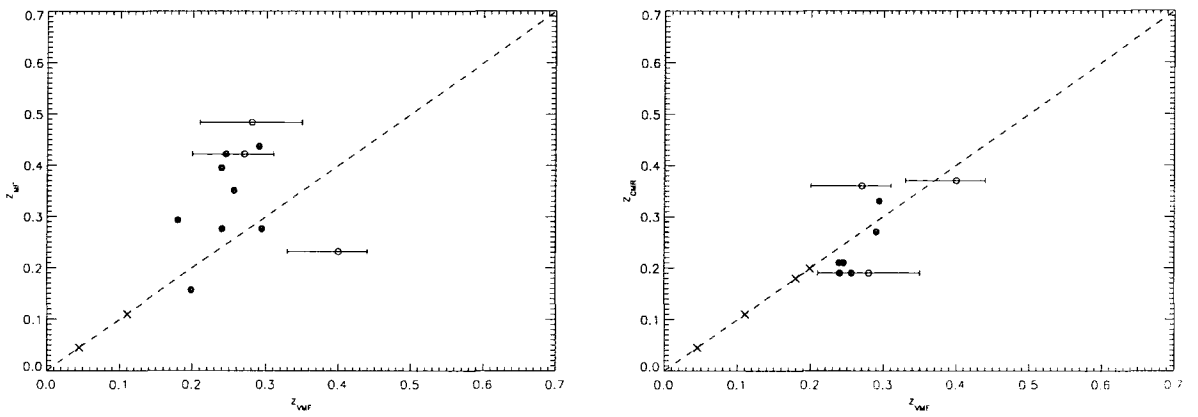

Figure 3.20: Comparison of the optical cluster finders' redshift estimates with Vikhlinin et al.'s redshifts. Open symbols are for VMF photometric redshifts with error bars showing their estimated range; filled points are for spectroscopic redshifts. Dashed line shows the one to one relation, and crosses on this line indicate undetected clusters. These numbers are tabulated in Figure 3.5. The CMR redshift appears to systematically underestimate the VMF spectroscopic redshift by $\approx$0.03, in all but one case. This is for VMF86 which is in fact two systems, as indicated earlier. The more significant candidate happens to be the higher redshift one, but if VMF measured a redshift for the lower redshift system, then this too would be underestimated by a similar amount.

using *four* photometric passbands.

3.4.3 Comparison of Optical Richness Measures with L_X

In this section, the relationship between the cluster candidates' optical and X-ray properties will be studied. This will begin by using X-ray fluxes from Vikhlinin et al. (1998) to examine their X-ray selected clusters. Next, X-ray fluxes and limits measured from the XDCS data will be used to look for correlations for the whole optical plus X-ray sample. Finally, interesting systems will be examined to determine the nature of the most extreme classes of object.

The plots below show the various optical richness measures introduced in Chapter 2 plotted against X-ray luminosity for the VMF clusters. The X-ray luminosity was calculated using the VMF measured flux and VMF quoted redshift, assuming thermal Bremsstrahlung emission from a 3keV cluster. The richness measures were taken directly from the CMR catalogue entries and thus assume the CMR estimated redshift. To illustrate the difference this makes, points for each cluster are also plotted using the CMR estimated redshift to calculate L_X. Relations from fits to X-ray detections in the optically selected sample (presented later) are also overplotted for reference.

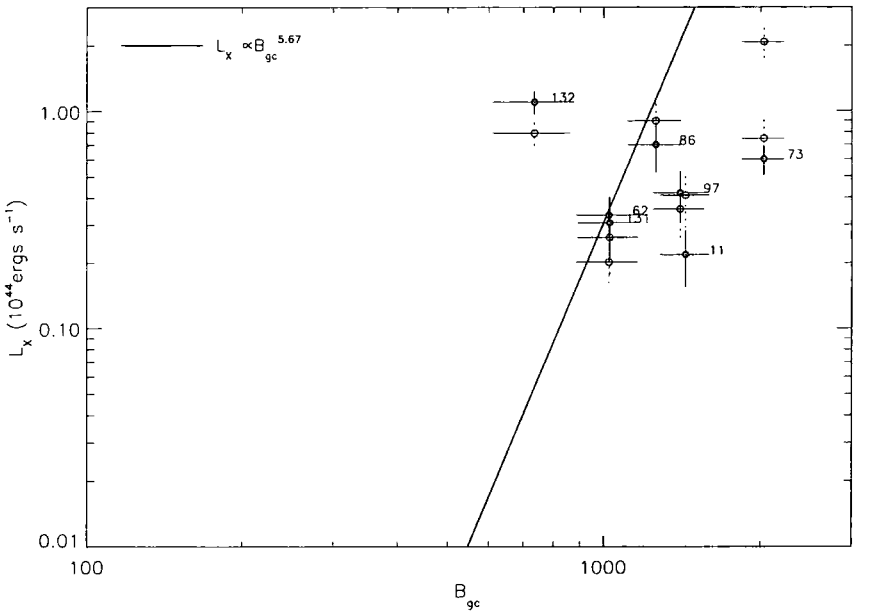

Figure 3.21: X-ray luminosity vs the B_{gc} richness measure. Filled points assume the VMF redshift for the X-ray luminosity, open points assume the CMR estimated redshift. Error bars in each case only take into account error in estimated flux. Filled points are labelled with VMF ID. The open point without a corresponding filled point is for VMF69, for which VMF do not estimate a redshift. Solid line is the power law fit to the X-ray detections for the whole optical sample, described later. See text for further details.

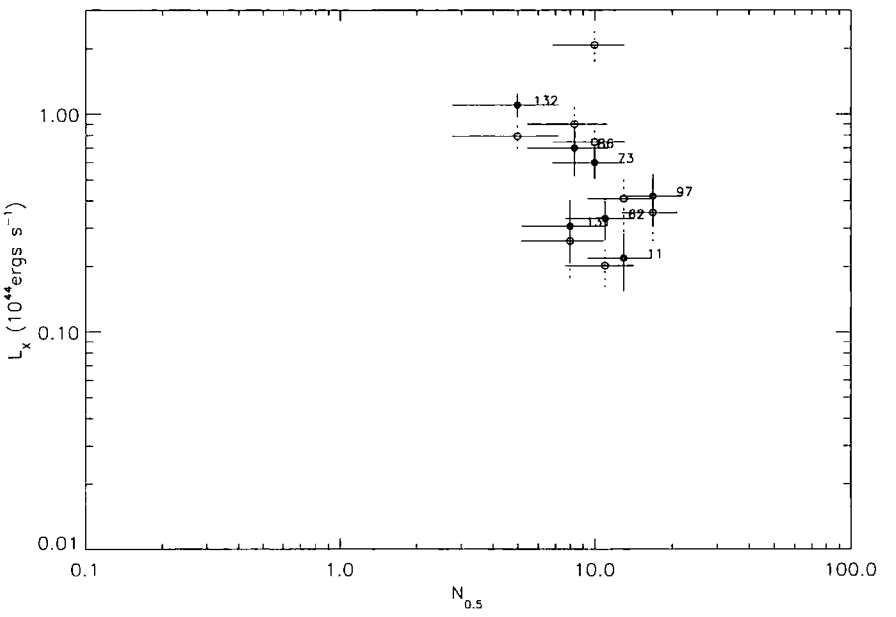

Figure 3.22: X-ray luminosity vs the $N_{0.5}$ richness measure. Symbols as previous figure. No fit to the data was possible. See later.

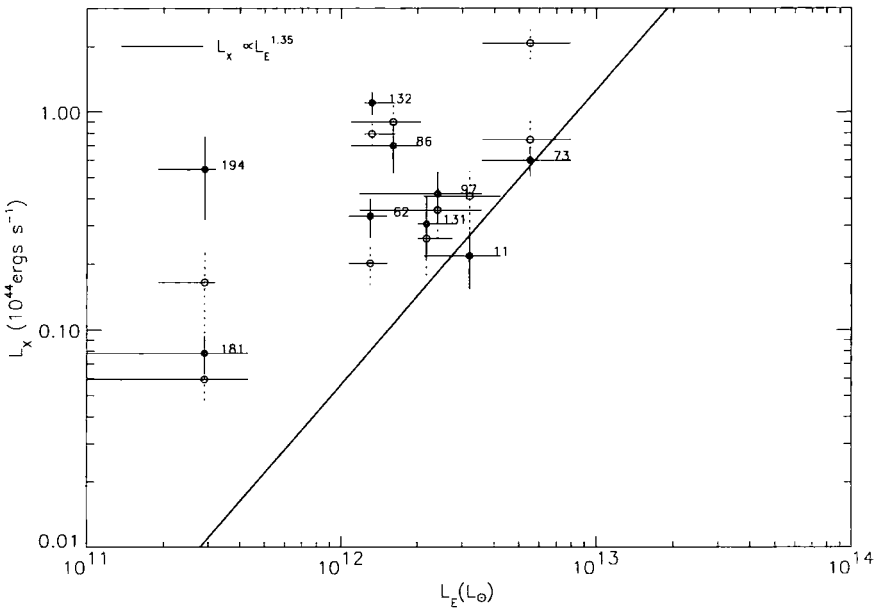

Figure 3.23: X-ray luminosity vs the L_E richness measure. Symbols as previous figure. The two extreme outliers to the left are the only candidates (VMF181 and 194) matched in the full but not the final CMR catalogue (detailed in previous section). See text for discussion.

One might expect that for a sample of X-ray selected clusters the optical richness measured would be systematically lower than for an optically selected sample. Figure 3.21 appears to show the opposite trend. For all the clusters except VMF132 (which is flagged as two projected systems), the B_{gc} measure is higher than the correlation measured below for the optically selected sample with X-ray detections. However, B_{gc} is a measure of the degree of correlation of excess galaxies. Thus, if the majority of galaxies in a field are due to cluster members and not just randomly superposed field galaxies, this could be understood to give a higher degree of correlation, matching that expected for cluster members. Thus, this trend appears understandable. The two projected systems VMF132 and VMF86 exhibit B_{gc} values below or on the correlation, as might be expected if the superposition produces an excess of galaxies, but in a less correlated way (assuming the multiple systems are not precisely aligned) than would be expected for an isolated cluster.

The N_{05} measure does not produce a good correlation (Figure 3.25) and will not be considered. Suffice it to note that a simple count of galaxies within a fixed physical radius produces a richness measure which could correspond to virtually any X-ray luminosity.

The L_E measure (Figure 3.23) produces points which lie reasonably close (typically within one to two sigma) of the fit to the whole sample, albeit systematically less rich, and with four outliers. The furthest two of these are the poorest matching candidates (only matched in the full but not the final catalogue), VMF181 and 194. These candidates both have more significant neighbouring candidates, implying that perhaps the more significant cluster, which was detected by its X-ray emission, lies some distance away from the optical candidate chosen (due to using the position quoted in VMF). Thus, it might be expected that not choosing the more significant optical centre would lead to an underestimate of L_E . The two other outliers, although lying much closer to the relation, are those systems (VMF86 and 132) flagged as projected groups. The L_E measure should not suffer from any bias due to projected groups at different redshifts. For VMF86, the estimated redshift is that of the higher redshift system. If the X-ray flux measured by VMF comes from the lower redshift system, this would result in an overestimate of the X-ray luminosity. Similarly for VMF132, although even if the redshift estimate is correct, if both systems are X-ray luminous, then the actual flux assigned to one system would result from the combined flux of two, biasing the flux measurement upward. Thus, for both the B_{gc} and L_E measures, the systematic offset from the optically selected X-ray detected relations (to be discussed next) can be understood.

The relationship between each of the richness measures and X-ray luminosity for cluster candidates in the optically selected catalogues will now be presented. Since the vast majority of the optically selected clusters have no X-ray selected counterparts, fluxes/ flux limit were measured at the positions of the optical candidates. Only the CMR candidates are considered, as the error in the estimated redshift is far less than for the MF technique, the number of false detections is lower, and cluster centres can be more precisely located (since the early-type galaxies are most concentrated in the cluster core, whereas overdense substructure can cause the MF technique to miss the true cluster centre). Aperture fluxes were measured from the X-ray images by Dr F. J. Castander. A one arcmin radius aperture was used. This was a compromise between choosing too large an aperture and increasing the chance of background contamination from point sources, and choosing too small an aperture and missing cluster flux. Most X-ray fluxes for clusters are measured in small radii and corrected upwards. Since most of the measurements are upper limits rather than detections, a smaller radius is favoured. The ROSAT count rate in the 0.5−2.0 keV band was converted to a flux in the same energy band using a conversion factor of 1.13×10^{-11} erg cm^{-2}, assuming a cluster temperature of 3 keV, and an average Galactic hydrogen column density of nH=5×10^{20}cm^{-2}. The background flux rate was determined for each field by placing 100 apertures randomly around each image and measuring fluxes in the same way. 3σ outliers were rejected from these estimates. The significance of each optical candidate X-ray flux measurement was determined relative to this background flux. If the measurement was a greater than 3σ event, this was classed as a detection. For other measurements, a 3σ upper limit was found by adding $3\times$ the standard deviation of the random aperture flux to the flux measured at that position. X-ray detections at $\geq3\sigma$ were visually inspected, and those showing contamination from an obvious bright point source were rejected from the analysis. These X-ray fluxes or limits were then converted to X-ray luminosities, assuming the CMR estimated redshift and a cluster temperature of 3 keV. 48 of the 268 usable apertures resulted in $\geq3\sigma$ X-ray detections.

A plot of each of the richness measures described in Chapter 2 versus the X-ray luminosity is given below. Simple linear regression to the X-ray detections has been performed, accounting for the errors in both X-ray luminosity and richness. For the L_E measure, the dominant source of error in the X-ray luminosity is not the estimated redshift (since the accuracy should be $\Delta z\approx0.04$), but the error in the X-ray flux measurement. For the other richness measures, the redshift estimate only enters into the richness estimate

through the fixed physical radius used for the counting. The best fit relations are: $L_X \propto B_{gc}^{5.67}$ and $L_X \propto L_E^{1.35}$ (it was not possible to fit a relation between $L_X$and $N_{0.5}$). A second fit was made after rejecting candidates flagged as "projected". This makes a slight difference to the fit for the L_X- B_{gc} relation, reducing the slope to $L_X \propto B_{gc}^{5.58}$, but only rejects one of the obvious extreme richness outliers (cm231951.2+123208, discussed below). For the L_X- L_E relation this makes little difference as this richness measure should be unaffected by projection. The new relation becomes $L_X \propto L_E^{1.31}$.

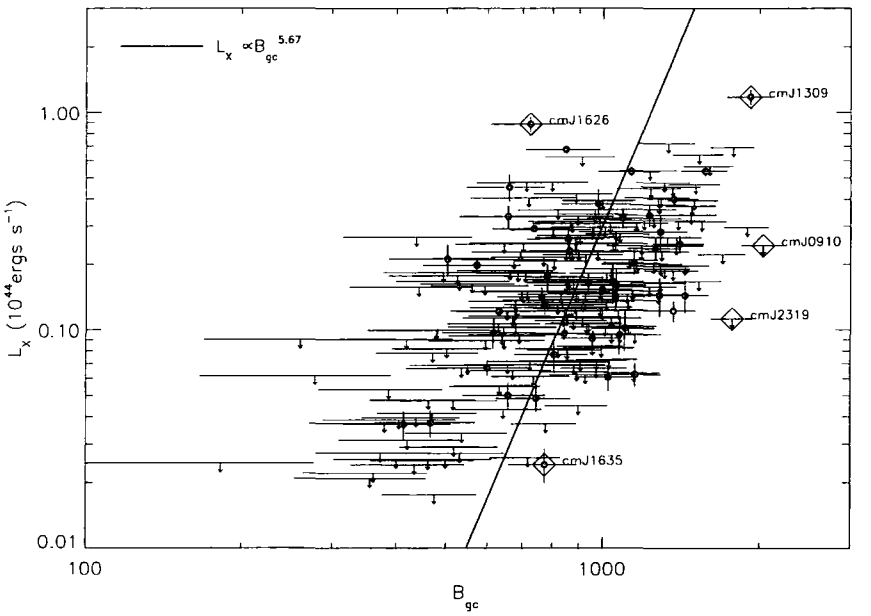

Figure 3.24: X-ray luminosity vs the B_{gc} richness measure. Filled points are $>3\sigma$ X-ray detections; downward arrows are 3σ upper limits. Solid line is the best fit relation of the detections. Outliers which will be examined in more detail are indicated by diamonds and labelled with the initial few characters of their IDs.

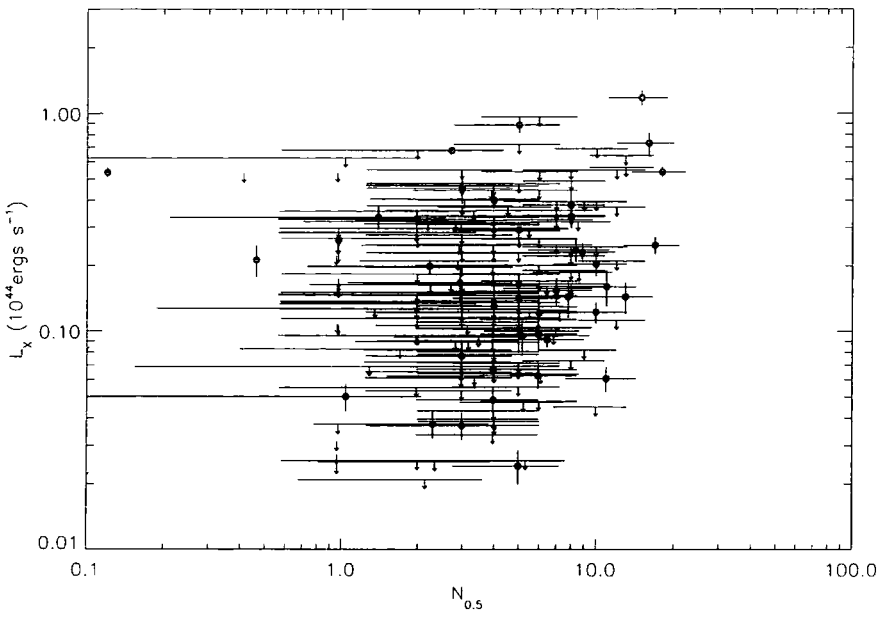

Figure 3.25: X-ray luminosity vs the $N_{0.5}$ richness measure. Symbols as for previous plot. No fit to the detections was possible.

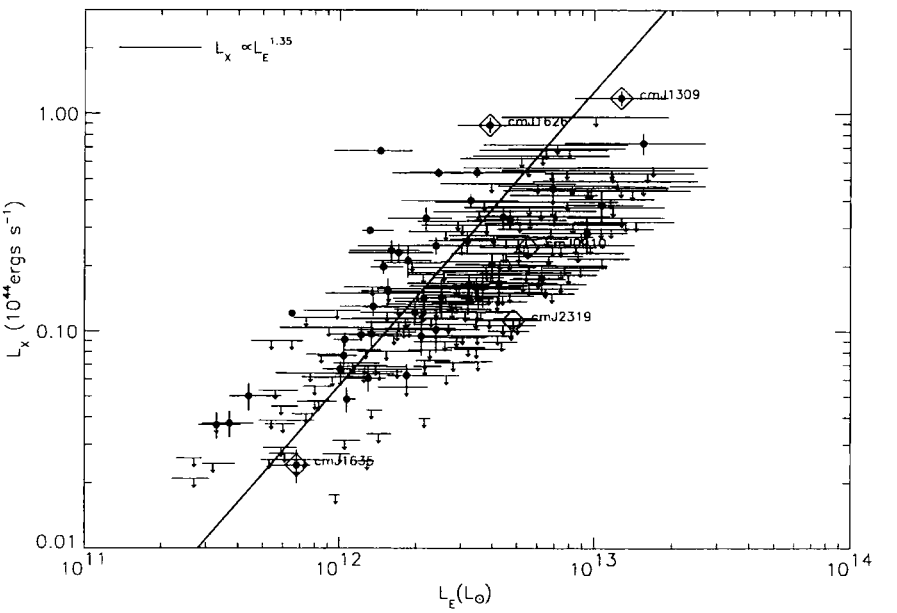

Figure 3.26: X-ray luminosity vs the L_E richness measure. Symbols as for previous plot.

Examples of outliers in these relations are now considered, to assess if clusters with similar richnesses do indeed exhibit very different X-ray luminosities. The following candidates are chosen as obvious outliers in the L_X- B_{gc} plot. Upper limits at the right hand side of the plot show rich systems with tightly constrained, unusually low X-ray luminosities. The two high $L_X$systems (cmJ130920.5+321014 and cmJ162617.5+781706) indicated have very different optical richnesses. Due to the volume probed, and the rarity of such luminous clusters, these systems are expected to be at the high redshift end of survey (the volume between 0.2<z<0.5 is similar to that between 0.5<z<0.7) and, indeed, they are both found to lie in the range 0.5<z<0.7. Conversely, in order to be detected, the faintest systems must lie at low redshift (cmJ163526.5+565433). The two very optically rich systems with low X-ray upper limits (cmJ231951.2+123208 and cmJ091045.1+424955) lie intermediate in redshift to these extremes.

Note that cmJ231951.2+123208 is flagged as a projection of two groups along the line of sight. This is discussed further below.

Candidate ID	L_X	B_{gc}	z_{est}	X-ray Detection?
cmJ163526.5+565433	0.0241540	773.320	0.19	det
cmJ130920.5+321014	1.17860	1916.03	0.61	det
cmJ162617.5+781706	0.885515	724.190	0.55	det
cmJ231951.2+123208	0.112378	1766.54	0.37(p)	lim
cmJ091045.1+424955	0.244131	2029.44	0.45	lim

Table 3.6: Table of properties for interesting outliers from L_X- B_{gc} relation.
(p) - candidate is flagged as "projected".
det - X-ray detection
lim - X-ray non-detection. Luminosity is 3σ limit

Plots as for the X-ray selected clusters (Figure 3.5) are given in Figure 3.28.

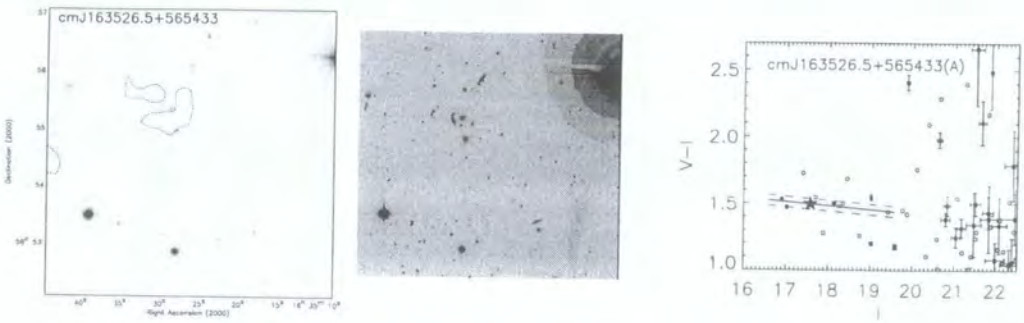

Figure 3.27: Plots as for Figure 3.5 for candidate cmJ163526.5+565433. Solid line in CMD indicates model CMR for estimated redshift. Dashed lines bound the colour slice (described in 2.12) and star indicates the position of M*. Photometric errors are indicated for inner (filled) points, but omitted from outer (open) points for clarity.

Figure 3.28: Plots as for Figure 3.5 for candidate cmJ130920.5+321014.

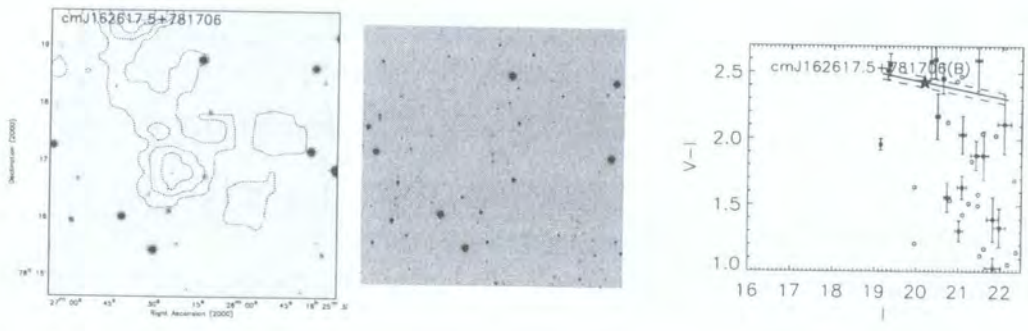

Figure 3.29: Plots as for Figure 3.5 for candidate cmJ162617.5+781706

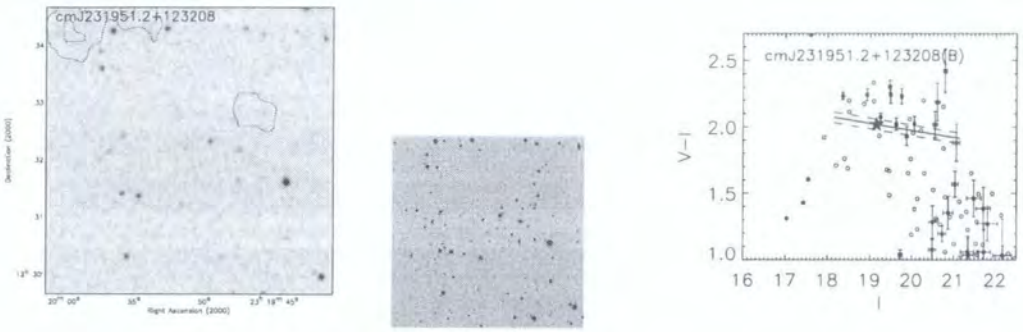

Figure 3.30: Plots as for Figure 3.5 for candidate cmJ231951.2+123208. This system is flagged as the projection of two groups/ clusters, as can be seen from the second, higher redshift CMR.

Figure 3.31: Plots as for Figure 3.5 for candidate cmJ091045.1+424955

From these figures, the example cluster candidates do indeed appear to have the properties measured in the catalogues and shown in Table 3.27. For example, the X-ray detections do not appear contaminated by point sources, and the redshift estimates seem entirely consistent with the predicted CMRs. This is confirmed by the fact that one of the examples (cmJ231951.2+123208) which was flagged as the projection of two groups will be shown to be two groups via spectroscopy in the next chapter. The redshifts derived are in good agreement with the estimated redshifts.

cm1626 and cm1635 have similar B_{gc} values, but their X-ray luminosities vary by almost two orders of magnitude. Examining the relation using L_E instead of B_{gc} shows that both these systems lie closer to the relation, although still at opposite sides of the fit. Their L_E measures differ by about 0.5 dex whereas their $L_X$differ by nearly 2 dex. The optically rich, but X-ray underluminous systems (cmJ2319 and cmJ0910) still lie below the vast majority of the X-ray detections in the L_E plot, but again they lie closer to the tighter correlation between L_X- and L_E , compared with L_X- B_{gc} . The most deviant of the two (cmJ2319) could move if the X-ray emission is due to the lower redshift (projected) system (at z=0.27 rather than 0.37). This would mean that the the X-ray luminosity would be lowered, as the source of the emission would lay nearer, and the L_E of the second CMR would need to be measured. Due to this ambiguity in assigning X-ray emission in the case of projected systems, it is best to neglect this datapoint although, as stated above, this projected system is the only one of such extreme B_{gc} richness. Note, however, that many neighbouring points not flagged as projections lay nearby in the L_X- L_E plot. An X-ray detection at very similar luminosity lies almost an order of magnitude lower in L_E in the plot. Thus, although the L_X- L_E correlation is tighter than that using B_{gc} , there is still significant intrinsic scatter.

The scatter in the relation could be attributable to a number of factors. The physical processes involved in the determination of $L_X$have been discussed in Chapter 1, but will be reiterated here, along with a discussion of L_E . The X-ray luminosity is dependent on the temperature and density of the gas. These in turn depend on the dynamical state of the cluster (which determines the depth of the gravitational potential, and the densities that can be reached by the gas). The presence of a cooling flow increases the luminosity by increasing the gas density. $L_X$can also be increased through unresolved point source contamination.

The optical properties of the cluster candidates obviously depend on the properties of the member galaxies. Since these systems were selected on the presence of a CMR, a

population of galaxies which formed their stars at high (z>2) redshift, and terminated star formation shortly after, is required.

The interplay between the intracluster medium and the cluster galaxies is likely to be important and not straightforward to model. Several workers (eg. Ponman, Cannon, & Navarro 1999, Bower et al. 2001) have recently investigated such interplay using numerical simulations. They propose energy injection at early times from supernovae in cluster galaxies as a method to "pre-heat" the ICM and produce observed relations such as the L_X- $T_X$relation. In addition, observations by Edge (2001) reveal the presence of cold gas in cooling flows which is fuelling star formation in cluster galaxies, at least in the central dominant cluster galaxy.

3.5 Radio Selection of Galaxy Clusters

Three methods using radio galaxies have been shown to successfully find clusters. Public radio survey data exists for fields overlapping with the XDCS, so these methods will be tested on this dataset. The first technique involves simply searching around radio loud galaxies or quasars for the presence of a clusters. Since a large number of radio galaxies are present in XDCS fields, and spectroscopic redshifts are not available, it will be difficult to tell which of these are associated with clusters. Therefore, this technique will not be used. The second method involves searching for overdensities of radio galaxies, and the third involves looking for galaxies with disturbed radio morphologies.

The data for this section are taken from two public 1.4GHz surveys, both undertaken with the Very Large array (VLA)[4]. The first is the all-sky, low resolution NRAO VLA Sky Survey (NVSS, Condon et al. 1998); the second is the smaller area but higher resolution Faint Images of the Sky at Twenty-cm (FIRST) survey (White et al. 1997).

3.5.1 Radio Galaxy Overdensity Selection

Owen et al. (1999) studied two optically-selected clusters from the Abell (1958) catalogue at z≈0.25. These were chosen to have similar richnesses (ARC4), but have very different blue fractions (A2125, A2645: f_b =0.29, 0.03). VLA radio observations indicated very different populations of radio galaxies: 27 for the former cluster, and only 4 for the latter. The radio galaxy excess occurs for 20cm radio luminosities below 10^{23} W Hz^{-1}. Locally,

[4]The National Radio Astronomy Observatory is operated by Associated Universities, Inc., under co-operative agreement with the National Science Foundation.

radio galaxies at these luminosities are mostly driven by star formation (rather than an AGN), and the radio galaxies are mostly later in type than E/S0. The cluster with the higher blue fraction appears to be in the process of a cluster-cluster merger. This is suggestive that clusters found to have a large number of associated radio sources may possess galaxies with large amounts of recent star formation, as evidenced by high blue fractions. This was the motivation for the Texas-Oxford Cluster Survey (TexOx) and, indeed, early results from their z$\sim$0.4 radio overdensity selected clusters (Gay et al. 2001) support this picture. The detection method they use is to select overdensities of 5 or more radio galaxies with a 1.4GHz flux greater than 2.3 mJy within a 6 arc minute diameter. Clusters identified from such overdensities of radio sources exhibit systematically higher blue fractions than clusters selected via other methods. Gay et al. (2001) also state that many of their optically confirmed clusters are likely to be at higher redshifts (0.4<z<0.7) at which distances the radio sources have to be so powerful that they are mostly AGN, or very powerful starbursts. They suggest that many of their candidates lacking optical identifications are clusters at z>1.

Data and Method

Using the publically available NVSS[5] the TexOx search criteria were applied to all NVSS data overlapping with XDCS fields.

This resulted in two radio overdensity candidates:

α (J2000)	δ (J2000)	No. of radio sources within 3' radius
09:11:42.7	43:03:54.	8
09:10:51.7	42:47:49.6	5

Only one lies near a CMR candidate. The second candidate lies 2.4 arc minutes from cmJ091045.1+424955. At the CMR estimated redshift of 0.45 this corresponds to a physical distance of 0.8 Mpc. This CMR candidate is an X-ray non-detection and has a 3σ limiting flux of 2.7×10^{14} erg cm^{-2} s^{-1} or an X-ray luminosity limit of 2.4×10^{43} erg s^{-1}. The TexOx survey found 4 radio overdensities near PDCS (5 deg^2, Postman et al. 1996) cluster candidates, and 6 in the Vikhlinin et al. (1998) catalogue (160 deg^2). Thus, finding one candidate associated with a CMR candidate within 12 deg^2 is in general agreement with these numbers (Postman et al. (1996) searched for candidates out to z$\sim$1.2, whereas both XDCS optical catalogues are restricted to z$\lesssim$0.7).

[5]http://www.cv.nrao.edu/ jcondon/nvss.html

3.5.2 Radio Morphology Selection

Blanton et al. (2001) used the FIRST survey to search for radio galaxies exhibiting double lobe emission with a bent morphology. See Blanton et al. (2001) and references therein. Briefly, a radio source's morphology can become distorted as a consequence of its motion through a surrounding intracluster medium (ICM). Thus, bending of a radio galaxy's lobe may be evidence for the presence of a dense plasma. Another explanation for disturbed radio morphology is interaction between neighbouring galaxies, although such systems are typically asymmetric, in contrast to the relatively symmetric appearance caused by ICM interaction.

Data and Method

Images and source catalogues from the FIRST[6] catalogue overlapping with XDCS fields were downloaded. The areal coverage of FIRST is less than that of the NVSS and so not all XDCS fields have FIRST data (only 26/ 39). All available images were visually inspected for the presence of sources showing a bent, double lobed nature (eg. Figure 1 of Blanton et al. 2001). Six double radio sources were found, but only one of these showed a clearly bent morphology. This is reproduced in Figure 3.32.

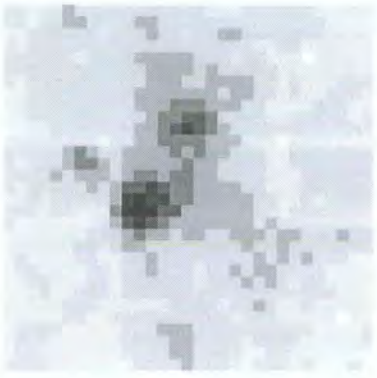

Figure 3.32: 1.4GHz image of bent double FIRST radio source at 14:14:56.35 +44:03:37.43 (J2000). Pixels are approximately 2.3 arcsec, and image is 70 arcsec on each side.

This source lies only 1.5 arcmins from CMR candidate cmJ141504.3+440250, which is about 450kpc at the estimated redshift of 0.37. This candidate is a marginal X-ray detection with a flux of 2.5×10^{14} erg cm^{-2} s^{-1} (3.99σ significance) or a luminosity of

[6]http://sundog.stsci.edu/

1.4×10^{43} erg s^{-1} at the CMR estimated redshift of 0.37. The X-ray detection is additional evidence for the presence of an ICM, although the detection is of too low a significance to lead to its inclusion in an X-ray selected catalogue. This is additional evidence that optically selected clusters can find systems containing an intracluster medium which is not sufficiently hot/ dense to be very X-ray luminous. Blanton et al. (2001) surveyed ~3000 deg^2 to find 384 bent double sources. Thus, finding one in the XDCS–FIRST overlap (~8 deg^2) is in good agreement with this number.

3.6 Conclusions

The procedure for the final construction of two optically selected catalogues has been detailed. An internal check of the redshift estimates for both these techniques was performed, using the regions were two independent observations of the same area were made. The X-ray selection of galaxy clusters has been outlined and surveys overlapping with XDCS fields have been examined. The survey of Vikhlinin et al. (1998) (VMF) overlaps with 29 of the 39 XDCS fields. 15 VMF clusters were found within these fields. Of the ten remaining fields, seven of these overlap with the Bright SHARC Survey, although none of these contain cluster candidates, albeit only to a brighter flux limit (about an order of magnitude) than is possible from the X-ray data. All of the XDCS fields have been searched for X-ray clusters by the RIXOS collaboration, although they found fewer than Vikhlinin et al. (1998), due to their detection algorithm not being optimised for extended sources.

A comparison with the VMF catalogue shows that the matched-filter (MF) technique recovers 9 out of 12 X-ray selected clusters (neglecting the 3 at lower redshifts than those for which the technique was designed). The colour-magnitude selection (CMR) method allows all the clusters at $z\gtrsim0.2$ to be detected. Furthermore, the CMR technique shows that at least one of the VMF clusters is in fact two distinct clusters at different redshifts, and suggests that perhaps another has a higher redshift group/ cluster projected along the line-of-sight. Comparison of the optical algorithms estimated redshifts with the Vikhlinin et al. (1998) spectroscopic redshift shows that the MF redshift is good to around 0.07 and the CMR to around 0.03. Comparing the MF catalogue with the CMR catalogue shows that around 22% of the MF candidates have no corresponding CMR candidate. Of the candidates which match at high significance between the two catalogues, around 11% of the MF candidates are likely to suffer line-of-sight projections, as judged by multiple

CMRs along the line-of-sight.

An examination of the relations between optical and X-ray luminosity revealed that the X-ray selected clusters of Vikhlinin et al. (1998) possess systematically higher values of B_{gc} relative to the best fit correlation for optically *selected* but X-ray *detected* cluster candidates. The VMF clusters also exhibited systematically lower values of L_E . The former observation might be explained in terms of the X-ray selected clusters possessing a higher ratio of cluster to field galaxies relative to the optically selected candidates (which may have a few non-CMR members superposed onto the true CMR, due to the selection process). Since, the B_{gc} measures the degree of correlation due to excess galaxies, increasing the fraction of cluster members (which follow the expected correlation function) might be expected to increase the B_{gc} signal. Another possibility is that the optically selected candidates may show a lower correlation value due to, for example, if these systems are dynamically younger they might be expected to be more irregular in shape, or have a higher fraction of infalling galaxies. Such structure might not necessarily follow the power law correlation exhibited by the X-ray selected clusters. The $N_{0.5}$ measure does not show any correlation with L_X.

The optically selected cluster sample was considered, and X-ray fluxes or flux limits measured for the position of each candidate. The correlation between $L_X$and B_{gc} shows considerable scatter. The relation for L_X- L_E shows a tighter correlation although still with some scatter. Examination of a sample of interesting outliers in these correlations showed that the measured properties do seem correct, and that the scatter is genuine.

Finally, two techniques utilising public radio data were utilised. The first involved searching for overdensities of radio galaxies and resulted in two cluster candidates. One of these was deemed to be associated with a CMR candidate, and the other may be at too high a redshift ($z \gtrsim 0.7$) to be seen in the XDCS data. The second technique searched for radio sources exhibiting a bent double lobed morphology, indicating motion relative to a dense medium. One was found. This lay very close to a CMR candidate which was also an X-ray detection (at $\approx 4\sigma$ - not sufficiently luminous to be detected by the VMF survey), providing further evidence for the presence of an intracluster medium.

Chapter 4

Verification of Cluster Candidates

4.1 Introduction

In order to confirm the reality of candidate cluster systems from the XDCS, spectroscopy is required to obtain redshifts to study the distribution of galaxies in all three dimensions.

Observing time was secured for follow-up via multiobject spectroscopy with the MOSCA[1] instrument on the Calar Alto 3.5m telescope (details of this instrument are given in §4.3). This was accomplished before either the data reduction or cluster-finding pipelines were finalised. Therefore, cluster candidates for spectroscopy were obtained "by hand" but in a manner consistent with the way in which the automated detection algorithms would select objects. The representiveness of such candidates is examined retrospectively and discussed in the next section. This chapter then goes on to detail the data reduction of the spectra; assess the significance of groupings of galaxies in redshift space and confront the significant groups with the results of the cluster finding algorithms; estimate velocity dispersions of these systems, and finally a brief comparison of photometric redshifts with the spectroscopic redshifts is presented (where further imaging data has been acquired).

4.2 Spectroscopic Sample Selection

Galaxy catalogues were constructed in the same manner as described in Chapter 2 except that the `SExtractor FLAG` parameter was not used to reject corrupted objects (eg, saturated/ merged objects) and the photometric calibration was not finalised. Plots of each WFC mosaic[2] were displayed and large overdensities selected visually. Colour-magnitude diagrams (CMDs) were created for regions around the centre of the overdensity to look for the presence of a colour-magnitude relation (CMR). Such a CMR was not

[1] `http://www.mpia-hd.mpg.de/MOSCA/index.html`

[2] Only the B rotations were used in this procedure, due to the order in which the data were reduced.

required to be particularly rich, and with hindsight it seems that the systems selected have less rich CMRs than typical CMR-selected candidates. One candidate (R294_1) did not appear to show a CMR, but represented such an extreme overdensity that it was added to the list of targets as a possible counter-example to the ubiquity of the CMR[3].

Candidates with no extended X-ray counterpart, as selected from Vikhlinin et al.'s (1998) catalogue were chosen. The only other criterion applied was that the RA range available for the observing run meant that the candidates had to come from the subset of XDCS originally observed during the June 1998 run. This subsample comprises 16 fields, or approximately 4.5 square degrees.

The manually selected candidates are listed in Table 4.1, and plotted in Figure 4.1. For each one, astrometry was performed using the `STARLINK` program `astrom` to convert pixel coordinates into sky coordinates as measured from the APM catalogue[4], to an *rms* accuracy of of $\approx$0.3 arc seconds, or subpixel. Multi-object slit masks were constructed using a constant slit width of 1.5 arcsec and a slit length of at least 10 arcsec. In order to be included as potential slit candidates, galaxies had to be brighter than I_C=20 (often a few galaxies fainter than this were allocated slits to fill the masks). Ideally, galaxies should be selected randomly for observation, with a simple magnitude selection. It is preferable to perform this selection in the I-band, rather than the V, as this procedure is less biased in terms of the star-formation activity of the galaxies (bluer passbands are dominated by short-lived, massive stars - see Chapters 5 & 6). However, the nature of multi-object spectroscopy means that as each slit is allocated, neighbouring galaxies are precluded from receiving a slit. Each slit will disperse the light from a target object along most of the length of the CCD, and so galaxies which lay along this spectral path cannot be selected, to prevent the resulting spectra from overlapping. Using more than one mask partially overcomes this problem, and allows omitted galaxies in one mask to be observed in another. Two multi-slit masks were designed for each candidate, by Dr R Bower, although not all of these were used.

4.2.1 Comparison with Automated Cluster-Finder Catalogues

The overdensities selected were compared with the final MF and CMR catalogues by searching for candidates within the MOSCA field. These candidates are tabulated below

[3]Such a candidate was also targeted, for this reason, by Oke, Postman, & Lubin (1998), but was found to not be a real cluster.

[4]`http://www.ast.cam.ac.uk/~mike/apmcat/`

(Tables 4.2 and 4.3). X-ray flux limits are measured only at the positions of CMR candidates, but are similar for the MF candidates (as the positions are close, on the sky). The estimated redshift of the CMR method exhibits smaller scatter (Chapter 3), so the luminosity limits should be more accurate for the CMR method. All measurements are 3σ upper limits, except for one marginal detection (3.4σ), but visual inspection of the X-ray image does not reveal obvious extended emission, which might be related to a cluster.

The cluster positions are shown graphically in Figure 4.1. This figure shows the surface density of galaxies brighter than I_C =20.0, within the MOSCA field, with a cross indicating the approximate centre of the overdensity which was identified as the candidate. The colour-magnitude diagram (CMD) for galaxies around this point is shown in the lower right panel. A (possibly poor/ weak) CMR was identified for all candidates except R294_1. The upper right panel shows the cluster candidates identified by the final automated techniques. Points indicate galaxies brighter than I_C =22.5 for the B-rotation data. The dashed circles indicate limits of ROSAT PSPC (described in Chapter 3) at radii of 3 and 19 arcmins. The square box shows the approximate extent of the MOSCA field (note: the usable area is contracted in one direction, as the spectra must fall near the centre of the CCD in the spectral direction, to avoid the spectrum being truncated by the chip edge - cf. slit positions in upper left panel). Dotted circles show position of MF candidates in the final catalogue with radii given by the group radii associated with each detection (see Chapter 2). Solid circles show positions and extent of CMR candidates[5]. Finally, the lower left panel shows the I-band image for the field observed. Allocated slit positions are overplotted. These differ slightly from the points in the upper panel (squares) which show the actual spectra extracted. This is because some slits resulted in multiple spectra (due to fortuitous placement of galaxies); and some resulted in no spectrum.

[5]Note: MF symbols are always larger than the line thickness used to indicate CMR candidates, to avoid confusion between CMR candidates and small radius MF candidates.

Candidate ID	α (J2000) [hh:mm:ss.s]	δ (J2000) [dd:mm:ss]
R110_1	14 28 22.0	+33 07 13
R220_2	17 23 37.9	+74 43 17
R236_1	17 02 58.9	+51 53 52
R294_1	23 19 54.5	+12 32 27

Table 4.1: MOSCA mask centres. Note: the IDs are just numbered subfields of the RIXOS fields, and should not be confused with the similar nomenclature used for X-ray candidates by the RIXOS collaboration.

Table 4.2: XDCS MF candidates in MOSCA Fields

Field	XDCS ID	Dist (arcmin)†	z_{est}
R1101	mfJ142824.2+330538	1.6448906	0.115
R2202	mfJ172321.8+744326	1.0702165	0.555
R2361	mfJ170257.8+514935	4.2857400	0.473
R2941	mfJ231954.5+123256	0.48399973	0.280

† - Distance of candidate from centre of MOSCA field.

Table 4.3: XDCS CMR candidates in MOSCA Fields. Dist indicates distance from field centre. ‡ - (p) in estimated redshift indicates that candidate is flagged as a line-of-sight projection by the method described in Chapter 3. X-ray fluxes and luminosities (using estimated redshifts) are 3σ upper limits for $<3\sigma$ detections. Visual inspection of the one detection does not show any obvious extended emission, which might be associated with a cluster.

Field	XDCS ID	Dist (arcmin)	z_{est} ‡	F_X (10^{-14}erg s^{-1} cm^{-2})	L_X (10^{44}erg s^{-1})
R1101	cmJ142812.0+330736	2.1298013	0.160	$\leq$1.84	$\leq$0.018
R2202	cmJ172333.0+744410	0.94534421	0.210	$\leq$3.28	$\leq$0.056
R2361	cmJ170244.2+515539	2.8962239	0.310 (p)	2.42 (3.40σ)	0.095
R2361	cmJ170232.6+514922	6.0559771	0.300	$\leq$2.24	$\leq$0.081
R2361	cmJ170258.9+514921	4.5046376	0.470	$\leq$2.24	$\leq$0.222
R2941	cmJ231951.2+123208	0.85513706	0.370 (p)	$\leq$1.94	$\leq$ 0.112

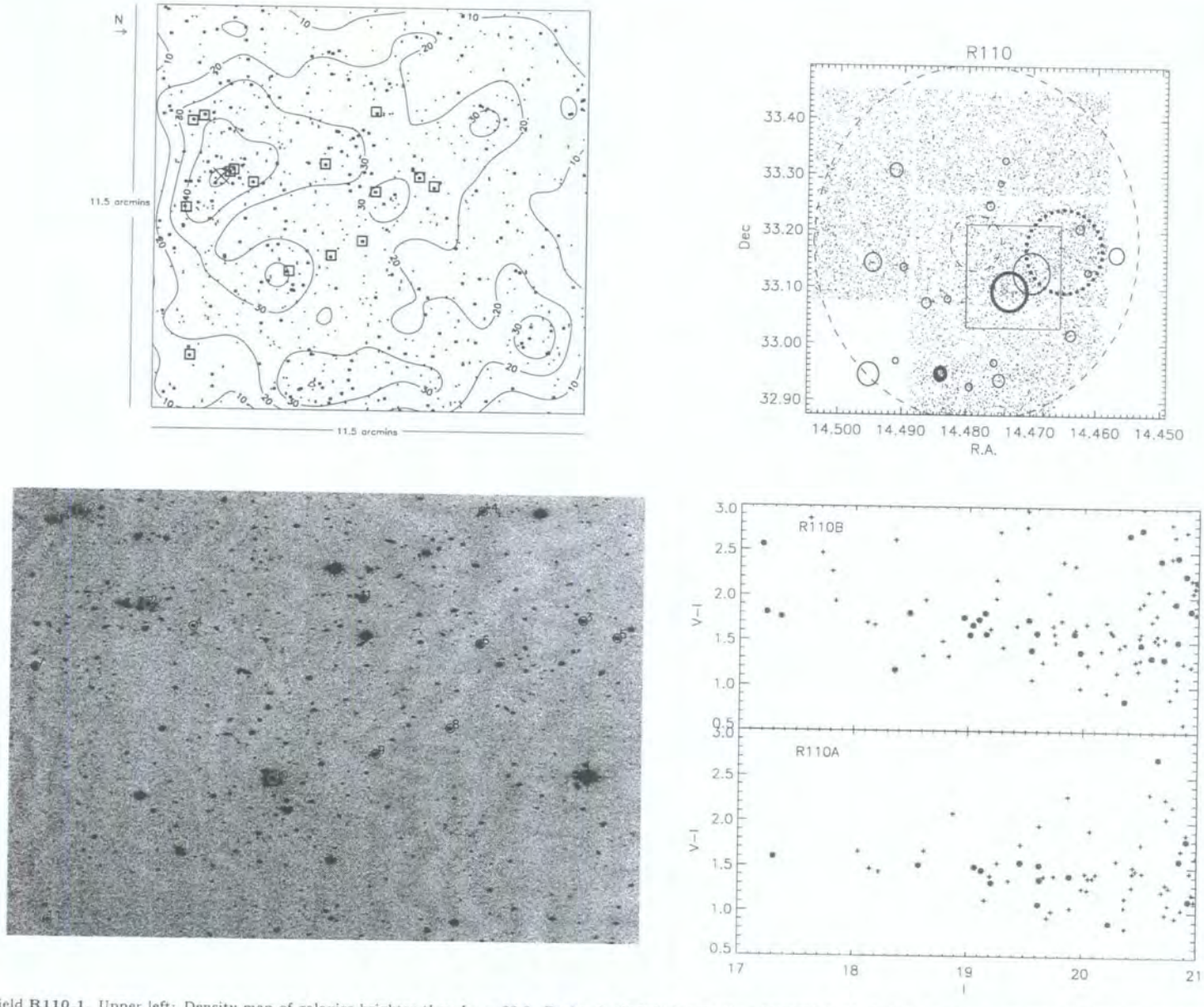

Figure 4.1: Field **R110_1**. Upper left: Density map of galaxies brighter than $I_C = 22.0$. Region is slightly bigger than MOSCA field of view. Larger points are galaxies brighter than $I_C = 20.0$. Cross shows position of candidate selected as an overdensity of galaxies. Squares show locations of slits for spectroscopy. Upper right: positions of cluster candidates (MF - dotted circles; CMR - thin solid lines) overlaid on I-band galaxy map for B-field. PSPC circumference is overlaid (dashed circle) and MOSCA field (square). Lower left: I-band image of MOSCA field shown above. Numbered circles are apertures of extracted galaxy spectra, listed in results tables (note: these differ slightly from slit positions, above, as some slits resulted in no spectrum and some in more than one). See text for further details. Lower right: CMD at position of cross in upper left panel.

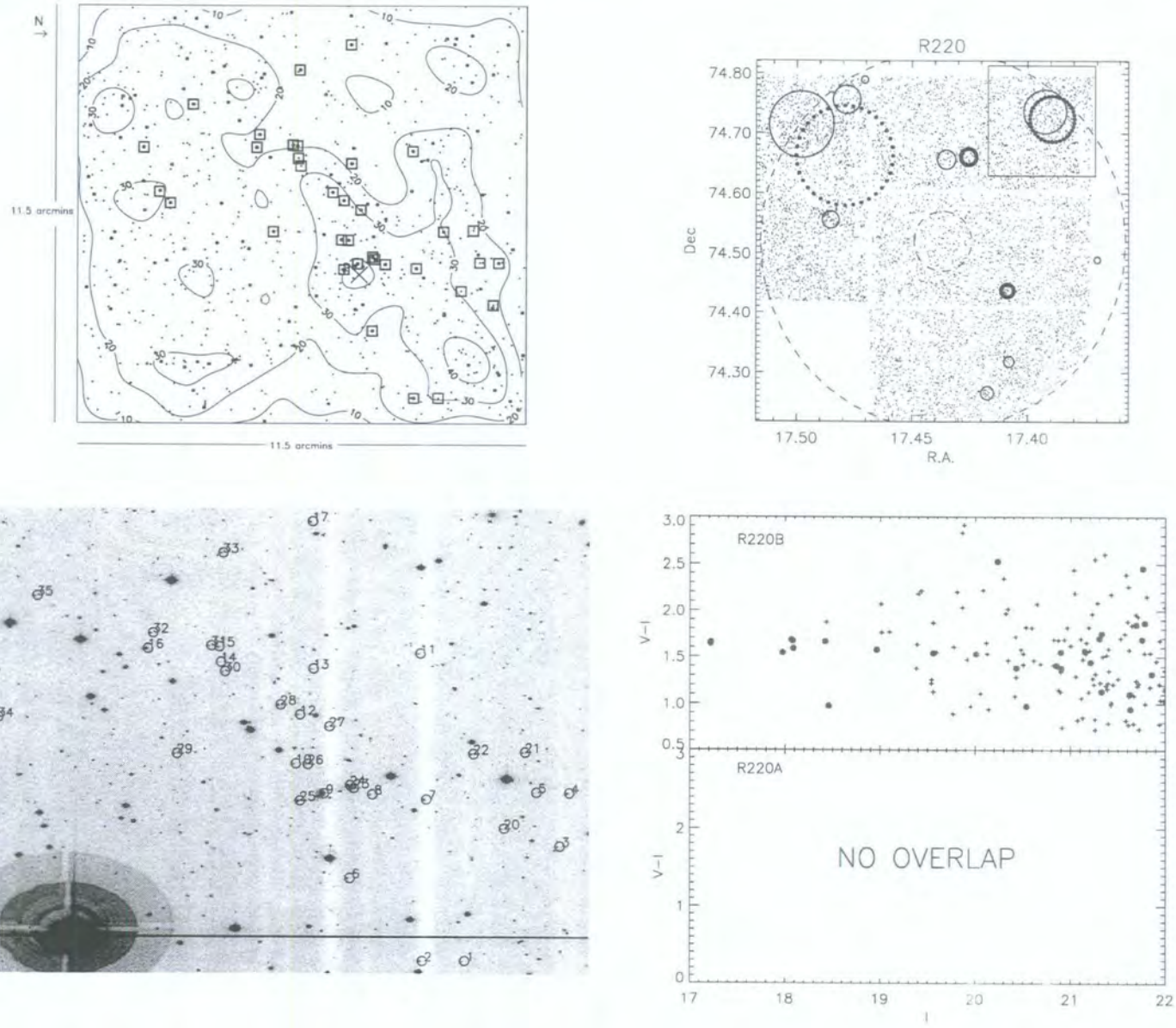

Figure 4.2: as previous figure, for field R220_2.

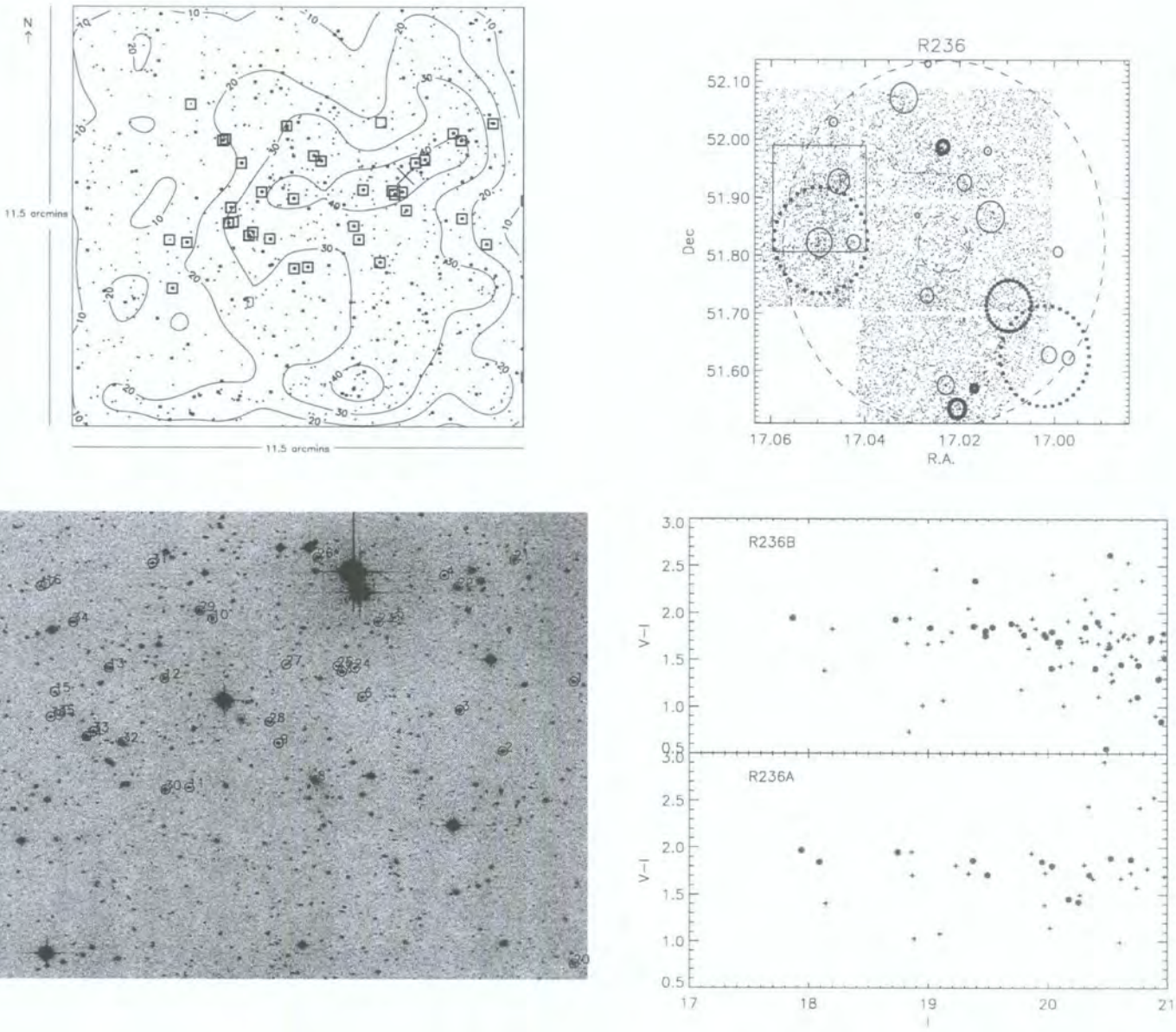

Figure 4.3: as previous figure, for field R236_1.

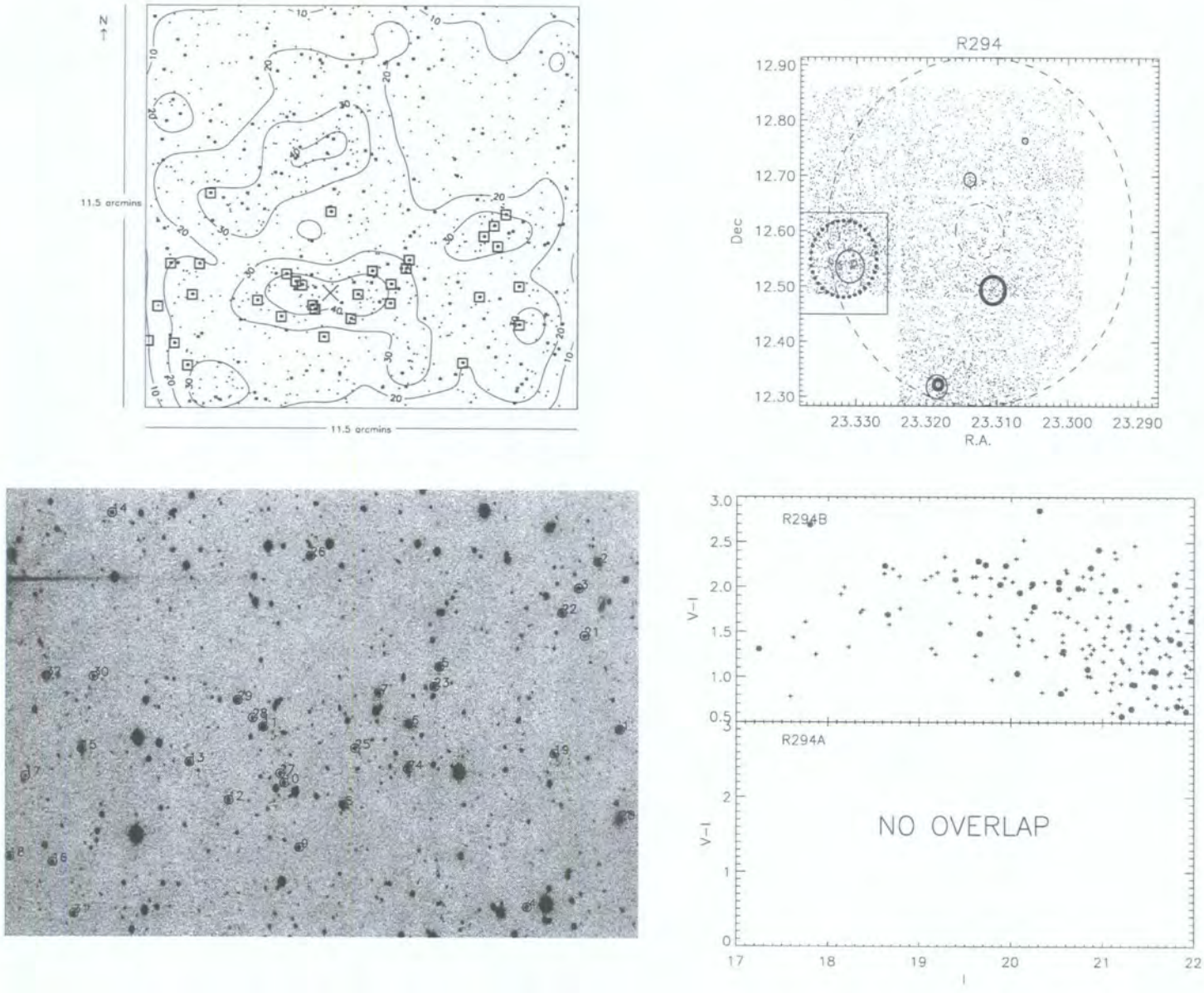

Figure 4.4: as previous figure, for field R294_1.

4.3 Spectroscopic Observations and Data Reduction

The spectra were secured over six nights of observations in July 2000 using MOSCA on the Calar Alto 3.5m.

Table 4.4: Log of observations of cluster candidates from Calar Alto

Night	Field	Mask	Exposure time (s)	Comments
26 – 27/07/00	R220_2	1	3 × 1800	poor seeing (low s/n)**
27 – 28/07/00	R110_1	1	3 × 1800	
28 – 29/07/00	R236_1	1	3 × 1800	
29 – 30/07/00	R220_2	2	3 × 1800	1 exposure corrupted
29 – 30/07/00	R236_1	2	3 × 1800	
30 – 31/07/00	R294_1	1	3 × 1800	
31/07 – 01/08/00	R220_2	1	3 × 1800	repeat of ** - improved data
31/07 – 01/08/00	R294_1	2	3 × 1800	

MOSCA is a focal reducer, installed at the Richey-Chretien Focus of the 3.5m telescope on Calar Alto. The reduction ratio of the optical system is 3.7, i.e. the effective focal ratio is f/2.7. This gives an image scale of 3 pixels per arcsec and a total FOV of 11x11 arcmin. A thinned CCD with 2048x4096 15 micron pixels is used as the detector.

The med-green grism was chosen. This gives a wavelength coverage of 4300 - 8200Å, with a central wavelength of 5500Å and a dispersion of around 2.5Å/ pixel and resolution of around 10ÅFWHM. This allows distinctive spectral features (see Figure 4.3.2) to be seen over a wide range of redshifts from $z \lesssim 0.1$ to $z \gtrsim 0.6$.

Before each night of observation, a series of bias frames (typically five) was taken. For the purpose of wavelength calibration (WLC) two different comparison arcs were observed. This was done to ensure an adequate number of emission lines over the full-wavelength range covered by the MOSCA med-green grism. A 15s exposure of the HgAr/Ne arc was taken. This was augmented by a 120s exposure of the Ar lamp using the 472/78 filter. The long exposure was used to make weak emission lines clearly visible, and the (BV-band) filter was used to suppress lines at the red end of the spectrum, which would otherwise become saturated. A combination of the HgAr/Ne spectrum and 100× the Ar spectrum was found to provide a good reference spectrum for WLC (hereafter, WLC refers to this composite arc spectrum image). So, such calibration frames were taken before twilight,

at the start of each run. Flatfield frames were taken using MOSCA's internal tungsten lamp. For the science observations, three exposures were made of each mask, each of 30 minutes duration. After each series of science frames, whilst the telescope was still pointing at the object, another HgAr/Ne frame was taken (although it was not needed, see later). This was done in case flexure in the instrument due to the telescope's different pointing position affected the arcs taken earlier in the evening (while the telescope was parked, and therefore pointing at zenith). The Ar arc was not repeated during the night as its longer exposure time added an unacceptable overhead.

4.3.1 Data Reduction

Data reduction was carried out using standard `IRAF` routines.

De-biasing

A Master-bias frame was made for each night, by median-combining all the bias frames for that night. Full 2D bias removal was necessary, as structure (appearing as broad banding) was visible in the individual bias frames. These master bias frames were subtracted from their relevant data frames, and overscan strip correction performed.

Flatfielding

Flatfielding performs two roles: to take out pixel-to-pixel variations due to intrinsic sensitivity differences in the detector, and to account for the way in which the slit is illuminated. The calibration frames taken for this purpose used the internal tungsten lamp. There are two main problems with using such a lamp for flatfielding. Firstly, the tungsten lamp is hot and therefore possesses a blackbody spectrum different from that of the night sky, which must first be removed before it can be used for flatfielding. Secondly, the lamp is located quite near to the CCD, and therefore the way in which the slits are illuminated is different from the way they are illuminated when pointed at the sky. Furthermore, imperfections in the machining of the slits result in variations in the illumination of the CCD. These could be compensated for by an *illumination correction*, described below. A number of experiments were tried to overcome these problems. To remove the blackbody spectrum of the tungsten, the `IRAF` task `apflatten` was used. This fits a high-order function along the spectral direction to each slit, simultaneously fitting each pixel in the spatial direction. A 35th order spline-3 was found to give a good fit to the lamp continuum. However, once this continuum had been removed, the counts in the flatfield towards

the ends of the spectrum were found to be quite low. This is bad because features of interest, such as Ca H+K absorption lines in a z$\sim$0.1 galaxy will lie very near the blue end of the spectrum. If the S/N in the flatfield is too low, noise will be added to these features. It was found that trying to use this flatfield just added noise to the spectrum.

The second use for the flatfield (illumination correction) was also investigated. The tungsten spectra were flattened as above (note: this process uses a fit to the shape of the spectrum simultaneously for each pixel in the spatial direction, and normalises them to the same level, therefore spatial information about the shape of the illumination across the slit is lost). The flattened tungstens were median-filtered in the spectral direction with a 20 pixel filter. This is to remove the attempt to correct pixel-to-pixel variation (which was found to add noise to the spectra), and to just try to account for the shape of the flatfield. The unflattened tungstens had a 1D function across each slit fitted to them. These slit functions were then multiplied by the flattened tungstens to provide the flatfield. This illumination correction is designed to improve the quality of the night-sky background subtraction (see below). It was found that this procedure did not significantly improve the background subtraction, and so flatfielding of the data was decided against.

Cosmic Ray Rejection

The three images for each mask were combined using `imcombine` in cosmic ray rejection mode. This did a good job of removing the cosmic rays, except for one mask where only two exposures were taken (three are necessary for successful cosmic ray rejection). Also, the routine `apall` (explained below) has a "`clean`" task, which attempts to remove cosmic rays. This was turned on in all cases, and did a good job of removing any remaining cosmic rays (and a fairly good job of removing them initially for the frame mentioned above). The processed 2D spectra were visually examined to ensure that emission lines were not removed, during this process.

Spectral Extraction

The `IRAF` routine `apall` was used for this task. In outline, a cross section through the spectra was taken (summming over 20 lines in the spectral direction). This makes the galaxy spectra stand out as peaks above the sky background. Apertures were defined for each galaxy, and also background apertures were defined either side of each galaxy (where possible - some galaxies lay very close to the edge of their slit). Note: slits can contain more than one galaxy, due to fortuitous placement. The background apertures

were defined as close as possible to the edge of the galaxy spectra, and kept as short as possible. This is because `apall` does not take account of the fact that the spectra may be tilted slightly, with respect to the columns of the CCD. The nightsky lines for subtraction are simply summed along a row, and subtracted from the galaxy flux on the same row. Hence, any tilt in the spectrum would result in the sky lines from one row being subtracted from the wrong part of the galaxy spectrum. All the galaxy spectra were found to be sufficiently well aligned with the CCD columns that the sky subtraction was not a problem. For one mask the spectra were tilted much more than the others, but by lowering the order of the fit to the shape of the background across the slit, sky subtraction was still reasonably successful. The galaxy spectrum was then traced as far as it was visible, along the spectral direction, the sky subtracted, and the result extracted to a 1D spectrum.

A similar procedure was carried out for the WLC arcs. The positions of the galaxy apertures and the galaxy traces were used as a references, but no background subtraction was carried out.

Wavelength Calibration

The WLC for each spectrum in the mask was carried out in the following way. Lines were identified with `identify` using a reference list for one arc in the mask. A 4th order chebyshev was fit in the dispersion direction to convert pixel coordinates to wavelength coordinates. The formal error on this fit was typically <1Å rms, but is really limited by the size of the resolution element (10Å). This solution was used as a reference to identify lines in the other spectrum in `reidentify`. This is an algorithm which tries to automatically identify lines in other slits assuming some zeropoint offset in the spectral direction from the previous solution (as the slits are at different locations on the mask), and assuming a roughly similar dispersion (it will differ slightly, due to distortions in the instrument). This task performs fairly well for most spectra, but it was necessary to reidentify some spectra from scratch, by hand, in a similar way to using `identify`. All solutions were verified by visual inspection. No flux calibration of the spectra was performed (as this is unnecessary for just calculating redshifts).

Once dispersion solutions were calculated, the reference spectrum transformation was applied to the corresponding science spectrum.

4.3.2 Spectroscopic Redshift Determination

All the wavelength-calibrated spectra were visually inspected to try to determine an approximate redshift where one was readily apparent. This method is probably biased to systems with clearly visible H+K lines, and probably to those which also have strong G-band absorption features. Note: this is not the final redshift quoted.

Next, the Fourier cross-correlation technique of Tonry & Davis (1979) was applied to the wavelength-calibrated spectra. This technique continuum-subtracts and Fourier transforms the galaxy spectrum and a reference template, applies high- and low-pass filtering, and looks for peaks in the cross-correlation function of the two.

The template used was a de-redshifted E/S0 (as used by the CNOC collaboration, courtesy of E. Ellingson), hence no emission lines were used in the initial redshift determination (emission line objects are considered below). Each mask was run through `fxcor`, and the redshift from the highest cross-correlation peak logged. Each spectrum was then de-redshifted using the `fxcor` redshift. The de-redshifted spectrum then had the position of prominent absorption lines (Ca H+K, G-band, H-beta and Mgb) and emission lines OII and Hβ overplotted. The spectrum was then visually inspected and a quality flag assigned to it, either: 2 - the redshift is confident; 1 - the redshift is less certain but looks compatible with the positions of the lines; or 0 - no redshift is possible (usually due to too low S/N).

Some spectra were also flagged for re-processing through `fxcor`, if the redshift was clearly wrong, and sufficient signal was present to get a better redshift estimate. The main reason for an incorrect redshift was the presence of large residuals from the subtraction of bright night sky lines. Note that in the Fourier cross-correlation, the direction (ie. absorption or emission) of lines is not taken into account; therefore, night sky residuals which approximate the positions of absorption features in the template can be confused.

Absorption lines in the galaxy spectrum were logged, and if a possible emission line was present, the 2D spectrum was inspected to check if the emission was a genuine galaxy feature, or a residual sky line.

For several spectra, for which the redshifts were readily apparent, and very strong emission was seen, the E/S0 template gave a poor redshift estimate. In this case an Sab/Scd template was substituted and found to give a much better fit. Emission line objects are clearly noted in the tables of results, below.

Furthermore, once groupings in redshift space had been located (§4.4.1), all the spectra

which failed to yield a redshift were re-examined to see if they were compatible with the redshift of any groupings. This yielded one extra redshift which had been missed previously.

Field	Number of Spectra		
	Class 0	Class 1	Class 2
R110_1	2	5	8
R220_2	14	7	14
R236_1	8	6	24
R294_1	7	8	17

Table 4.5: Summary of Spectral Quality. 2 - secure redshift; 1 - less confident; 0 - rejected.

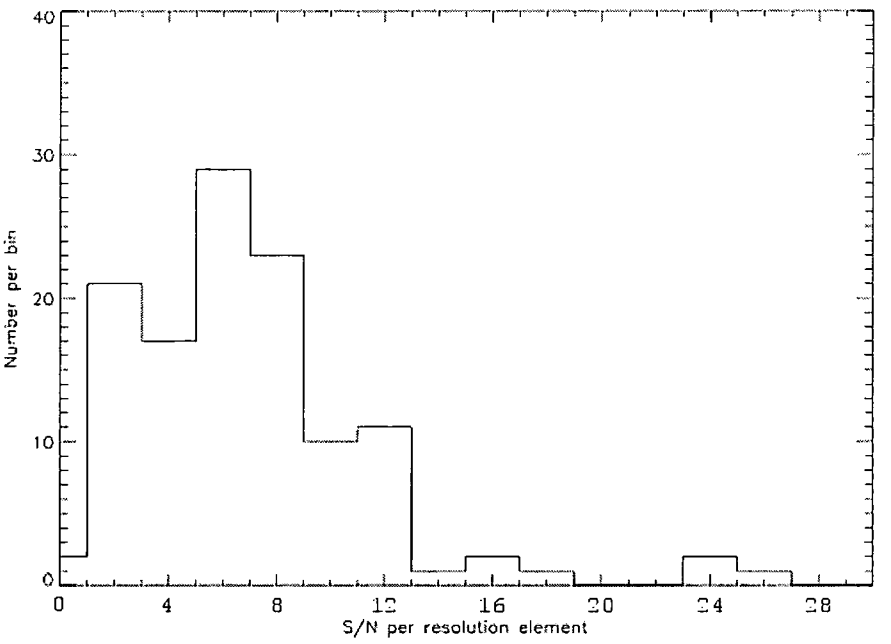

Figure 4.5: Histogram of S/N per 10Å resolution element, for all the spectra. A S/N of around 3 is typically sufficient to yield a redshift.

Table 4.6: Cluster Candidate R110_1, mask1

Spectrum Number[a]	I_{BEST}	V-I	SExtractor FLAG[b]	z	Δz (kms^{-1})	TDR[c]	Confidence[d]	Lines[e]
1	18.512	1.28	0	0.15078	167.788	5.04	1	H,K,Mgb
2	19.478	1.164	0	0.21132	167.216	4.93	2	H,K,G,Hβ(*em*),Mgb,Hα
3	18.807	1.401	0	—	—	—	0	
4	19.399	1.018	0	0.12877	111.410	7.18	2	H,K,Mgb,Hα
5	19.061	0.965	0	0.20590	179.222	4.90	1	H,K,Mgb
6	18.363	1.569	0	0.21847	148.330	11.69	2	H,K,G,Mgb
7	19.11	1.152	0	—	—	—	0	
8	17.384	1.422	2	0.22065	126.439	10.05	2	H,K,G,Hβ,Mgb
9	18.613	—[‡]	24	0.05247	236.459	4.96	1	H,K,G,Mgb
10	17.448	1.578	18	0.21740	88.620	19.08	2	H,K,G,Mgb,Hα
11	18.891	1.512	3	0.17425	381.831	3.72	1	H,K,G,Hβ,Mgb
12 (1a)	17.868	1.475	0	0.19644	138.245	6.84	2	H,K,G,Hβ,Mgb
13 (1a)	17.856	1.56	2	0.19594	99.380	15.68	2	H,K,G,Hβ,Mgb
14 (1a)	18.695	1.472	0	0.19651	150.636	9.15	2	H,K,G,Hβ,Mgb
15	18.679	1.261	0	0.18734	341.038	4.93	1	H,K,G,Hβ,Mgb

[a] Aperture number – label in brackets refers to group ID (see below)

[b] SExtractor FLAG – only objects with values <4 are retained in the final XDCS catalogue (see Chapter 2 for details)

[c] Tonry & Davies R parameter

[d] 2 – secure redshift; 1 – less confident; 0 – rejected

[e] Spectral features found by visual inspection. Hβ is in absorption unless otherwise stated

[‡] V-band object corrupted by cosmic ray (as indicated by SExtractor FLAG)

Table 4.7: Cluster Candidate R220_2, mask1

Spectrum Number[a]	I_{BEST}	V-I	SExtractor FLAG[b]	z	Δz (kms^{-1})	TDR[c]	Confidence[d]	Lines[e]
1	20.594	1.358	0	0.46556	235.109	4.24	1	G,Hβ,Mgb
2	19.499	2.034	0	0.46995	179.880	7.07	2	H,K,G,Hβ,Mgb
3	20.386	1.443	3	0.34478	267.242	4.90	1	H,K,Hβ
4	18.974	2.241	0	0.44490	135.212	8.48	2	H,K,G,Hβ,Mgb
5	20.884	0.977	0	0.16320	357.823	4.71	1	H,K,G
6	19.776	1.218	0	0.20864	76.124	6.406	2[†]	OII,Hβ(em),Mgb,Hα
7 (2a)	19.094	1.661	0	0.25974	174.097	9.88	2	H,K,G,Hβ,Mgb
8 (2a)	19.746	1.537	0	0.26269	226.063	7.96	2	H,K,G,Hβ,Mgb
9 (2a)	18.59	1.654	3	0.25894	103.578	14.01	2	H,K,G,Mgb,OII,Hα
10	19.786	1.256	0	0.05351	325.511	3.19	1[†]	H,K,G
11	20.195	1.34	0	—	—	—	0	
12	19.538	1.765	0	0.33694	163.836	9.80	1	H,K,G,Hβ,Mgb
13	20.402	0.905	0	—	—	—	0	
14	21.052	0.959	0	—	—	—	0	
15	19.199	1.729	2	0.34265	158.752	5.86	2	H,K,G
16	18.216	1.45	0	0.17925	115.004	7.92	2	H,K,G,Hβ,Mgb
17	19.639	1.32	0	—	—	—	0	
18	19.027	0.849	0	0.08128	243.733	5.87	1	H,K,G
19	19.717	1.354	0	—	—	—	0	

[a] Aperture number – label in brackets refers to group ID (see below)

[b] SExtractor FLAG – only objects with values <4 are retained in the final XDCS catalogue (see Chapter 2 for details)

[c] Tonry & Davies R parameter

[d] 2 – secure redshift; 1 – less confident; 0 – rejected

[e] Spectral features found by visual inspection. Hβ is in absorption unless otherwise stated

Table 4.8: Cluster Candidate R220_2, mask2

Spectrum Number[a]	I_{BEST}	V-I	SExtractor FLAG[b]	z	Δz (kms^{-1})	TDR[c]	Confidence[d]	Lines[e]
20	20.454	0.939	0	—	—	—	0	
21	20.179	1.69	0	—	—	—	0	
22	19.796	1.631	0	0.42996	238.252	4.92	2	H,K,Hβ,Mgb,OII
23 (2a)	18.178	1.639	3	0.25921	105.401	14.46	2	H,K,G,Hβ,Mgb
24 (2a)	18.689	1.667	3	0.26020	68.459	12.04	2	H,K,G,Hβ,Mgb
25 (2a)	18.546	1.588	0	0.25890	73.117	21.11	2	H,K,G,Hβ,Mgb
26	20.564	0.969	0	—	—	—	0	
27	20.25	1.469	0	—	—	—	0	
28	19.331	1.872	0	0.33824	139.260	9.88	2	H,K,G,Hβ,Mgb
29	20.194	1.403	0	—	—	—	0	
30	20.787	1.072	0	—	—	—	0	
31	20.29	1.743	3	—	—	—	0	
32	20.124	1.688	0	—	—	—	0	
33	19.339	2.468	0	0.25435	161.092	4.90	2	H,K,G,Mgb,OII
34	19.271	1.588	0	—	—	—	0	
35	20.242	1.391	0	0.32247	462.418	5.76	1	4000Åbreak

[a] Aperture number – label in brackets refers to group ID (see below)

[b] SExtractor FLAG – only objects with values <4 are retained in the final XDCS catalogue (see Chapter 2 for details)

[c] Tonry & Davies R parameter

[d] 2 – secure redshift; 1 – less confident; 0 – rejected

[e] Spectral features found by visual inspection. Hβ is in absorption unless otherwise stated

Table 4.9: Cluster Candidate R236_1, mask1

Spectrum Number[a]	I_{BEST}	V-I	SExtractor FLAG[b]	z	Δz (kms^{-1})	TDR[c]	Confidence[d]	Lines[e]
1	19.666	1.049	0	0.27667	190.864	4.82	2	H,K,Mgb,OII,Hα
2 (3a)	19.44	1.612	0	0.29721	141.738	13.21	2	H,K,G,Mgb,OII
3	18.58	1.38	0	0.17387	73.007	24.38	2	H,K,G,Mgb,Hβ
4	19.643	1.853	0	0.35303	136.441	5.79	2	H,K,G,Mgb,Hβ
5 (3b)	19.919[†]	1.884	0	0.34349	172.520	4.40	2	H,K,G,Hβ,Mgb
6 (3a)	19.342	1.69	0	0.30382	115.327	11.82	2	H,K,G,Mgb
7	19.732	1.064	0	0.17252	167.094	6.10	2	H,K,G,Mgb
8 (3b)	18.369	1.942	0	0.34427	119.157	13.16	2	H,K,G,Mgb,Hβ
9 (3a)	19.555	1.263	0	0.29716	261.829	4.24	2	H,K,G,Mgb,Hα
10 (3b)	19.046	1.678	2	0.34819	117.877	12.42	2	H,K,G,Mgb,Hβ
11	20.087	0.824	0	—	—	—	0	
12 (3a)	19.176	1.307	0	0.29954	166.899	5.65	2	H,K,G,OII,Hα
13 (3a)	—[‡]	—[‡]	0	0.29671	92.235	17.06	2	H,K,G,Mgb
14 (3a)	18.619	1.707	3	0.29663	73.527	20.00	2	H,K,G,Hβ,Mgb
15	19.448	0.602	0	0.39967	76.398	6.46	2[†]	Hα,Hβ(em),OII
16	18.804	1.199	2	—	—	—	0	
17	19.928	2.151	3	—	—	—	0	
18	19.324	1.926	0	0.40845	275.871	3.04	1[†]	H,K,G,Mgb,Hβ
19	21.249	0.931	0	—	—	—	0	

[a] Aperture number – label in brackets refers to group ID (see below)

[b] SExtractor FLAG – only objects with values <4 are retained in the final XDCS catalogue (see Chapter 2 for details)

[c] Tonry & Davies R parameter

[d] 2 – secure redshift; 1 – less confident; 0 – rejected

[e] Spectral features found by visual inspection. Hβ is in absorption unless otherwise stated

[‡] I-band image corrupted by cosmic ray
(this is not noted by the SExtractor FLAG as this parameter is measured from the V-band image)

Table 4.10: Cluster Candidate R236_1, mask2

Spectrum Number[a]	I_{BEST}	V-I	SExtractor FLAG[b]	z	Δz (kms^{-1})	TDR[c]	Confidence[d]	Lines[e]
20 (3b)	19.298	1.89	2	0.34710	201.586	6.26	2	H,K,G,Hβ,Mgb
21 (3b)	19.269	1.94	2	0.34912	90.516	14.53	2	H,K,G,Hβ,Mgb
22 (3b)	18.806	1.944	0	0.34637	108.762	13.92	2	H,K,Hβ,Mgb
23 (3b)	19.486	1.839	0	0.34868	101.140	15.03	2	H,K,G,Hβ,Mgb
24 (3b)	20.204	1.617	0	0.34533	150.188	8.49	2	H,K,G,Hβ,Mgb
25	21.027	1.07	0	0.31194	374.466	4.24	1	H,K
26	17.739	1.135	0	—	—	—	2	star
27	19.952	1.865	0	—	—	—	0	
28 (3b)	19.764	1.875	0	0.34695	112.469	12.55	2	H,K,G,Hβ,Mgb
29 (3b)	18.728	1.854	0	0.34781	74.759	19.64	2	H,K,G,Hβ,Mgb
30 (3b)	18.982	1.881	0	0.34733	166.769	7.96	2	H,K,G,Hβ,Mgb
31	20.213	1.4	0	—	—	—	0	
32	18.288	1.007	0	0.17632	150.815	5.14	2	OII,H,K,G,Mgb,Hα
33	19.664	1.311	0	0.27177	286.665	3.48	1	H,K,G
34	17.238	2.408	0	—	—	—	0	
35	21.529	1.806	0	0.30840	528.003	3.59	1	
36	20.14	1.157	0	0.30753	227.232	5.69	1	H,K,G,Mgb
37	20.641	1.502	0	—	—	—	0	
38 (3a)	20.086	1.634	0	0.30335	136.611	11.14	1	H,K,Hβ,Mgb

[a] Aperture number – label in brackets refers to group ID (see below)

[b] SExtractor FLAG – only objects with values <4 are retained in the final XDCS catalogue (see Chapter 2 for details)

[c] Tonry & Davies R parameter

[d] 2 – secure redshift; 1 – less confident; 0 – rejected

[e] Spectral features found by visual inspection. Hβ is in absorption unless otherwise stated

Table 4.11: Cluster Candidate R294_1, mask1

Spectrum Number[a]	I_{BEST}	V-I	SExtractor FLAG[b]	z	Δz (kms^{-1})	TDR[c]	Confidence[d]	Lines[e]
1	18.423	1.351	0	0.12522	179.947	7.22	2	H,K,G,Mgb
2	18.285	1.734	0	0.30395	74.329	15.96	2	H,K,G,Hβ,Mgb
3	19.667	1.954	0	0.57961	309.194	5.26	1	H,K,G,Hβ,Mgb
4	20.267	0.531	0	—	—	—	0	
5 (4b)	19.046	1.713	0	0.32571	118.619	14.24	2	H,K,G,Hβ,Mgb
6	18.086	1.309	0	0.12427	130.648	10.31	2	H,K,G,Hβ,Mgb
7 (4c)	19.228	2.233	0	0.45223	174.766	8.56	2	H,K,G,Hβ,Mgb
8 (4a)	18.308	1.608	2	0.26919	74.540	21.02	2	H,K,G,Hβ,Mgb
9	18.922	2.201	0	0.06476	617.654	4.57	1	H,K,G,Hβ,Mgb
10 (4c)	19.08	2.116	0	0.45408	128.151	11.56	2	H,K,G,Hβ,Mgb
11 (4c)	18.94	1.916	0	0.44350	173.832	6.90	2	H,K,G,Hβ,Mgb,OII
12 (4a)	18.991	1.58	0	0.26845	142.743	8.53	2	H,K,G,Hβ,Mgb,OII
13 (4b)	19.017	1.704	0	0.32172	78.432	20.51	2	H,K,G,Hβ,Mgb
14	19.943	1.653	0	—	—	—	2	star
15	19.788	0.796	0	0.25477	255.342	4.95	1	H,K,Mgb
16	19.027	1.28	0	0.16085	171.017	9.64	2	H,K,G,Hβ,Mgb
17	20.779	1.172	0	—	—	—	0	
18	19.253	2.187	0	0.14634	189.056	4.91	1	H,K,G,Mgb
19	19.538	1.794	16	0.46492	310.987	4.66	1	H,K,Hδ,G,Mgb

[a] Aperture number – label in brackets refers to group ID (see below)

[b] SExtractor FLAG – only objects with values <4 are retained in the final XDCS catalogue (see Chapter 2 for details)

[c] Tonry & Davies R parameter

[d] 2 – secure redshift; 1 – less confident; 0 – rejected

[e] Spectral features found by visual inspection. Hβ is in absorption unless otherwise stated

Table 4.12: Cluster Candidate R294_1, mask2

Spectrum Number[a]	I_{BEST}	V-I	SExtractor FLAG[b]	z	Δz (kms^{-1})	TDR[c]	Confidence[d]	Lines[e]
20	22.247	1.273	0	0.12895	171.313	4.98	1	H,K,Mgb
21	20.199	1.467	0	—	—	—	0	
22 (4b)	19.149	1.77	0	0.32547	178.939	4.19	2	H,K,G,Hβ,Mgb
23	19.393	1.758	3	—	—	—	0	
24	18.321	1.438	0	0.11081	531.952	2.13	1[†]	H,K,G,Mgb
25	19.689	2.08	0	0.45390	169.112	5.61	1[†]	H,K,G,Mgb
26	18.808	1.742	0	0.29590	95.335	12.49	2	H,K,G,Hβ,Mgb
27 (4c)	19.582	2.18	0	0.45478	124.981	6.53	2[†]	H,K,G,Hβ,Mgb
28	20.323	0.97	0	—	—	—	0	
29 (4c)	19.016	2.145	0	0.45381	184.131	7.37	2[†]	H,K,G,Hβ,Mgb
30	20.041	1.445	0	—	—	—	0	
31	19.473	1.456	0	—	—	—	0	
32 (4a)	18.76	1.132	0	0.26438	151.828	3.01	2[†]	OII,Hα,Hβ(em),D4000,G

[a] Aperture number – Label in brackets refers to group ID (see below)

[b] SExtractor FLAG – only objects with values <4 are retained in the final XDCS catalogue (see Chapter 2 for details)

[c] Tonry & Davies R parameter

[d] 2 – secure redshift; 1 – less confident; 0 – rejected

[e] Spectral features found by visual inspection. Hβ is in absorption unless otherwise stated

The tables show measurements from the spectra. The R parameter of Tonry & Davis (1979) is a goodness of fit measure of the redshift obtained by cross-correlation in Fourier space. All redshifts were confirmed by visual inspection, by overplotting the spectral features shown in Figure 4.3.2 on the de-redshifted spectra. In order to be considered a confident redshift, two or more spectral lines had to be clearly visible and other features had to have some good reason for not being seen (eg, strong sky residuals concealing a feature which should have been present). The "confidence" column indicates the confidence in the redshift measurement following this method. If the primary maximum gave a poor fit - which occurred mainly due to inadequate sky subtraction (and is particularly common in mask 2 of R294_1, due to the spectra being skewed), then secondary maxima were selected and the same procedure followed. Night sky residuals is also the main reason for some spectra with reasonably high ($\gtrsim$3) TDR values being rejected. The cross-correlation method attempts to fit these residuals to spectral features in the galaxy template.

Table 4.13: Galaxy Groupings in Redshift Space

Field	Galaxy grouping	Centroid[a] α (J2000)	Centroid[a] δ (J2000)	N[b]	N_{TOT}[c]	median z	Δz[d]	N^e_{Absp}
R110_1	1a	14 28 27.9	33 05 24	3	8(13)	0.196	<0.001	3
R220_2	2a	17 23 25.1	74 43 45	7	14(21)	0.260	0.003	5
R236_1	3a	17 02 59.2	51 53 25	6(7)	24(30)	0.297(0.297)	0.007(0.007)	3(4)
R236_1	3b	17 02 52.4	51 54 00	11	24(30)	0.347	0.004	11
R294_1	4a	23 20 00.2	12 32 06	3	17(25)	0.268	0.001	1
R294_1	4b	23 19 48.0	12 32 58	3	17(25)	0.325	0.003	3
R294_1	4c	23 19 55.6	12 32 20	5	17(25)	0.454	0.010	4

[a] Centroid of members of grouping, using class 2 redshifts.

[b] Number of galaxies in grouping – class 2 spectra (class 1 & 2 spectra).

[c] Total number of class 2 (class 1 & 2) spectra in field.

[d] Maximum redshift separation between a galaxy in the grouping and the median redshift of the grouping.

[e] The number of absorption line only (ie. no emission) galaxies in the grouping.

Note: galaxies must be within 1500 kms^{-1} in the rest-frame, at the median redshift, to be considered members of the grouping (see text).

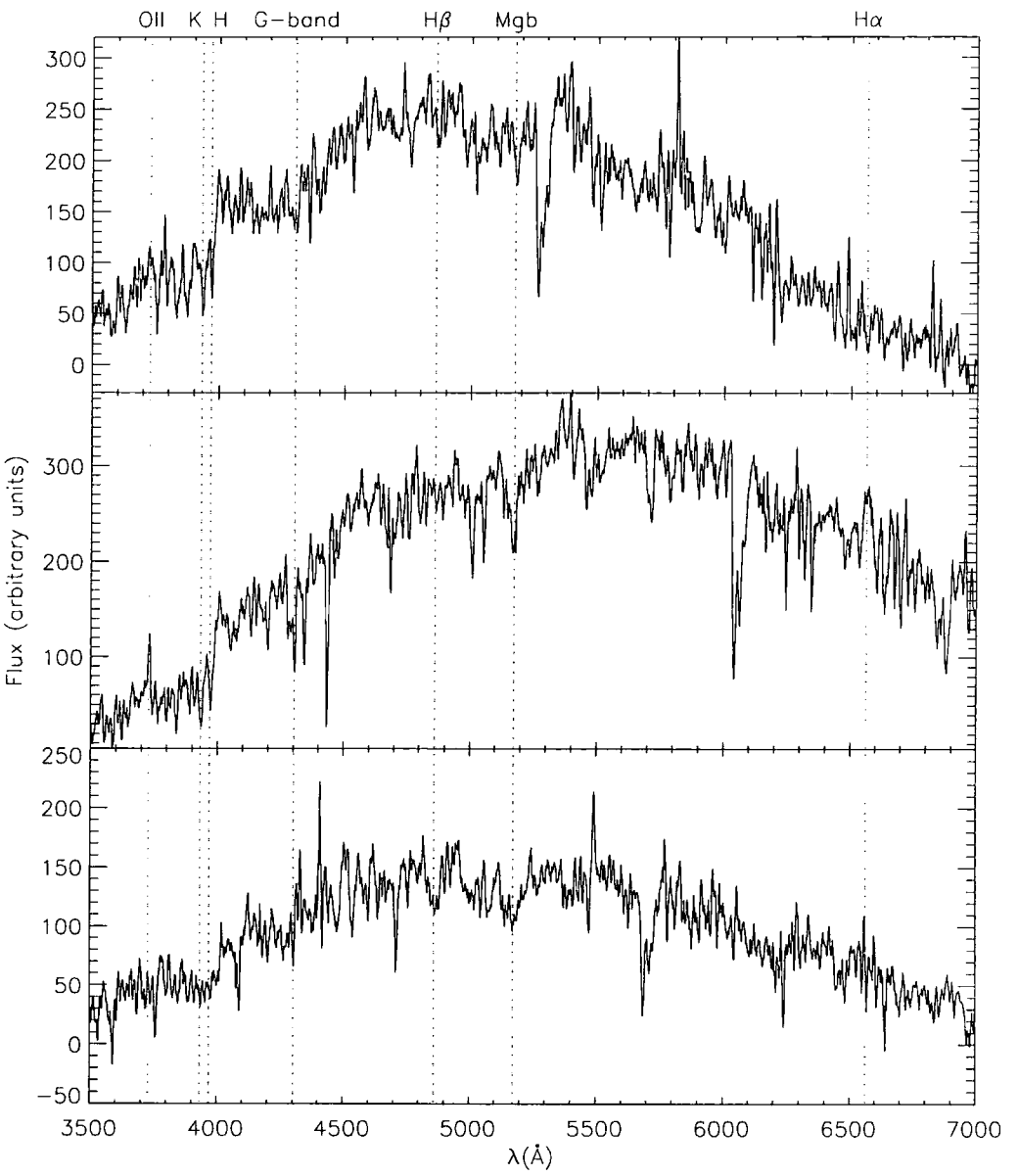

Figure 4.6: Representative de-redshifted spectra. From top to bottom: spectrum with confident redshift; spectrum with confident redshift and emission lines; spectrum with less confident redshift.

4.4 Analysis of Redshifts

Groupings in redshift space were extracted by searching for 3 or more secure redshifts separated by 1500 kms^{-1} or less. This is the same method adopted by Holden et al. (1999) and corresponds to 3 times typical cluster velocity dispersions they measure. It should be noted that a larger value was also tried, but 3σ clipping (described later) removed any extra galaxies added. The results of groupings found by this technique are illustrated in Figure 4.8 and analysed below.

4.4.1 Significance of Clustering in Redshift Space

Ramella et al. (2000) and Holden et al. (1999) used similar techniques to assess the significance of cluster clustering in redshift space. Ramella et al.'s (2000) method is followed here. The selection function was calculated as follows. Figure 4.7 shows the number of galaxies for which redshift measurements were possible, as a function of magnitude. Henceforth, only secure redshifts will be considered. Note that all cluster members are class 2 (ie. secure) redshifts, except one which is class 1, in the whole sample. Of the 121 spectroscopic targets, 61 resulted in secure redshifts, and a further 26 with less secure measurements. Two of these objects were stars.

The majority of galaxies which fail to yield a redshift are fainter than $I_c = 20.0$.

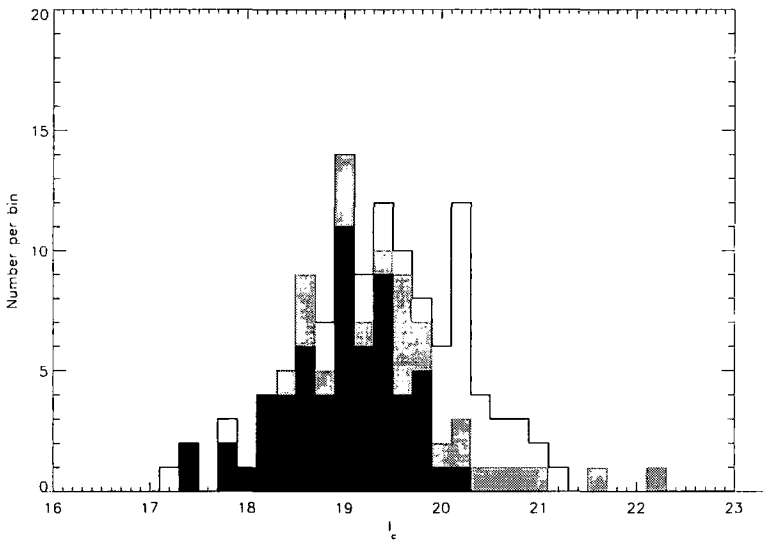

Figure 4.7: The I-band magnitude distribution of galaxies for which spectroscopy was attempted. The empty histogram is galaxies for which no redshift was determined; the black histogram is galaxies with confident redshifts; and the grey histogram is galaxies with less confident redshifts.

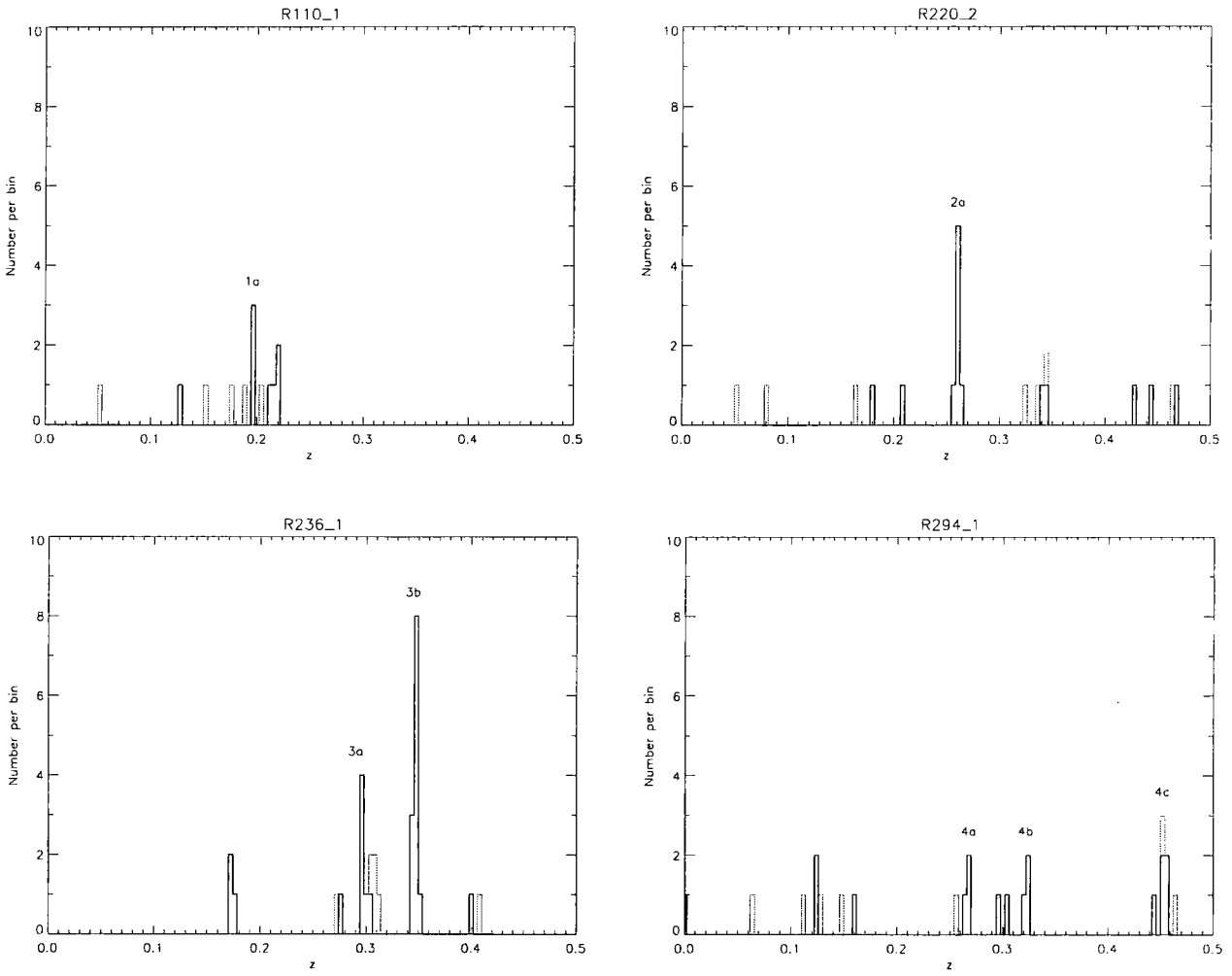

Figure 4.8: Large scale redshift distributions for cluster candidates: R110_1 (upper left), R220_2 (upper right), R236_1 (lower left), R294_1 (lower right). Line thickness indicates confidence in the redshifts. Bold lines are confident redshifts. The bin size is 0.004, which corresponds to a rest frame velocity of 1200 to 800 kms^{-1} at the left and right sides of the plot, respectively.

As with the 2D data in Chapter 2, it is important to model the clustering of field galaxies, when constructing mock galaxy distributions. By using the Canada France Redshift Survey (CFRS, Lilly et al. 1995) to construct a simulated field redshift distribution (as was done by Holden et al. 1999) and bootstrap resampling sets of galaxies, an estimate can be made of the fraction of spurious clustering detected in redshift space. Sets of 15 galaxies were extracted - the mean number per field (2 masks) for which confident redshifts were secured. 10000 galaxy sets were generated, applying bootstrap resampling, and the fraction of sets containing a grouping of more than 4 galaxies within 1500 kms^{-1} of their median redshift found. This occurs by chance ~6% of the time. For field R110_1, only 3 galaxies were found within this velocity difference, but fewer than average redshifts (8) were obtained (due to only one; rather than two masks being used). The velocity difference between these 3 is less than 1000 kms^{-1} . This also occurs about 6% of the time, and is therefore approximately as significant. If the velocity difference is reduced to 1000 kms^{-1} , the likelihood of finding 4 or more galaxies this close together, in an observation of a 15 galaxy set is only 2%. These numbers are used as a guideline to the significance of groupings in redshift space.

Ramella et al. (2000) take this technique further by trying to reproduce more accurately the magnitude selection function. To do this they take the histogram of magnitudes for which spectra were obtained and divide this by the total number of galaxies in the same area in the same magnitude bin (ie. the histogram shown in Figure 4.7 is divided by the field galaxy number counts - Figure 2.15 - the result is shown in Figure 4.9).

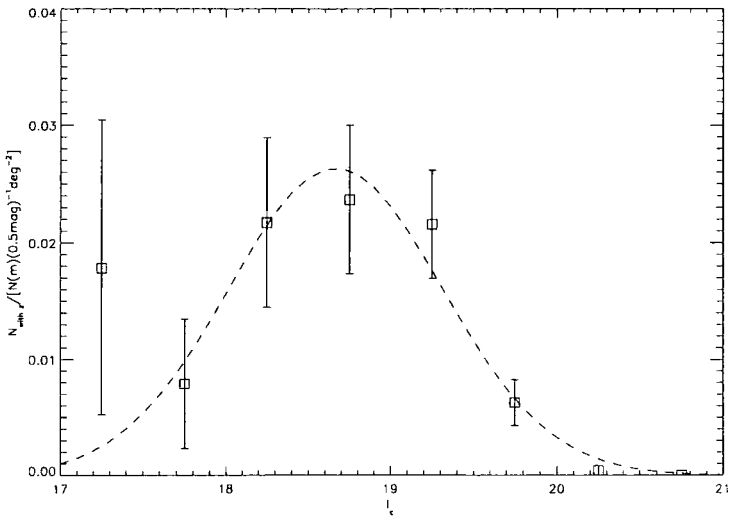

Figure 4.9: The function $s(m)$

If the luminosity function is universal and the local normalistion is the same everywhere (ie. no clustering), then the redshift distribution is given by:

$$N(z) = \frac{dV(z)}{dz} \int_{m_1}^{m_2} f[L(m,z)]s(m)dm \tag{4.1}$$

(Ramella et al. 2000) where dV is the volume element given in Equation 2.17, m_1,m_2 are the magnitude limits and f is the Schechter LF given in Chapter 2. Applying the selection function, s(m) gives the redshift distribution shown in Figure 4.10. Ramella et al. (2000) note that using such a distribution gives a false impression of the significance of groupings, as the clustering in redshift space must be accounted for. In order to do this, the CFRS is again bootstrap resampled, but this time using the magnitude selection function $s(m)$. In Ramella et al.'s (2000) method, they compare the N(z) distribution of their data with that of the CFRS using their selection function, and state that a Kolmogorov-Smirnov test shows the two datasets have similar distributions. Using the XDCS spectroscopic sample, however, a KS test shows the bootstrapped CFRS N(z) and the N(z) in Figure 4.10 are significantly different at the >90% level. It appears that this is because a larger fraction of the redshifts in the XDCS sample are cluster members. The Ramella et al. (2000) sample targeted higher redshift candidates, and so recovered a lower fraction of cluster members than the data presented here (most of the XDCS cluster candidates lie in the range $0.2<z<0.4$). Therefore Ramella et al.'s (2000) data follow the CFRS N(z) as most of their data are field galaxies (so it is correct when they state that magnitude selection is the main process leading to the inclusion of galaxies in the sample). In the XDCS sample however, significant groupings of 6 or more redshifts (more than the in individual groupings in the Ramella et al. (2000) data) are present, and thus the total (cluster + field) sample is not represented by the field survey of the CFRS. This difference in N(z)'s provides reassurance that significant clusters have been found.

Using Gaussian $s(m)$ leads to different probabilities of false detections. For n_{req}=4, P(false)=0.19; and for n_{req}=5, P(false)=0.03. This illustrates that magnitude selection has a big effect on the significance assigned.

To summarise these tests: the CFRS has been used to simulate the redshift distribution of field galaxies. Two different magnitude selection functions have been used to sample this survey. Bootstrap resampling of the data is used to calculate the probability, P(false), of incorrectly identifying a grouping of n_{req} galaxies in redshift space - the galaxies being selected in the same way as for the MOSCA targets. For the simplest selection function (a step function in magnitude, selecting galaxies brighter than

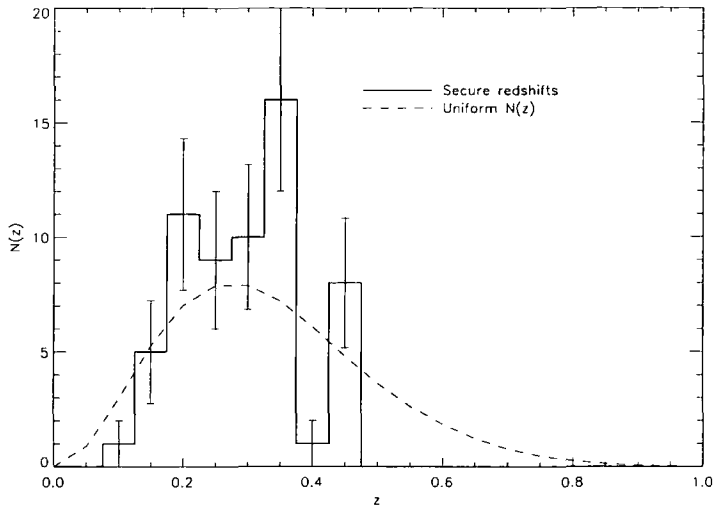

Figure 4.10: The redshift distribution function. The dashed line shows the N(z) described by Equation 4.1.

m_{lim}), P(false)≈0.06 for n_{req} =4. For the best-fit Gaussian magnitude selection function, P(false)≈0.19 for n_{req} =4, and P(false)≈0.02 for n_{req} =5.

These are the most recent techniques used in the literature for estimating the significance of redshift groupings found from optical cluster surveys. However, there are several problems with them. Firstly, using the CFRS to model the field does not take any account of the presence of groups within it. Thus, for finding the lowest velocity dispersion systems, which will be numerous in any wide-field survey (and therefore the CFRS), these methods underestimate the significance of systems found. Secondly, not all the available information is used. The most basic spectral properties (ie., whether or not the cluster members possess emission lines) and the colours can be used to infer the types of galaxies in the sample. Absorption line systems with red colours at the given redshift are highly indicative that a galaxy is of early-type. Since, these systems dominate the cores of known clusters, but are much less common in the field, their presence increases the likelihood of a cluster. This technique, however, would be biased against systems not containing early-type galaxies.

It should be noted that using a mean $N(z)$ from many fields would tend to overestimate the significance of clustering found in any one pencil beam survey, especially if galaxies lie in sheets along the line of sight.

By taking the field galaxy luminosity function from the CNOC2 survey (Lin et al. 1999), the expected number of early-type galaxies in a given volume can be calculated. Lin et al.'s (1999) parameters for the R_C-band luminosity function in the q_0=0.1 cosmology are taken. This is a Schechter LF with two additional parameters to model the evolution in luminosity and density. Lin et al. (1999) state that to convert their LFs to another band, a good approximation is to just apply an appropriate offset in M* based on the mean rest-frame colour for that galaxy type. Thus, to calculate the LF at z=0.3 for early-type galaxies, a rest-frame colour of R_C-I_C=0.71 is used (Kodama & Arimoto 1997) to correct M* to the I_C-band, along with a correction for the different value of h ($+5\log h$). The value of $\Phi^\star$ is taken from the R_c value, only correcting for the h difference, and applying the evolutionary parameters P and Q (Table 2, Lin et al. 1999) to correct to a redshift of 0.3. The difference in $\Phi^\star$ over the range of interest for the extreme XDCS spectroscopic candidates (ie., $0.2 \lesssim z \lesssim 0.5$) is less than a factor of 2, and so, for simplicity, a fiducial redshift of 0.3 is used here. This results in a space density of early-type galaxies in the field at redshift 0.3 of 0.04 Mpc^{-3}.

The number of galaxies in each redshift grouping showing only absorption features is given in Table 4.13. Since these systems do not show emission lines and have colours consistent with early-type galaxies at the cluster redshift (Table 4.6), these are taken to be early-type galaxies. Now, a generous estimate of the volume from which each of these redshift groupings is drawn is to take an angular size of 5 arcmins (approximately the maximum separation on the sky between galaxies in the same redshift grouping) at a redshift 0.3, and assume the volume is a sphere of this radius (this is about the same size as given by a line-of-sight velocity difference of a 1000 kms^{-1} , again a generous value for these groupings). This translates into a volume of $\approx$ 8 $\mathrm{h}^{-1}\mathrm{Mpc}^3$. Since, the space density of early-type galaxies in the field at this redshift is of 0.04 $\mathrm{h}^{-1}\mathrm{Mpc}^3$, the expected number in such a volume is 0.32. Assuming the field can be modelled by a Poisson distribution with this expectation value, the likelihood of finding 11 early-type galaxies (the maximum found - candidate 3b) is only $\approx 1\times10^{-8}$. The likelihood of finding 1 (the minimum - candidate 4a) is 25%; and the likelihood of finding 3 (the minimum of all the remaining candidates) is 0.3%.

This argument is an over-simplification as firstly it assumes the field can be modelled as a Poisson distribution, which is not strictly correct because of clustering, but not a bad approximation (it just raises the expectation value slightly). Secondly, the candidates were selected to be overdense and contain a (possibly weak) CMR. This means the fields

selected were not typical regions of space. However, selecting galaxies on the CMR was not guaranteed to select early-type galaxies at the same redshift, but this is the result which was found from the spectroscopy. Therefore the method is still valid. Thus, by this simple argument, it seems reasonable to assume that all the groups containing at least 3 early-type galaxies are significant. This method therefore rejects grouping 4a (which contains three galaxies within 0.01 in redshift; but only one of these is early-type). In summary, all the redshift space groupings are found to be significant by this technique, except candidate 4a which contains 3 galaxies, but only 1 of which is early-type (ie. red and emission-free). This candidate is found to be significant by the previous two methods which do not take colour/ type into account. Clusters of this nature (ie. not dominated by early-type galaxies) have not been observed before, so this system must be treated cautiously.

4.4.2 Cluster Velocity Dispersion Estimates

The cluster redshift and velocity dispersion were calculated following Beers, Flynn & Gebhardt (1990). They recommend using the median and standard deviation when dealing with tiny (n$\sim$5) datasets. Only the secure redshifts were considered. Redshifts within $\sim$2000kms^{-1} of the peak in the redshift histogram were extracted and the median value was taken to be the cluster redshift. The standard deviation was computed, and any value exceeding 3 standard deviations from the median excluded (this was only the case for the clusters in field R236_1: one value was rejected from each), and the standard deviation then re-computed. This was then transformed to the velocity dispersion in the cluster's rest-frame. The confidence interval for the velocity dispersion was found by applying the statistical jack-knife technique to the data (Carlberg et al. 1996, for example). This simple resampling technique uses "pseudo-values" δ_i of the data, by calculating the difference between a statistical measure, f, calculated for the whole dataset, and for the dataset with one value removed $\delta_i = f(x_1, ..., x_n) - f(x_1, ..., x_i, x_{i+1}, ..., x_n)$. The estimate of the variance is $[n/(n-1)\sum_i \delta_i^2]^{1/2}$ (Efron 1981). For very small N ($\sim$ 3) this error estimate is likely to be highly biased as only two data points are being resampled each time and the factor of $\sqrt{n/(n-1)}$ is likely to be an underestimate. These values must be treated cautiously for the three groupings with only 3 galaxies.

Table 4.14: Cluster Velocity Dispersion Estimates. Columns are: ID of redshift grouping; Field ID; Number of galaxies (N) used in redshift determination; velocity dispersion (σ_z); velocity dispersion in cluster rest-frame; and error on this quantity from jack-knife estimate (see text). This error estimate is likely to be biased in the presence of very small N (ie. $\sim$3), and so such error estimates should be treated cautiously. Most of the more reliable systems show velocity dispersions in the range 300 kms^{-1} – 700 kms^{-1} , typical of massive groups and low - intermediate mass clusters.

Grouping ID	Field	N	z	σ_z	σ_v^{rest} (kms^{-1})	$\Delta\sigma_v^{rest}$ (kms^{-1})
1a	R110_1	3	0.196440	0.00031	78	95
2a	R220_2	7	0.259740	0.00143	341	346
3a	R236_1	6	0.297210	0.00315	728	504
3b	R236_1	11	0.347100	0.00179	398	262
4a	R294_1	3	0.268450	0.00259	612	750
4b	R294_1	3	0.325470	0.00224	506	620
4c	R294_1	5	0.453810	0.00467	962	1051

4.4.3 Comparison of Significant Redshift Groupings with Cluster Candidates

Now that the groupings in redshift space have been identified and their significances assessed, the final step is to compare these with the candidates detected with the cluster-finding algorithms. Firstly, a simple comparison will be made by just finding the nearest candidate in the catalogues (Tables 4.2 and 4.3) with the centroids of the groupings found with MOSCA (Table 4.13). These are tabulated below for the MF algorithm (Table 4.15) and for the CMR algorithm (Table 4.16).

One candidate is found in each field by the MF, despite the fact that in redshift space, multiple groups are seen in fields R236_1 and R294_1. This is due to a fundamental limitation of the MF - it is unable to disentangle projections along the line-of-sight. Comparing the estimated redshifts with the spectroscopic measurement, for the two isolated groups the offset is Δz=0.143 and 0.269 (for R110_1 and R220_2, respectively). For the multiple systems, the estimated redshift is closer to the spectroscopic redshift of each individual, but in neither case intermediate between the spectroscopic redshifts. For field R236_1, the redshift offset is smaller than Δz=0.1 for both groups, but the estimated redshift is *higher* than the measured redshift for both. For R294_1 the estimated redshift is always *lower* than the measured redshift of each group.

For the CMR-finder, the offset between measured and estimated redshift for the two isolated groups (R110_1 and R220_2) is $\Delta z \leq 0.05$ for both, a substantial improvement over the MF accuracy. For the multiple systems, although only one estimated redshift is given for each field, in the table (for the most significant candidate), these candidates were flagged as line-of-sight-projections in Table 4.3). The estimated redshift of the most significant CMR candidate is always intermediate between the spectroscopic redshifts, and always $\lesssim$0.1. Now, the full catalogues (described in Chapter 3) may be examined for these projected systems, to see how well these agree with the spectroscopically determined groups.

The full CMR catalogues in the region of the R236_1 and R294_1 fields are given in Table 4.17. The candidates are split between A and B rotation results for R236_1, as here the two rotations overlap[6]. This is not the case for R294_1. The cross-correlation analysis showing the offset of each CMR candidate from each MOSCA candidate (position given by centroid of redshifts), and their respective redshifts, is given in Table 4.18.

[6]R110_1 also has overlapping A and B rotation, although the V-band A-rotation data is slightly trailed and so rejected from this analysis.

Field	ID	MF Candidate ID	Separation[a] (arcmin/ Mpc)	z^b_{spec}	z^c_{est}	Δz^d
R110	1a	mfJ142824.2+330538	0.803/0.16	0.196	0.053	0.143
R220	2a	mfJ172321.8+744326	0.372/0.09	0.260	0.529	0.269
R236	3a	mfJ170257.8+514935	3.838/1.04	0.297	0.440	0.143
R236	3b	mfJ170257.8+514935	4.495/1.35	0.347	0.440	0.093
R294	4a	mfJ231954.5+123256	1.626/0.41	0.268	0.232	0.036
R294	4b	mfJ231954.5+123256	1.582/0.46	0.325	0.232	0.093
R294	4c	mfJ231954.5+123256	0.660/0.23	0.454	0.232	0.222

Table 4.15: Nearest MF candidate to each MOSCA group

[a] Separation between the centroid of the spectroscopic grouping and the nearest MF candidate in arc minutes and physical distance (Mpc) at z_{spec}.

[b] Spectroscopic redshift of the former grouping.

[c] MF estimated redshift [d] Difference between these two redshifts.

The accuracy of the estimated redshifts, Δz is somewhat larger, for the first three groupings, than the average error found from Chapter 3 of $\Delta z \approx 0.08$.

Field	ID	CMR Candidate ID	Separation (arcmin/ Mpc)	z_{spec}	z_{est}	Δz
R110	1a	cmJ142812.0+330736	3.995/0.81	0.196	0.160	0.036
R220	2a	cmJ172333.0+744410	0.670/0.17	0.260	0.210	0.050
R236	3a	cmJ170244.2+515539	3.228/0.88	0.297	0.310	0.013
R236	3b	cmJ170244.2+515539	2.092/0.63	0.347	0.310	0.037
R294	4a	cmJ231951.2+123208	2.187/0.56	0.268	0.370	0.102
R294	4b	cmJ231951.2+123208	1.147/0.33	0.325	0.370	0.045
R294	4c	cmJ231951.2+123208	1.082/0.38	0.454	0.370	0.084

Table 4.16: Nearest CMR candidate to each MOSCA group. Columns as for previous table.

The purpose of this is to enable the closest match in projected and redshift space to be located. To illustrate this, Figure 4.11 shows this data projected into 2D along a line of constant declination (so the R.A. offset gives the approximate sky-plane offset). It can be seen that for R236_1, both the A and B catalogues identify 3 candidates at approximately the same redshifts: two close to the MOSCA groups and one at slightly higher redshift. This illustrates that agreement between the A and B redshift estimates is good, and the agreement with the spectroscopic redshifts is also good ($\leq$0.05 - Table 4.18). The possibility of a higher redshift candidate, not reached by the depth of the MOSCA spectroscopy, is likely given that it is identified independently in both rotations, and because the lower redshift groups agree so well with the spectroscopy. For R294_1, two candidates are found. Given that the lowest redshift of the three MOSCA groups in this field (4a) is not significant from the space density of early-type galaxies analysis (and won't be found by the CMR algorithm, because it does not contain significant numbers of early-type galaxies), the most likely interpretation is that the CMR-finder detects the two highest redshift groups and underestimates the redshifts of both (albeit by only $\lesssim$0.08). Thus, the candidates from the full catalogue in Table 4.18 are naturally associated with the nearest groups in 2D space, and these are then found to be also the nearest in redshift space. Therefore, the CMR finder performs excellently, correctly finding and separating all the systems identified spectroscopically.

Field	CMR candidate ID	z_{est}	σ
R236A	cmJ170240.9+515512	0.270	5.15
R236A	cmJ170242.7+515222	0.470	4.35
R236A	cmJ170244.2+515539	0.310	5.55
R236B	cmJ170248.5+515051	0.390	4.55
R236B	cmJ170250.6+515506	0.300	6.85
R236B	cmJ170252.1+515717	0.490	4.85
R294B	cmJ231945.8+123304	0.270	4.85
R294B	cmJ231951.2+123208	0.370	5.05

Table 4.17: Groups from full CMR-catalogue for those systems flagged as "projections"

The velocity dispersions of the detected groups are now plotted against their integrated luminosity of early-type galaxies, corrected for passive evolution: the L_E measure (Chapter 2). These are compared with data from the most X-ray luminous z$\sim$0.2 sample of Smail et al. (1998). Smail et al. (1998) measured X-ray temperatures rather than

Field	ID	CMR Candidate ID	Separation (arcmin/ Mpc)	z_{spec}	z_{est}	Δz	σ	Field
R236	3a	cmJ170240.9+515512	3.336/0.91	0.297	0.270	0.027	5.15	R236A
R236	3a	cmJ170242.7+515222	2.751/0.75	0.297	0.470	0.173	4.35	R236A
R236	3a	cmJ170244.2+515539	3.228/0.88	0.297	0.310	0.013	5.55	R236A
R236	3a	cmJ170248.5+515051	3.044/0.83	0.297	0.390	0.093	4.55	R236B
R236	3a	cmJ170250.6+515506	2.143/0.58	0.297	0.300	0.003	6.85	R236B
R236	3b	cmJ170240.9+515512	2.138/0.64	0.347	0.270	0.077	5.15	R236A
R236	3b	cmJ170242.7+515222	2.212/0.66	0.347	0.470	0.123	4.35	R236A
R236	3b	cmJ170244.2+515539	2.092/0.63	0.347	0.310	0.037	5.55	R236A
R236	3b	cmJ170248.5+515051	3.196/0.96	0.347	0.390	0.043	4.55	R236B
R236	3b	cmJ170250.6+515506	1.137/0.34	0.347	0.300	0.047	6.85	R236B
R236	3b	cmJ170252.1+515717	3.288/0.99	0.347	0.490	0.143	4.85	R236B
R294	4a	cmJ231951.2+123208	2.187/0.56	0.268	0.370	0.102	5.05	R294B
R294	4b	cmJ231945.8+123304	0.539/0.16	0.325	0.270	0.055	4.85	R294B
R294	4b	cmJ231951.2+123208	1.147/0.33	0.325	0.370	0.045	5.05	R294B
R294	4c	cmJ231945.8+123304	2.496/0.87	0.454	0.270	0.184	4.85	R294B
R294	4c	cmJ231951.2+123208	1.082/0.38	0.454	0.370	0.084	5.05	R294B

Table 4.18: Cross-correlation of full CMR catalogue with MOSCA groups. The closest matches in projected space are found to be closest in redshift space, showing the excellent resolution and accuracy of the CMR technique.

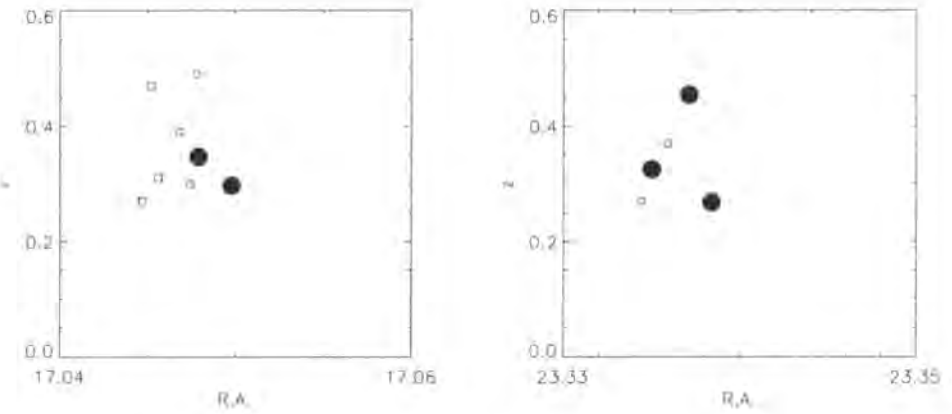

Figure 4.11: R.A. vs z (declination slice) plot for MOSCA groups and CMR candidates (R236_1 (left) and R294_1 (right). Filled circles are MOSCA groups (note: the lowest-z point in the R294_1 is not significant in terms of early-type galaxies); open circles are CMR candidates from B-rotation data, and open squares are CMR candidates from A-rotation data. For R236_1, two candidates in each rotation are seen near the spectroscopically determined group. Also, a higher redshift candidate is seen in both rotations. The spectroscopy may not go deep enough to have found members of this group. In R294_1 two candidates are found within $\Delta z \lesssim 0.08$ of the most significant (ie. the two highest redshift) spectroscopic groups.

velocity dispersions, so their data are transfromed using the relation of Wu et al. (1999): $\sigma = 10^{(2.49\pm0.02)}T^{0.64}$. A power law fit is made to the Smail et al. (1998) points. No attempt is made to model the scatter in the relation, given so few points. For the groups in R236_1, the richness measures of both the A- and B-rotations are plotted, each seen as a pair of points at a given velocity dispersion. The point with dashed error bars is the less significant repeat observation, and also the one with the most discrepent estimate of the redshift. Both measurements are compatible with each other, just outside the one sigma errors. The biggest disagreement occurs for the lower velocity dispersion pair of points. The repeat observation in this case would not be significant enough to make the 4.8σ cut into the final CMR candidate, and so its measured parameters should be regarded more cautiously than that of the other points. This lower significance candidate predicts a much greater estimated redshift (z=0.39 vs 0.31 for the other rotation, vs z_{spec} =0.297) and thus measures a higher L_E (since for the same measured magnitude, the assumed distance is greater so the intrinsic luminosity must be higher).

All the points fall systematically left of the Smail et al. (1998) relation - at a given optical luminosity, the XDCS clusters have lower measured velocity dispersion, albeit with large errors. All but two of the points are compatible with the relation within the one sigma error bars. The problems with estimating velocity dispersions from so few redshifts have been emphasised already, so the velocity dispersion errors may be underestimated and all the data may be compatible with the relation. Given the tendancy for the velocity dispersion to be underestimated with so few redshifts, there is no evidence from these data that the X-ray dark clusters studied exhibit different mass to light ratios from the z$\sim$0.2 X-ray luminous clusters studied by Smail et al. (1998). However, the main point is that these clusters have much lower X-ray luminosities, but comparable optical richnesses to the Smail et al. (1998) X-ray luminous clusters.

Further spectroscopic observations are underway for several of the XDCS clusters as part of other projects, and so these should allow much more accurate estimates of the systems' velocity dispersions.

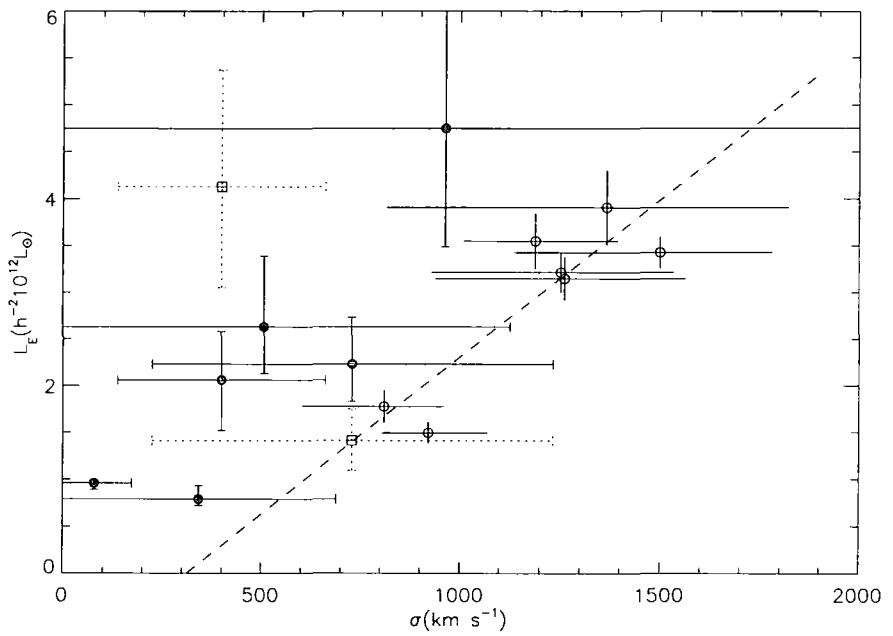

Figure 4.12: L_E vs σ for the groups/ clusters identified (filled circles, open squares with dashed error bars show data from less significant counterpart in overlapping rotation). The data are compared with data from Smail et al. 1998 (open circles) after conversion to the assumed cosmology and converting their X-ray temperatures to velocity dispersions using the relation of Wu et al. (1999). Error bars include the scatter in this relation. Dashed line is a simple powerlaw fit to the Smail et al. points (see text for details).

4.5 Conclusions

Spectroscopy has been undertaken for four XDCS subfields. Each field was centred on a candidate initially identified manually, but retrospectively found to be in perfect agreement with the automated detection algorithms. The candidates identified were required to not show significant X-ray emission. Candidate groups in redshift space were identified, and the significance of these groups evaluated by three different techniques. The first two involved bootstrap resampling the Canada-France Redshift Survey using different selection functions. Using a simple magnitude limited selection showed (in general agreement with Holden et al.'s (1999) method) that 3 concurrent redshifts was a significant grouping; using a Gaussian magnitude selection greatly reduced the significance of these groups (showing the technique is very sensitive to the simulated selection function), but the drawbacks of both these techniques were discussed. An argument based on the space-density of early-type galaxies showed that three early-type galaxies constituted a robust group. Using this latter argument one group was detected in each of two of the fields, and two groups were detected in the other two fields. The matched-filter (MF) found one candidate in each of the fields (it cannot distinguish multiple systems projected along the line-of-sight), however the colour-magnitude finder correctly separated such systems and also detected a higher redshift system, not revealed by the spectroscopy (most likely as galaxies sufficiently faint were not targeted). The error in the estimated redshift from the MF is around 0.1, whereas the CMR redshift error is around 0.04, for groups in the redshift range 0.2 - 0.4. Velocity dispersions for most of these systems are around 300 - 700 kms^{-1} (corresponding to massive groups to low - intermediate mass clusters) but these are estimated from tiny numbers of galaxies $\approx$5, and have jack-knife estimated errors of around 60 - 100% (and for the systems with only 3 redshifts, these errors are likely underestimated). Finally, the luminosity in early-type galaxies versus the velocity dispersion was compared with the relation taken for the high X-ray luminosity cluster sample of Smail et al. (1998), and seen to be consistent, although the errors on the XDCS velocity dispersions are very large.

Chapter 5

Near-Infrared Observations of Candidate Clusters

5.1 Introduction

The evolution of the colour-magnitude relation (CMR) has been characterised empirically, as a function of redshift, by several studies (eg., Aragon-Salamanca et al. 1993, Ellis et al. 1997, Stanford, Eisenhardt & Dickinson 1998, Kodama et al. 1998). Comparison with stellar population synthesis (SPS) codes shows that the colours of galaxies on the relation are compatible with a single age stellar population formed in a burst at high redshift and thereafter aged passively until the epoch of observation. This process is exactly that expected in the monolithic collapse picture of galaxy formation (Eggen, Lynden-Bell. & Sandage 1962) and appears to be in conflict with the hierarchical merging picture. However, such evolution in the context of hierarchical models, using multimetallicity spectral synthesis codes, has been examined and found to be viable by Kauffmann & Charlot (1998). In such models, instead of ellipticals forming their stars in a single monolithic collapse at high redshift, most of the stars form at more modest rates in disc galaxies, which then merge to form ellipticals. Instead of a "closed-box" model of chemical evolution, metals can be ejected from galaxies. This naturally leads to a mass-metallicity relation (as less massive galaxies can more easily eject their metals) which in turn produces a colour magnitude relation.

Ellis et al. (1997) and Stanford, Eisenhardt & Dickinson (1998) used the exquisite resolution of the Hubble Space Telescope (*HST*), to be able to morphologically select early-type galaxies (those having Hubble type E, E/S0, or S0) and found that at all redshifts, it is these which dominate the colour-magnitude relation. The former survey used V and I band imaging (with I-band selected galaxies), and the latter used several

passbands from the optical to the near-infrared (NIR, with NIR selected galaxies). These studies confirmed the earlier conjectures of eg., Aragon-Salamanca et al. (1993), that the galaxies responsible for the reddest colours in the high redshift clusters were early-type, as had been observed for local clusters (eg., Bower, Lucey & Ellis 1992).

Aragon-Salamanca et al. (1993) examined the optical-NIR colour distributions of 10 $z \geq 0.5$ clusters, and cautioned against the selection biases associated with selecting high redshift clusters in optical passbands. Briefly, the galaxy "star-formation activity (SFA)" mix depends upon the passband in which the survey is selected. Shortward of 5000Å, the spectral energy distribution is dominated by massive stars on the main sequence. Such massive stars are short-lived and therefore, blue selected surveys are biased toward actively star-forming galaxies. Between 5000Å and 1μm, the main sequence contribution drops from 60% to 30%. Longward of 1μm, the supergiant, asymptotic giant branch (AGB), and giant stars contribute in roughly equal amounts, whereas the main-sequence contribution continues to drop (Bruzual & Charlot 1993). Thus, NIR selected surveys are sensitive to all stellar populations and not heavily weighted toward massive, short-lived stars. NIR light is a good indicator of the total mass of the stellar population as opposed to just indicating the ongoing star-formation activity. SFA also largely correlates with morphological type, although the two are not identical. Generally, the reddest galaxies at a given redshift are passively-evolving (ie. not actively star-forming) galaxies of early morphological type. Bluer galaxies have higher star-formation rates and are of later types. Even at moderate redshifts ($z \sim 0.5$) the I passband begins to sample bluer rest-frame optical bands. However, the near-infrared K-band still samples rest-frame NIR light. Since the NIR spectral energy distributions (SEDs) of all but the most vigorously star-forming galaxies are very similar, galaxies selected in NIR passbands should be almost completely free from redshift and SFA-dependent biases associated with selecting samples in optical passbands.

As one of the techniques of the XDCS involves selecting concentrations of red galaxies (the CMR-finder), it is important to establish how these red selected samples relate to galaxy samples selected independently of colour. For this NIR data is essential. Furthermore, using another photometric passband allows another check of the reality of candidates, by searching for the CMR in another colour. Lastly, the technique of photometric redshift estimation may provide a way to reject field contamination and locate bluer cluster members which may be missed by the red sequence selection.

5.1.1 The Sample

As with the spectroscopic data, the candidate clusters for NIR follow up were also selected prior to the finalisation of the photometry and cluster finding pipelines. Hence the candidates must again be found retrospectively from the catalogues. The fields in Table 5.2 were observed in the NIR with the instruments listed in the table. The candidates were selected visually, as detailed in Chapter 4 (selecting I-band overdensities and requiring at least a poor CMR), except that several of the fields were selected by an early version of the automated CMR technique. They were also required not to show X-ray emission, by not appearing in the Vikhlinin et al. (1998) catalogue. All optically selected candidates show no emission with greater than 3σ confidence (as detailed in Chapter 3). Flux and luminosity limits are given in Table 5.3. The exception is R283_1 which is contaminated by a bright quasar at z=0.287 (according to NED[1]). This is unlikely to be associated with the target cluster candidate, which has an estimated redshift of 0.19 (and an error of around ± 0.04, from previous chapters). Since the wavelet decomposition technique of Vikhlinin et al. (1998) is capable of removing contaminating point sources before searching for extended emission, this is still regarded as a valid X-ray underluminous cluster target.

After the superior performance of the CMR finder over the MF algorithm in previous chapters, only the CMR candidates will be considered henceforth. The candidates that these correspond to in the final catalogues were found by examining the full CMR list for the nearest candidate to the centre of the NIR field. These are listed in Tables 5.3. All the candidates were found at greater than 5σ although some of these candidates do not appear at the exact same position in the final catalogue. This is essentially an issue of centering, due to the way in which neighbouring/ overlapping candidates affect the selection of final candidates (Chapter 3). For example, an overlapping, higher significance candidate may cause another candidate to be omitted from the final catalogue, but the only criterion used here is to take the *nearest* candidate (from either rotation) to the centre of the NIR field which was observed. This method was chosen in order to maximise the area available in the NIR images, by selecting the most central high significance candidate. This also corresponds to the centre that would be found without the benefit of repeat observations (which in some cases cause a slightly different centre).

[1]http://nedwww.ipac.caltech.edu/ - The NASA/IPAC Extragalactic Database (NED) is operated by the Jet Propulsion Laboratory, California Institute of Technology, under contract with the National Aeronautics and Space Administration.

The H-band was chosen as it is almost equivalent to the K-band, but the sky background in H is much lower. This means that longer exposures are possible, and hence overheads are reduced and observing efficiency is increased. The H-K colour depends only weakly on K-band magnitude (eg. McCracken 1999).

Instrument	Dates	Observers
PISCES	23&24/05/2000	Bell, Gilbank, & McCarthy
PISCES	14&15/05/2000	Bell & McCarthy
INGRID	28/11/2000	Bower & Kodama
Ω'	23-25/07/1999	Ziegler

Table 5.1: NIR Observing Runs.

Candidate Field	α (J2000) [hh:mm:ss.s]	δ (J2000) [dd:mm:ss]	Passband	Instrument	Observation Date
R228_1	08:39:51.37	+36:38:02.9	H	PISCES	15/12/2000
R283_1	04:16:56.17	+01:07:57.9	H	PISCES	14/12/2000
R110_1	14:28:31.38	+33:07:01.0	H	PISCES	23/05/2000
R217_1	14:15:29.70	+43:56:08.9	H	PISCES	24/05/2000
R220_1	17:29:52.77	+74:41:40.0	H	PISCES	23/05/2000
R220_2	17:23:31.14	+74:43:19.0	H	PISCES	24/05/2000
R221_1	8:49:29.6	37:48:28	H	INGRID	28/11/2000
VMF131	13:09:58	32:22:17	K' [2]	Ω'	23–25/07/1999
VMF165	14:44:21.2	63:45:45	K'	Ω'	23–25/07/1999

Table 5.2: Log of NIR Observations.

Instruments:

PISCES – McCarthy, et al. (2001)

INGRID – `http://www.ing.iac.es/Astronomy/instruments/ingrid/`

Ω' – `http://www.mpia-hd.mpg.de/IRCAM/OPRIME/OPrime.html`

[2]This filter is referred to as K_m by the Calar Alto Observatory, but is equivalent to the K' filter.

Candidate Field	CMR candidate ID	Offset (arcmins)	σ	z_{est}	F_X (10^{-14}ergs s^{-1} cm^{-2})	L_X (10^{44}ergs s^{-1})
R228_1	cmJ083950.0+363727	0.64	5.55	0.270	$\leq$4.48	$\leq$0.04
R283_1	cmJ041650.9+010541	2.63	5.05	0.190	—†	—
R110_1	cmJ142812.0+330736	4.10	5.05	0.160	$\leq$1.84	$\leq$0.017
R220_1	cmJ172946.3+744238	1.07	5.45	0.160	$\leq$4.48	$\leq$0.043
R220_2	cmJ172333.0+744410	0.86	6.05	0.210	$\leq$3.28	$\leq$0.056
R221_1	cmJ084929.6+374844	0.28	5.65	0.300	$\leq$2.82	$\leq$0.103
VMF131	cmJ130955.4+322225	0.56	6.55	0.270	9.0$\pm$2.9‡	0.262$\pm$0.084
VMF165	cmJ144412.8+634528	0.96	6.25	0.230	17.4$\pm$3.2‡	0.358$\pm$0.067

Table 5.3: CMR candidate parameters. "Offset" gives the distance of the CMR selected candidate from the centre of the observed NIR field. Flux and luminosity limits are 3σ upper limits.

† - Flux measurement is contaminated by bright quasar.

‡ - Fluxes are taken from Vikhlinin et al. (1998).

5.2 Near-Infrared Data Reduction

Near-infrared data is used in several places in this thesis. The general reduction method is described here, and the different methods applied to data from different instruments commented on.

5.2.1 Introduction

Wide format NIR imaging arrays are becoming increasingly commonplace in astronomy. Up until the mid 1980s, only single element NIR detectors were in use. Now, devices comprising only a factor of a few fewer pixels than optical CCDs are available (1024^2 arrays are fairly widespread, and 2048^2 detectors are being developed). All the NIR cameras described in this thesis utilise the Rockwell HAWAII detector (see Mackay et al. (1998) for a review of these devices). The main difference between CCDs and direct read out (DRO) arrays, such as the HAWAII, is that a CCD is a continuous sheet of silicon covered in electrodes, which collect charge and are then read out by passing charge through adjacent collection sites to the registers; whereas DROs are individual detectors with their own independent amplifiers and read out electronics (an "X-Y addressable array"), bonded to a semiconductor substrate. The advantage for DRO devices is that each pixel can be read out independently of its neighbours. This allows for parallelisation which leads to very high read out rates (the importance of this will become obvious, below, as many short exposures with frequent read outs are required in NIR astronomy).

The night sky is much brighter in the near-infrared than in the optical; and spatial and intensity variations in the sky background are much larger and occur over a shorter timescale. The sky brightness can vary on scales of minutes to hours, largely due to emission by OH molecules in the atmosphere. This effect is particularly pronounced in the 1.65μm H-band. Toward longer wavelengths, such as the K-band (2.2μm), thermal emission from the surroundings (eg. telescope and dome) becomes increasingly noticeable. The data described here are *background limited*, ie. the sky level in the observations is kept as large as possible without saturating the detector. Such a high signal means that the flatfield can be well characterised. This is important to ensure that objects as faint as possible can be separated from the sky noise.

In order to remove these variations, the following observing strategy is usually employed. Science exposures are relatively short ($\approx 10 - 60$) sec to avoid sky saturation. This means that many exposures must be co-added to achieve the necessary depth. A

2D dither pattern is used in which a pointing is made, an exposure taken, and then the telescope offset by a few arc seconds before the next exposure is made. The offset must be large enough so that extended objects do not overlap in time-adjacent images. A typical observation of a target may result in ~100 science frames. Thus, using offset, time-adjacent frames, a picture of the local sky pattern can be built and hence removed from each image.

5.2.2 Dark Subtraction

NIR detectors typically suffer from high levels of dark current (thermal excitation processes in the device can generate electron-hole pairs in the same way as an incoming photon would). In order to remove this, for every science frame, several equal duration images were made by clocking up charge within the device without actually exposing it to the night sky[3]. Master darks were constructed from median combination of such frames. The master dark was then subtracted from each raw science image, as with the bias frame in optical astronomy.

5.2.3 Removal of Sky Variations

Using the notation introduced in Chapter 2, the NIR data is described by:

$$raw = (object + sky) \times qe + zero \tag{5.1}$$

The *sky* variable is now dominant and so can no longer be neglected. The *qe* is again the flatfielding term, but here, *zero* is better characterised by the dark current of the device.

Two techniques are widely used to correct for the *sky* and *qe*: flatfielding and sky subtraction, similar to the method previously described for the I-band data (where the sky variation is substituted for the fringing, but the former being simpler to remove); and the in-field chopping technique of Cowie et al. (1990).

[3]This is equivalent to taking an image whilst keeping the shutter closed in optical astronomy. NIR devices do not have conventional shutters; instead the charge in each pixel is reset and its level read at the start and end of an exposure. The difference then gives the science frame. With PISCES this is done internally, whereas with INGRID a "pre-scan" and "post-scan" image are produced and the difference must be calculated by the user.

Flatfielding and Sky Subtraction

Each frame has a master dark frame subtracted from it, is then divided by a master flatfield, and finally has a local sky frame subtracted from it.

The master flatfield is made by median-combining many science frames, as with the optical data. It was found that around 100 frames is sufficient for this. Adding more data just increases the computational cost without significantly improving the quality of the flatfield. If the count level in the data varies systematically through the night (due to sky brightness variation) then an offset can be applied to each frame, prior to medianing, to bring the counts to a common level. This master flat is then applied to each image.

The sky frame is made by taking time-adjacent frames and combining them in a similar method to the flatfield. Here, however, only the ~10 temporally nearest frames are used in making the sky image. This is necessary to ensure accurate mapping of the local sky variation. So, each science image has a unique sky frame constructed and subtracted from it. The optimal number of frames was found from both examining the median sky level through the night (to find the variation timescale) and experimentation with different numbers of frames followed by checking the accuracy of photometry of the same object from frame-to-frame, for a number of objects.

Note that during the median combination, astronomical objects can be removed with simple `minmax` rejection using the `IRAF` task `imcombine`. Asymmetric rejection of pixels is appropriate as positive fluctuations in pixel value occur due to astronomical objects, cosmic rays, and temporarily hot pixels; however, negative fluctuations only arise due to temporarily cold pixels. Hence the positive fluctuations are more common than the negative. If this rejection is not performed, the median will not be representative of the true background level (where astronomical objects overlap in several frames, for example).

Thus, instrumental signatures are removed

$$const \times \frac{raw - < dark >}{< flat > - < dark >} - < sky > = object \tag{5.2}$$

where *const* is a suitable normalising constant to make the average *qe* correction unity. Finally, a constant value (the average sky level) is added back on to the object counts, to maintain the correct propagation of errors, based on Poisson noise.

In-field Chopping

An alternative is to just construct frames which can be thought of as local flatfields, to correct for both effects simultaneously. This technique was first used by Cowie et al.

(1990). Dark correction will be ignored for the sake of clarity, as it is the same as above.

$$< localflat >= sky \times qe \times const \tag{5.3}$$

where again, *const* makes the average correction over the device unity. Now, by *dividing* the raw data by this local flat:

$$\frac{raw}{< localflat >} = \frac{obj \times qe + sky \times qe}{qe \times sky/const} \tag{5.4}$$

if the sky variation level is small (which is true over the time intervals considered) then the sky can be written as $sky = sky_0 + \Delta sky$, where sky_0 is the median sky level, and Δsky is the variation about this value. The normalising *const* then becomes, sky_0, also. Thus

$$\frac{raw}{< localflat >} = \frac{obj + sky_0 + \Delta sky}{(sky_0 + \Delta sky)/sky_0} \tag{5.5}$$

Taylor expanding the denominator gives $(1 + \Delta sky/sky_0)^{-1} \approx (1 - \Delta sky/sky_0)$, and so

$$(obj + sky_0 + \Delta sky)(1 - \Delta sky/sky_0) \approx obj + sky_0 \tag{5.6}$$

neglecting the terms in $obj \times \Delta sky/sky_0$ and $O(\Delta sky^2)$ (remembering that $obj \ll sky_0$ since the data are background limited). Thus the data have been flatfielded and sky subtracted in one simple step, and the average sky level is naturally preserved (again to ensure correct Poisson noise propagation). A comparison between normalised sky values for both these techniques shows that the in-field chopping results in a flatter field by a factor of about 2. Similar results were found by Aragon-Salamanca (1993) (cf. his Figure 2.3). Normalised sky values were obtained using `SExtractor` to mask objects in the images (by setting the `CHECKIMAGE_TYPE` option to "-OBJECTS").

5.2.4 Image Registration and Mosaicking

Although the above reduction was carried out in the `IRAF` environment, the `STARLINK` package `CCDPACK` was preferred for image registration and mosaicking. `CCDPACK` is more user friendly and robust than the equivalent `IRAF` routines, and offers several useful extras in the mosaic-making routine. Briefly, the `FINDOBJ` task locates astronomical objects by peak finding (like a simplified version of `SExtractor`) and `FINDOFF` uses a cross-correlation algorithm to match these objects between frames, calculating the offsets introduced by the dither pattern. `REGISTER` then calculates the transformation of

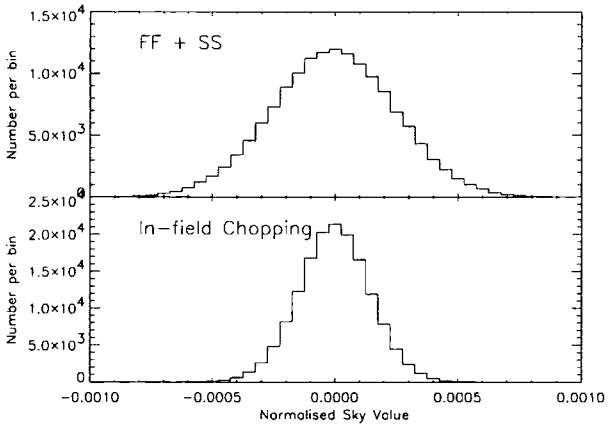

Figure 5.1: Histogram of normalised sky values, for the two NIR reduction techniques (median sky value has been subtracted). Top: flatfielding plus sky-subtraction method; bottom: in-field chopping method. See text for details.

each frame to a reference frame, using a six parameter fit which accounts for translation, rotation, magnification and shear. The transformations are then applied using `TRANNDF` and the mosaic formed by median-combination using `MAKEMOS`. This latter task offers a sophisticated sky matching algorithm to equalise the sky levels in each frame before combination. The equalisation can take the form of either a shift or scale to the counts or both (though the last option is rather time consuming). It was found that for the majority of data, a small ($\lesssim$ 1% of sky) shift to the counts made the resultant mosaic cosmetically much better, although the shift makes a negligible difference to photometric measurements.

5.2.5 Non-Photometric Data Correction

For the non-photometric data, an extra step was added after the registration and prior to mosaicking. It was necessary to compensate for extinction variations by scaling each frame in a field to a reference frame (taken from each field). Several (~15) bright, unsaturated stars were identified in the aligned images and photometry of these reference stars was used to calculate a scale-factor and zero-point shift to transform the counts between individual frames. This was achieved with `IRAF`'s `linmatch` which uses object magnitudes and errors and sky magnitudes and errors to fit the transformation equation (the size of this scaling was typically enough to make ~tenths of a magnitude differences). It was found that using only bright objects to calculate this scaling resulted in accurate photometry (as

evidenced by frame-to-frame aperture photometry of bright objects), but in the combined mosaic, the photometric errors were artificially inflated. This was due to the fact that this method did not result in a sufficiently flat sky background; and **phot** uses the sky variance to calculate photometric errors. A slight (< 1% of sky) zero-point shift calculated within `MAKEMOS` corrected this, giving sensible photometric errors whilst negligibly changing the aperture magnitudes.

5.2.6 Supplementary Steps and Instrumental Differences

5.2.7 Object Detection and Photometry

Object detection was performed similarly to the method described in Chapter 2, using the `SExtractor` package. The NIR frame was used as the detection image (since the seeing is best in the NIR frame, and using as red a band as possible is desired, as described in Chapters 1 & 2). `SExtractor` was run in "dual image mode" using the H-band (for the Ω' data, read K' -band for H-band) frame as the detection image and each of the V,I,H frames (convolved to the worst seeing of each set) in turn as the measurement image. Aperture photometry was performed using **phot** with an aperture of diameter 2.6 $\times$ the FWHM of the poorest seeing image. Total H-band magnitudes are taken from `SExtractor` `MAG_BEST` magnitudes. Star/ galaxy separation used `SExtractor` 's `CLASS_STAR` parameter. Objects with `CLASS_STAR` ≤ 0.99 were considered to be galaxies.

PISCES

PISCES is a 1024x1024 HgCaTe HAWAII detector with 0.494 arc second pixels, giving a field of view of 8.5 arcmins. H (1.65μm) passband observations were made with the PISCES camera (McCarthy, et al. 2001) on the 2.3m Bok telescope, Kitt Peak National Observatory.

The linearity of the detector was measured by Drs Eric Bell and Don McCarthy using a series of dome flats with a stable lamp. The level of non-linearity was found to be at the level of around 3% at 20 000 counts - the regime in which the data were taken. A 3% non-linearity translates into a 0.03 magnitude error in photometry. This level was considered acceptable, and therefore no linearity correction was made.

The PISCES chip comprises quadrants which suffer from crosstalk, such that a bright feature like a cosmic ray hit in one quadrant appears with negative intensity in a corresponding position in each of the other three quadrants (see McCarthy, et al. (2001)

for details). These features were removed using a routine kindly provided by Dr Roelof de-Jong[4]. The usable field of PISCES is a circular region within the square detector, due to the re-imaging and cold baffling in the instrument which blocks thermal emission from the surfaces normally present in Cassegrain optical configurations. The vignetted pixels are easily seen in the data frames, as the background counts drop off with radial distance from the optical centre. The counts of data frames were inspected using `imexam`, and the maximum usable area estimated. The rest of the image was assigned a bad pixel mask.

PISCES also suffers from radial distortions which must be corrected prior to image registration. Geometrical correction was performed by calculating a distortion map from a single data frame. This was done again using a routine kindly provided by Dr Roelof de-Jong [5]. In outline, this program uses the coordinates in the image header to extract a region of sky covered by the observation from the USNO A2 astrometric catalogue (Monet 1998). Objects are then matched between the reference catalogue and the data frame. The results of this comparison are then used by the `IRAF` routine `Geomap` which calculates the geometrical transformation between the two images. Hence, a distortion map of the instrument is created, which can be applied to all PISCES images from a given run. The density of objects in the A2 catalogue is sufficiently high that only one data frame is needed to calculate the transformation. A single transformation proved adequate for every field of both observing runs.

INGRID

The INGRID instrument is detailed in Chapter 6.

Omega Prime

The Ω' NIR detector is currently only an engineering grade 1024^2 device. Like the other two cameras, the Ω' array is divided into 512^2 butted quadrants, however one quadrant exhibits a significantly different sky level from the other three (this is a consequence of the controller electronics, as each quadrant reads out separately). Several reduction techniques were attempted, to normalise the sky levels, with independent reduction of the four sub-arrays, but it appears that the sky in one quadrant is simply saturated, and hence unusable. Thus the images were masked to exclude bad pixels between the chips (as with INGRID) and the saturated quadrant included in the mask. The standard

[4]available from `http://gaffa.as.arizona.edu/~rdejong/gzip/corquad.tar.gz`

[5]available from `http://gaffa.as.arizona.edu/~rdejong/gzip/matchusno.tar.gz`

technique described above was found to be sufficient to place the remaining 3 quadrants on the same median-sky level.

5.3 Photometric Calibration

Standard stars from the catalogue of Hunt et al. (1998) were observed for both PISCES runs. Conditions for the first run were excellent, with no trace of cloud. The second run showed patchy cloud which caused photometric variations at the level of tenths of a magnitude. The standard stars were used to calibrate the photometric zeropoint for the first run. No extinction or colour terms were fitted, the former was neglected as extinction in the NIR is low, the latter as only single band observations of the standard stars were made. Plots of magnitude offsets for PISCES data compared with Hunt et al.'s (1998) magnitudes are shown in Figure 5.2. The first run shows only two outlier points which were rejected from the fit, whereas the second run shows considerable scatter from only a few points. In order to calibrate this latter data, data from the 2MASS point source catalogue were used[6]. The publically available 2MASS NIR photometry overlaps with several PISCES fields. Magnitudes of all available point sources in the PISCES fields were measured using 8 arcsec diameter apertures, as was done for the 2MASS point sources. The difference of these measurements was plotted as a function of PISCES magnitude (the higher signal-to-noise ratio data). The results of one comparison field are plotted in Figure 5.3. In order to test the accuracy of this method, 2MASS data was checked against PISCES data with an accurate calibration from the standard stars. It was found that the brightest sources were saturated in the PISCES data and the faintest sources had low signal-to-noise in the 2MASS images. Therefore a restricted magnitude range of $13<H<14.4$ was found to give the best agreement. For the field shown in the plot, the standard star zeropoint is 23.64 ± 0.05 and the 2MASS comparison gives a zeropoint of 23.5 ± 0.1.

Thus, this method was deemed suitable to calibrate the second PISCES run data, and also the non-photometric INGRID data (described fully in Chapter 6). For the Ω' data, the standard stars were all saturated and no overlap with the 2MASS survey existed in the publically available second incremental release data. This data was calibrated by fitting the K-band zeropoint so that the colour of the clusters' CMRs agreed with model colours, at the spectroscopically determined redshift of the cluster (Vikhlinin et al. 1998).

[6] http://irsa.ipac.caltech.edu/2mass/

In Chapter 4 it was shown that the CMR can be used to estimate the redshift of a group/cluster, accurate to $\Delta z \approx 0.05$. Conversely, knowing the redshift allows the V-K colour to be estimated to the level of about 0.2 magnitudes (at the redshifts of these clusters). This data is to be used largely to illustrate a technique in two-colour space, so a precise calibration is not necessary.

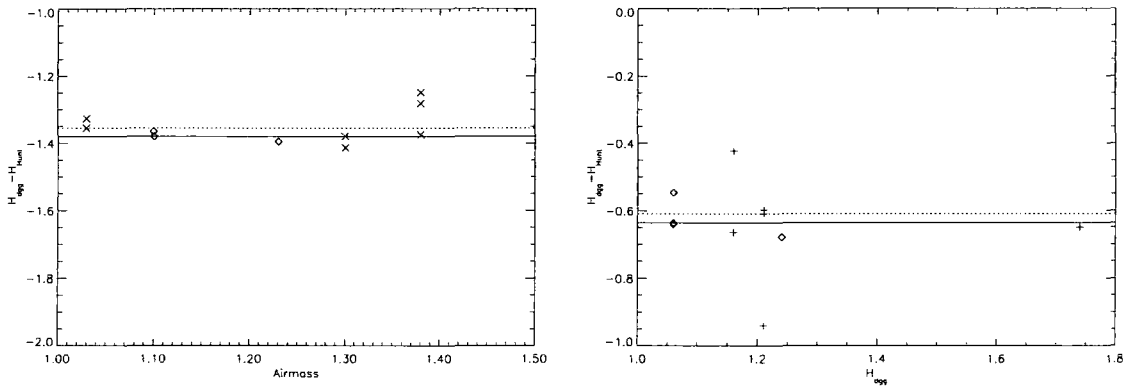

Figure 5.2: Standard star calibrations for the PISCES runs. Left: May 2000 (crosses - first night, diamonds - second night). Right: December 2000 (crosses - first night, diamonds - second night). Solid lines are fits to the first night's data, and dotted lines are fits to the second night's data. Fits are just median values: no extinction terms were fitted. The second run was non-photometric and so calibration was performed using the 2 Micron All Sky Survey (2MASS) overlapping observations.

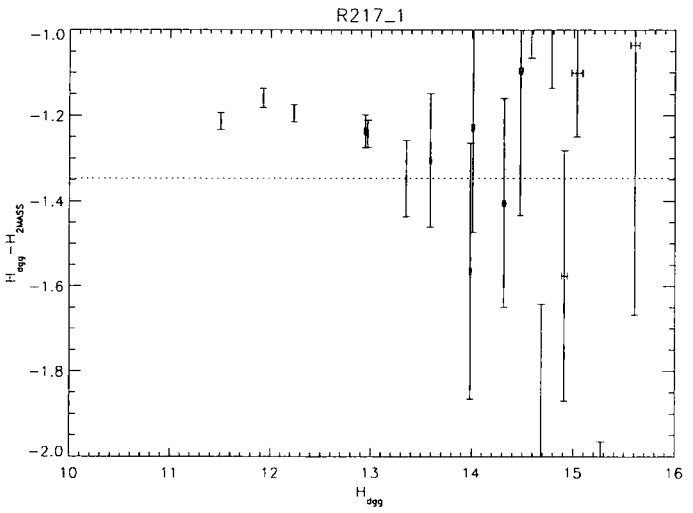

Figure 5.3: Comparison of stars in one PISCES field with magnitudes taken from the 2MASS point source catalogue. Sources brighter than H=13.0 are saturated in PISCES data, and those fainter than H=14.4 have unacceptably large photometric errors in 2MASS. The comparison with the standard star solution zeropoint for this field is very good (see text).

5.3.1 Photometric Accuracy

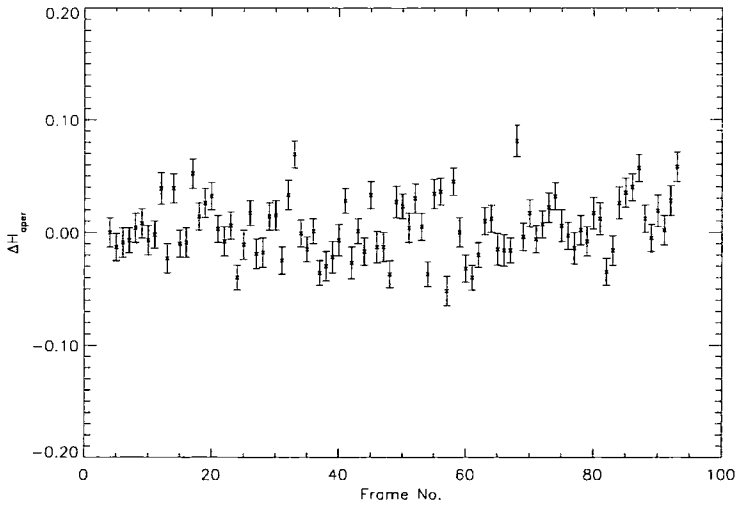

Figure 5.4: Field-to-field variation from aperture photometry of one galaxy. Taken from the first 100 PISCES frames (for field R220_1). Frames are about 45 seconds apart (40s exposure time + read out time). The galaxy has a measured magnitude of H=16.3. Offset is with respect to the first frame. The median value of the errors from `phot` (taken from the sky variance) is 0.013 magnitudes. The 1σ error calculated from the standard deviation of all these magnitude measurements is 0.026. Therefore, `phot` errors are doubled for all NIR measurements, to be conservative.

5.4 Photometric Redshift Estimates

Spectroscopic redshifts were discussed in the previous chapter. Using only broad-band photometry, estimates of a galaxy's redshift may be also obtained. Whereas with spectroscopic data, fine absorption and emission features in the galaxy's spectrum may be observed and used to find the redshift; photometric redshifts are only sensitive to strong "breaks" in the overall shape of a galaxy's spectrum. There are two main methods for photometric redshift estimation, the first is SED-fitting which uses model templates of galaxy spectra, and finds the most likely fit to the template given observed broad-band colours. The second uses an empirical training set. Using a large sample of photometric and spectroscopic data, empirical relations between galaxy colour and redshift can be established, such that further observations with just photometric data may have redshifts fit from these relations. There are many degeneracies in using broad-band colours to find the redshift of a galaxy such that the effects of dust, age and metallicity can produce galaxies of the same colours at different redshifts, and vice versa. For a more detailed discussion, see Bolzonella et al. (2000) and references therein.

In the absence of a large spectroscopic sample for the XDCS, it was decided to attempt SED-fitting of VIH photometry to estimate photometric redshifts for the fields of the cluster candidates. This was achieved using the publically available code `hyperz` (Bolzonella et al. 2000). This code takes magnitudes and magnitude errors and for a given set of parameters (eg., cosmology, allowed levels of reddening, range of SED templates) produces a likelihood distribution, showing the likelihood of each redshift given the data. Two such probability curves are illustrated in Figure 5.5. The photometry used comes from two absorption line galaxies in Chapter 4 with spectroscopic redshifts (the left one at z=0.2 and the one on the right at z=0.3). While `hyperz` fits the correct redshift for the first galaxy (as indicated by the peak of the solid line), the second galaxy shows several peaks and plateaus. In order to try to improve the fitting technique, `hyperz` was modified as suggested by Wittman et al. (2001). The standard `hyperz` package weights all redshifts as equally likely, although this is not the case. Given a magnitude limit, a luminosity function and a cosmology, the number of galaxies as a function of redshift, N(z), can be calculated (Equation 4.1). Wittman et al. (2001) used this fact to essentially apply a different Bayesian prior distribution in the calculation of the likelihood (such a photometric redshift technique was implemented by Kodama, Bell, & Bower (1999)). The N(z) distribution used in Chapter 4 (equation 4.1) was normalised to unity and multiplied by

the resulting P(z) from **hyperz**. The estimated redshift is then found by taking moments of the resulting distribution, such that $z_{phot} = \int_0^{z_{max}} P(z)zdz$. In the case of the redshift estimates in Figure 5.5, this technique improves the photometric redshift (z_{phot}) so that both now predict the correct redshift, to within the binsize of Δz=0.05.

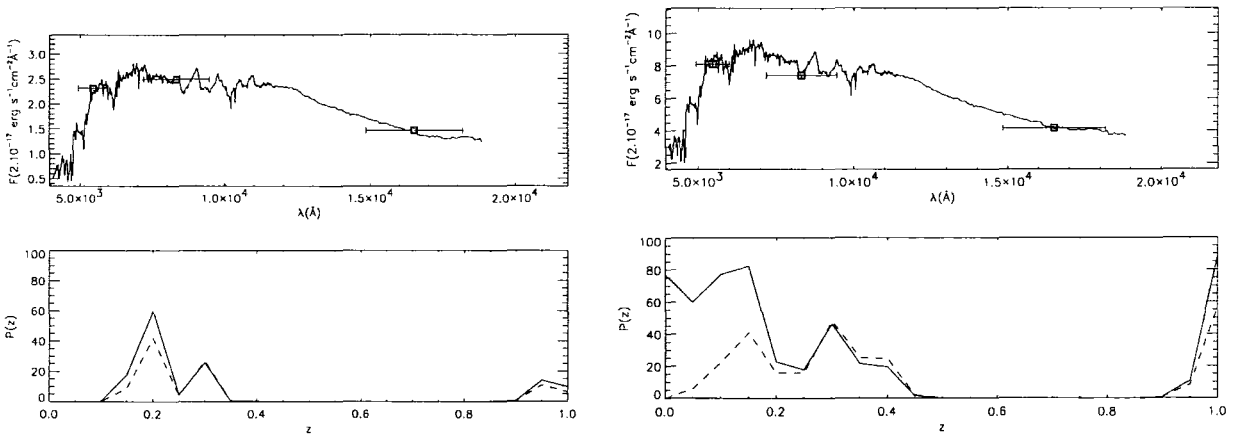

Figure 5.5: SED fits and probability distributions from **hyperz**. Squares show photometric measurements in the V,I, and H passbands (left to right), with the widths of the filters indicated by the horizontal error bars. The lower plots show the P(z) from the **hyperz** code (solid line), and the P(z) assuming the prior distribution explained in the text (dashed line). Both best fit SEDs are elliptical templates. The one the left is well fit by a z=0.2 elliptical (as seen from the single prominent peak in the P(z) plot); whereas the galaxy on the right has multiple peaks in the P(z) distribution.

The comparison between photometric and spectroscopic redshifts in the XDCS fields with NIR imaging *and* spectroscopy (Figure 5.6) shows that z_{phot} using only VIH data for the XDCS cluster candidates does not give a reliable indication of the true redshift. The main reason for this seems to be the absence of a bluer filter (U or B), as none of the filters lie blueward of the 4000Å break below a redshift of 0.4. Since no strong spectral features are bracketed (such as the 4000Å break), the technique does not work well at the redshifts of the cluster candidates targeted in Chapter 4 ($z \approx 0.2-0.4$). A further test is provided by using model SEDs at various redshifts to produce colours in the XDCS VIH passbands, and attempting to recover the input redshift using **hyperz**. The results of this experiment are shown in Figure 5.8 and are similarly poor to those found from Figure 5.6.

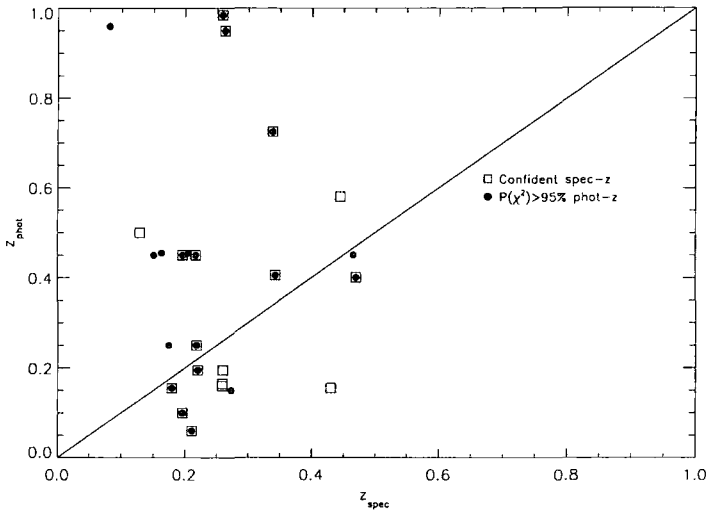

Figure 5.6: Comparison between photometric and spectroscopic redshift. Phot-z is taken directly from **hyperz**. Squares are confident spectroscopic redshifts and filled circles are confident (χ^2 probability >95% from **hyperz**) photometric redshifts.

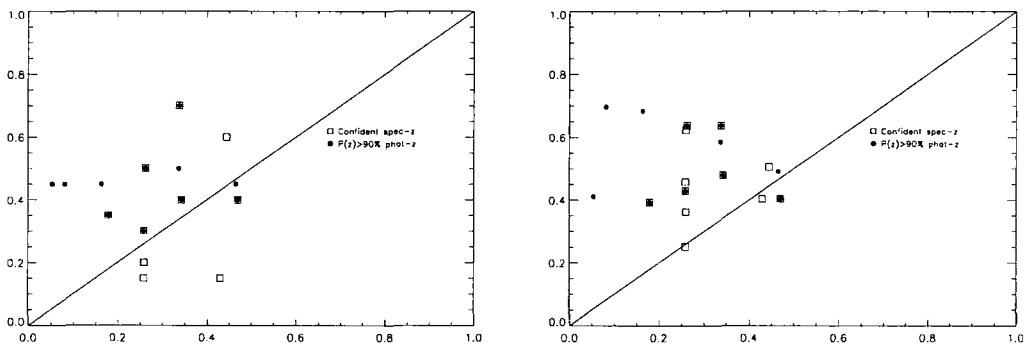

Figure 5.7: Comparison between photometric redshift (ordinate) and spectroscopic redshift (abscissa). Phot-z is found by taking **hyperz** probability convolved with N(z) PDF. The redshift is taken as the peak value (left); and by taking moments of the P(z) distribution (right), see text.

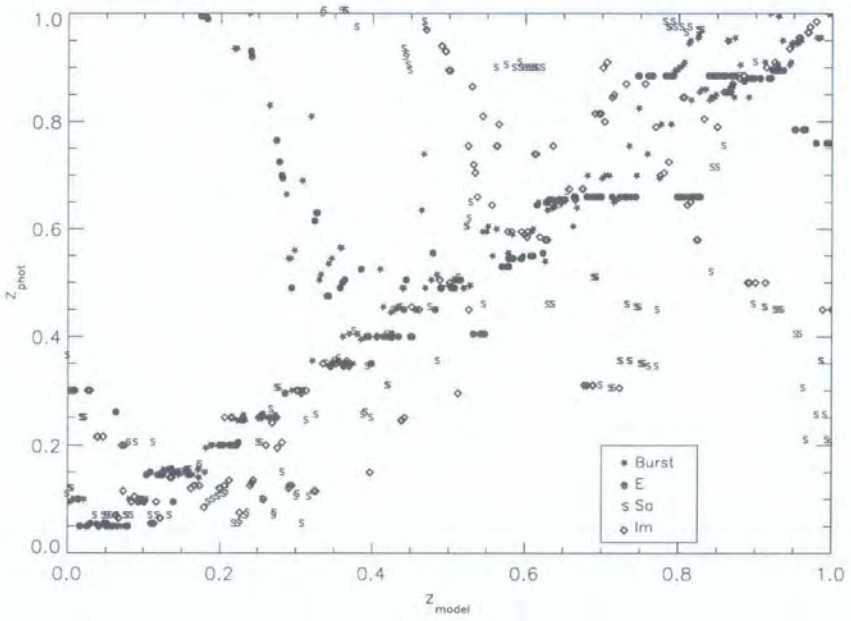

Figure 5.8: Tests of photometric-redshifts on model SEDs. 1000 templates were generated using Bruzual & Charlot's 1993 model SEDs. Four different types were used: elliptical, burst, Sc and irregular. Redshifts were distributed randomly between 0 and 1, and then observed V, I and H magnitudes were calculated. `hyperz` was then run to estimate the redshifts, and the results plotted as a function of the input model redshift.

5.5 Colour-Magnitude and Colour-Colour Diagrams

The NIR and I-band optical images of the candidates are presented in Figure 5.9. In each case the image on the left is the NIR data and the image on the right illustrates the WFC data. The WFC data are taken from I-band images, but the V-band exposures were taken at the same pointing position. These show that for some candidates the cluster candidate centre lay near the edge of a WFC chip or , in one case (R110_1), the centre of the NIR image passed between two WFC chips. The streaks around the edges of some fields are caused by interpolation within the `IRAF geotran` routine, where no data exist. Circles indicate galaxies with `SExtractor MAG_BEST` total H magnitudes brighter than 19.0. These also clearly indicate where masked regions have been rejected. The initial region for object detection was the central 500 pixel radius of the PISCES frame. Further masking was applied where the images are truncated.

Now, in order to examine the significance of colour-magnitude relations in as unbiased a manner as possible, the NIR images are used to select objects. Doing so samples galaxies in a way that depends mainly on stellar mass, and less critically on current star-formation activity or redshift (described earlier). Firstly, to illustrate the technique, the known X-ray luminous clusters will be examined. These comprise two clusters from Vikhlinin et al.'s (1998) catalogue imaged in the K-band with Ω' (V131 and V165).

The colour-magnitude diagrams (Figure 5.13) for the two fields show the data split into two samples. Filled points are drawn from a region close to the cluster candidate (1.5 arcmin radius); whereas the open points are drawn from an annulus of equal area, as far from the candidate centre as the image allows (refer to Figure 5.9). Model CMRs are overplotted at the estimated redshift given by the CMR finding algorithm (using the V-I, I CMR). If a slight shift in the redshift of the model allows a better simultaneous match to the V-I, K and V-K, K, then this is applied. Next, the same data is studied in two-colour space. The colour-magnitude relation at this model redshift is overplotted on the V-I, I-K colour-colour diagrams. To quantify the overdensity thus found, this relation is bounded by lines at a distance of 0.1 magnitudes (comparable to the size of the scatter in such data, eg. Stanford, Eisenhardt & Dickinson (1998)). The number of galaxies in the box so constructed in both the "cluster" and "field" regions (ie. inner circle and outer annulus) are counted and compared. The results are tabulated in Table 5.5. The probability of such an event occurring by chance, P(false), is calculated. This calculation assumes that points are given by a Poisson distribution with a mean given by the number of galaxies

in the outer annulus. Values are taken from Gehrels's (1986) tables for one-sided Poisson confidence intervals.

A further simple quantity to measure is the number of galaxies which lie on the CMR in the optical data, but blueward of the optical-NIR relation (N_{blue}). This corresponds to galaxies identified as part of the CMR with the CMR finder, but which are likely not real CMR members (when a further colour is considered). This could also include galaxies redward of the relation, but these can only be caused by luminous, high redshift spirals which are rare. N_{blue} is simply a count of the number of galaxies drawn from the inner region, with colours on a slice parallel, but to the left of the CMR overplotted in the two colour diagram.

Field	z^a_{est}	z^b_{model}	N^c_{inner}	N^d_{outer}	P(false)^e	N^f_{blue}
VMF131	0.270	0.29	13	5	0.01	1
VMF165	0.230	0.25	16	5	0.001	3

[a] Estimated redshift from CMR algorithm.

[b] Model redshift used in analysis – may be shifted slightly from z_{est} if this new value gives a better fit to VI-K and VH-K CMDs.

[c] Number of galaxies in inner (candidate cluster) region.

[d] Number of galaxies in outer (field) region.

[e] Probability of obtaining N_{inner} galaxies, or more, from a Poisson distribution with mean of N_{outer}.

[f] Number of galaxies with colours compatible with V-I colour slice, but with I-K colours blueward of this.

Inspection of both the CMDs and two colour diagrams (2CDs) shows that such a test is very strict and the true significance of such a detection is likely to be higher. Several points from the inner regions lie just outside the model CMR bounding box, and are thus ignored in the calculation. Also, (particularly for V165) a number of points from the outer region lie within the tight CMR slice at the bright end. This suggests that perhaps the outer annulus is too close to the cluster and is sampling cluster early-type galaxies. Both these effects lead to an underestimate of the cluster signal. Both cluster show at least one galaxy which lies on the CMR in V-I,I but bluewward of the relation in V-K. These would lead to a slight increase in the cluster signal in the CMR catalogue as 1/14 and 3/19 galaxies which would be identified as CMR members in two colour photometry

are not found to be so in three band photometry. These bluer galaxies lie at the faint magnitude end of the range considered, and are thus weighted less than brighter galaxies by the magnitude weighting process in the CMR algorithm (Chapter 2). Furthermore, most of these galaxies lie close (within 0.2 mags) to the CMR, and may be due to early-type galaxies with a small amount of residual star-formation, or may be later-type cluster members. They may even be CMR members, if the scatter in the V-K,K colour magnitude relation has been underestimated.

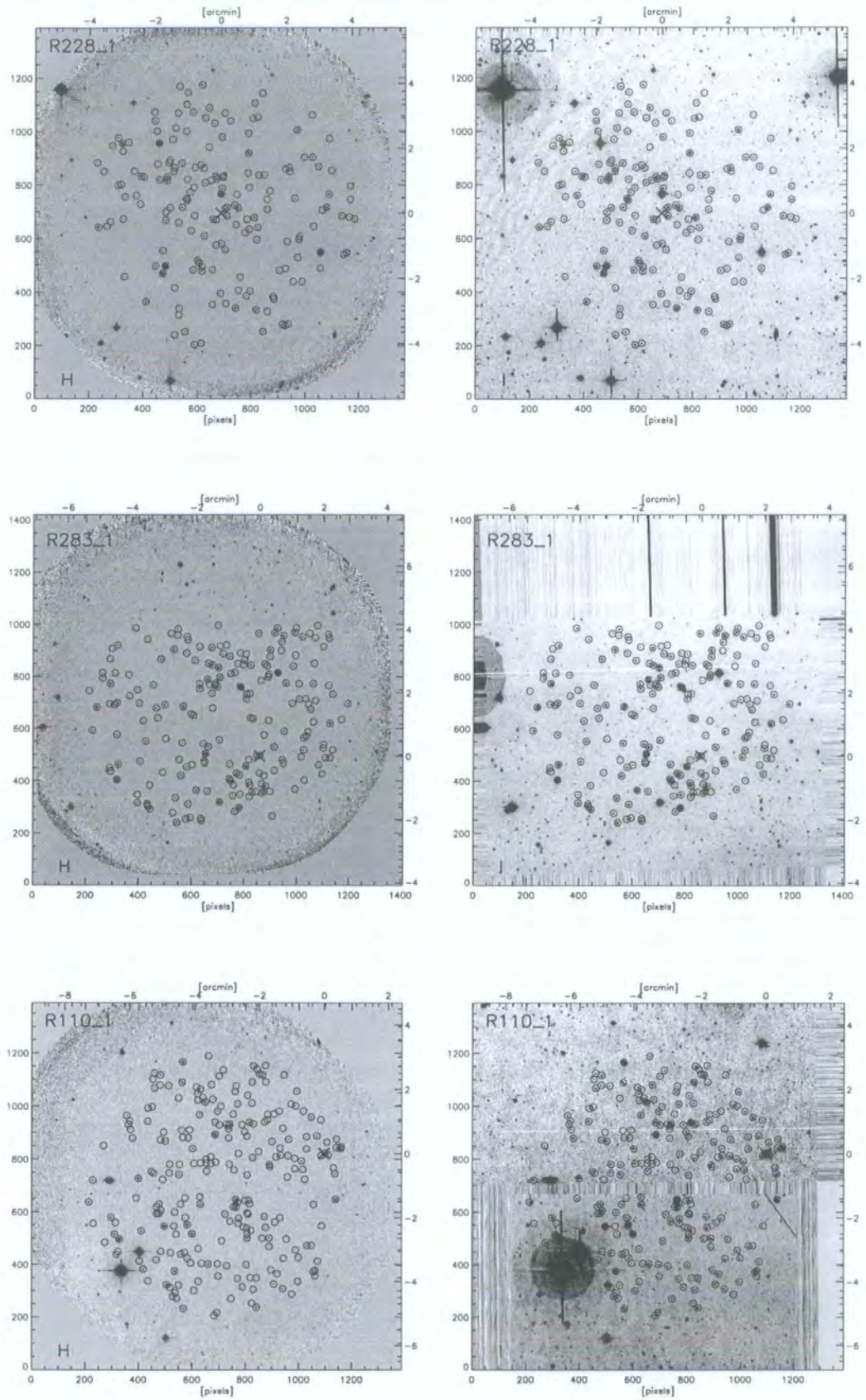

Figure 5.9: NIR (left) and I-band (right) images of cluster candidates. Circles indicate galaxies brighter than H=19.0. Axes show scale in pixels (note: optical images were always registered to NIR images, and therefore take on the NIR detector's pixel scale) and arc minutes. See text for further details.

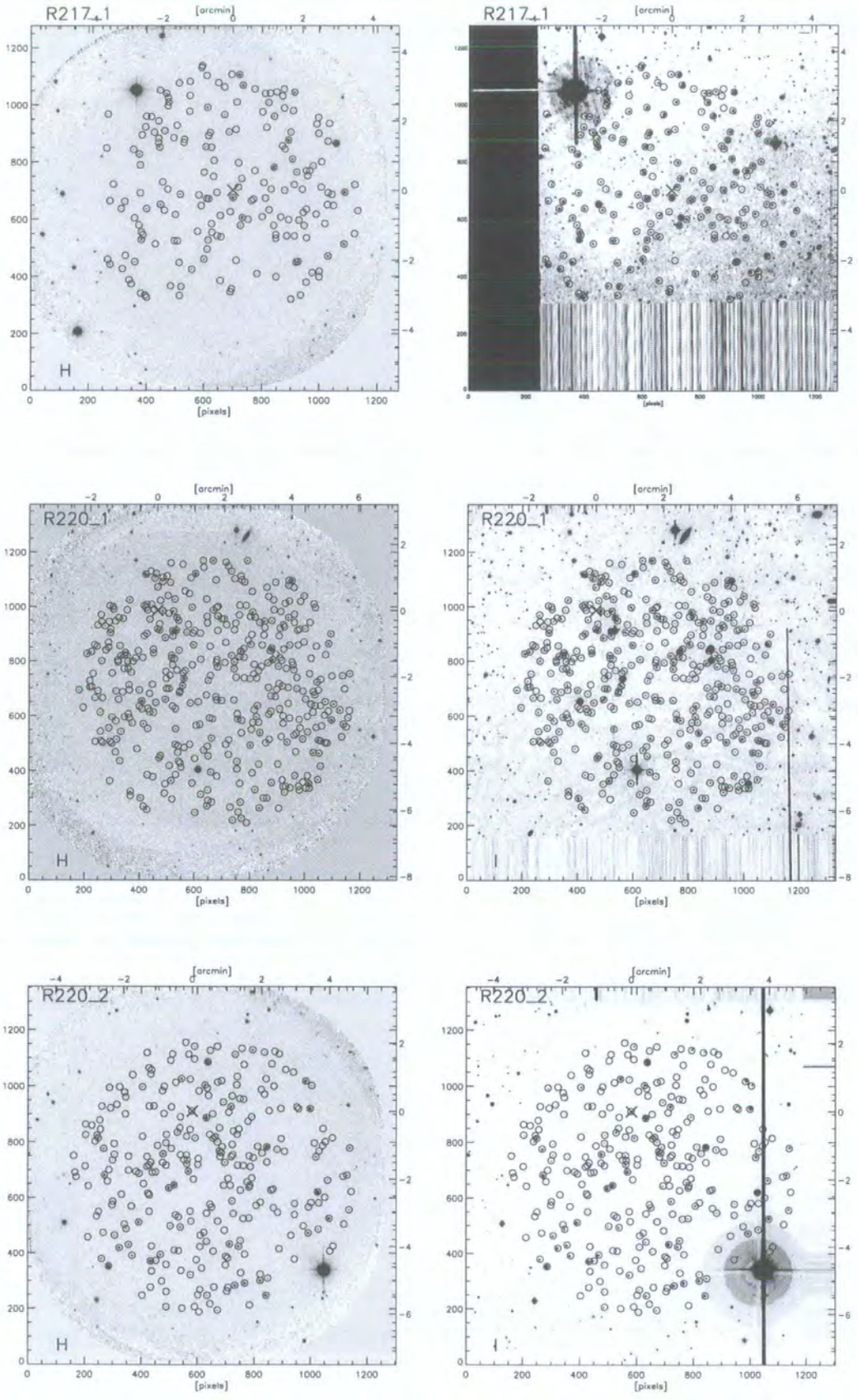

Figure 5.10: previous figure continued

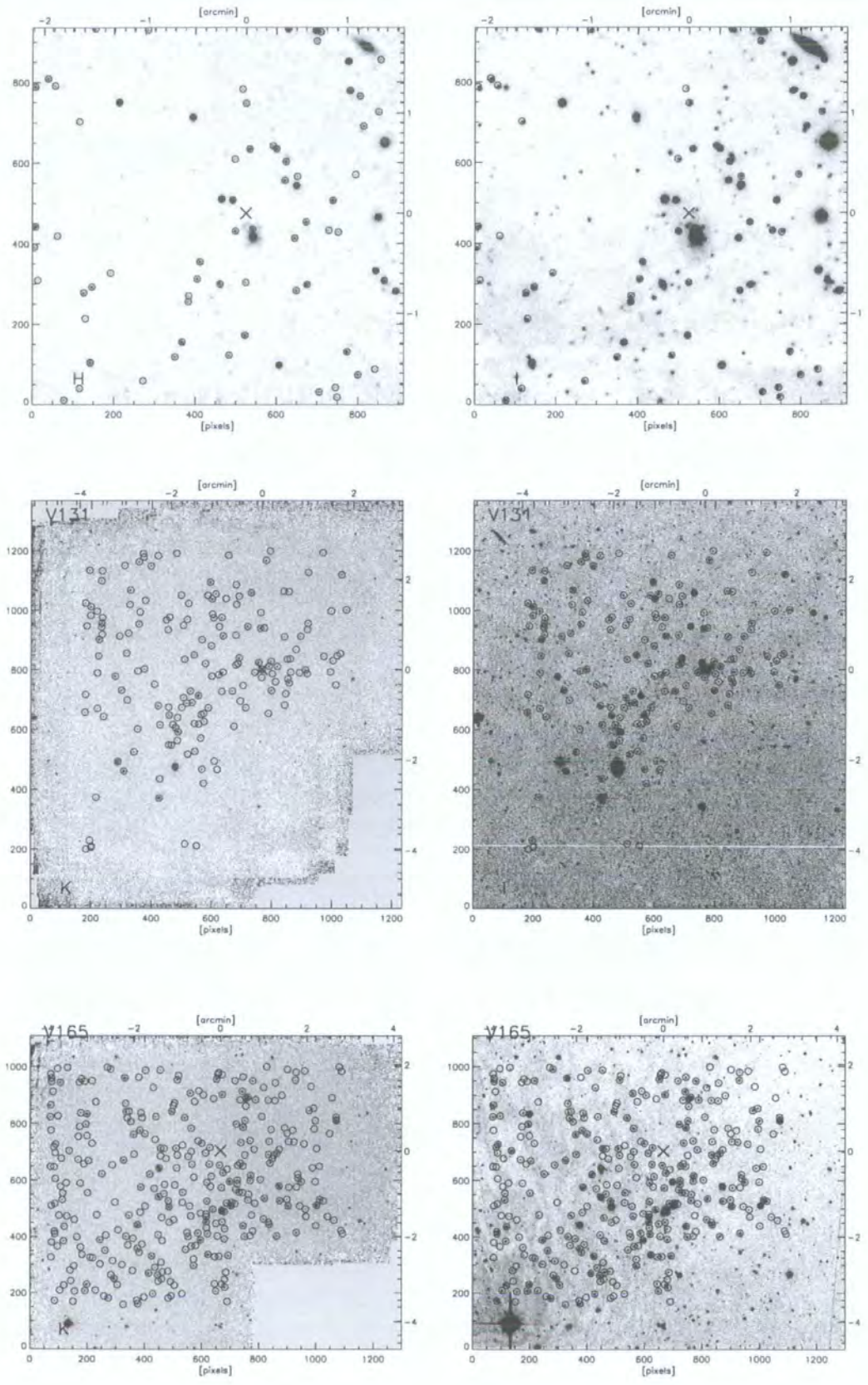

Figure 5.11: previous figure continued

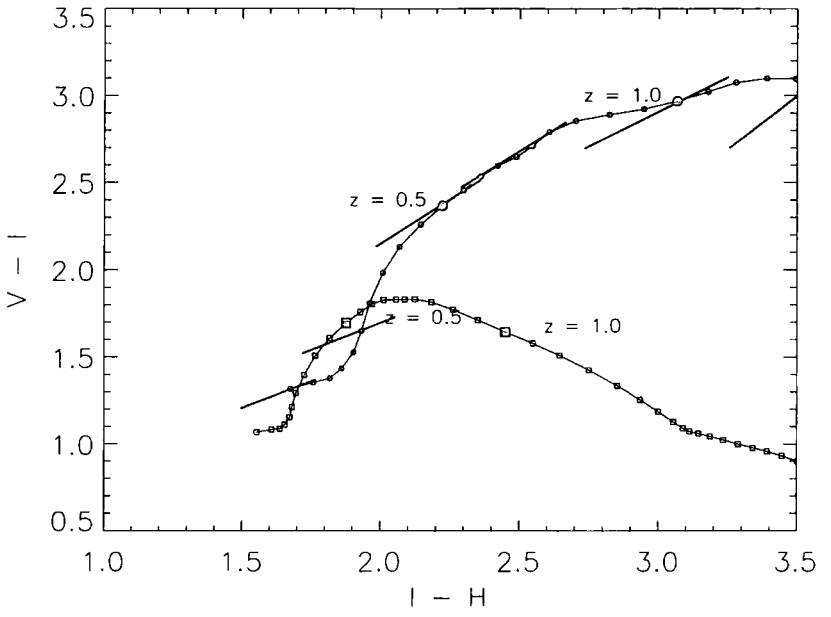

Figure 5.12: Model tracks for elliptical (circles: upper line) and Sa (squares: lower line) galaxies. Filled points mark Δz=0.5 intervals, with redshifts labelled. The thick, straight lines on the elliptical track mark the colour-magnitude relation at that redshift.

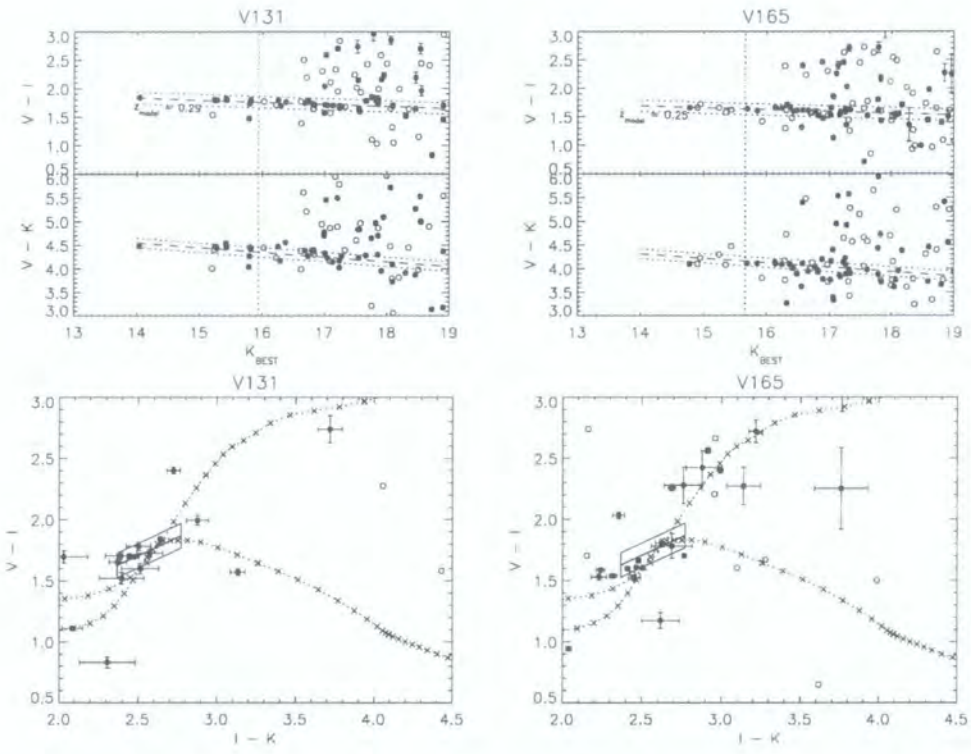

Figure 5.13: CMDs (top) and 2CDs (two colour diagrams, bottom) for the Vikhlinin et al. (1998) clusters: V131 and V165. CMDs show V-I and V-K colours as a function of K-band total magnitudes. Dashed line shows model CMR at redshift indicated in label. Dotted lines bound the CMR 0.1 magnitudes either side. Dotted vertical line indicates the magnitude of an M* elliptical at this redshift. Filled points are galaxies within inner region around candidate centre, open circles are drawn from an equal area, further from candidate. See text for details. In the 2CDs, model CMR is plotted as thick line, again bounded by 0.1 magnitudes; crosses indicate the tracks of model elliptical (upper line) and Sa (lower line) galaxies. See next figure, and text.

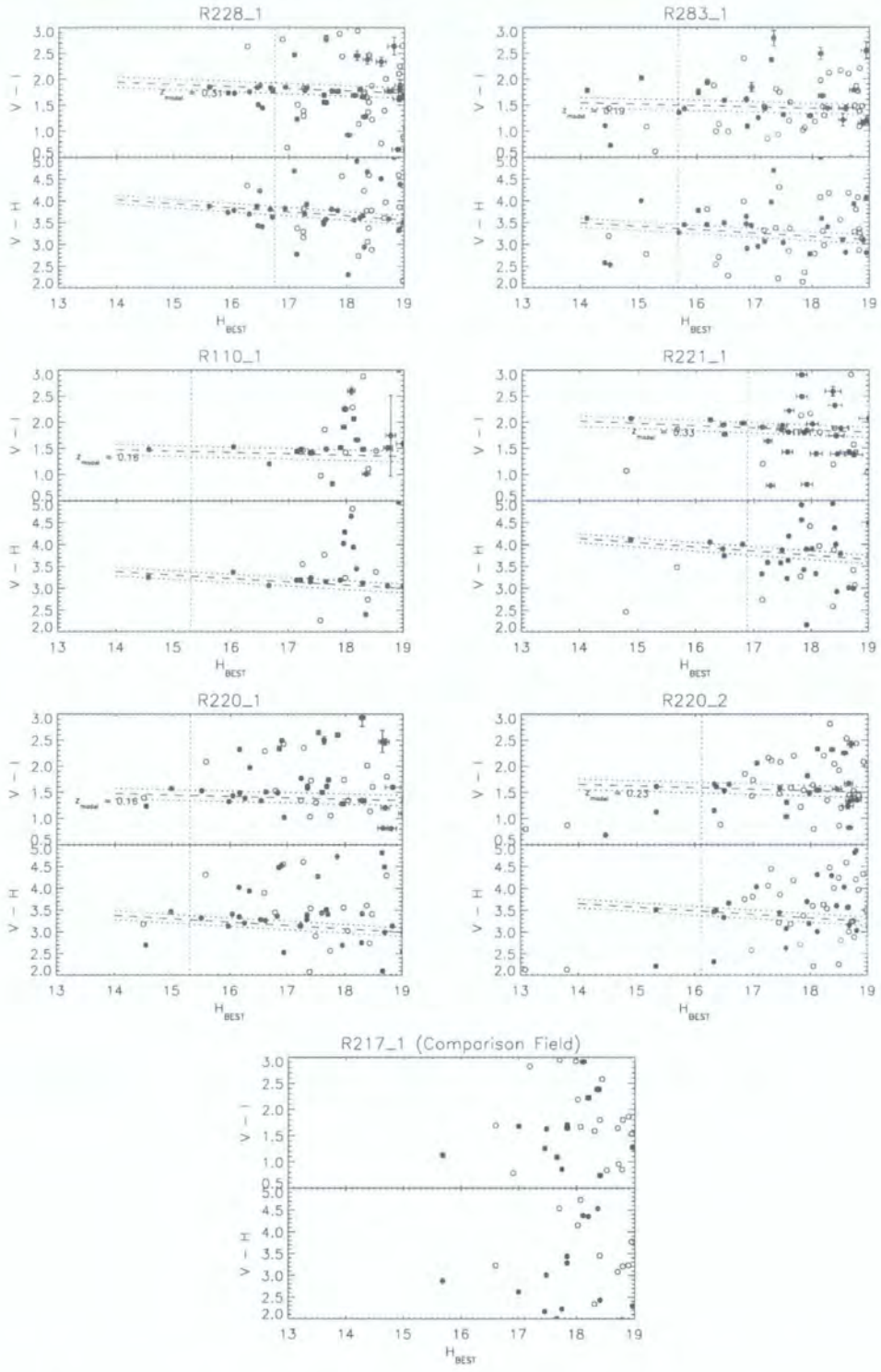

Figure 5.14: Optical-NIR CMDs for optically selected cluster candidates. Symbols as for previous figure.

A similar analysis as demonstrated on the Vikhlinin et al. (1998) clusters in the K-band is now performed on the H-band data. For the H-band data, field R217_1 is devoid of CMR selected candidates and will be used as a comparison field. Thus, the estimate of

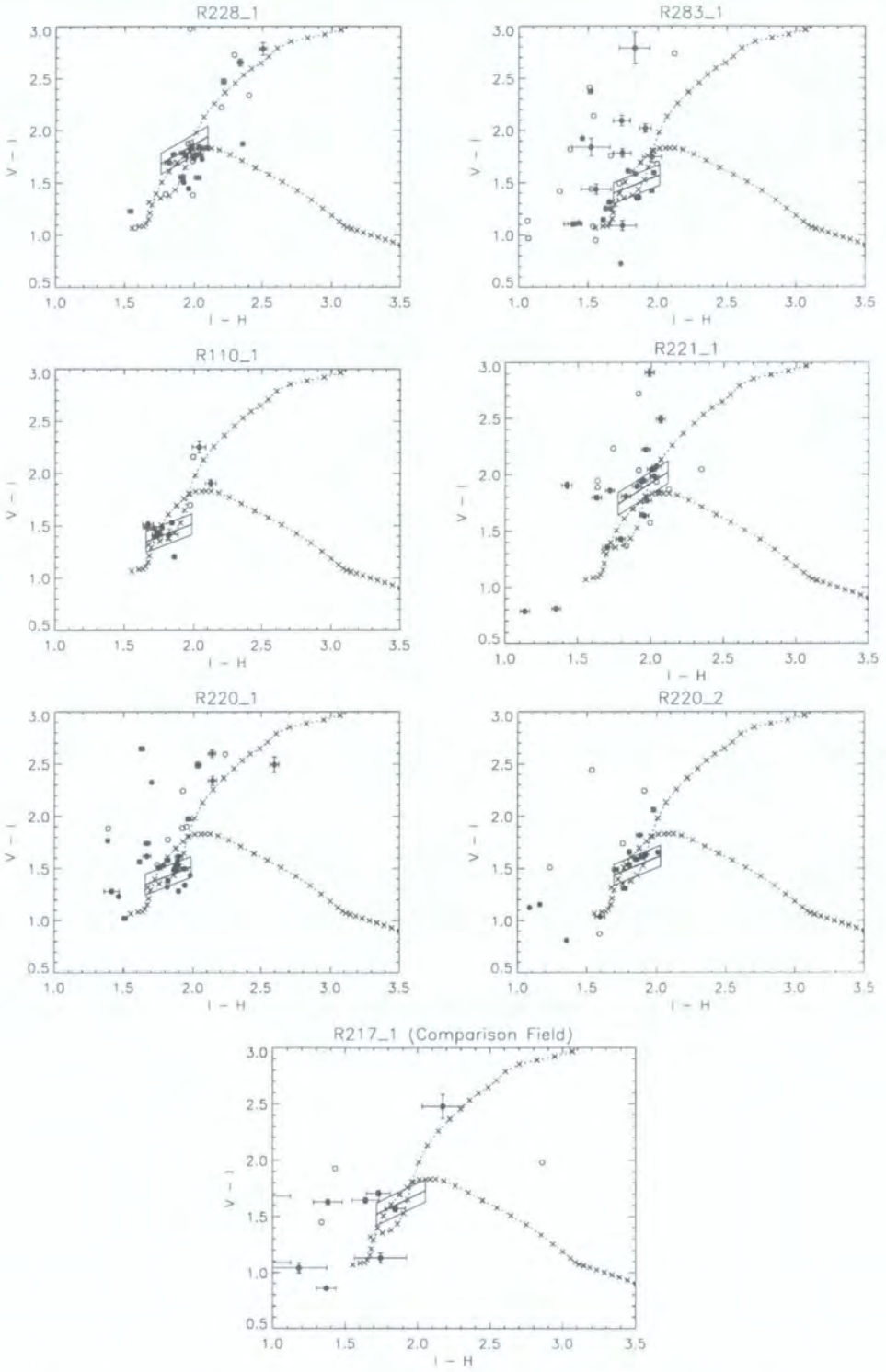

Figure 5.15: Optical-NIR Two-Colour Diagrams for optically selected cluster candidates. Symbols as for previous figure. The colour magnitude relation in the comparison field (R217_1) is shown at an example redshift of 0.25.

the number of field galaxies of a given colour can be obtained in two ways: from the outer annulus at the edge of the candidate's field, and from the comparison field, scaled to the same area. Both these methods are given in Table 5.5. A magnitude limit of H=18.0 is used in the analysis.

Field	z_{est}	z_{model}	N_{inner}	N_{outer}	$N^a_{comparison}$	P^b_1	P^c_2	N^d_{bluer}
R228_1	0.270	0.31	8	3	0	0.04	$< 5 \times 10^{-4}$	0
R283_1	0.190	0.19	2	1	1	0.26	0.26	2
R110_1	0.160	0.16	6	0	0	0.003	0.003	0
R220_1	0.160	0.16	6	1	0	0.02	0.003	2
R220_2	0.210	0.23	7	2	1	0.03	0.02	0
R221_1	0.280	0.33	5	1	2‡	0.04	0.13	2

Columns as for previous table except:

[a] Number of galaxies from comparison (R217_1) field.

[b] Probability of obtaining N_{inner} galaxies, or more, from a Poisson distribution with mean of N_{outer}.

[c] Probability of obtaining N_{inner} galaxies, or more, from a Poisson distribution with mean of $N_{comparison}$.

[d] Number of galaxies with colours compatible with V-I colour slice, but with I-H colours blueward of this. ‡ Two points with are only just included in the model CMR box due to their large colour errors. If these are excluded the probability is P=0.007.

5.6 Discussion and Conclusions

The first thing to notice is that all cluster candidate fields are overdense in bright galaxies, with respect to the comparison field, many with colours on or near a CMR. It is these bright galaxies, which are intrinsically rare in the field, which give the CMR technique most of its discriminatory power.

With the exception of R283_1, all the candidate fields show a low probability of exhibiting such a tight concentration of galaxies in projected distance and multicolour space by chance (using either the outer image area or the comparison field to model the back-

ground galaxy distribution). The candidates were selected on the basis of a tight colour-magnitude relation in V-I vs I. It can be seen for the case of R283_1 that replacing the I-band magnitude axis with the H-band increases the scatter of the relation, and several galaxies are scattered outside the model relation colour slice (Figure 5.14). This is also evidenced by the increased scatter over the other candidates in the I-H colour (Figure 5.15). Several of the other candidates show galaxies just outside the limits of the model CMRs in two colour space, despite showing tight concentrations of galaxies. This suggests that the analysis used may be too strict - requiring an exact colour match based on a single model relation as a function of redshift. Factors such as internal reddening by dust in the cluster galaxies could move the relation slightly in the 2CD. That said, the scatter in candidate R283_1 is much larger ($\approx 2\times$) than in the other, more probable, candidates. Therefore, this candidate is most likely spurious.

Half the candidates show some bluer I-H galaxies on the V-I, I CMR. Typically this corresponds to 1 galaxy out of 7 assigned to the V-I, I CMR not being genuine CMR members, or a contamination level of around 15%. Although, as mentioned earlier, these may still be CMR members, as the colour cuts used are strict.

To summarise, the techniques of near-infrared (NIR) data reduction have been detailed. Observations were made of 5 cluster candidates from the CMR catalogue, plus one blank comparison field, in the H-band and two Vikhlinin et al. (1998) clusters in the K-band. Photometric redshifts were examined and compared with spectroscopic redshifts of galaxies (of all colours) in Chapter 4. It was found that using VIH photometry yields insufficiently accurate photometric redshifts at z$\sim$0.3 in order to separate cluster and field galaxies.

The VMF clusters were used to demonstrate the appearance of genuine clusters as a tight overdensity in two colour optical near-infrared space, and also as two simultaneous colour-magnitude relations. This method was applied to the other five CMR candidates as a test of their reality. Using a comparison with field colour distributions, these were shown to be inconsistent with chance concentrations at the $\gtrsim 2\sigma$ level (although this simple test is somewhat pessimistic and overly restrictive). One candidate exhibited much larger scatter than the others (although still showing a concentration of bright red galaxies) and was found to occur $\approx$25% of the time by chance, assuming a Poisson distribution of galaxies of a given colour. If this candidate is spurious, then this amounts to a one false detection out of 20 in this work (counting the Vikhlinin et al. (1998) clusters in common, the spectroscopically confirmed candidates of Chapter 4 and the multicolour

confirmations of this chapter). Such an estimate is in good agreement with detailed simulations of Gladders & Yee (in prep.) who estimate a spurious detection rate from their red sequence survey of around 5%. The fact that this spurious detection was found using a third passband points out the advantages of further colours in isolating cluster early-type galaxies. Although the photometric redshift fits to individual galaxies were shown to be worse than fitting the colour-magnitude relation, further passbands are more useful for simultaneous colour fits to spatial concentrations of galaxies. This is a possible improvement of the current CMR finder, and will be examined in more detail in the next chapter.

The addition of B-band imaging is planned to allow photometric redshifts to be used for these fields. This will allow bluer cluster members to be located. With this improved dataset, the NIR data can be used in conjunction with stellar population synthesis models to measure stellar masses for galaxies in these systems, and to study such properties as a function of cluster X-ray luminosity.

Chapter 6

A Near-Infrared Survey for Distant Galaxy Clusters

6.1 Introduction

In recent years, several candidate clusters at $z \gtrsim 1$ have been put forward. However, few have spectroscopic confirmation, and the selection functions with which they were found are difficult to understand, or the samples are heavily biased.

Clusters at these high redshifts are incredibly powerful astrophysical tools. The abundance of massive clusters constrains Ω (Eke, Cole & Frenk 1996). The colours of member galaxies can place very tight limits on the formation epoch of their stellar populations. Kodama et al. (1998) showed that the CMR at $z>1$ is very sensitive to the stellar formation epoch. Changes in the relation are expected to be particularly prominent as the star formation phase of ellipticals is approached.

The methods used to select high-redshift clusters include: searching for extended X-ray emission; targeted searches around high-redshift radio galaxies/ quasars; and optical / NIR searches for the colour-magnitude relation (CMR) as described in Chapter 2. The methods which have been used to *successfully* find $z \gtrsim 1$ cluster candidates are summarised below.

Currently only 3 clusters at $z \gtrsim 1$ have published spectroscopic confirmation. Soucail et al. (2001) obtained spectroscopy for 44 galaxies in the field of the Hattori et al. (1997) cluster and identified 6 red galaxies at z=1.00. Stanford et al. (1997, 2001) obtained similar numbers of spectroscopic members for their two systems. Such small number statistics make any sort of dynamical analysis (even a simple velocity dispersion) unreliable. The selection of these clusters is described below.

6.1.1 X-ray Selection

The first of these techniques, X-ray selection, suffers from many biases (also described in Chapter 1). Potentially the most important bias is the fact that this only probes clusters with a limited range of thermal histories (the most massive, with hot dense intracluster plasmas). Hierarchical models predict that massive clusters at low redshifts grew from smaller clusters and groups at higher redshift (eg, Kauffmann et al. 1996). So, massive clusters at high redshift would be incredibly massive by lower redshifts, and thus they have no counterparts in the local universe. This makes the X-ray selected clusters less useful in terms of building a picture of cluster evolution as a series of snapshots of clusters seen at different epochs. Also, such massive clusters are rare and a large volume must be examined in order to find them.

The best studied z$\gtrsim$1 clusters are probably $CIG0848+4453$ and $RXJ0848.9+4452$. The former was discovered by Stanford et al. (1997) in a NIR survey and the latter in the ROSAT Deep Cluster Survey (RDCS) by Rosati et al (1999). These two clusters lie within 4.2 arc minutes of each other on the sky, and their redshifts are z=1.27 and 1.26 respectively. The X-ray selected cluster was drawn from 50 square degrees surveyed down to an X-ray flux of 1×10^{-14}erg s^{-1}cm^{-2}. It should be noted that the limiting factor in identifying high redshift cluster candidates is the optical follow up, and Rosati et al (1999) estimate that several z$\gtrsim$1 clusters remain to be identified in the RDCS. The NIR selected cluster was also found to be X-ray luminous from archival ROSAT imaging.

Stanford et al. (2001) observed this pair of clusters with the Chandra X-ray observatory[1] and found best fit temperatures of $kT = 5.8^{+2.6}_{-1.7}$keV, and $kT = 1.6^{+0.8}_{-0.6}$keV. These temperatures are in line with expectations from the X-ray luminosities (3.3 and 0.7 $\times 10^{44}$ erg s^{-1} bolometric, respectively) expected if the clusters lie on the local $L_X - T_X$ relation. This translates into a mass (under the assumption of hydrostatic equilibrium) within $1h_{65}^{-1}$Mpc of $4.0^{+2.4}_{-1.9} \times 10^{14}$ h_{65}^{-1} $M_\odot$ for the most massive cluster. (The authors did not calculate a mass for the less luminous cluster, due to its strong departure from spherical symmetry, and uncertain T_X.) The two clusters show very different morphologies as traced by X-rays, and galaxies in the optical and NIR. The more luminous cluster shows symmetric, spatially concentrated X-ray emission like that seen in lower redshift relaxed clusters. The second has weak, amorphous X-ray emission and appears to be two groups in the process of merging. However, both these systems are dominated by red galaxies.

[1]Note: an incredibly long exposure was required (a total of 185ks!). The flux of the fainter cluster is $\sim 1 \times 10^{-15}$ erg s^{-1} cm^{-2} - an order of magnitude less than the limit used in the XDCS PSPC observations.

which appear to have little or no recent star formation (Stanford et al. 1997, Rosati et al 1999) and the median I-K colours are the same to within 0.05 magnitudes. This suggests that cluster early type galaxies were in place prior to the formation of the cluster. Since the X-ray selected cluster was found without direct reference to its member galaxies (and the NIR-selected cluster could also have been found in the X-ray survey), this is additional evidence for all clusters showing overdensities of red galaxies, even at these redshifts.

6.1.2 Targeted Searches

Targeted searches around radio galaxies/ quasars seems to be the currently most popular technique. The idea is that radio-loud galaxies (RLGs) provide signposts for clusters, since RLGs are found almost exclusively in giant elliptical galaxies, which themselves lie almost exclusively in clusters. At $z\sim0.5$, about half of the powerful FRII (Fanaroff & Riley 1974) double radio sources (Hill & Lilly 1991) are found in clusters of Abell Richness Class (ARC) 0, or richer. A similar environment dependence is seen for quasars at similar redshifts (Yee & Green 1987). The method adopted by previous investigators has been to obtain optical and/or NIR imaging for the region around the RLG and look for the presence of an overdensity of faint/red galaxies (ie. galaxies likely to be at high redshift).[2]

The two largest surveys of this kind have been carried out by Best (2000) and Hall et al. (1998). Best (2000) probed the environments of 28 3CR radio galaxies in the redshift range $0.6<z<1.8$. He found K-band overdensities of galaxies in these fields, the mean counts being comparable to ARC 0 clusters; and a sharp peak in the angular cross-correlation function, centred on the radio galaxy. The $z\lesssim0.9$ radio galaxy environments generally showed a well defined NIR CMR; whereas for the higher redshift objects, the CMRs are less prominent, but a statistical excess of red galaxies (in J-K) is present. Best (2000) concluded that although large field-to-field variations were seen, the mean of all the radio galaxy fields lies in a (proto-) cluster environment.

Hall et al. (1998) carried out an optical and K-band search around 31 Radio-Loud Quasars (RLQs) in the range: $1<z<2$ and found a population of predominantly red r-K galaxies in these fields, these red excess populations being indistinguishable from each other, but significantly redder than the field. The excess was marginally significant

[2]Spectroscopic confirmation of the brightest of such faint objects (say, M^* at $z=1$) is still quite observationally expensive, but possible in $\sim$2 hours of 8m telescope time.

($\sim 2\sigma$) only for K>19, the field of view of these observations was only 3×3 arcmins, and the depth varied from field to field, making background subtraction difficult. As a further note, the hypothesis that these excess galaxies were associated with intervening MgII absorption line systems along the line of sight to the quasar was tested, but rejected when it was found that the overdensities of the systems with and without MgII absorbers were comparable. A follow up, wider field NIR study (Hall et al. 2001), showed that these fields have a surface density of extremely red objects (EROs, R-K>6) 2.7 times that of the general field. If these are early-type galaxies at the redshift of the quasar, then they have luminosities of only $\sim L^{\star}$, although this is very sensitive to the presence of dust. Only one of the four RLQ fields has an excess of *J-K selected EROs (J-K>2.5)*, but these are mostly unrelated to the quasars. Hall et al. (2001) claim that, overall, their observations support the idea that radio-loud quasars at z>1 are found in galaxy overdensities, with all but the reddest galaxies showing evidence for recent star-formation (from a variety of techniques, such as SED-fitting, narrow-band imaging). Obviously, spectroscopy is essential to confirm these hypotheses.

The problem with this targeted selection technique is that the relationship between radio-loud objects and the cluster environments in which they are found is not well known. Theoretical arguments to produce radio sources require a high AGN power, and a dense environment to confine the radio lobes, and convert the jet kinetic energy efficiently into radiation. In order to establish what subsample of the total cluster population these searches target, arguments involving the lifetime and visibility of the radio sources must be made. The richness of galaxies on the CMRs in Best's sample shows a range in environmental densities for these RLG selected clusters.

An extreme example of this method is the cluster candidate discovered by Haines et al. (2001). They identified a CMR with deep optical and NIR imaging in the field of a Large Quasar Group (LQG). LQGs are associations of 4-25 quasars which trace structures 100-200h^{-1}Mpc across (eg., Clowes & Campusano 1991). The CMR and photometric redshifts are consistent with a z=1.2 cluster[3]. The LQG contains $\sim$20 quasars within $\Delta z \sim 0.1$ of this. Spectroscopic follow up of this system is underway.

[3]The authors also claimed evidence for an overdensity of blue galaxies at the same redshift, which they interpreted as the signature of a cluster-cluster merger, although with only 3-band photometry, many degeneracies exist between age, dust and redshift, making the photometric redshift technique difficult.

6.1.3 Blank Field Optical/ NIR Searches

Searching blank fields directly for the CMR in multi-band optical/ NIR data, without first requiring a RLG is another possibility. As mentioned above, the Stanford et al. (1997) cluster was first identified in a blank-field NIR survey (Eisenhardt et al, in preparation). A simple method of filtering the galaxy catalogue from the 100 arcmin^2 [4] $BRIzJ$ K_s imaging to only leave galaxies with J- K_s $\geq$1.9 (potentially z$\gtrsim$1 galaxies) revealed a spatially concentrated group of galaxies, which was then spectroscopically confirmed to be a cluster.

The Munich Near-Infrared Cluster Survey (MUNICS, Drory et al. 2001) is currently the widest NIR cluster survey. It covers $\sim$1 deg^2 in the K′ and J passbands (to 50 per cent completeness limits of $\sim$19.5 and 21, respectively). The survey is broken up into 16 6×6 arcmin^2 regions targeted at QSOs with redshifts in the range 0.5<z<2 and the remaining area covers 7 random 28×13 arcmin^2 strips at high Galactic latitude. Additional optical imaging and spectroscopy has been taken and, when completed, the survey aims to identify clusters at redshifts of order unity and select a sample of early-type galaxies in the field of redshift up to about 1.5 for evolutionary studies.

Optical colour surveys for high redshift clusters have been carried out by Olsen et al. (1999b), Gladders & Yee (2000). Most of the EIS V-band imaging is too shallow to detect cluster candidates at z$\gtrsim$0.7 using just their V- and I-band data (Olsen et al. 1999b). The Red Cluster Sequence Survey of Gladders & Yee (2000) has provided many z$\gtrsim$1 candidates, using R and z′ imaging, but so far with no published spectroscopic confirmation (although features which seem to be arcs from strong gravitational lensing are seen around some candidates).

Gravitational lensing is another possibility for high redshift cluster selection. Lawrence et al. (1994) discovered a triple quasar system caused by gravitational lensing of a z=3.26 quasar. The lens was partially accounted for by a z=1.01 giant elliptical galaxy. X-ray imaging of the region revealed the signature of a hot ICM (Hattori et al. 1997). For a while the cluster lacked a counterpart in the optical, and was nicknamed a "Dark Cluster", but deep optical and NIR imaging by Benitez et al. (1999) identified an overdensity of red galaxies. Another lensing technique was used by Smail & Dickinson (1995) who looked for the weak-shear signature of a cluster gravitational potential in the field of the z=1.206 radio galaxy 3C324; and also Bower & Smail (1997) who performed a similar search in

[4] This was an unusually large area for a NIR survey in 1997, when it was undertaken, and is still wide-field by today's standards.

archival HST images of z$\sim$1 radio sources, resulting in the identification of a significant shear signal around a radio-loud quasar at z=0.927.

To summarise: *(i)* X-ray selection finds clusters which possess hot, dense ICMs, potentially out to high redshifts. However, optical/ NIR follow-up imaging is required to confirm these (the limitations of this technique are described in more detail in Chapter 1). *(ii)* Targeted searches aimed at objects such as high-redshift radio sources have certainly produced good candidate clusters, and may represent the most efficient starting point for a cluster survey, given the large number of wide-area, publically-available radio catalogues. However, such candidates would only represent a (probably quite small) subsample of clusters; and the biases within such a sample are not clear. *(iii)* Blank-field optical and NIR surveys require a considerable investment of telescope time (especially in the NIR given the area of current detectors, but these are increasing all the time), but given that all the other methods require optical/ NIR follow-up anyway it is clear such large areas surveys area required. More than one technique is possible with the same optical/ NIR dataset, ie. colour-selection of high-redshift early-type galaxies, and gravitational weak-shear mapping. All known clusters possess a sequence of red early-type galaxies, so it is natural to search for this. The requirement for the weak-shear mapping is that the instrumental distortions are small (to measure accurate ellipticities for galaxies) and that the redshift distribution of background galaxies is well-known. This means that the use of many optical/ NIR bands is desirable to accurately measure the colours of early-type galaxies and to measure N(z) for the lensing analysis with photometric redshifts.

6.1.4 The Advantages of the NIR

Figure 6.1 shows a z=0 and z=1 Elliptical galaxy SED, with the optical and NIR passbands V, I, J, and K overplotted. It can be seen immediately that at high redshift the optical passbands begin sampling the restframe ultraviolet portion of the galaxy spectrum. For comparison, a late-type spiral is also illustrated. Its ultraviolet emission is much greater than that of the elliptical, as this wavelength regime is dominated by the light of short-lived, massive stars (eg, Bruzual & Charlot 1993). Thus, selecting samples of high redshift galaxies in optical passbands results in a sample biased toward actively star-forming galaxies. The figure also demonstrates that the NIR portions of the SEDs are very similar for ellipticals and spirals, and thus K selected samples are relatively insensitive to galaxy type. Furthermore, comparing the low and high redshift E SED, the K-band flux is actually *increased* at high z and thus k-corrections in the K-band are small

or even negative over a wide redshift range (eg, Cowie et al. 1994).

The problem with a NIR-based survey is that even with recent improvements in large format NIR detectors, the overheads in conducting such a survey are high (see §6.6). To cover the equivalent area of XDCS to a similar depth would require $\sim$ 50 nights of 4m telescope time. A more efficient NIR survey can be made by selecting areas from XDCS which contain overdensities of red objects with V-I colours consistent with z$\sim$1 passively evolving ellipticals, from the models of Kodama & Arimoto (1997). Such colours are difficult to achieve with objects other than ellipticals at high redshift. At the depths required to see such objects, the XDCS photometric errors become quite large, and incompleteness starts to become problematic but the brightest z$\sim$1 ellipticals (the most powerful points on the CMR for indicating a possible cluster, Chapter 2) should be visible.

Ideally such a survey would include the J and K bands. The J-K colour is useful as an indicator of z>1 galaxies (for example, Pozzetti & Mannucci 2000, Stanford et al. 1997).

6.2 Sample Selection

The NIR observations were made using the Isaac Newton Group Red Imaging Device (INGRID), at the bent-Cassegrain focus of the 4.2m WHT on the nights of 28-30 November 2000, by Drs Bower and Kodama. INGRID is a 1024^2 HAWAII-2 detector with a pixel scale of 0.242"/pixel and a field of view of 4.13 arcmins.

Fields from the second XDCS run were selected (to meet RA restrictions for the observing run). For each field, a simplified version of the CMR detection algorithm was run. This consisted of filtering the object catalogues (created as described in Chapter 2), to find galaxies redder than V-I=2.5 (consistent with the Kodama & Arimoto (1997) prediction for z=1.00 ellipticals, allowing for the considerable photometric errors). A simple top-hat filter of radius 200 pixels (67 arcsec), corresponding to the approximate core size of a cluster at z$\sim$1 ($\sim$0.5Mpc), was run over the data: the centre of the search cell being located by the galaxy positions, as before. All locations containing more than 4 red galaxies in the search cell were retained. To narrow down the list, candidates which did not have overlapping imaging in the other rotated field of the WFC (eg. candidates at the edge of the A-rotation field, without overlapping B-rotation imaging, in the notation of Chapter 2) were rejected. All candidates were visually inspected to make sure detections were due to real objects and not eg. stellar diffraction spikes, or excessively deblended objects. False detections were removed by hand, and the list re-sorted. To improve the

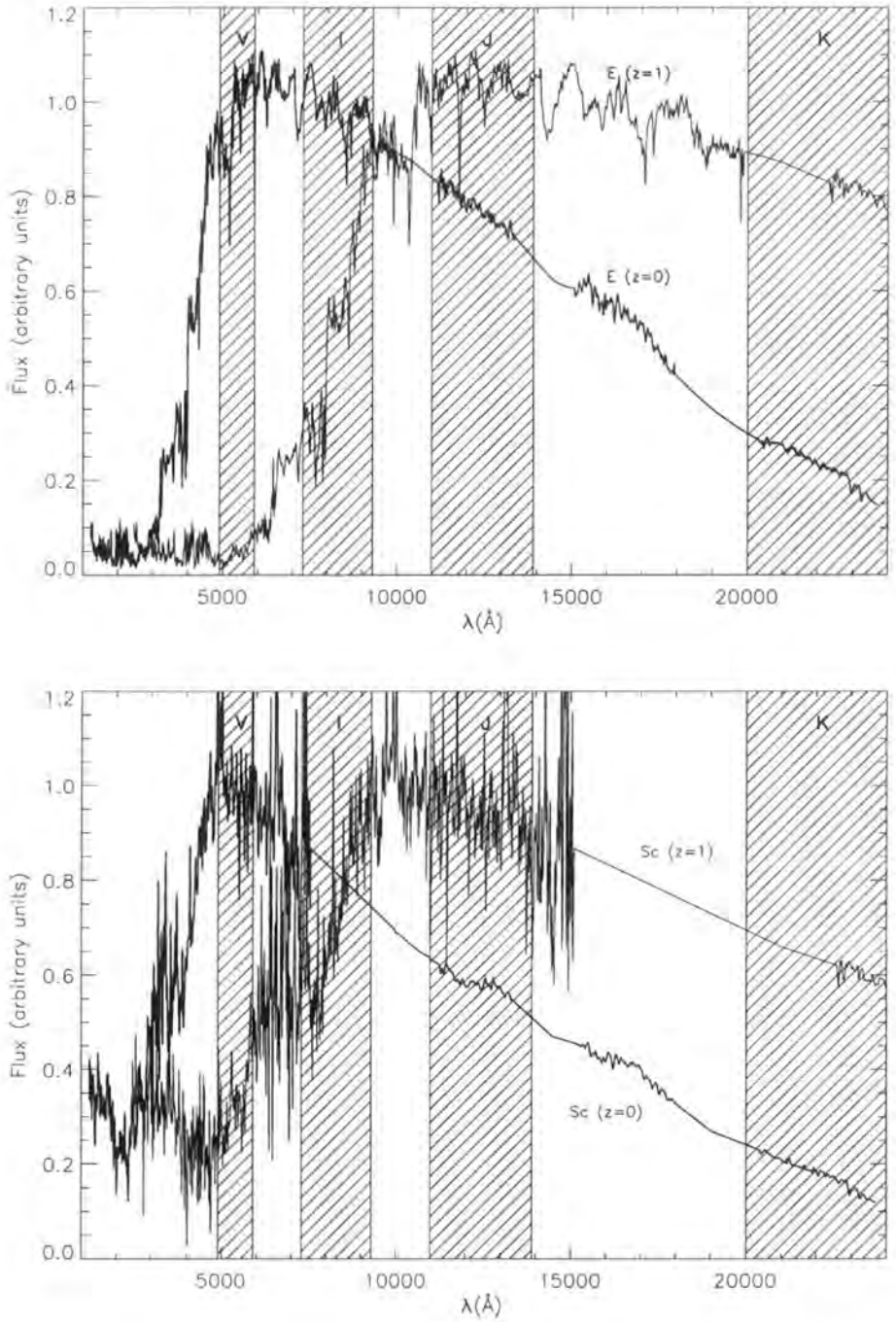

Figure 6.1: Top panel: Elliptical SED (Mannucci et al. 2001) at z=0 (thick line) and z=1 (thin line), with optical and NIR passbands superposed. V, I, J and K filter widths (between half-maximum transmission) are shown hatched. Note the prominent feature of the spectral break at 4000Å(z=0). At redshift ∼1 the V-band filter is already sampling the restframe ultraviolet emission. Bottom panel: Same plot for a type Sc spiral galaxy. Here the ultraviolet light is dominated by emission from short-lived stars, and a sharp upturn occurs toward shorter wavelengths. Note the prominent emission lines: OII (3727Å, restframe) and Hα (6563Å).

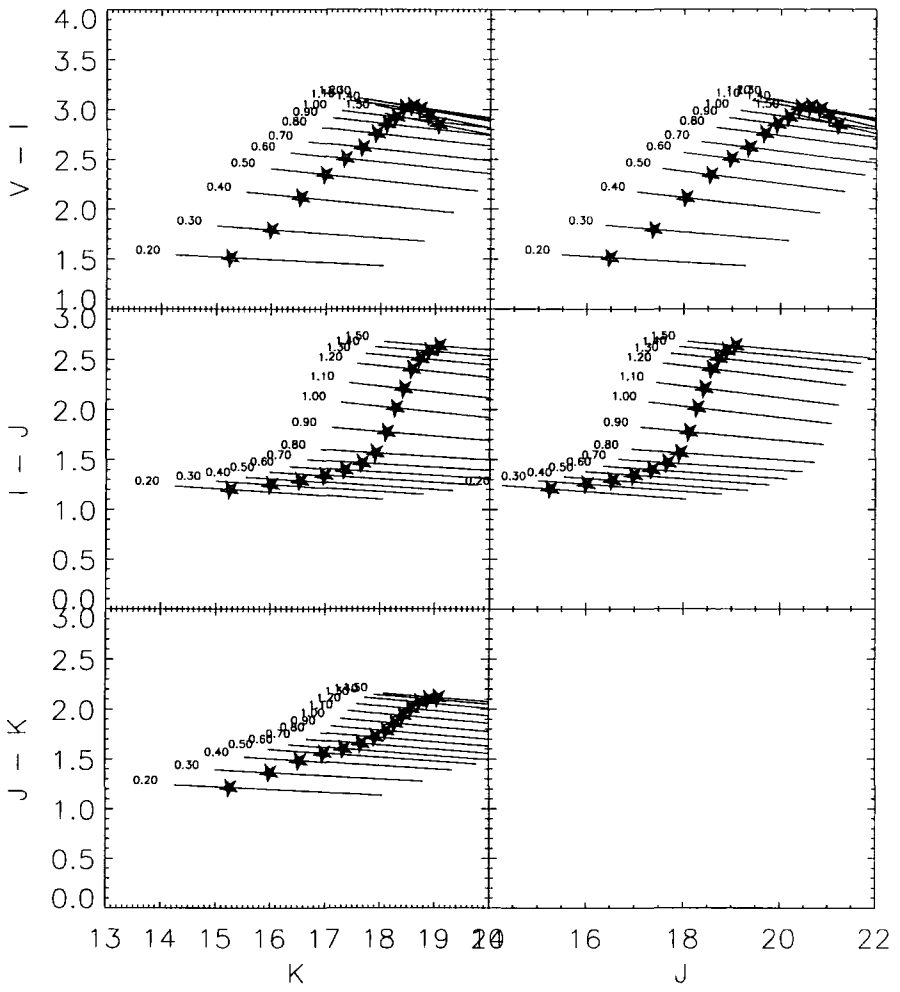

Figure 6.2: Model CMRs in the optical and NIR. Numbers to the left of each line indicate the redshift, stars indicate the position of an L* elliptical. The reddest passband available (for VIJ and VIJK datasets, as will be used in this survey) is plotted on the horizontal axis (hence, the lower rightmost panel is empty).

depth and accuracy of the photometry, 4.5 × 4.5 arcmin regions (slightly larger than the field of view of INGRID) were excised from the images, and the A and B data for each band coadded. Object detection was re-run using `SExtractor` on the I-band image, the photometry repeated, and the cluster detection routine repeated. Although coadding the I-band images reduced the effect of residual fringing (see Chapter 2), some still remained, causing many spurious detections in some fields. These were again removed by visual inspection. A search of the NASA Extragalactic Database[5] was conducted to check for previously discovered clusters within the INGRID field of view. One was found - GHO 1313+2911, a candidate from Gunn, Hoessel & Oke's (1986) catalogue (lacking spectroscopic confirmation). This was rejected from the list. This resulted in a list of 28 candidates containing 4 or more red galaxies within the original 67 arcsec search cell. Objects for INGRID imaging were selected randomly from this complete list, given the available RA range, by the observers at the telescope. J-band observations were made first, and quick CMDs plotted at the telescope. Those fields showing the best CMRs were chosen for K-band imaging. The candidates that were imaged in the NIR are listed in Table 6.1 and illustrated in Figure 6.3.

[5]The NASA/IPAC Extragalactic Database (NED) is operated by the Jet Propulsion Laboratory, California Institute of Technology, under contract with the National Aeronautics and Space Administration.

Figure 6.3: Coadded Optical Images of INGRID targets. I and V-band images with red objects (as described in text) circled. See also Table 6.1.

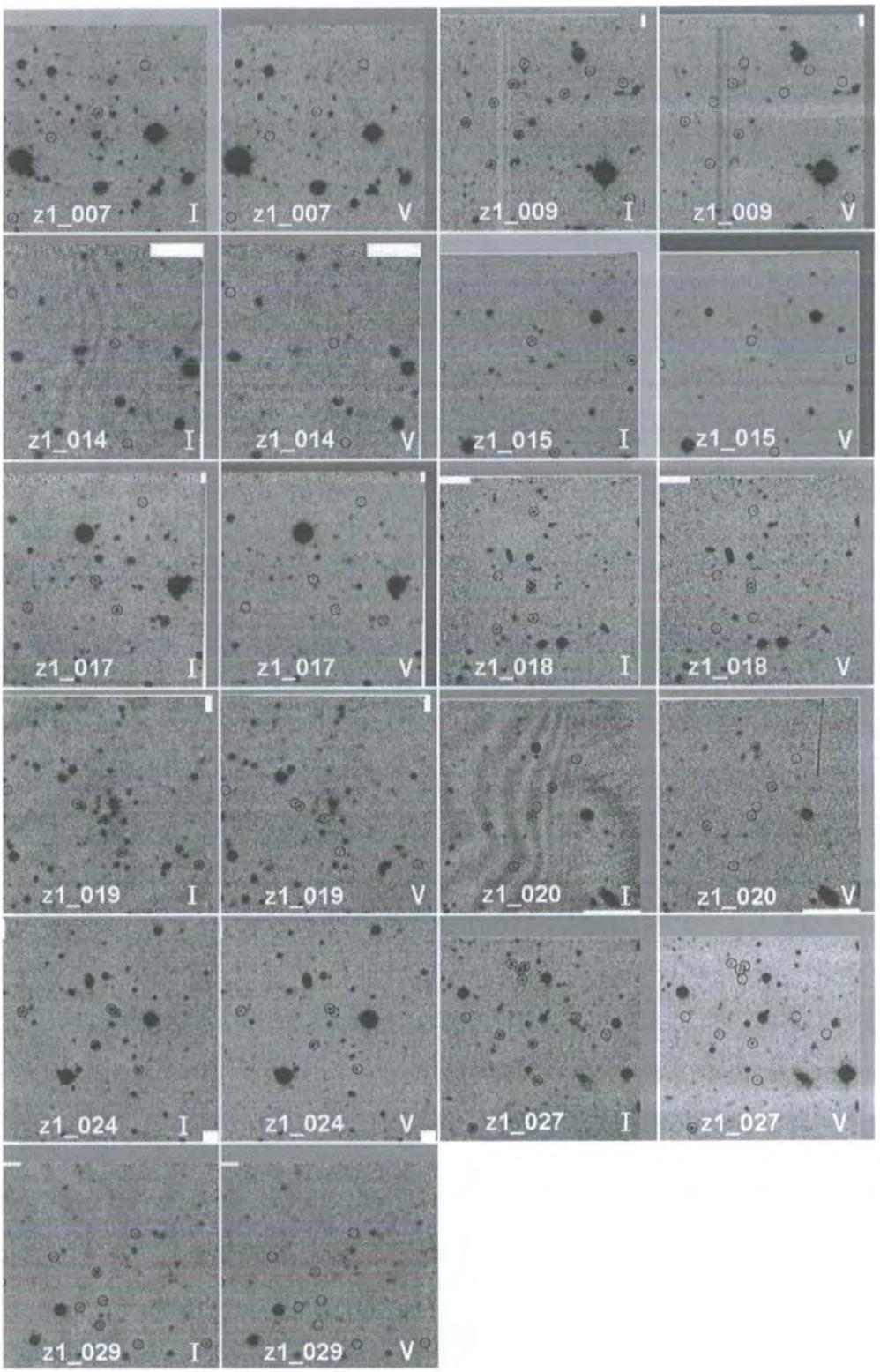

6.3 Near Infrared Observations

6.3.1 Observations and Data Reduction

Observations

The K-band filter used here is the "K-short", K_s [6] filter (McLeod, et al. 1995). Each field was observed for typically 3600s in J and 450s in K_s , using a 9-point 2D dither pattern which was itself slowly dithered around the sky.

Table 6.1: Log of observations of cluster candidates with INGRID.

Field ID	RIXOS ID	α (J2000) [hh:mm:ss]	δ(J2000) [dd:mm:ss]	Passbands
z1_007	R211A	07:19:37.56	71:09:45.4	J, K_s
z1_009	R257B	09:05:26.30	34:18:08.3	J
z1_014	R292B	01:43:58.62	04:14:35.1	J, K_s
z1_015	R123B	11:18:09.00	21:15:49.0	J
z1_017	R211A	07:24:41.36	71:31:04.1	J
z1_018	R133B	10:57:36.00	49:57:45.7	J, K_s
z1_019	R245A	03:28:58.01	02:57:40.0	J, K_s
z1_020†	R262A	01:24:57.24	03:55:44.7	J, K_s
z1_024	R213B	08:04:48.00	65:00:57.6	J
z1_026	R293A	08:19:41.70	37:32:24.0	J, K_s
z1_029	R245B	03:29:02.94	02:51:07.7	J, K_s

† NED search shows a quasar at z=1.2 and associated absorption line systems within 2 arcmins of centre.

Conditions on all 3 nights were non-photometric, due to light cirrus. Calibration data were obtained and are described below.

Data Reduction

Data reduction was carried out with a combination of `IRAF` and `CCDPACK` routines. The optical WFC reduction was described in Chapter 2.

Each INGRID science observation consists of a post-scan and pre-scan image, containing the initial and final count levels of the device. The pre-scan was subtracted from the

[6] which is narrower and cuts-off at a shorter wavelength than the standard K-band filter (1.99 - 2.30 μm, FWHM), thus reducing contamination from the thermal background (eg., telescope and dome).

post-scan to give the raw image. Thereafter, the standard techniques described in Chapter 5 were used. Flatfielding and sky-subtraction was achieved using the local flatfielding technique described in §5.2.3. A median of the 8 nearest time-adjacent frames was used.

The images in each field were mutually aligned using `CCDPACK` routines, to cross-correlate bright objects between the fields and calculate the offsets, as described in §5.2.4. Shifting of the images to their registered positions was achieved in `IRAF` using sub-pixel shifts. Since the observing run was non-photometric, it was necessary to compensate for extinction variations by scaling each frame in a field to a reference frame (taken from each field). The correction method of §5.2.5 was used. Variations at the level of $\lesssim$0.3 magnitudes were measured and corrected.

The scaled data then had their bad pixels masked (a row and column of bad pixels occurs at the interface of the quadrants which make up the INGRID chip) and were then mosaicked using median combination within the CCDPACK routine `makemos`.

The optical WFC data were geometrically mapped to the NIR INGRID data.

Object detection and Photometry

For the fields possessing K_s -band imaging, a coadded frame was made from the J and K_s frames. `SExtractor` was run in `dual image mode` using the J+ K_s image for object detection, and the K_s image for determination of photometric properties, such as `MAG_BEST` magnitudes and the `CLASS_STAR` parameter. Using the coadded images for object detection has the advantage that the depth of the images is increased, and the colour bias of detected objects is reduced. For fields with only J-band imaging, `SExtractor` was run on the J image. The positions of objects and their stellaricity indices were taken from the catalogues. The x,y positions were used to place a photometry aperture using `qphot` in `IRAF`. The seeing during the INGRID run was mostly around 1 arc second or less; whereas the WFC data were acquired during ~2 arc second seeing. So, to compensate for the differences in the PSF (when measuring colours of objects), bright stars were located, their PSFs measured and the median seeing for each band calculated. The different bands were then convolved to the worst seeing, assuming a Gaussian PSF (as described in Chapter 2). The diameter of the aperture was chosen to be 2.6 times the FWHM of the seeing of the convolved frames (as in Chapter 2), so that all aperture magnitudes would be placed on the same photometric system, after calibration.

The optical catalogues measured from the NIR data change slightly from the initial WFC catalogues for two reasons. Firstly the seeing in the NIR frames is much better and

therefore star/ galaxy separation using these data for shape measurement is improved. Secondly objects detected in the NIR data but not in the optical images are now included, but as limits in the optical/ optical-NIR colours. The revised optical catalogues can be seen in the V - I, I CMDs in Figure 6.6 and 6.4.2. A potential problem with star/ galaxy classification could be caused by the mosaicking process. The roundness of stars could be affected if the offsets between individual exposures are not correctly measured before combining them. In order to assess this potential contamination, two tests were performed. Firstly, the colours of objects classified as stars by `SExtractor` 's (`CLASS_STAR` > 0.97) were examined to check that objects classified as stars did not have the colours of galaxies (this contamination is less likely than the reverse, by the argument above). It can be seen from Figure 6.8 that the separation between stars and galaxies in I,J,K colour-colour space is reasonably well defined. The colours of stars classified by `SExtractor` `CLASS_STAR` in all fields is shown in Figure 6.5. From all the fields, a total of 7 objects classified as stars have IJK colours which place them within the locus of galaxies, or a potential false positive rate of $\approx$1 per field. In order to assess the reverse misclassification (ie. stars classified as galaxies) the two colour diagrams in §6.5 can be examined. If the I-K<4 region is inspected first, then a generous limit for the locus of stars is J-K<1.3. Each field has one or two objects within the search radius (ie. filled symbols) within this region. The model galaxy tracks of Figure 6.9 show that only the lowest redshift galaxies (z<0.3) occupy this region, so confusion for this project is not a problem. For the I-K>4 cut (potentially high redshift galaxies) taking a J-K<1.5 cut for the stellar locus, only z1_007 has any number of objects in this region. This suggests that star/ galaxy classification could be slightly worse for this field. In any case, the colours of the objects of interest still lie well away from the stellar locus. Thus, stellar contamination does not present a problem for high redshift cluster finding with IJK data.

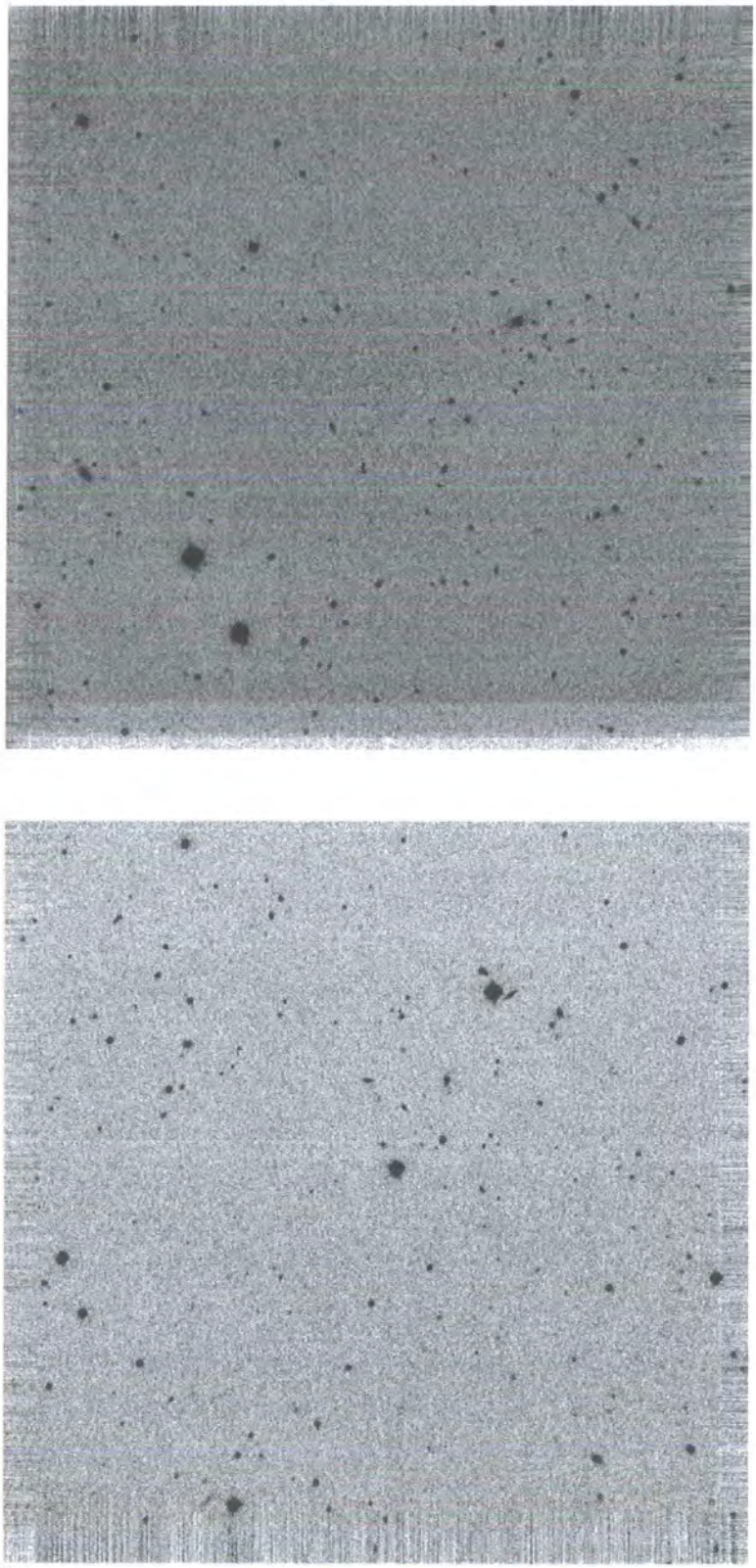

Figure 6.4: Typical J-band (left) and K_s -band (right) INGRID images.

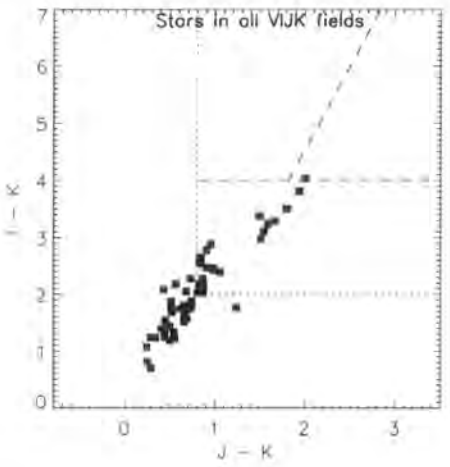

Figure 6.5: The colour of stars in all IJK fields, as classified by `SExtractor` . Dotted lines show the region plotted in the galaxy two-colour diagrams.

Since the fields are quite small, comparing number counts with the literature to assess the completeness is not the best way to estimate the limiting magnitudes of the data. Limiting magnitudes for the field were determined by taking the 1σ limit from the background rms estimated from `SExtractor` after running it on each passband image. The `SExtractor` catalogues generated in this way contain an estimate of the *threshold* (ie. peak flux above the background) and aperture magnitudes for each entry. In this way the magnitude of an object giving a *threshold* entry of 3 times the background rms can be found, and thus 3σ limiting magnitudes estimated. Although depths vary slightly from field to field, conservative 3σ limiting magnitudes for the survey are V$\sim$23.5, I$\sim$23., J$\sim$21.0, K$\sim$19.5.

Calibration Data

For the purpose of photometric calibration, short snapshots of regions of each field containing bright stars were obtained from the UKIRT[7] Fast-Track Imager, UFTI, on the 3.8m UK Infra-Red Telescope in service time, and from INGRID as part of another project. These were interleaved with observations of standard stars from the UKIRT Standards list (Hawarden et al. 2001). The UFTI images were typically 120 - 180 sec integrations, reduced in the standard way. The UFTI snapshots were calibrated onto the UKIRT system from observations of the standard stars. No colour or extinction terms

[7]UKIRT is operated by the Joint Astronomy Centre on behalf of the Particle Physics and Astronomy Research Council of the United Kingdom.

were fitted - the former was neglected as not all fields contained colour information [8] (ie. J *and* K_s observations) and the latter as extinction in the NIR is low, and both science and calibration images were observed at similar airmasses. Such short exposures seemed acceptable as bright, unsaturated stars with sufficient signal-to-noise to allow accurate (~0.01 mag) calibration were present in each field[9]. The standard star solution results in a good calibration of the photometric zeropoint for the night (star-to-star dispersion ~0.01 - 0.02 mags). These zeropoints are then applied to the UFTI snapshots of the science fields. The error in this calibration is negligible in comparison with calculating the photometric offset between the snapshot and the science frame, taken with the different instruments, and so only this latter error is considered in the photometric solution. So, by observing these bright stars in both the original science frames and the calibration images, a simple zero-point offset should be enough to calibrate each frame. The drawback with this method is that some calibration fields contained very few stars, which did not give consistent zero-point offsets between the science and calibration images. This is possibly because the stars are variable; or may be due to a small colour term becoming noticeable with stars of extreme colours. The number of stars used in each solution is given in Table 6.2. As a result of this, some fields resulted in unacceptable calibrations. This was identified by plotting colour-magnitude diagrams in K, J-K and in J, I-J and examining the distributions. Several fields had distributions which were clearly different from the others (and from the literature, eg., Cowie et al. (1996)) by as much as 0.5 - 1.0 magnitudes. Thus four fields were rejected (z1_009, z1_014, z1_015, z1_018). For these fields, each calibration star in turn was assumed to give the correct zeropoint and the colour-magnitude diagrams replotted (to see if a sensible calibration could be obtained from any one star; typically these fields only contained two or three calibration stars), but in no case did a sensible calibration result. [10] The same procedure was repeated for the INGRID calibration data.

Galactic reddening in the NIR is low and comparable to the uncertainties in the

[8] Also, Minezaki et al. (1998) find no colour term between the K and K_s filters.

[9] Bright galaxies are much rarer, so in order to obtain a calibration of similar accuracy, a much longer integration must be obtained (a sizeable fraction of the science frame exposure time!). This then becomes unfeasible within the confines of service time.

[10] Calibration against the 2MASS catalogue (as described in Chapter 5) was also tried. However, few fields overlapped (4, and one of these was already well-calibrated from UFTI) and the brightest sources in the 2MASS fields were either saturated in the INGRID data, or were the same objects as those which give a poor calibration from the UFTI snapshots.

absolute calibration of the NIR data. Therefore NIR extinction corrections are ignored. Note: reddening by the Milky Way makes the greatest difference to the optical-NIR colours (ie. I - J, I - K); since the optical bands, V and I, have roughly comparable reddening, but reddening in I is greater than J or K. Reddening corrections to the WFC data were applied to each field using the dust maps of Schlegel, Finkbeiner & Davis (1998), as described in Chapter 2.

Table 6.2: NIR Zeropoints from Calibration data

Field	zpt_J	$N_J^\dagger$	$\sigma_J^\ddagger$	Date	zpt_K	$N_K^\dagger$	$\sigma_K^\ddagger$	Date	Instrument
z1_007	28.47	5	0.11	30/03/2001	25.05	5	0.03	29/03/2001	INGRID
z1_009	—	—	—	17/03/2001	n/a	n/a	n/a	n/a	UFTI
z1_014	—	—	—	04/02/2001	—	—	—	04/02/2001	UFTI
z1_015	—	—	—	17/03/2001	n/a	n/a	n/a	n/a	UFTI
z1_017	28.32	2	0.05	31/03/2001	n/a	n/a	n/a	n/a	INGRID
z1_018	—	—	—	17/03/2001	n/a	n/a	n/a	n/a	UFTI
z1_019	28.28	2	0.12	01/02/2001	24.78	1	/	01/02/2001	UFTI
z1_020	27.27	1	/	04/02/2001	24.64	1	/	04/02/2001	UFTI
z1_024	28.28	6	0.08	31/03/2001	n/a	n/a	n/a	n/a	INGRID
z1_026	28.30	3	0.04	17/03/2001	25.27	2	0.04	17/03/2001	UFTI
z1_029	28.33	2	0.28	01/02/2001	24.90	2	0.03	01/02/2001	UFTI

† Number of stars used to measure zeropoint difference between calibration snapshot and science image

‡ Dispersion of zeropoint offset from these N stars. This is the dominant error in the calibration (see text).

n/a in the K-band columns indicates no K-band images were taken for that field.

— indicates that the zeropoint solution was unacceptable (see text).

6.4 Colour-Magnitude Diagrams

Firstly CMDs will be considered for each colour individually. The diagrams will be inspected for the presence of a CMR, by comparison with model relations, as would be done with a CMR survey technique. Promising candidates from this method will then be scrutinised in colour-colour space, again via comparison with model colours. For both these tests, spatial information will be used by comparing the inner region of each image (the cluster candidate) against the outer region (representative of the background), as has been shown to work well in previous chapters.

6.4.1 VIJ Data

Figure 6.6 shows colour-magnitude diagrams (CMDs) for the two fields with acceptable calibrations and only J-band INGRID data. K-band follow up was not performed as preference was given to the other fields with J-band imaging, which the observers judged at the telescope to have better colour-magnitude relations (CMRs) from a quick reduction.

z1_017

z1_017 shows several red galaxies with colours compatible with the model z=1 CMR, but most of these points are just blue limits, as the optical data are quite shallow. The I-J, J diagram shows 9 galaxies within the inner search radius whose 1σ colour errors allow them within 0.2 mags of the model CMR.

z1_024

z1_024 shows only four galaxies in the inner region of the optical CMR compatible with the z=1 CMR; and none in the optical-NIR CMR. Several galaxies in the search region have similar I-J colours, and a z=0.8 model CMR is a good fit to these colours (14 galaxies then fall within 0.2 mags of this CMR); but again the optical CMR does not have many galaxies within this colour slice.

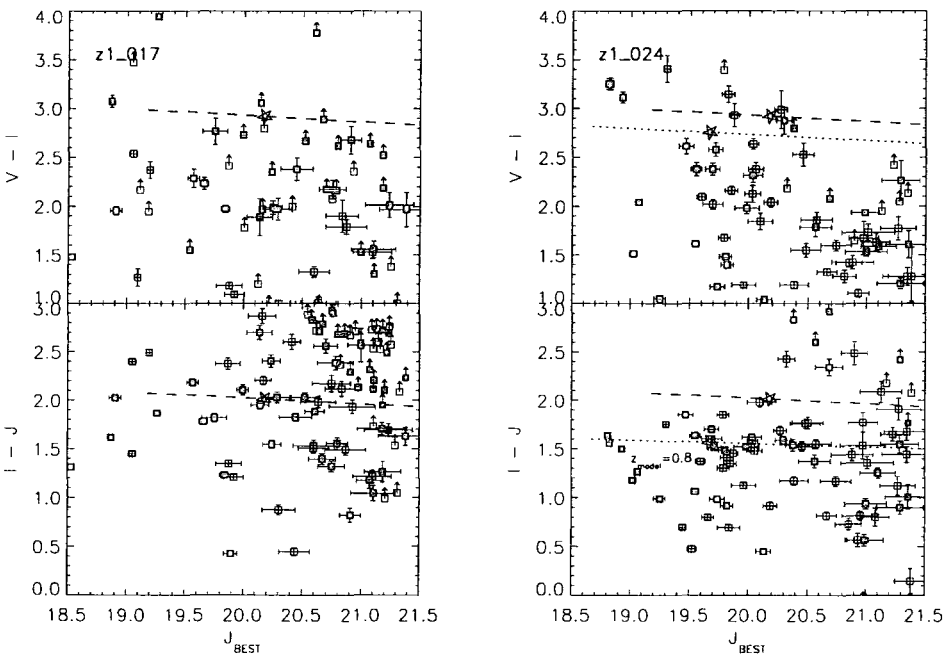

Figure 6.6: V-I, I-J vs J Colour-Magnitude diagrams. Dashed line shows z=1 model CMR, as described in text (star indicates M*). Dotted line shows an alternative model CMR (at redshift indicated). Filled squares are galaxies within the central 67 arcsec search radius, open squares are other galaxies in the field. Error bars are 1σ random photometric errors. Calibration errors are estimated in Table 6.2.

6.4.2 VIJK Data

The best candidates from VIJ CMDs (from a quick reduction of the J-band data, at the telescope) were followed up the next night with K-band imaging.

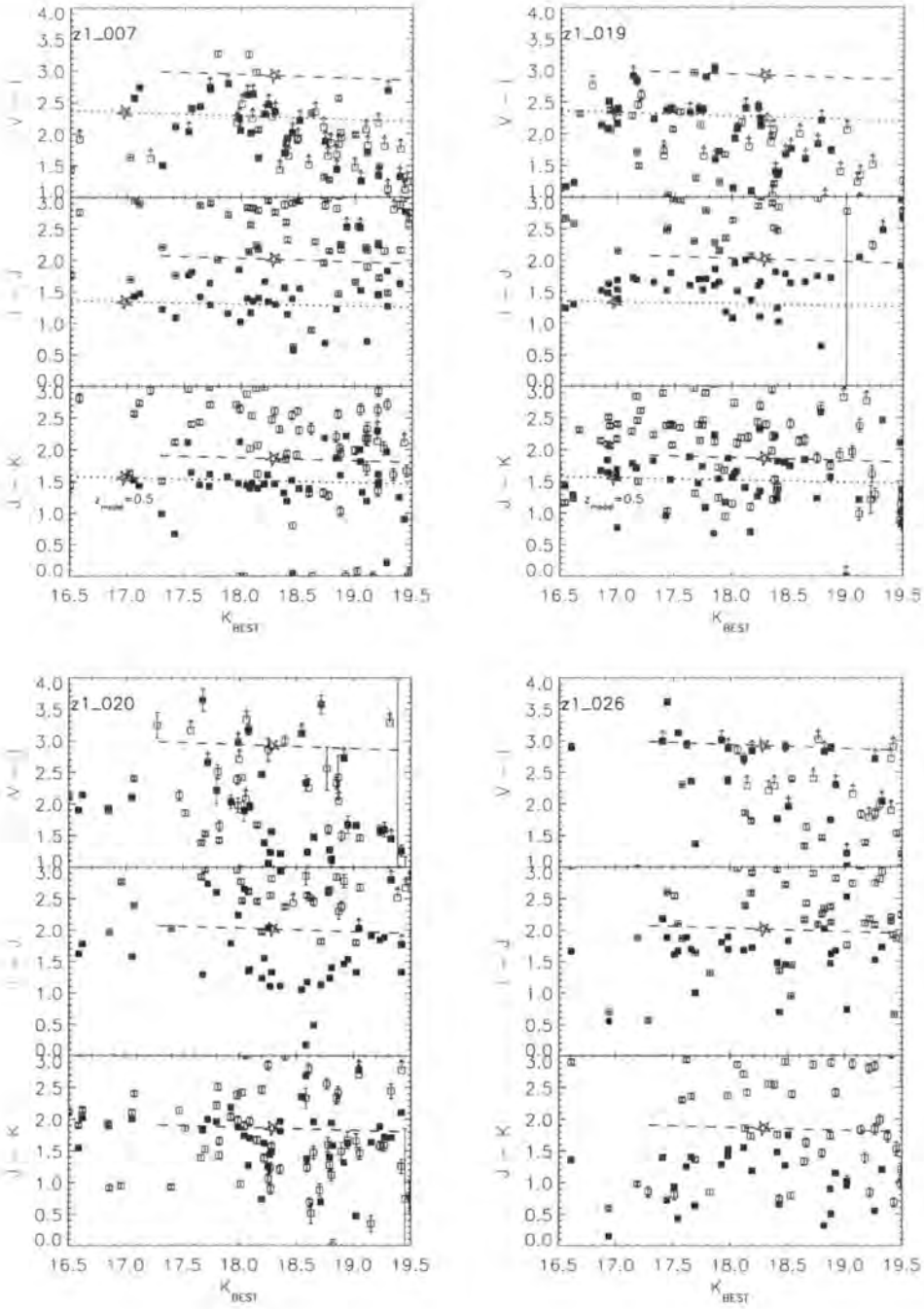

continued...

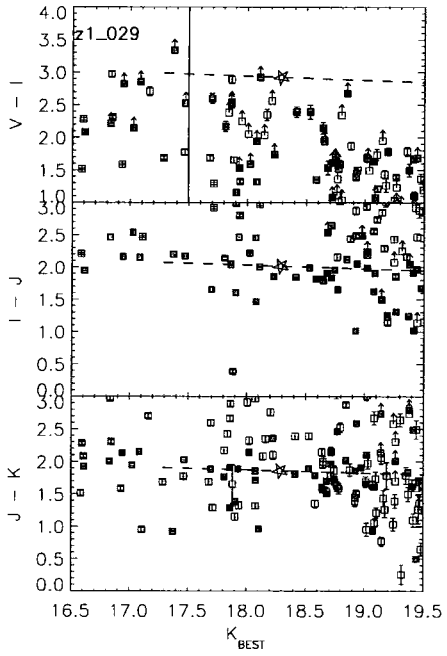

Figure 6.7: V-I, I-J, J-K vs K Colour-Magnitude diagrams. Symbols as Figure 6.6.

z1_007

z1_007 has several red galaxies in V-I with colours compatible with the z=1 model line. The optical-NIR and NIR-NIR CMDs both show overdensities of similar coloured objects, blueward of the z=1 line. Overplotting a lower redshift model (z=0.5) appears to be a good fit to all 3 CMDs simultaneously, and indeed, examining the colour-colour diagram in Figure 6.5.1, an overdensity in colour-colour space suggestive of a z=0.5 cluster is seen.

z1_019

As with z1_007, a lower redshift model provides a better fit to all three CMDs, although the I-J colour is somewhat too red. A few red galaxies consistent with the z=1 CMR are seen in all three colours, although a prominent CMR appears blueward of these few galaxies. A z=0.5 fits this CMR in V-I, and this also fits several of the bluer galaxies in the I-J and J-K colours.

In order to see if internal reddening of cluster ellipticals could account for the offset in I-J, the following experiment was tried. An elliptical spectrum which extended from the optical to NIR (Mannucci et al. 2001) was taken and redshifted to z=0.5. Then, the reddening law of Cardelli, Clayton & Mathis (1989) was applied to the spectrum, using the `IRAF` task **deredden**. Several values for the absolute extinction at 5550Å, $A(V)$, were used, up to $A(V)$=1.0, and the broadband colours of the reddened spectrum measured using the task **sbands**. It was found that to produce a sufficient amount of reddening in I - J (ie. ≈0.3 mags), an extinction of $A(V)$=1.0 is required[11]. This is quite high. Typical reddening values for ellipticals are more like $A(V) \approx 0.3$ (Groudfrooij et al. 1994); but also such extinction reddens the V - I colour by a comparable amount ($\approx$ 0.4 mags). It should be noted that colour gradients within the galaxies is not a plausible explanation. The photometric apertures used are quite large (5 arcsec diameter) and ellipticals become bluer at larger radii.

An alternative explanation is an error in the calibration of this field (the J and K bands are only calibrated from 2 and 1 stars respectively).

[11] Using the "canonical value" for the ratio of $A(V)$ to the colour excess between 4350Å and 5550Å, E(B-V) $R(V) = A(V)/E(B-V) = 3.1$ (Cardelli, Clayton & Mathis 1989); although this value exhibits scatter from elliptical to elliptical (Groudfrooij et al. 1994).

z1_020

z1_020 shows a good fit CMR in J-K at $z_{model} = 1$, but not in either of the other colours. Since the model CMRs are fairly close in colour for redshifts between ~0.5 and 1.0; this illustrates a problem of the CMR-finder technique if only J and K band imaging data is used.

z1_026

The V-I $z_{model} = 1$ CMR looks consistent with the data, but the other colours are not compatible. This emphasises the problem of increased field contamination, particularly with only single colour photometry, at these redshifts.

z1_029

z1_029 appears to be a very good z=1 cluster candidate. All three CMDs show many red galaxies with compatible colours.

To summarise, candidates z1_007 and z1_019 show promising z~0.5 CMRs and z1_029 shows a potential z=1 CMR. These will next be examined in two-colour space.

6.5 Colour-Colour Diagrams

6.5.1 IJK Data

For the fields with I, J and K imaging, colour-colour diagrams provide a stricter test than just looking at individual CMDs. A concentration in colour-colour space is effectively a simultaneous fitting of two CMRs.

In this section, the redshifts of the best fit model CMRs will be used to decide on the region of colour-colour space to examine for an overdensity. This region will then be compared with the field distribution as determined firstly from a background annulus around the candidate, and secondly from a composite background annulus constructed from the galaxy colours of the background annuli of all fields (this composite field is plotted in the lower right panel of Figure 6.5.1). For simplicity, a box extending 0.1 magnitudes either side of the model CMR at the estimated redshift of the candidate will be taken.

Young, dusty star-forming galaxies at intermediate redshifts can show similar optical-NIR colours to passively-evolving elliptical galaxies at $1<z<2$. Pozzetti & Mannucci (2000) suggested this degeneracy could be broken by examining the positions of galaxies in the I-K, J-K colour-colour plane and tested that the separation of these two classes of objects was robust to many changes in the modelling, such as dust, metallicity and IMF assumptions. However, overplotting the models of KA97 (which are calibrated to fit the observed evolution of the CMR for cluster ellipticals over a range of redshifts (Kodama et al. 1998)), even at $z=1$, ellipticals are beginning to cross into the starburst region defined by Pozzetti & Mannucci (2000). So, the division appears to be not as clear as first suggested. The Pozzetti & Mannucci (2000) dividing lines will be overplotted on the data to guide the eye with reference to the KA97 models. Furthermore, although dusty starbursts and ellipticals may be well separated, ordinary spirals follow the same locus as ellipticals (but spirals need to be at a higher redshift than ellipticals to produce a given colour, so the former are likely to be fainter). This is because the I-K colours for $z\lesssim1$ galaxies of all types is very similar, as the 4000Å break is still redward of both filters (see Figure 6.1). This degeneracy is split by using the V-J colour, which can now measure the strength of the break to distinguish between the different galaxy types. Even though the current V-band imaging is too shallow for direct detection of high redshift cluster candidates, it is sufficiently deep to distinguish whether an overdensity in IJK two colour space is due to spirals or ellipticals (see Figure 6.9).

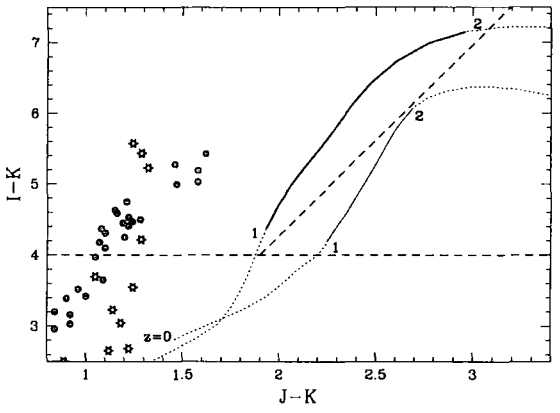

Figure 6.8: Predicted colours of ellipticals (thick line) and starbursts (thin line), from Pozzetti & Mannucci (2000). Dotted lines are for z<1 and solid lines for 1<z<2. The dashed lines indicate an ERO selection limit of I-K>4, and separate where the populations of ellipticals (left of diagonal line) and starbursts (to the right) are expected to fall. Stars and dots show stars from Pickles (1998) and brown dwarfs from Leggett et al (1998).

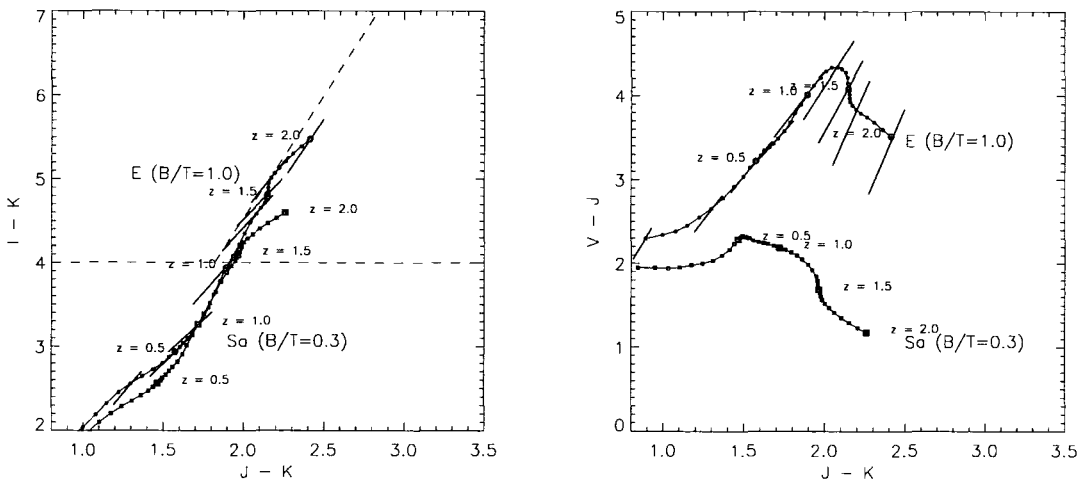

Figure 6.9: Model Two-Colour Diagrams in I,J,K and V,J,K. Although the Pozzetti & Manucci (2000) plot shows a clear separation between high redshift ellipticals and dusty starbursts, the distinction between ellipticals and higher redshift spirals is minimal. The separation in V,J,K is much greater.

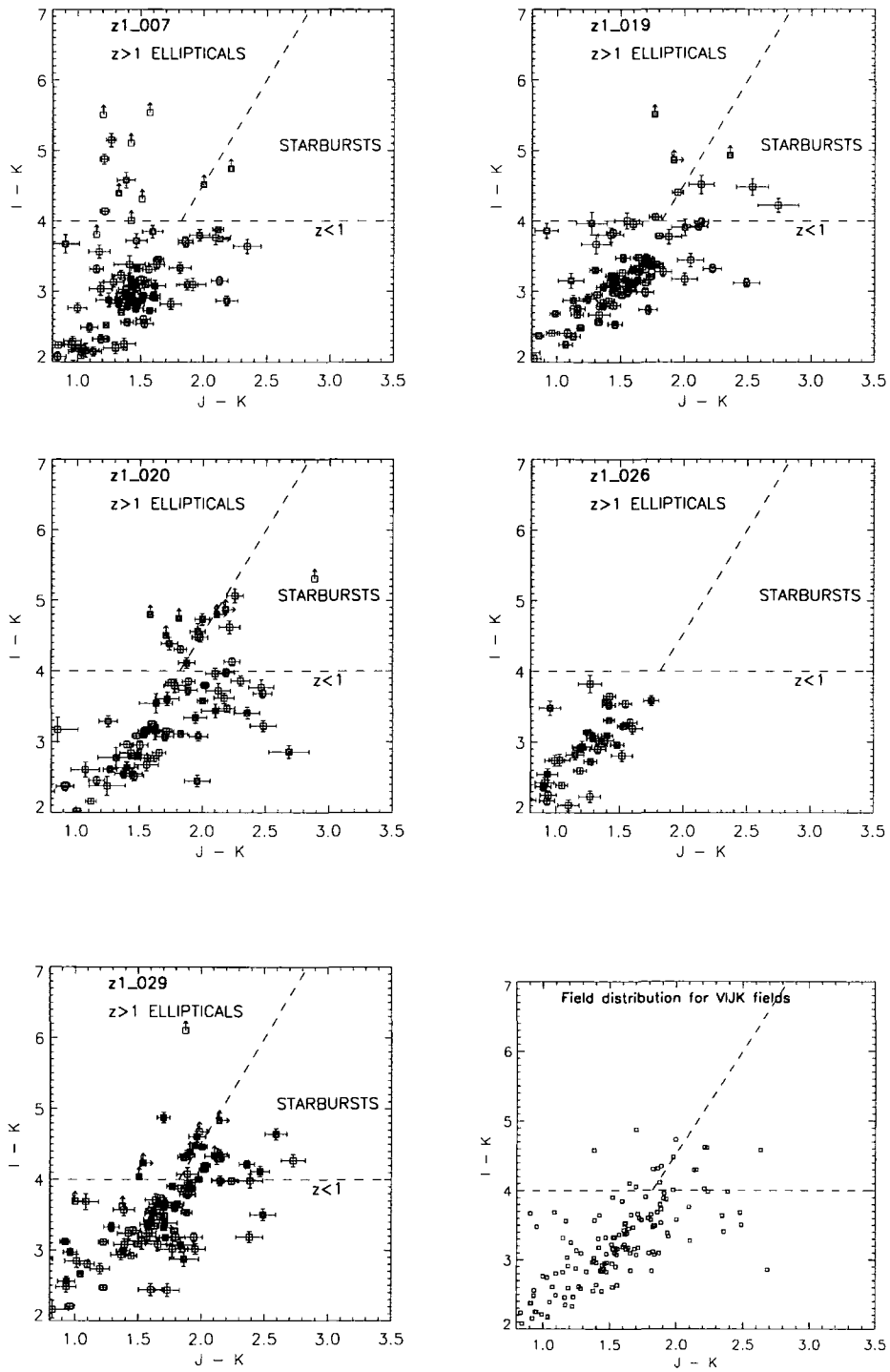

Figure 6.10: I-K vs J-K Colour-Colour diagrams. Filled symbols are galaxies within the central 67 arcsec radius; open symbols are galaxies in the "background annulus" - ranging from 67–120 arcsec radius. cf. Figure 6.8.

The three cluster candidates showing the most convincing CMRs (z1_007, z1_019, and z1_029) also show overdensities in colour-colour space, compatible with the model CMRs in IJK. [12] The V-band colour limits (in Figure 6.11) show that almost all the objects are too red to be late-type spirals at higher redshift, and most are too red to be earlier-type spirals (which reside between the Sa and E tracks). Thus, taking these to be the best candidates, the number of galaxies in the overdensities can be measured.

Two different measures for characterising the colours of field galaxies are used. A local background is constructed by taking the galaxies within an annulus extending from the outer edge of the inner search radius (67 arcsec) to a radius just within the limit of the usable field (120 arcsec). A composite background is constructed by combining all these annuli. The numbers of galaxies are then corrected to the number expected within the inner search radius by normalising the areas (for reference, the local background comprises an area of 2.2 times the inner area, and the composite background 11.5 times the inner area). It seems reasonable to use these annuli as representative background regions, as only the inner area was colour selected.

[12] z1_026 also shows a slight concentration in two-colour space, but this field appears particularly underdense.

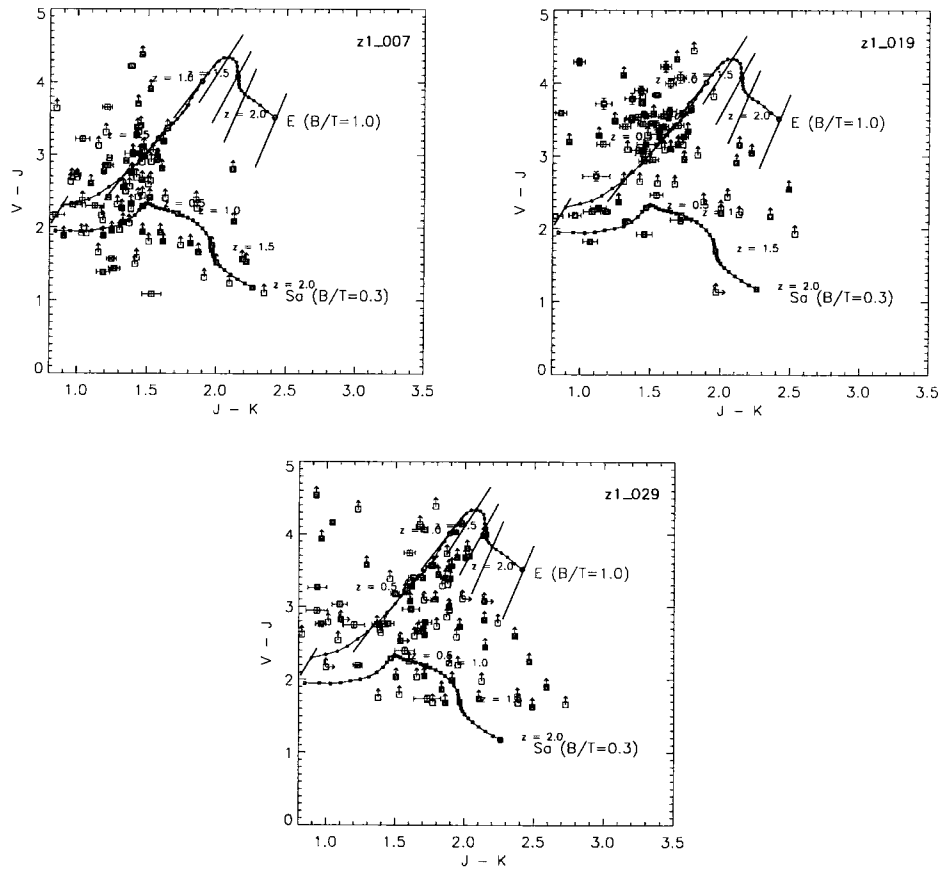

Figure 6.11: V-J vs J-K Colour-Colour diagrams. Symbols as for previous figure.

Table 6.3: Quantifying the overdensities in two-colour space

Candidate	N^a_{red}	N^b_{local}	$N^c_{composite}$	Model Reddening	
				J - K	I - K
z1_007	13(17)†	2(11)	1.7(3)	-0.1	+0.1
z1_019	3(13)†	11(12)	1.6(2.0)	+0.0	+0.2
z1_029	13	8	1.6		

a – number of galaxies in overdensity

b – number of background galaxies in local annulus

c – number of background galaxies in composite field

† – values in parentheses are after reddening the model slightly to locate a better centroid for the overdensity (see text).

A small shift has been applied to the observed colours for two of the candidates so as to locate a better centroid for the overdensity. One possibility for needing such an offset is that reddening in cluster ellipticals makes the observed colours redder than the model predictions. These levels of reddening can be achieved with about 0.4 mags of extinction in A_V assuming the Cardelli, Clayton & Mathis (1989) reddening law for z1_007 and about 1 mag A_V in z1_019, using the method described earlier. The numbers in parentheses in Table 6.3 in the N_{red} column show how the overdensity increases after this correction. Another possibility is a slight zero-point error in the calibration of the colours. To be conservative, *all* the data is shifted in this process (and so the background counts in the table change also). This naturally accounts for the latter possibility. If the former possibility is correct, then arbitrary numbers of galaxies within the initial overdensity could be shifted by reddening and the remainder could be called field galaxies. Hence, shifting all the data results in a conservative increase in the significance of the overdensity.

To give some indication of the significance of these overdensities, a simple approximation is to assume the background counts are Poisson-distributed and that the overdensities are just due to fluctuations in the background. Taking numbers from Table 6.3, assuming the background counts (from the composite region) have a mean of 2 galaxies, the probability of finding 13 galaxies by chance is $\approx 2 \times 10^{-7}$. These numbers apply to candidates z1_029; z1_007; and (reddened-)z1_019. The probability of z1_007 after reddening

is $\approx 1 \times 10^{-3}$.

There are several problems with such a naive interpretation of these numbers; but they are useful as an indication. Firstly, the IJK overdensities were identified *a posteriori* as they were initially selected to contain overdensities of galaxies with similarly red optical colours. Since very little wide area NIR data exists, the distribution of IJK colours given V-I colours is not well known. In order to calculate this, a wider area survey is required. Archival NIR data is amassing quickly, given the recent number of new NIR surveys, so it should soon be possible to build a database of optical-NIR galaxy colours and examine it using the selection function applied here.

The background area used to examine the field distribution of galaxy colours may still not be large enough. Certainly for the z$\sim$0.5 candidates, the local annulus used (1.1 – 2.0 arcmins radius) is sampling the outskirts of the cluster, therefore the background - subtracted number of galaxies is underestimated, as cluster members would be subtracted as part of the background. Furthermore, field-to-field variation in background counts even in shallower data is relatively large (eg., Figure 2.15).

The two cluster candidates at z$\sim$0.5 are potentially visible with the matched filter (MF) and CMR techniques used for the main XDCS sample. So, the next question is "were these found in those catalogues?". Firstly, z1_007: mfJ071929.3+710923 lies only 46 arc seconds from its position and has an estimated $I_C^\star$=18.2 (or z=0.25); cmJ071935.8+710947 has an estimated cluster centre only 9 arcsec from z1_007's position and an estimated redshift of 0.55. Secondly, z1_019: mfJ032900.2+025637 is 71 arcsec away, with $I_C^\star$=18.4 (z=0.27); cmJ032903.1+025640 is 97 arcsec away with z=0.37. The comparison between redshift estimates from the MF and CMR techniques was made in Chapter 3. The MF redshifts for both clusters are underestimates with respect to the CMR finder estimates, which agree reasonably well ($\Delta z \approx \pm 0.1$) with the multicolour technique. This agreement between the two colour-based methods may not seem too surprising (as they are both colour-based); but the CMR finder used V,I data and the multicolour finder used IJK data. Thus, this agreement is reassuring. Both of the z$\sim$0.5 candidates are just detected in the X-ray: z1_007 at 3.00σ and z1_019 at 6.09σ. The fluxes are 2.67 and 3.51 $\times 10^{-14}$ respectively, corresponding to luminosities of 3.8 and 2.0 $\times 10^{43}$ erg s^{-1} assuming the CMR-estimated redshifts. Neither of these fields was covered by Vikhlinin et al. (1998), but both are in the SHARC survey area. No X-ray detected cluster has been reported in either of these fields. The fluxes of both these fall below the bright SHARC limit. However, regardless of that, most X-ray selected surveys require a much higher significance detection

(8σ above the background, for example, Romer et al. 2001) in order to tell if a source is extended. Thus, these two clusters (in two of the deepest ROSAT fields) would have been missed by an X-ray survey, but with the benefit of optical selection they are found with high-significance, and the X-ray emission can be considered additional confirmation of these systems' reality.

Finally, as emphasised in the introduction, the only definitive way to confirm the existence of genuine high-redshift clusters is with spectroscopy. Candidate z1_019 was selected as an interesting member of a pair of clusters at z$\sim$0.4 (selected using the methods of Chapter 2), and has been awarded time for a wide-field spectroscopic survey using the 8m VLT and 6.5m Magellan telescopes. z1_029, as the most convincing z$\sim$1 candidate was applied for as a target for the Gemini Multi-Object Spectrograph (GMOS) for the first queue-scheduled observing runs on Gemini. Time has been awarded, but is yet to be scheduled.

6.6 Predictions for a Future NIR Cluster Survey

The planned UKIRT wide-field camera, WFCAM, set to become operational in late 2003, offers exciting possibilities for high-redshift cluster finding. A number of NIR surveys using this instrument are planned, known collectively as the UK Infrared Deep Sky Survey (UKIDSS). UKIDSS is likely to consist of two surveys appropriate to cluster detection. A 4000 square degree "shallow" survey, to depths of J=20 and K=18.4 has recently been approved; and a deeper survey (DXS - the Deep eXtragalactic Survey) to K$\sim$21 and J$\sim$23 covering 20 to 30 square degrees is probable[13]. If such a deep survey is not undertaken by WFCAM, then the project will be undertaken by VISTA[14], but observations will not begin until 2006 at the earliest.

It is necessary to choose passbands bracketing the 4000Å break at the redshift of interest, for maximum sensitivity (§5.4); and, to ensure sufficient CMR members, Chapters 5 and 4 show that galaxies brighter than M*+1 provide the strongest signal for a CMR. Hence galaxies this bright should be imaged with $>5\sigma$ precision photometry. Using the 1μm z-band, both these surveys bracket the 4000Å break out to z=1.1, whereafter the break begins to enter the broad z-filter. However, the model predictions for a z=1.1 elliptical give a z-band M* of 21.7. The SDSS only reaches z$\sim$20. Also, point source de-

[13] A Galactic Plane survey and ultra-deep but small area survey are also planned, but are not useful for cluster finding.

[14] http://www.vista.ac.uk

tection limits are typically 0.5-1.0 magnitudes fainter than for galaxies. So, even deeper photometry is required.

A number of wide-field optical surveys on 4-8m class telescopes are also upcoming. Panoramic imagers such as SuprimeCam on Subaru and MegaCam on the CFHT are among the instruments which will be utilised. The selection of UKIDSS fields which overlap with these optical fields will be of vital importance for cluster selection. The necessity of optical photometry has been shown earlier in this chapter. Now, assuming J and K band imaging plus a number of optical bands are available, a detection procedure based on the following could be adopted:

The main problem for $z>1$ versus intermediate redshift cluster detection is that of increased field contamination. This chapter has cited many examples of the tight CMR still being present at $z\gtrsim1$. Thus, a CMR-type detection method still seems the most efficient. Given the numerous bands available, a powerful method for isolating this red sequence is to search multicolour space for concentrations of galaxies on small spatial scales with similar colours (a natural extension of the two colour space method, §6.5). The scatter in the CMR for galaxies brighter than M^*+1 at $z\sim1$ still appears to be less than 0.1 magnitudes (eg, Stanford et al. 1997, Rosati et al 1999). Now, this should be sufficiently narrow for this technique to work well - galaxies at other redshifts would not show the same colours in all bands simultaneously, so field contamination is very effectively rejected. A similar idea is being used at lower redshifts ($z\lesssim0.5$) on the SDSS dataset (the C4 algorithm, Nichol et al. 2000), with the exception that they also require a coincident X-ray detection (requiring coincident X-ray detections in this higher redshift regime will miss a large fraction of clusters, even with deep Chandra/ XMM observations, as will be demonstrated below).

Like the two-band CMR-finder, this technique offers the great advantage over individual photometric redshift fits to individual galaxies (eg, Kodama, Bell, & Bower 1999) that the average colour of several galaxies is used in the fit, offering much higher signal-to-noise ratio measurements (Chapter 5).

The next question is: *how many clusters could be found using such a technique?* Returning to the literature and taking the lower temperature of the pair of Lynx field clusters at $z\sim1.3$ as typical, the photometry given in the paper can be used. This cluster is particularly suitable as it was found in a NIR survey. Stanford et al. (1997) plot CMRs in several optical/NIR bands. These show that ten galaxies brighter than M^*+1 exhibit the same colours in all bands simultaneously. Given the potential for complete

field subtraction, an overdensity of ten galaxies with multiple colours closer than 0.1 magnitudes would represent a secure detection. This is approximately the size of the scatter in high redshift CMRs, and consistent with the width of colour slices used to find CMRs in lower redshift data (0.08 mags, Chapter 2). As already stated, this cluster has a temperature of $1.6^{+0.8}_{-0.6}$keV. Now, the Press-Schechter formalism can be used to predict the number of clusters of this temperature and greater, as a function of redshift. Code for modelling the evolution of the temperature function (Eke, Cole & Frenk 1996) was kindly provided by Vince Eke. Figure 6.12 shows the cumulative number of clusters hotter than this, for redshifts z >0.8. It should be pointed out that clusters at lower redshifts than this will have been efficiently discovered and studied by optical surveys, and that the NIR makes the greatest contribution to cluster studies at higher redshifts. However, UKIDSS will offer the possibility of work such as stellar population studies of the already discovered lower redshift clusters, K-band light being a good tracer of stellar mass (Chapter 5), the 4000 square degree "shallow" survey being particularly useful here.

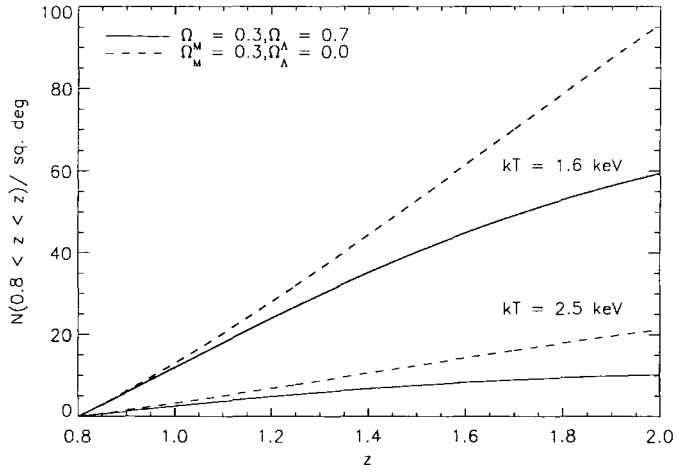

Figure 6.12: N(z) for ~2keV Clusters from Press-Schechter. Two different low matter density cosmologies are indicated. Counts are cumulative for clusters at redshifts greater than 0.8.

Press-Schechter predicts ~30 clusters per square degree at 0.8<z<1.3 (dependent on cosmology, see Figure 6.12). This is in good agreement with the fact that the cluster was found in 100 arcmin^2 of imaging data. Allowing for the error bars on the temperature, the number of 2.5keV clusters is only a factor of two or so lower. The biggest uncertainty is the scatter in the cluster mass-to-light ratios at these redshifts; but note similar problems exist in X-ray selected surveys, ie., the scatter in the L-T relation. Romer et al. (2001)

make predictions for the number of $z \gtrsim 1$ clusters expected in a serendipitous survey with the X-ray Multi-Mirror mission (XMM-Newton) satellite. Using models for the X-ray properties of clusters coupled with, again, the Press-Schechter formalism, they predict that $\sim$1 $z \gtrsim 1$ cluster per square degree should be found with XMM. The main limitation on such a survey is the need to carry out optical/NIR imaging to confirm the clusters and study member galaxies. Thus, a significant extra amount of observing time must be figured into their survey. Furthermore, a higher background than anticipated within the instrument has recently being measured[15], reducing XMM's sensitivity to high redshift clusters.

The other question is the epoch of formation of the cluster early-type galaxies. As the formation redshift is approached, the galaxy colours become bluer and the scatter increases, removing the signature for which the technique is searching [16]. Given current data for the evolution of the CMR (the biggest lever-arm being the uniformity of red galaxy colours at z$\sim$1.3) it seems likely that the epoch of formation is still at much higher redshift. Models with a formation redshift $z_f \gtrsim 4$ predict colours in good agreement with the highest redshift observations. Thus, it should be possible to trace the CMR at least to redshifts z$\sim$2.

Aside from the collapsed structures accounted for in Press-Schechter, further systems in a state of formation could be found by UKIDSS. Red early-type galaxies appear to be in place prior to the formation of the cluster (Stanford et al. 2001). Filaments and large scale structure (LSS) is traced by red galaxies. The Luminous Red Galaxy Survey (Eisenstein et al. 2001) being undertaken by the SDSS collaboration shows that LSS can be efficiently mapped by a sample of the most luminous red galaxies at each (photometrically obtained) redshift. The cluster finding technique described could also be utilised for this purpose.

6.7 Conclusions

The optical data from the XDC Survey has been used to identify potential high redshift clusters, by searching for overdensities of red galaxies. Near-infrared imaging of these

[15] `http://xmm.vilspa.esa.es/docs/documents/CAL-TN-0016-1-0.ps.gz`

[16] Also, Nakata et al. (2001) have recently found evidence for a possible truncation of the CMR in a cluster candidate around the z=1.2 radio galaxy 3C324. Using photometric redshifts, galaxies with the colours of early-type members are absent, fainter then about $M^*+1.5$. This shows that a survey depth greater than this limit may not be of any benefit for cluster detection. The adopted earlier limit of M^*+1 thus seems justified.

regions has been used to compare these galaxies' colours with the predicted optical-NIR colours of high redshift early-type cluster galaxies. This technique has produced three cluster candidates (two at $z_{est} \approx 0.5$, and one at $z_{est} \approx 1.0$). Follow up spectroscopy is necessary to verify the nature of these systems. A possible extension of this technique has been discussed, with reference to the forthcoming UK Infrared Deep Sky Survey (UKIDSS), and predictions for the number of clusters which might be found have been made.

Chapter 7

Conclusions and Future Work

In this thesis, a new survey for galaxy clusters (the X-ray Dark Cluster Survey, XDCS) utilising ~12 square degrees of concurrent optical and X-ray data has been presented. This survey is comparable in size and depth to the large public European Southern Observatory Imaging Survey (EIS). The main aim of this work was to look for X-ray underluminous or "dark" clusters which would be found in optical surveys but missed in deep X-ray searches.

7.1 An Optical and X-ray Survey for Galaxy Clusters

The details of the optical reduction and calibration were presented in Chapter 2. V- and I-band imaging to depths of ~23.5 and 22.5 respectively, covering 39 of the deepest archival ROSAT PSPC fields, each of 19 arcmins radius, was obtained as the basis for the optical survey. Two detection algorithms were presented for this data: the first is presented here for the first time and is a modification of the Matched-Filter (MF) algorithm used extensively in recent cluster surveys. This algorithm was specifically designed to search for extended and possibly irregular overdensities in the I-band data, which may be characteristic of unrelaxed, dynamically young systems (such as those hypothesised to be missing from X-ray surveys by Bower et al. (1997)). The second technique uses colour information to search for the ubiquitous signature of early-type galaxies in the cores of clusters, the colour-magnitude relation (CMR). These techniques are based on two of the most popular, reliable, recent methods for finding clusters and are being utilised by a number of surveys, but each relies on a different set of properties and assumptions for the cluster targets. Thus, a comparison of the systems found by each is important. The X-ray survey utilised data from existing surveys, many of which possess spectroscopic confirmation of the clusters found.

7.2 Catalogues of Galaxy Clusters

Chapter 3 presented the catalogues of clusters found by the different techniques and the results of different optical richness measurements. A comparison between the X-ray and optical surveys showed that the MF method recovers ≈75% of the X-ray selected clusters, whereas the CMR method can recover 100%. Furthermore, the CMR method is capable of resolving projected groups along the line of sight, and reveals that at least one of the X-ray selected clusters is clearly 2 systems, nearby on the sky, but at very different redshifts. In terms of gross numbers, the MF technique finds ~200 cluster candidates, the CMR technique ~300 and the X-ray selection ~10. The scatter in the relationship between optical and X-ray luminosity is large. Using the integrated optical luminosities of cluster early-type galaxies (L_E) produces the tightest correlation with L_X, although the scatter is still considerable. The scatter using the amplitude of the correlation function B_{gc} in place of L_E is larger still, and a simple count of the number of galaxies within a fixed physical distance produces no discernable correlation. The source of the scatter cannot be addressed with the present data, although factors affecting each quantity have been discussed. For example, $L_X$is affected by the density and temperature of the intracluster gas, which is in turn affected by the dynamical state of the cluster. The early-type galaxy luminosity is dependent on the star formation epoch, and the period of last star formation.

Selection techniques utilising publically available radio survey data were also explored. Radio overdensity selection finds two cluster candidates, one of which is probably associated with a CMR candidate. Radio morphology selection finds one candidate, which is indicative of motion through a dense medium. This is confirmed by an X-ray detection (although at too low significance to be an X-ray selected cluster).

7.3 Verification of Cluster Candidates

Spectroscopic follow up for a subsample of candidate clusters found in the optical survey, but with no counterpart in the X-ray surveys, was undertaken in Chapter 4. These systems have integrated early-type galaxy luminosities of ~1-5×$10^{12}L_{\odot}$ (which is typical of the most X-ray luminous clusters at z~0.2 studied by Smail et al. (1998)) but X-ray luminosities one to two orders of magnitude lower. This corresponds to the optically rich, X-ray faint edge of the scatter observed in the L_X- L_E relation of Chapter 3. These candidates were originally found manually, but later comparison with the automated techniques revealed that they were all found by these algorithms, and are thus representative

of the cluster candidates found in the XDCS.

Four fields possessing large overdensities of galaxies, found by both optical detection algorithms, were observed. Each was found to contain at least one significant grouping in redshift space. Two of the fields contained a single overdensity of galaxies in redshift space, and the remaining two fields showed two significant groupings along the same line-of-sight. The MF was unable to resolve such projections (due to the fundamental limitation of the assumed model in the technique - too many degeneracies in the model exist if more than one cluster luminosity function is permitted). The estimated redshift error from the MF technique is $\approx$0.1 at redshifts of $\sim$0.2. The CMR finder, on the other hand, correctly identified all the clusters found in redshift space (correctly resolving the projected structures) and estimated the redshifts to an accuracy of $\approx$0.05 at redshifts $0.2 \lesssim z \lesssim 0.5$. Furthermore, this latter technique also hinted at the presence of a higher redshift group in one field, not probed deeply enough by the current spectroscopy. This last field did not originally appear to possess a colour-magnitude relation, and was targeted specifically because it was such a significant I-band overdensity that it represented a possible counter-example to the ubiquity of the CMR. However, with the benefit of hindsight and the automated CMR finder (which correctly spatially resolves the red galaxy clumps), two CMRs can be seen in the field. Thus no evidence for the non-universality of the CMR has been seen in this thesis.

7.4 Near-Infrared Observations of Candidate Clusters

Chapter 5 described near-infrared (NIR) observations of a further subsample of X-ray dark cluster candidates. After the superior performance of the CMR finder in the previous chapter, only CMR candidates were studied in this work. The NIR offers a less biased view of cluster galaxies, independently of morphological type or star-formation activity. The CMR candidates were examined in colour-magnitude space for colour-magnitude relations using NIR-selected galaxies. A technique comparing galaxies in colour-colour space in candidate regions with those in field regions was used to show that all but one of the V-I, I CMR candidates were significant overdensities in VIH colour-colour space. This technique was shown to work in VIK space for two X-ray selected Vikhlinin et al. (1998) clusters. Use of photometric redshifts requires deep B-band imaging, which may then allow identification of bluer cluster members.

7.5 A Near-Infrared Survey for Distant Galaxy Clusters

Pushing the optical detection of clusters to the highest possible redshift, colour selection of overdensities of bright red galaxies with the colours of z$\sim$1 passively-evolving ellipticals was performed on the XDCS optical data. Such candidates were imaged with deep NIR photometry. J-band observations were made, and the most promising candidates showing possible high redshift CMRs in the VIJ data were imaged further in K. Observing conditions meant that only about half the data were usable. The colour-magnitude diagrams in V-I, I-J and J-K versus K were examined and compared with model colours for the CMR (these models having been calibrated against spectroscopically confirmed cluster photometry). A stricter test in two-colour space was applied which resulted in two cluster candidates at z$\sim$0.5 and one at z$\sim$1. Spectroscopy is required to confirm these candidates and is underway for one of the z$\sim$0.5 systems, and the z$\sim$1 system has been awarded time on Gemini, but has yet to be scheduled. Finally, the techniques developed in this and the previous chapters were used to outline a technique applicable to forthcoming wide field NIR surveys, and using the Press-Schechter formalism, estimate the numbers of clusters that such a survey could find.

7.6 Discussion and Interpretation of Results

The original motivation for this work was the studies of Bower et al. (1994) and Bower et al. (1997) which found that in an optically selected survey of galaxy clusters at z$\sim$0.4, the X-ray emission was systematically lower than expected for a non-evolving X-ray luminosity function, relative to local samples. Their spectroscopic analysis indicated that these systems had velocity dispersions comparable to those of more X-ray luminous systems, which suggested that if the clusters were virialised then they had dynamical masses similar to the more X-ray luminous/ massive systems; or that the systems were in fact unvirialised and their velocity dispersions were thus inflated above that of a relaxed system.

This thesis has constructed similar optically selected samples, albeit from a smaller area (11 deg^2 versus 27 deg^2) but with a more quantifiable selection function and using more efficient selection techniques. The relationship between X-ray luminosity and richness (as measured three different ways) shows considerable scatter.

During the course of this work, results from a similar study by Donahue et al. (2001) were published. They conducted an optical and X-ray survey in 23 deep ROSAT fields (4.8 deg^2) using Postman et al.'s (1996) Matched Filter algorithm on I-band data. The

depth of their photometry was about 0.5 magnitudes deeper than that of the XDCS, although their areal coverage was lower by more than a factor of two. Donahue et al. (2001) detected 57 X-ray candidate clusters and 152 candidates in the optical. Their MF algorithm detected 74% (26 out of 35) of the most reliable X-ray candidates. This number is in good agreement with the 75% (9 out of 12) found with the MF algorithm used here. This thesis has shown that an even higher recovery rate is possible using CMR techniques.

Donahue et al. (2001) also find that within their optically selected sample, optical and X-ray luminosity are correlated, with considerable scatter. Their measure of richness is essentially the number of $L^{\star}$ galaxies (Λ in equation 2.9) contributing to the cluster signal at their MF estimated redshift. This thesis has shown that the MF estimated redshifts are much poorer than those estimated from the CMR finder. This will potentially increase the scatter of the relation. They state that although there is significant scatter within the relation, there is no need to impose a bimodal distribution of X-ray luminous and X-ray faint clusters. This seems to be borne out by this work, as the distribution of detections in Figure 3.26 appears continuous.

Possible reasons for this scatter include:

1). Variations in the efficiency of galaxy formation. If galaxy formation is more efficient at a given epoch/ environment, then for a given mass of gas, a higher fraction can be converted to stars, increasing the light to mass ratio of a cluster. Furthermore, this leaves less gas available for production of X-ray emission, decreasing the X-ray luminosity. So, higher galaxy formation efficiency leads to increased optical luminosity and decreased X-ray luminosity.

2). The dynamical state of the cluster. As mentioned before, if a cluster is dynamically unrelaxed then the hot intracluster gas will not be centrally concentrated to densities sufficient for X-ray emission (Chapter 1). If the cluster galaxies are already in place, as seems to be the case (Chapter 6), then such a cluster would have an unusually low X-ray luminosity for its optical luminosity.

3). Thermal history of the gas. The presence of cooling gas in the cluster raises the ICM density and increases X-ray luminosity (Chapter 1). Conversely, injecting energy into the ICM at early times (eg., by AGN or through supernovae / feedback from galaxy formation) decreases the ICM density and lowers X-ray luminosity. Both these effects could contribute to scatter in the optical – X-ray luminosity relation.

4). Projection effects. Groups of galaxies projected along the line of sight would

appear as higher optical luminosity clusters (since the number of galaxies observed is simply additive); whereas the X-ray luminosity would appear extremely low for a cluster of such optical richness, as the X-ray luminosity scales as the square of the gas density. This was shown to probably not be a significant factor in Chapter 3, by considering separately optical cluster candidates flagged as projections. Although again, the volume probed by this survey is relatively small, so large scale filaments viewed "end-on" may be too rare to be included.

These mechanisms all assume that the fundamental parameter is the cluster mass. The best measurement for the cluster mass in this thesis is the velocity dispersions determined in Chapter 4. This suggested that within the (large) errors, a sample of optically selected, X-ray underluminous clusters had optical luminosities consistent with those of the most X-ray luminous clusters. Clearly better mass estimates are required for a larger number of clusters.

7.7 Future Prospects for Cluster Surveys

The best testbed for cluster finding in the coming years will be the Sloan Digital Sky Survey (SDSS, York et al. 2000). With multicolour photometry and spectroscopy over π steradians, a variety of cluster selection techniques will be possible. Clusters to z$\sim$0.3 should be detectable in the main spectroscopic sample, and the photometry should allow colour selection techniques, such as those presented in this thesis, to z$\sim$0.5. The sheer area of the survey means that a large number of deep archival ROSAT fields and also forthcoming X-ray observations with satellites such as Chandra and XMM will overlap with the Sloan optical and spectroscopic dataset. This will provide the possibility of constructing X-ray selected samples within the survey area. Also, the ROSAT All Sky Survey (RASS) covers the entire sky, albeit to a very shallow depth. This is already being used by one of the SDSS cluster finding algorithms, C4 (Nichol et al. 2000), which requires galaxies of similar colours in multicolour data *plus* an X-ray detection. This thesis has shown that genuine galaxy clusters exist which are not seen in some of the deepest available X-ray images. Using shallower X-ray data will further limit the number of clusters which can be detected by this method. Simply drawing a line at a constant X-ray flux limit across a plot such as Figure 3.26 illustrates that there are many optically selected candidates of sufficient optical richness to be easily detectable in the data which would be missed if a coincident X-ray detection is required, due to the intrinsic scatter in

the optical richness - L_X relation.

Also, the collaboration seems to be concentrating on non-parametric, or semi-parametric methods (eg. Kim et al. 1999): for example, using mild colour cuts instead of the strict colour slices used by the CMR finder, to attempt to reduce field contamination and increase the signal from cluster galaxies. Whilst this is important to see if any clusters are missed (eg. clusters lacking early-type galaxies - which can potentially be found in the spectroscopic survey, if they exist), there appears to be no evidence for such systems. All known clusters (at least in the redshift range which can be probed by Sloan) exhibit a sequence of early-type galaxies, with colours well fit by model predictions assuming a single age, passively evolved stellar population. If such observations are borne out by Sloan, this provides constraints on the star formation histories of cluster galaxies - implying that a fraction must have formed their stars at high redshift and not have undergone more recent star formation (which would bluen the colours).

The main power of the CMR technique is that this relation is apparently universal and thus virtually all field contamination can be reduced by searching strictly around the expected colours. The properties of galaxies on the colour magnitude relation can be studied in detail with the SDSS data. Since clusters found by the CMR method depend on the properties of galaxies on the CMR, it will be important to study these galaxies as a function of different cluster environment. For example, although *tight* constraints cannot be made on the star formation epoch of these ellipticals (as the redshifts are too low), it will be possible to study in detail differential properties of early-type cluster galaxies from cluster to cluster. If X-ray underluminous clusters are due to a more recent formation epoch for the cluster, are the ages of stars in such cluster ellipticals also younger? This could be examined by measuring spectral line indices (to derive ages) for early-type galaxies in clusters spanning a range of X-ray luminosities.

Comparison of further techniques, not possible with the data utilised here, will be possible with SDSS. For example, weak lensing measurements of clusters selected by other means are already being made, and this is a valid selection technique in its own right. This will allow mass estimates of clusters. Mass estimates can be compared with dynamical masses from velocity dispersions obtained in the spectroscopic survey, and from X-ray masses where sufficient data exist. This will allow an examination of the mass to light ratios of clusters, and comparison with optical richnesses. The large numbers of clusters should allow relations such as the L_E to mass relation (limited in this work by few clusters with spectroscopy and few redshifts for each of these) to be well characterised.

Weak lensing studies were not possible with the XDCS data as the seeing was too large to accurately measure ellipticities of galaxies, and also because the distortions within the wide field camera (WFC) are significant. Cosmological weak lensing surveys have been proposed for a number of forthcoming large telescopes such as the 8m class Dark Matter Telescope[1]. Mass estimates can be used to study the mass function and its evolution (as described in Chapter 1). Through such studies cosmological parameters (such as Ω, Λ, σ_8) can be constrained. Although, these parameters may have already been measured by cosmic microwave background experiments, cluster abundances probe fluctuations on vastly different scales. Discrepancies between the two different techniques can reveal physics of the early universe such as non-Gaussian fluctuations. Differences between the different techniques on individual clusters can reveal properties of the clusters probed by the different physics underlying each method. For example, as stated before, a high dynamical mass but a low X-ray mass may indicate that a system is dynamically young. Galaxies would still be infalling, producing a high velocity dispersion, but the X-ray emission would be low as there has been insufficient time to establish a dense intracluster medium.

Furthermore, there are plans to use the surface brightness fluctuation (SBF) selection method (described in Chapter 1) to select clusters in the Sloan survey. Comparing this technique to the more traditional/ well studied techniques will be important as the selection function is difficult to understand. This could not be studied with the XDCS data as extremely accurate flatfielding is necessary, such as that obtained with drift-scan telescopes. This method is also being used to construct a large cluster sample (The ESO Distant Cluster Survey, EDisCs[2]), spanning a wide redshift baseline, with which to study in detail the evolution of cluster galaxies using 35 nights of VLT observations. Thus, the way in which these objects were selected and the impact it is likely to have on the properties of the galaxies must be understood.

8m class telescopes such as the VLT will be central to conducting deeper and more detailed studies of distant clusters. Wide field optical imaging capabilities on 8m class telescopes such as the SuPrime Camera on Subaru will offer unprecedented studies of large samples of faint objects. These will be vital for use in conjunction with deep NIR surveys. Prospects for future NIR surveys such as UKIDSS and VISTA have been discussed in Chapter 6. Such surveys will reveal large numbers of high redshift clusters with which

[1] http://www.dmtelescope.org/

[2] http://www.mpa-garching.mpg.de/~ediscs/

to study clusters and groups in the distant past, close to the epoch of formation (the importance of deep optical coverage with large telescopes such as Subaru has already been emphasised in Chapter 6). This would allow the last episode of star formation in cluster ellipticals to be probed directly. For example, does colour selection fail to find clusters at a firm redshift cutoff (corresponding to a universal star formation redshift and universal star-formation rate for cluster ellipticals), or do the properties (eg. slope, scatter) of the CMR vary from cluster to cluster in very high redshift systems (indicating variance in the star-formation epochs). Such studies could again look for trends as a function of X-ray luminosity, dynamical mass, weak-lensing mass (as suggested at lower redshift) to try to disentangle the important physics underpinning such differences.

With more and more large public surveys being conducted, the possibility of cross-comparing techniques over any given survey (as demonstrated in Chapter 3 using NVSS and FIRST 1.4GHz data) is increasing all the time. For example, cross-correlating the FIRST survey with a UKIDSS cluster survey would effectively allow a very large sample selected in the way that targeted searches for high redshift clusters around radio loud galaxies are currently conducted. The results of such a comparison may reveal the (very small - see Chapter 3) subset of all clusters which are found by such targeted observations, and may hence provide estimates of the lifetimes of AGN (/radio-loud galaxies) in the cluster environment.

In conclusion, there has never been a more rapid period of growth for large, well defined astronomical surveys.

Appendix A | *INT WFC Observing Logs*

Table A.1: INT Observing Log, 19/20 June 1998

RIXOS ID	Filter	RA h:mm:ss	Dec deg:mm:ss	Rotator PA	UT	Airmass	Exptime (s)
R265A	V	13:10:35.340	+32:22:15.00	180	22:02:07.6	1.075765	899.150
R265A	I	13:10:35.340	+32:22:15.00	180	22:21:31.8	1.105098	599.490
R265B	I	13:10:20.660	+32:19:09.00	360	22:44:58.8	1.156263	599.600
R265B	V	13:10:20.660	+32:19:09.00	360	22:59:13.4	1.201702	899.020
R217B	V	14:13:39.780	+43:58:41.00	360	23:22:12.6	1.129656	898.760
R217B	I	14:13:39.780	+43:58:41.00	360	23:40:22.3	1.158710	599.439
R217A	I	14:13:57.020	+44:01:47.00	180	23:56:27.9	1.193405	599.440
R217A	V	14:13:57.020	+44:01:47.00	180	00:10:23.1	1.235541	899.180
R110A	V†	14:28:50.410	+33:12:17.00	180	00:55:18.8	1.336526	899.070
R110A	I	14:28:50.410	+33:12:17.00	180	01:18:45.3	1.436668	599.510
R236B	V	17:01:14.970	+51:47:50.00	360	02:12:09.7	1.218442	899.210
R236B	I	17:01:14.970	+51:47:50.00	360	02:36:37.9	1.218442	599.510
R236A	I	17:01:35.030	+51:50:56.00	180	02:51:31.9	1.250481	599.420
R236A	V	17:01:35.030	+51:50:56.00	180	03:05:17.4	1.291289	899.170
R294A	V	23:18:51.350	+12:37:33.00	180	03:24:25.1	1.438864	899.140
R294A	I	23:18:51.350	+12:37:33.00	180	03:42:52.6	1.357060	599.010
R294B	I	23:18:38.650	+12:34:27.00	360	03:57:59.0	1.292432	599.530
R294B	V	23:18:38.650	+12:34:27.00	360	04:11:59.0	1.234158	899.220
R205B	V	23:12:14.590	+10:45:15.00	360	04:47:27.1	1.140620	899.270

Table A.2: INT Observing Log, 20/21 June 1998

RIXOS ID	Filter	RA h:mm:ss	Dec deg:mm:ss	Rotator PA	UT	Airmass	Exptime (s)
R278A	V	13:32:40.310	+11:07:12.00	179	21:45:19.8	1.087716	898.650
R278A	I	13:32:40.310	+11:07:12.00	179	22:03:22.3	1.109399	599.449
R278B	I	13:32:07.690	+11:05:32.00	360	22:21:11.8	1.142725	599.550
R278B	V	13:32:07.690	+11:05:32.00	360	22:34:35.0	1.178840	899.079
R268C	V	13:56:05.600	+18:18:16.00	270	23:43:28.6	1.265151	899.250
R268C	I	13:56:05.600	+18:18:16.00	270	00:01:27.0	1.327828	598.910
R268D	I	13:56:00.000	+18:26:16.00	90	00:16:26.7	1.399398	599.000
R268D	V	13:56:00.000	+18:26:16.00	90	00:29:49.6	1.491236	898.720
R110B	I	14:28:23.880	+33:09:54.00	360	00:57:24.9	1.353825	599.440
R110B	V†	14:28:23.880	+33:09:54.00	360	01:11:10.9	1.433409	899.110
R223B	V	16:33:54.400	+57:08:06.00	360	01:30:30.9	1.208485	899.250
R223B	I	16:33:54.400	+57:08:06.00	360	01:49:21.7	1.233131	599.450
R223A	I	16:34:53.400	+57:09:46.00	180	02:04:33.5	1.258357	599.459
R223A	V†	16:34:53.400	+57:09:46.00	180	02:18:23.5	1.291515	899.140
R220A	V	17:27:10.940	+74:31:58.00	180	02:41:16.7	1.506845	899.020
R220A	I	17:27:10.940	+74:31:58.00	180	02:59:53.2	1.527696	599.420
R220B	I	17:25:11.060	+74:30:18.00	360	03:14:48.4	1.552128	599.280
R220B	V	17:25:11.060	+74:30:18.00	360	03:28:16.3	1.578830	898.970
R281B	V	0:10:12.600	+10:57:22.00	360	03:52:10.5	1.588069	898.530
R281B	I	0:10:12.600	+10:57:22.00	360	04:10:46.7	1.479956	599.480
R281A	I	0:10:45.200	+10:59:02.00	180	04:27:37.9	1.390070	599.540
R281A	V	0:10:45.200	+10:59:02.00	180	04:41:21.4	1.316870	899.189

Table A.3: INT Observing Log, 21/22 June 1998

RIXOS ID	Filter	RA h:mm:ss	Dec deg:mm:ss	Rotator PA	UT	Airmass	Exptime (s)
R254A	V	13:45:14.500	+55:54:03.00	179.	21:46:09.1	1.142706	899.060
R254A	I†	13:45:14.500	+55:54:03.00	179.	22:04:34.5	1.153668	399.180
R254B	I	13:44:10.300	+55:52:23.00	360.	22:24:14.4	1.176263	599.520
R254B	V	13:44:10.300	+55:52:23.00	360.	22:37:32.6	1.196745	898.610
R274B	V	14:06:02.530	+22:22:52.00	360.	22:57:00.2	1.101976	899.050
R274B	I	14:06:02.530	+22:22:52.00	360.	23:15:42.0	1.136322	599.449
R274A	I	14:06:41.470	+22:24:32.00	180.	23:46:50.5	1.221127	598.970
R274A	V	14:06:41.470	+22:24:32.00	180	00:12:36.7	1.329770	899.010
R215D	V	14:19:14.890	+54:22:23.00	360	00:58:11.0	1.441854	899.310
R215D	I	14:19:14.890	+54:22:23.00	360	01:18:11.3	1.512075	599.550
R215C	I	14:20:16.710	+54:24:03.00	180	01:33:32.9	1.578033	599.230
R215C	V	14:20:16.710	+54:24:03.00	180	01:48:24.2	1.669614	898.930
R122A	V	16:30:15.660	+78:09:50.00	180	02:28:50.9	1.661313	899.030
R122A	I	16:30:15.660	+78:09:50.00	180	02:48:04.5	1.687588	599.370
R122B	I	16:27:20.340	+78:08:10.00	360	03:02:41.9	1.717508	599.380
R122B	V	16:27:20.340	+78:08:10.00	360	03:16:53.1	1.749540	899.120
R272B	V	18:05:57.810	+69:48:40.00	360	03:36:10.7	1.438898	898.680
R272B	I	18:05:57.810	+69:48:40.00	360	03:55:20.3	1.467887	599.430
R272A	I	18:07:42.190	+69:50:20.00	180	04:09:32.9	1.492619	599.489
R272A	V	18:07:42.190	+69:50:20.00	180	04:23:43.0	1.528791	899.150
R205B	I	23:12:14.590	+10:45:15.00	360	04:45:56.4	1.133010	599.440
R205C	I	23:12:39.220	+10:47:38.00	180	05:00:05.8	1.109161	599.440
R205C	V	23:12:39.220	+10:47:38.00	180	05:14:14.5	1.093874	179.850

Table A.4: INT Observing Log, 17/18 January 1999

RIXOS ID	Filter	RA h:mm:ss	Dec deg:mm:ss	Rotator PA	UT	Airmass	Exptime (s)
R245A	V	3:28:43.800	+02:48:48.00	180	20:50:50.5	1.112922	1198.729
R245A	I	3:28:43.800	+02:48:48.00	180	21:14:15.6	1.120276	798.750
R245B	I	3:28:07.800	+02:47:08.00	360	21:33:26.0	1.136450	799.369
R245B	V	3:28:07.800	+02:47:08.00	360	21:49:46.7	1.161470	1198.879
R293F	V	8:19:36.500	+37:30:22.00	360	22:16:31.7	1.338284	1198.810
R293F	I	8:19:36.500	+37:30:22.00	360	22:39:28.4	1.264518	799.160
R293E	I	8:20:10.600	+37:31:22.00	180	22:58:34.5	1.207108	799.260
R293E	V	8:20:10.600	+37:31:22.00	180	23:14:59.4	1.156742	1198.800
R248A	V	9:09:58.100	+42:54:50.00	180	23:40:32.7	1.231178	1078.370
R248A	I	9:09:58.100	+42:54:50.00	180	00:01:43.0	1.184513	719.280
R248B	I	9:09:08.900	+42:53:10.00	360	00:20:16.9	1.143247	718.910
R248B	V	9:09:08.900	+42:53:10.00	360	00:35:21.2	1.111841	1078.879
R216A	V	9:22:14.700	+62:16:26.00	180	01:07:48.4	1.244042	1078.880
R216A	I	9:22:14.700	+62:16:26.00	180	01:28:43.6	1.227312	718.770
R216B	I	9:20:57.300	+62:14:46.00	360	01:46:26.6	1.213613	718.320
R216B	V	9:20:57.300	+62:14:46.00	360	02:01:22.9	1.205020	1078.740
R260F	V	10:46:53.000	+54:17:46.00	360	02:23:34.5	1.167020	1078.980
R260F	I	10:46:53.000	+54:17:46.00	360	02:44:40.8	1.146553	719.490
R260Ax	I	10:47:45.200	+54:19:26.00	180	03:02:44.7	1.131628	718.830
R260A	V	10:47:45.200	+54:19:26.00	180	03:47:29.5	1.109622	1078.510
R287A	V	11:26:06.900	+54:23:38.00	180	04:09:56.9	1.114467	1078.919
R287A	I	11:26:06.900	+54:23:38.00	180	04:31:09.3	1.109802	719.330
R287B	I	11:25:05.100	+54:21:58.00	360	04:49:02.0	1.109029	719.370
R287B	V	11:25:05.100	+54:21:58.00	360	05:04:03.2	1.112620	1078.960
V165A	V	14:45:15.500	+63:37:25.00	180	05:36:49.2	1.335985	1079.129
V165A	I	14:45:15.500	+63:37:25.00	180	05:58:02.6	1.306264	719.350
V165B	I	14:43:54.500	+63:35:45.00	360	06:16:12.6	1.279420	719.569
V165B	V	14:43:54.500	+63:35:45.00	360	06:31:16.4	1.259524	1078.442

Table A.5: INT Observing Log, 18/19 January 1999

RIXOS ID	Filter	RA h:mm:ss	Dec deg:mm:ss	Rotator PA	UT	Airmass	Exptime (s)
R262A	V	1:24:52.600	+03:48:39.00	180	20:08:36.6	1.195514	1078.950
R262A	I	1:24:52.600	+03:48:39.00	180	20:29:37.5	1.238945	719.449
R262B	I	1:24:16.600	+03:46:59.00	360	20:53:05.6	1.315635	719.410
R262B	V	1:24:16.600	+03:46:59.00	360	21:08:55.6	1.393511	1078.220
R213B	V	8:03:48.600	+64:59:10.00	360	22:36:55.9	1.381444	1198.700
R213B	I	8:03:48.600	+64:59:10.00	360	23:00:29.3	1.346938	659.410
R213A	I	8:05:13.800	+65:00:50.00	180	23:20:33.1	1.318912	659.400
R213A	V	8:05:13.800	+65:00:50.00	180	23:34:59.3	1.295048	1198.790
R257A	V	9:05:51.800	+34:08:50.00	180	00:15:41.6	1.114649	1078.830
R257A	I	9:05:51.800	+34:08:50.00	180	00:36:60.1	1.081776	719.340
R257B	I	9:05:08.400	+34:07:10.00	360	00:55:27.4	1.054447	719.420
R257B	V	9:05:08.400	+34:07:10.00	360	01:10:38.8	1.034601	1078.930
R231B	V	10:09:45.500	+54:44:10.00	360	01:37:44.1	1.177170	1079.000
R231B	I	10:09:45.500	+54:44:10.00	360	01:58:57.4	1.155408	718.829
R231A	I	10:10:47.900	+54:45:50.00	180	02:15:54.6	1.140550	719.260
R231A	V	10:10:47.900	+54:45:50.00	180	02:31:58.2	1.126969	1078.959
R133A	V	10:57:23.000	+49:42:50.00	180	03:00:25.8	1.099163	1078.810
R133A	I	10:57:23.000	+49:42:50.00	180	03:21:55.4	1.085431	719.480
R133B	I	10:56:27.400	+49:41:10.00	360	03:38:35.3	1.076459	719.210
R133B	V	10:56:27.400	+49:41:10.00	360	03:53:54.9	1.071596	1078.920
R227B	V	11:36:12.800	+29:47:10.00	360	04:16:17.8	1.007143	989.010
R227B	I	11:36:12.800	+29:47:10.00	360	04:36:11.1	1.001538	659.390
R227A	I	11:36:54.200	+29:48:50.00	180	04:51:17.2	1.000251	659.349
R227A	V	11:36:54.200	+29:48:50.00	180	05:05:53.9	1.002801	989.140
R224A	V	13:16:44.600	+29:06:50.00	180	05:32:57.0	1.022004	988.920
R224A	I	13:16:44.600	+29:06:50.00	180	05:52:45.1	1.010236	659.520
R224B	I	13:16:03.400	+29:05:10.00	360	06:10:19.6	1.002687	659.439
R224B	V	13:16:03.400	+29:05:10.00	360	06:24:27.1	1.000211	989.130

Table A.6: INT Observing Log, 19/20 January 1999

RIXOS ID	Filter	RA h:mm:ss	Dec deg:mm:ss	Rotator PA	UT	Airmass	Exptime (s)
R283A	V	4:17:10.700	+01:06:14.00	180	9:58:13.1	1.214562	989.040
R283A	I	4:17:10.700	+01:06:14.00	180	2:11:27.2	1.149506	659.460
R283B	I	4:16:34.700	+01:04:34.00	360	2:29:22.5	1.171677	659.370
R283B	V	4:16:34.700	+01:04:34.00	360	2:43:35.5	1.199621	989.050
R255B	V	7:58:05.900	+37:46:34.00	360	3:07:40.4	1.113819	989.050
R255B	I	7:58:05.900	+37:46:34.00	360	3:27:26.0	1.085091	659.370
R255A	I	7:58:51.500	+37:48:14.00	180	3:43:14.4	1.064325	659.520
R255A	V	7:58:51.500	+37:48:14.00	180	3:57:34.3	1.045395	988.920
R228A	V	8:39:10.300	+36:32:02.00	180	0:24:32.5	1.056936	989.160
R228A	I	8:39:10.300	+36:32:02.00	180	0:44:18.8	1.038725	659.430
R228B	I	8:38:25.500	+36:30:22.00	360	0:59:56.4	1.025515	659.430
R228B	V	8:38:25.500	+36:30:22.00	360	1:13:53.8	1.016272	988.990
R285B	V	9:43:24.400	+16:30:22.00	360	1:34:48.5	1.074399	898.590
R285B	I	9:43:24.400	+16:30:22.00	360	1:53:05.6	1.054421	659.390
R285A	I	9:44:02.000	+16:32:02.00	180	2:08:24.0	1.040787	659.380
R285A	V	9:44:02.000	+16:32:02.00	180	2:22:38.3	1.030493	899.280
R273B	V	10:42:27.100	+12:02:46.00	360	03:32:50.5	1.046633	989.090
R273B	I	10:42:27.100	+12:02:46.00	360	03:52:36.4	1.044102	659.200
R273A	I	10:43:03.900	+12:04:26.00	180	04:08:45.3	1.046268	659.480
R273A	V	10:43:03.900	+12:04:26.00	180	04:23:04.4	1.053976	989.010
R258A	V	11:18:34.900	+07:47:02.00	180	04:43:35.4	1.074207	989.140
R258A	I	11:18:34.900	+07:47:02.00	180	05:11:17.4	1.088920	659.350
R258B	I	11:17:58.500	+07:48:22.00	360	05:27:33.9	1.106028	659.450
R258B	V	11:17:58.500	+07:48:22.00	360	05:41:42.9	1.129838	989.190
R126B	V	12:21:13.200	+28:12:58.00	360	06:02:46.4	1.008908	899.060
R126B	I	12:21:13.200	+28:12:58.00	360	06:20:58.8	1.018802	599.110
R126A	I	12:21:54.000	+28:14:38.00	180	06:34:58.0	1.030330	599.330
R126A	V	12:21:54.000	+28:14:38.00	180	06:47:56.8	1.047649	899.000

Table A.7: INT Observing Log, 20/21 January 1999

RIXOS ID	Filter	RA h:mm:ss	Dec deg:mm:ss	Rotator PA	UT	Airmass	Exptime (s)
R292A	V	1:43:39.000	+04:20:42.00	180	20:17:54.5	1.188824	1198.939
R292A	I	1:43:39.000	+04:20:42.00	180	20:41:13.3	1.239159	898.580
R292B	I	1:43:03.000	+04:18:52.00	360	21:04:35.5	1.316812	899.270
R292B	V	1:43:03.000	+04:18:52.00	360	21:22:53.6	1.405190	1198.860
R211B	V	7:20:56.400	+71:19:34.00	360	21:47:07.6	1.484867	998.930
R211B	I	7:20:56.400	+71:19:34.00	360	00:11:20.0	1.357749	799.330
R211A	I	7:22:50.000	+71:21:14.00	180	00:29:42.7	1.357318	799.300
R211A	V	7:22:50.000	+71:21:14.00	180	00:46:14.8	1.358653	1198.6
R221A	V	8:48:41.900	+37:41:02.00	180	02:45:11.6	1.033362	1198.260
R221A	I	8:48:41.900	+37:41:02.00	180	03:09:55.7	1.052486	719.280
R221B	I	8:47:56.500	+37:39:22.00	360	03:26:52.4	1.074356	719.320
R221B	V	8:47:56.500	+37:39:22.00	360	03:42:10.6	1.104825	1198.750
R123B	V	11:18:49.500	+21:18:29.00	360	04:09:41.3	1.009709	1078.909
R123B	I	11:18:49.500	+21:18:29.00	360	04:30:50.7	1.008981	719.320
R123A	I	11:19:28.100	+21:20:09.00	180	04:46:57.0	1.012537	719.230
R123A	V	11:19:28.100	+21:20:09.00	180	05:02:11.4	1.021929	1078.920
R116A	V	12:04:32.300	+56:11:02.00	180	05:30:11.0	1.129799	1078.880
R116A	I	12:04:32.300	+56:11:02.00	180	05:51:19.3	1.136804	719.160
R116C	I	12:03:31.000	+56:09:22.00	360	06:20:13.7	1.157149	719.310
R116C	V	12:03:31.000	+56:09:22.00	360	06:35:23.6	1.175498	1079.000

Appendix B | *INT WFC Instrumental Corrections*

B.1 Linearity Correction

A resonably large (~10% of sky) non-linearity occurs in two of the science devices, and to a lesser extent in the other two[1]. This non-linearity arises in the ADC, after the bias is applied. Therefore it is appropriate to correct for this effect *after* bias-subtraction. CCDs 1 and 3 share an ADC and are essentially linear to better than 1%, CCDs 2 and 4 share another ADC and suffer from significant non-linearity.

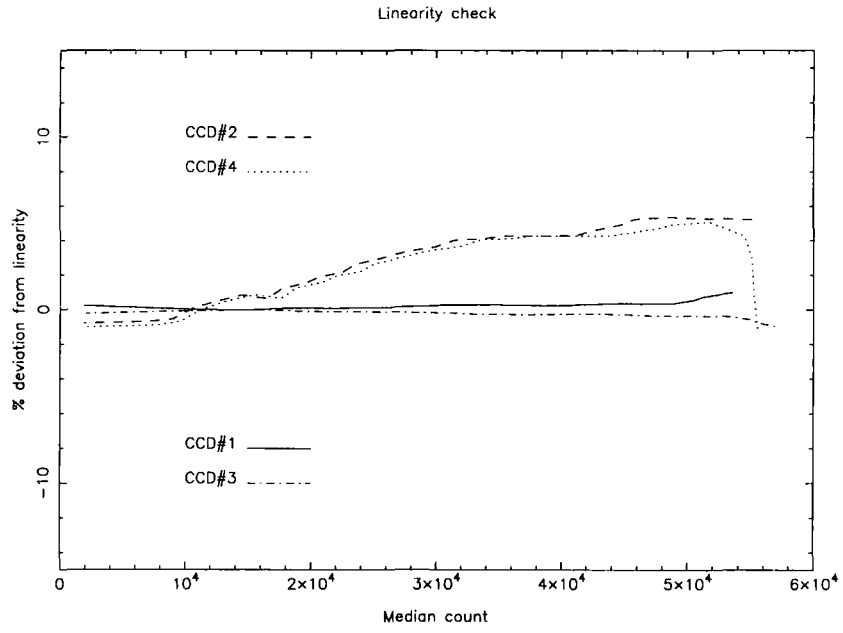

Figure B.1: WFC linearity curve, taken from the Wide Field Survey webpage `http://www.ast.cam.ac.uk/~wfcsur/`.

Taking CCD 1 as a reference, polynomial corrections can be used to bring the other

[1] "The only uniform CCD is a dead one." - Mackay (1986)

three CCDs into agreement to better than 0.5%. The values measured by the Wide Field Survey nearest in time to our observations were used (taken from `http://www.ast.cam.ac.uk/~wfcsur/`). For run 1 the August 1998 polynomials were applied, and for run 2 the October 1998 values were used. The non-linearity was found to remain stable between October 1998 and August 1999.

B.1.1 August 1998

$$CCD_2 = 0.987086 \times \text{value} - 1.06221\text{E-}06 \times \text{value}^2 + 5.19301\text{E-}13 \times \text{value}^3$$
$$CCD_3 = 0.993867 \times \text{value} + 4.15398\text{E-}07 \times \text{value}^2 - 1.02134\text{E-}12 \times \text{value}^3$$
$$CCD_4 = 0.987744 \times \text{value} - 1.15224\text{E-}06 \times \text{value}^2 + 2.58758\text{E-}12 \times \text{value}^3$$

B.1.2 October 1998

$$CCD_2 = 0.991703 \times \text{value} - 1.40928\text{E-}06 \times \text{value}^2 + 5.84305\text{E-}12 \times \text{value}^3$$
$$CCD_3 = 0.993855 \times \text{value} + 5.36676\text{E-}07 \times \text{value}^2 - 5.50707\text{E-}12 \times \text{value}^3$$
$$CCD_4 = 0.995565 \times \text{value} - 1.10012\text{E-}06 \times \text{value}^2 + 5.77076\text{E-}12 \times \text{value}^3$$

These scalings were applied using the `IRAF` routine `imexpression`.

B.2 Distortion Correction

The equations given below were applied to convert to global pixel coordinates, with the origin at the centre of the WFC rotator. This solution was measured in conjunction with `STARLINK` staff Mark Taylor and Peter Draper, and is designed to correct for the barrel distortion suffered by the camera. This distortion means that objects are shifted radially inwards by an amount dependent on their distance from the optical centre of the system. At the extreme edges it is so severe that the same object is offset from itself as viewed in the two different rotations by around 10 arcsec. This solution provides good internal astrometric calibration at the level of around two pixels (ie. sub-arcsecond). This was verified by mosaicking the data for several pointings.

To convert from chip coordinates to global WFC pixel coordinates, correcting for translation rotation and shear, with the origin at the rotator centre of the system, the following transformations were calculated:

$$x_{WFC} = a_{xn} \times (x_n + b_{xn}) + c_{xn} \times (y_n + d_{xn})$$
$$y_{WFC} = a_{yn} \times (y_n + b_{yn}) + c_{yn} \times (y_n + d_{yn})$$

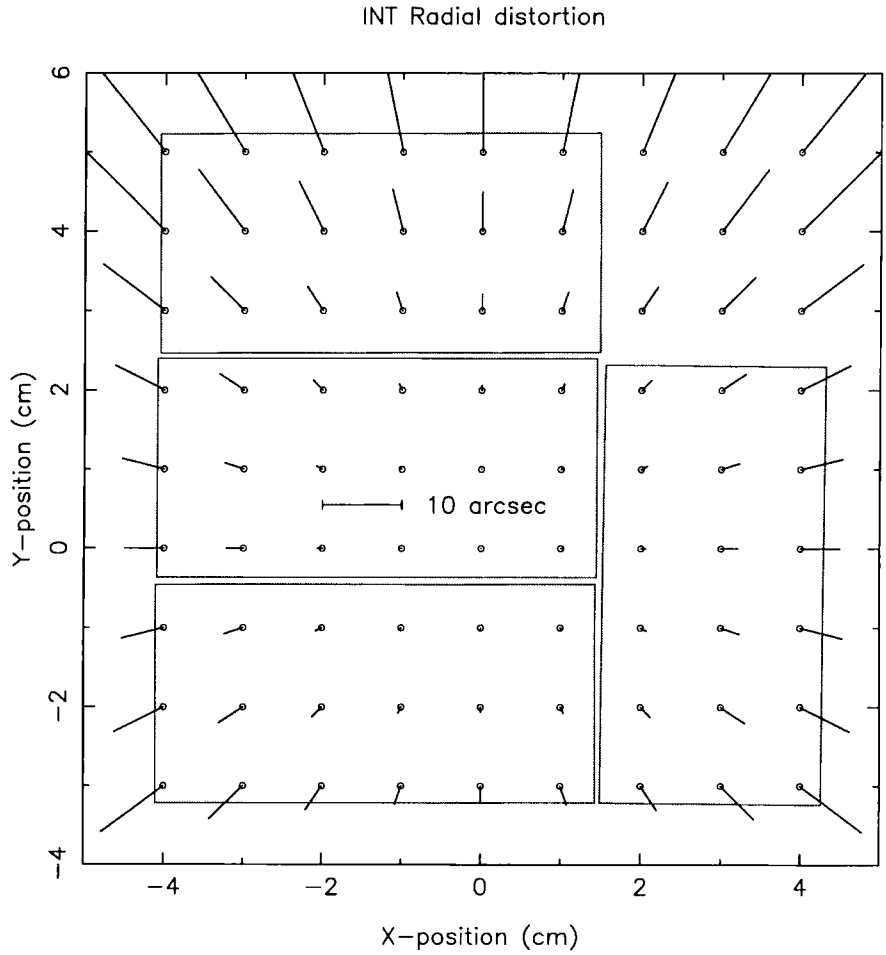

Figure B.2: Illustration of the distortions suffered by the WFC. Figure from the WFS webpage.

where x_{WFC}, y_{WFC} refer to global WFC coordinates; x_n, y_n are the pixel coordinates of the n^{th} chip and the coefficients a_n,b_n are given below.

Finally, the radial distortion term was corrected as follows:

$$r_{measured} = pixel\ scale \times \sqrt{x_{WFC}^2 + y_{WFC}^2}$$
$$r_{true} = r_{measured} \times (1.0 + k_{DISCO} \times r_{measured}^2)$$

The value of $r_{measured}$ is used to convert the measured radial distance to its true value, r_{true}. The pixel scale was measured to be 0.333 pixels arcsec^{-1}. The disco factor, $k_{DISCO} = -5.3 \times 10^{-10}$ pixel^{-2} (the minus sign indicating a barrel distortion).

Table B.1: Coefficients for correcting the WFC instrumental distortion to the sky tangent plane

n	a_{xn}	b_{xn}	c_{xn}	d_{xn}
1	0.999999946853034	+336.74	-0.00032602749849675	-3039.14
2	-0.0108409002911821	-3180.68	0.999941235713818	-1729.67
3	0.999998008075429	-3876.73	-0.00199595720731426	-2996.3
4	1.000000000000000	-1778.00	0.00000000000000000	0.00
n	a_{yn}	b_{yn}	c_{yn}	d_{yn}
1	0.00032602749849675	336.74	0.999999946853034	-3039.14
2	-0.999941235713818	-3180.68	-0.0108409002911821	-1729.67
3	0.00199595720731426	-3876.73	0.999998008075429	-2966.3
4	0.00000000000000000	0.00	1.000000000000000	-3029.

B.3 Internal Photometric Calibration

The relative zeropoints can be found by examining the relative sky levels in the four chips. Thus the median counts in each chip were found relative to the median counts in chip four.

The relative zeropoint (wrt chip 4), zpt_n is then:

$$zpt_n = -2.5 \log \left(\frac{median\ counts_n}{median\ counts_4} \right) \tag{B.1}$$

where subscript n refers to the n^{th} chip.

Due to contamination from astronomical objects, a simple application of the median to each CCD is usually biased higher than the median sky value. Five subregions of

100×100 pixels were extracted from each chip and the median value in each found. The median of these five subregions then gave the median sky level of that chip. This was found to a better estimate of the median sky level. The relative zeropoint and its error were calculated from using every available science mosaic from each run, and computing the median and median absolute deviation of these values, given below.

Table B.2: Relative zeropoints for the WFC, June 1998

CCD	$Zpt_I - Zpt_4$	Error	$Zpt_V - Zpt_4$	Error
1	0.14	0.02	0.02	0.04
2	0.10	0.02	0.09	0.03
3	0.11	0.03	0.00	0.05

Table B.3: Relative zeropoints for the WFC, January 1998

CCD	$Zpt_I - Zpt_4$	Error	$Zpt_V - Zpt_4$	Error
1	0.52	0.01	0.42	0.02
2	0.47	0.01	0.45	0.02
3	0.48	0.01	0.37	0.02

As a check of the accuracy of this method, aperture photometry of objects from the science data itself was compared, where repeat measurements existed. For each pair of observations of a field, objects were matched with the counterpart in the other rotation. The difference in instrumental magnitude was then computed. This was done on a chip by chip basis. Since chip four overlaps with itself, the same objects measured with the same CCD should have the same instrumental magnitude, within the measurement errors, if the observation is made at the same airmass. This was typically the case as the fields were observed AI, AV, BV, BI, or some variation on this pattern. (NB, in a couple of cases the B-observation was made on a different night from the A-observation.) Hence, if the observations are made nearby in time, this can be used as a necessary, but not sufficient, condition to test if the night was photometric.

Note: The instrument was serviced between the two runs, and the gain of the CCDs altered significantly. Therefore it was necessary to calculate different relative zero points for each observing run.

The median offset in the V-band instrumental magnitudes for all objects brighter than V=22.0 was measured for chip 4 for each pair of observations; and the offset in the I-band for objects brighter than I=20.5. Above these cutoffs, the counts in the objects

is sufficiently high that the instrumental error in measuring a magnitude is small. All observations with $mag_{(A-B)CCD4}$ <0.05 (ie. small extinction differences between the two pointings) were then used to calculate the relative zero point offsets between CCDs. The median value of each of these offsets was calculated and this taken to be the zero point offset between the nth chip and chip 4. The median absolute deviation of all measured offsets was used to estimate the error in measuring the zero point offsets.

This was found to be in good agreement with the measurements made using the relative sky levels.

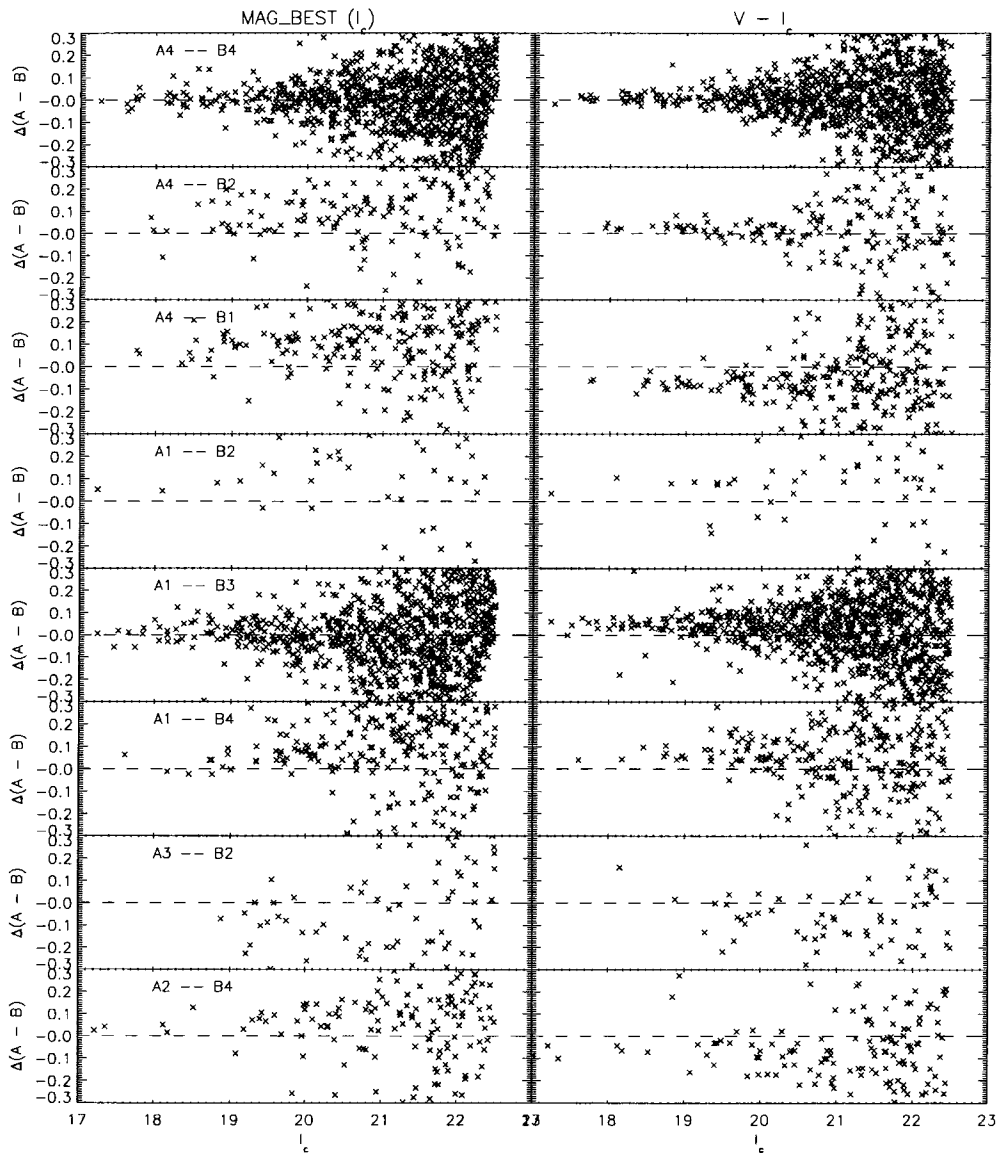

Figure B.3: Internal photometric errors. The plots show a comparison between photometry of objects present in both A- and B-frames of a single typical field. The left column is the difference in MAG_BEST between A- and B-images, and the right column is the difference in V-I colour. Labels in the plots show which chips are being compared (ie. "A1 – B2" is chip 1 in the A-pointing - chip 2 in the B-pointing). The levels of the random and systematic errors are clearly visible. This plot is pessimistic as it does not take account of mismatching objects in the pairs of chips, nor of matching spurious objects such as comsic rays and diffraction spikes with real objects. Some panels show few points due to the small overlapping area between pairs of chips.

Bibliography

The following abbreviations are used in this bibliography:

A&A: Astronomy and Astrophysics

AJ: The Astronomical Journal

ApJ: The Astrophysical Journal

ApJL: The Astrophysical Journal Letters

ApJS: The Astrophysical Journal Supplement

ARA&A: Annual Reviews of Astronomy and Astrophysics

JRASC: Journal of the Royal Astronomical Society of Canada

MNRAS: Monthly Notices of the Royal Astronomical Society

PASP: Publication of the Astronomical Society of the Pacific

Abell G. O., 1958, ApJS , 3, 211

Abell G. O., Corwin H. G. & Olowin R. P., 1989, ApJS , 70, 1

Adami C., Holden B. P., Castander F. J.,Nichol R. C., Mazure A., Ulmer M. P., Postman M., Lubin L. M., 2000, AJ , 120, 1

Alpher R. A., Bethe H. A., Gamov G., Phys. Rev., 73, 803

Alpher R. A., & Herman R. C., 1948, Nature, 162, 774

Andersen V. Owen F. N., 1994, ApJ , 108, 361

Andreon S., Pello R., Davoust E., Dominguez R., Poulain P., 2000, A&AS , 141, 113

Andreon S., 2001, ApJ , 547, 623

Aragon-Salamanca A., 1993, PhD Thesis, University of Durham.

Aragon-Salamanca A., Ellis R. S., Couch W. J., & Carter D., 1993, MNRAS , 248, 128

Bahcall N. A., 1981 ApJ , 247,787

Bartelmann M., 1996, A&A , 313, 697

Beers T. C., Flynn K., Gebhardt K.,1990, AJ , 100, 32

Benitez N., Broadhurst T., Rosati P., Courbin F., Squires G., Lidman C., Magain P., 1999, ApJ , 527, 31

Bertin E., Arnouts, 1996, A&AS , 117, 393

Best P. N., 2000, MNRAS , 317, 720

Blanton E. L., Gregg M. D., Helfand D.J., Becker R. H., & Keighly K. M., 2001, AJ , 121, 2915

Bolzonella M., Miralles J. M., Pello R., 2000, A&A , 363, 476

Bower R. G., Lucey J. R., Ellis R. S., 1992, MNRAS , 254, 601

Bower R. G., Coles P., Frenk C. S. & White S. D. M., 1993, ApJ , 405, 403

Bower R. G., Bohringer H., Briel U. G., Ellis R. G.,Castander F. J.,Couch W. J., 1994, MNRAS , 268, 345

Bower R. G., Castander F. J., Couch W. J., Ellis R. S., Bohringer H., 1997, MNRAS , 291, 353

Bower R. G., & Smail I. R., 1997, MNRAS , 290, 292

Bower R. G., Benson A. J., Lacey C. G., Baugh C. M., Cole S., & Frenk C. S., 2001, MNRAS , 325, 497

Bracewell R. N., 1965, The Fourier Transform and its Applications, McGraw Hill, New York

Bramel D. A., Nichol R. C., Pope A. C., 2000., ApJ , 533, 601

Briel U. G. & Henry J. P., 1993, A&A , 278, 379

Bruzual G. & Charlot S., 1993, ApJ , 405, 538

Cabanac R. A., de Lapparent V., Hickson P., 2000, A&A , 364, 349

Cappi A., Chinarini G., Conconi P., Vettolani G., 1989, A&A , 223, 1

Cardelli J. A., Clayton C., & Mathis J. S., 1989, ApJ , 345, 245

Carlberg R. G., Yee H. K., Ellingson E.,Abraham R., Gravel P., Morris S., Pritchet C. J., 1996, ApJ , 462, 32

Carlberg R. G., Yee H. K. C., & Ellingson E., 1997, ApJ , 478, 462

Castander F. J., Ellis, R. S., Frenk C. S., Dressler A., Gunn J. E., 1994, ApJ , 424, 79

Castander F. J., Bower R. G., Ellis R. S., Aragon-Salamanca A., Mason K. O., Hasinger G., McMahon R. G., Carrera F. J., Mittaz J. P. D., Perez-Fournon I., Lehto H. J., 1995, Nature, 281, 59

Cash W., 1979, ApJ , 228, 939

Cen R., Ostriker J. P., 1994, ApJ , 431, 451

Charlot S., & Longhetti M., 2001, MNRAS , 323, 887

Clowes R. G., Campusano L. G., 1991, MNRAS , 249, 218

Cole S. M., Aragon-Salamanca A., Frenk C. S., Navarro J. F., Zepf S. E., 1994, MNRAS , 271, 781

Cole S. M., Lacey C. G., Baugh C. M., & Frenk C. S., 2000, MNRAS , 319, 168

Coles P., & Lucchin F., 1995, Cosmology, The Origin and Evolution of Cosmic structure, Wiley

Colless M., 1989, MNRAS , 237, 799

Condon J. J., Cotton W. D., Greissen E. W., Yin Q. F., Perley R. A., Taylor G. B., & Broderick J. J., 1998, AJ , 115, 1693

Couch W. J., Ellis R. S., Malin D. F., & MacLaren I., 1991, MNRAS , 249, 606

Cowie L. L., Gardner J. P., Lilly S. J., & McLean I., 1990, ApJL , 360, 1

Cowie L. L., Gardner J. P., Hu E. M., Songalia A., Hodapp K.-W., & Wainscoat R. J., 1994, ApJ , 434, 114

Cowie L. L., Songalia A., Hu E. M., Cohen J. G., 1996, AJ , 112, 839

da Costa L., Scodeggio M., Olsen L. F., Nonino M., Rengelink R., Bender R., Franx M., Jorgenson H. E., Renzini A., Rosati P., 1999, A&A , 343L, 29

Dalcanton J. J., 1996, ApJ , 466, 92

Dalton G. B., Efstathiou G., Maddox S. J., Sutherland W. J., 1994, MNRAS , 269, 151

,Dalton G. B., Maddox S. J., Sutherland W. J, Efstathiou G., 1997, MNRAS , 289, 263

Davis M. & Peebles P. J. E., 1983, ApJ , 294, 70

De Sitter W., 1917, MNRAS , 78, 3

de Bernardis P., et al., 2001, astro-ph/0105296

Donahue M., Mack J., Scharf C., Lee P., Postman M., Rosati P., Dickinson M., Voit G. M., Stocke J. T., 2001, ApJL , 552, 93

Dressler A., 1980, ApJ , 490, 577

Drory N., Feulner G., Bender R., Botzler C. S., Hopp U., Maraston C., Mendes de Oliveira C., Snigula J., 2001, MNRAS , 325, 550

Edge A. C., Stewart G. C., Fabian A. C., & Arnaud K.A., 1990, MNRAS , 245, 559

Edge A. C., 2001, MNRAS , 328, 762

Efron B., 1981, Biometrika, 68, 589

Eggen O. J., Lynden-Bell D., & Sandage A. R., 1962, ApJ , 136, 748

Eisenstein D. J., Annis J., Gunn J. E., Szalay A. S., Connolly A. J., Nichol R. C., Bahcall N. A., Bernardi M, et al., 2001, astro-ph/0108153

Eke V. R., Cole S. M. & Frenk C. S., 1996, MNRAS , 282, 263

Ellis R. S., Smail I. R., Dressler A., Couch W. J., Oemler Jr. A. E., Butcher H., & Sharples R. M., 1997, MNRAS , 483, 582

Evrard A. E., ApJ , 363, 349

Fabian A., 1998, Cooling Flows in Clusters of Galaxies, Kluwer Academic Press, p315

Fairley B. W., Jones L. R., Scharf C., Ebeling H., Perlman E., Horner D., Wegner G., Malkan M., 2000, MNRAS , 315, 669

Fanaroff B. L. & Riley J. M., 1974, MNRAS , 167, 31

Fioc M., & Rocca-Volmerange B., 1997, A&A , 326, 950

Friedmann A., 1922, Z. Phys., 10, 377

Gal R. R., de Carvalho R. R., Odewahn S. C., Djorgovski S. G., Margoniner V. E., 2000, AJ , 119, 12

Gay P. L., Hill G. J., Rawlings S., Croft S. D., 2001, Gas and Galaxy Evolution, ASP Conference Proceedings, Vol. 240., p642

Gehrels N., 1986, ApJ , 303, 336

Gioia I. M., Henry J. P., Maccacaro T., Morris S. L., Stocke J. T., Wolter A., 1990, ApJ , 356, 35

Gladders M. D. & Yee H. K. C., 2000, AJ , 120, 214

Gonzalez A. H., Zaritsy D., Dalcanton J. J., Nelson A., 2001, ApJS , in press

Groudfrooij P., de Jong T., Hansen L., & Norgaard-Nielsen,H. U., 1994, MNRAS , 271, 833

Gullixson C. A., 1992, ASP Conf. Series, Vol 23, 130

Gunn J. E., Hoessel J. G., & Oke J. B., 1986, ApJ , 306, 30

Haines C. P., Clowes R. G., Campusano L. E., Adamson A. J., 2001, MNRAS , 323, 688

Hall P. B., Green R. F., Cohen M., 1998, ApJS , 119, 1

Hall P. B., Sawicki M., Martini P., Finn R. A., Pritchet C. J., Osmer P. S., McCarthy D. W., Evans A. S., Lin H., Hartwick F. D. A., 2001, AJ , 121, 1840

Harris W. E., PASP , 102, 949

Hattori M., Ikebe Y., Asaoka I., Takeshima T., Bohringer H., Mihara T., Neumann D. M., Schindler S., Tsuru T., Tamura T., 1997, Nature, 388, 146

Hawarden T. G., Leggett S. K., Letawsky M. B., Ballantyne D. R., Casali M. M., 2001, MNRAS , 2001, 325, 563

Henry J. P., Soltan A., Briel U., & Gunn J. E., 1982, ApJ , 262, 1

Henry J. P., & Lavery R. J., ApJ , 280, 1

Hill G. J. & Lilly S. J., 1991, ApJ , 367, 1

Hoekstra H., Franx M., Kuijken K., Van Dokkum P. G., 2001, astro-ph/0109445

Holden B. P., Nichol R. C., Romer K. A.,Nichol R. C., Ulmer M. P., 1997, AJ , 114, 170

Holden B. P., Nichol R. C., Romer K. A.,Metevier A., Postman M., Ulmer M. P., Lubin L. M., 1999, AJ , 118, 2002

Holden B. P., Adami C., Nichol R. C., Castander F. J.,Lubin L. M., Romer K. A., Mazure A., Postman M., Ulmer M. P., 2000, AJ , 120, 23

Holder G. P., Mohr J. J., Carlstrom J. E., Evrard A. E., & Leitch E. M., 2000, ApJ , 544, 629

Hunt L. K., Mannucci F., Testi L., Migliorini S., Stanga R. M., Baffa C., Lisi F., Vanzi L., 1998, ApJ , 115, 2594

Hubble E., 1925, Observatory, 48, 139

Hubble E., 1929, Proceedings of the National Academy of Sciences, 15, 168

Hubble E., 1936, The Realm of the Nebulae, Yale University Press, New Haven

Huchra J P. & Geller M. J., 1982, ApJ , 257, 423

Jeans J. H., 1902, Phil. trans. R. Soc., 199A, 1

Jenkins A., Frenk C. S., White S. D. M., Colberg J. M., Cole S., Evrard A. E., Couchman H. M. P., Yoshida N., 2001, MNRAS , 321, 372

Jones L. R., Scharf C. A., Ebeling H., Perlman E., Wegner G., Malkan M., & Horner D., 1998, ApJ , 495, 100

Jones L. R., Ponman T. J., & Forbes D. A., 2000, MNRAS , 312, 139

Kauffmann G., Charlot S., White S. D. M., 1996, MNRAS , 281, 487

Kauffmann G., & Charlot S., 1998, MNRAS , 294, 705

Kahn F. D. & Woltjer L., 1959, ApJ , 130, 105

Kaiser N., 1986, MNRAS , 222, 323

Kaiser N., & Squires G., ApJ , 1993, 404, 441

Katgert P., Mazure A., Perea J., den Hartog R., Moles M., Le Fevre O., Dubath P., Focardi P., Rhee G., Jones B., Escalera E., Biviano A., Gerbal D., Giuricin G., 1996, A&A , 310, 8

Kawasaki W., Shimasaku K., Doi M., Okamura S., 1998, A&AS , 130, 567

Kepner J. V., Fan X., Bahcall N., Gunn J., Lupton R., Xu G., 1999, ApJ , 517, 78

Kim R. S., Kepner J. V., Strauss M. A., Bahcall N., Gunn J. E., Lupton R. H., Schlegel D. J., SDSS Collaboration, 1999, A&AS , 194, 8801

Kodama T. & Arimoto N., 1997, A&A , 320, 41

Kodama T., Arimoto N.,Barger A. J.,Aragon-Salamanca A., 1998, A&A , 334, 99

Kodama T., Bell E. F., Bower R. G., MNRAS , 302, 152

Kolb E. W., & Turner M. S., 1990, The Early Universe, Addison-Wesley Publishing

Landolt A. U., 1992, AJ , 104, 372

Lawrence C. R., Schneider D. P., Scmidt Mj., Bennett C. L., Hewitt J. N., Burke B. F., Turner E. L., Gunn J. E., Science, 223, 46

Ledlow M. J., & Owen F. N., 1996, AJ , 112, 9

Lewis A. D., Ellingson E., Morris S. L.,Carlberg R. G., 1999, ApJ , 517, 587

Lidman C. E. & Peterson B. A., 1996, AJ , 112, 2454

Lilly S. J., Cowie L. L, & Gardner J. P., 1991, ApJ , 369, 79

Lilly S. J., le Fevre O., Crampton D., Hammer F., Triesse L., 1995, ApJ , 455, 50

Lin H., Yee H. K. C., Carlberg R. G., Morris S. L., Sawicki M., Patton D. R., Wirth G., Shepherd C. W., 1999, ApJ , 518, 533

Lobo C., Iovino A., Lazzati D., Chincarini G., 2000, A&A , 360, 896

Longair M. S.,Seldner M., 1979, MNRAS , 189, 433

Lubin L. M., & Postman M., 1996, AJ , 111, 1795

Lumsden S. J., Nichol R. C., Collins C. A., Guzzo L., 1992, MNRAS , 258, 1

Mackay C. D., 1986, ARA&A, 24, 255

Mackay C. D., Beckett M G., McMahon R. G., Parry I. R., Piche F., Ennico K. A., Kenworthy M., Ellis R. S., Aragon-Salamanca A., 1998, SPIE, 3354, 14

Maddox S. J., 1988, IAUS, 130, 521

Mannucci F., Basile F., Cimatti A., Daddi E., Poggianti B. M., Pozzetti L., & Vanzi L, MNRAS , in press

Mason K. O., et al. 2000, MNRAS , 311, 456

Mathiesen B. F., & Evrard A. E., 2001, ApJ , 546, 100

McCarthy, Jr. D. W., Ge J., Hinz J. L., Finn R. A., de Jong R. S., 2001, PASP , 113, 353

McCracken, H. J., 1999, PhD Thesis, University of Durham

McLeod B. A., Bernstein G. M., Riecke M. J., Tollestrup E. V., Fazio G. G., 1995, ApJS , 96, 117

Metcalfe N., Shanks T., Campos A., McCracken H. J., Fong R., 2001, MNRAS , 323, 795

Milgrom M., ApJ , 270, 371

Miller N. A., Owen F. N., Burns J. O., Ledlow M. J, Voges W., 1999, AJ , 118, 1988

Minezaki T., Kobayashi Y., Yoshii Y.,& Peterson B. A., 1998, AJ , 115, 229

Mitchell R. J., Culhane J. L., Davison P. J., & Ives J. C., 1976, MNRAS , 176, 75

Monet D. G.,1998 A&AS , 193, 120.03

Nakata F., Kajisawa M., Yamada T., Kodama T., Shimasaku K., Tanaka I., Doi M., Furusawa H., 2001, astro-ph/0110597

Navarro J. F., Frenk C., & White S. D. M., 1997, ApJ , 490, 493

Nichol R. C., Ulmer M. P., Kron R. G., Wirth G. D., Koo D. C., 1994, ApJ , 432, 464

Nichol R. C., Holden B. P., Romer A. K., Ulmer M. P., Burke D. J., & Collins C. A., 1997, ApJ , 481, 644

Nichol R. C., Miller C. J., Reichart D., Wasserman L., Genovese C., SDSS Collaboration, A&AS , 197, 107

Nonino M., Bertin E., da Costa L., Deul E., Erben T., Olsen L., Prandoni I., Scoddegio M., Wicenec A., Wichmann R., Benoist C., Freudling W., Guarnieri M. D., Hook I., Hook R., Mendez R., Savaglio S., Silva D., & Slijkhuis R., 1999, A&A , 137, 51

Oke J. B., Postman M., Lubin L. M., 1998, AJ , 116, 549

Olsen L. F., Scodeggio M., da Costa L., Benoist C., Bertin E., 1999, A&A , 345, 681

Olsen L. F., Scodeggio M., da Costa L., Slijkhuis R., Benoist C., Bertin E., Deul E., Erben T., Guarnieri M.D., Hook R., Nonino M, Prandoni I., Wicenec A., & Zaggia S., 1999, A&A , 345, 363

Opik E., 1922, ApJ , 55, 406

Ostrander E. J., Nichol R. C., Ratnatunga K. U., Griffiths R. E., 1998, AJ , 116, 2644

Owen F. N., Ledlow M. J., Keel W. C., Morrison G. E., 1999, AJ , 118, 6330

Peebles P. J. E., 1965, ApJ , 142, 1317

Peebles P. J. E., 1972, Comm. Ap. and Space Phys, 4, 53

Penzias A. A. & Wilson R. W., 1965, ApJ , 142, 419

Piccinotti G., Mushotzky R. F., Boldt E. A., Holt S. S., Marshall F. E., Serlemistos P. J., & Shafer R. A., ApJ , 253,485

Pisani A., 1996, MNRAS , 278, 697

Ponman T. J., Allan D. J., Jones L. R., Merrifield M., McHardy I. M., Lehto H. J., & Luppino G. A., 1994, Nature, 369, 462

Ponman T. J., Cannon D. M., & Navarro J. F., 1999, Nature, 397, 135

Postman M., Lubin L. M., Gunn J. E., Oke J. B., Hoessel J. G., Schneider D. P., Christensen J. A., 1996 AJ , 111, 615

Pozzetti L. & Mannucci F., 2000, MNRAS , 317L, 17

Press W. H. & Schechter P., 1974, ApJ , 187, 425

Press W. H., Teukolsky S. A., Vetterling W. T. & Flannery B. P., 1992, Numerical Recipes in FORTRAN, Second Edition, Cambridge University Press.

Ramella M., Biviano A., Boschin W., Bardelli S., Scodeggio M., Borgani S., Benoist C., da Costa L., 2000, A&A , 360, 861

Rhodes J., Refrigier A., Groth E. J., 2001, ApJ , 552,85

Romer A. K., Nichol R. C., Holden B. P., Ulmer M. P., Pildis R. A., Merrelli A. J., Adami C., Burke D. J., Collins C. A., 2000, ApJ , 126, 209

Romer A. K., Viana P. T. P., Liddle A. R., Mann R. G., 2001, ApJ , 547, 594

Rosati P., Stanford S. A., Eisenhardt P. R., Elston R., Spinrad H., Stern D., & Dey A., 1999, AJ , 118, 76

Schechter P.,1976, ApJ , 203, 297

Schlegel D. J., Finkbeiner D. P., Davis M., 1998, ApJ , 500, 525

Scott E. L., 1957, ApJ , 62, 248

Serlemitsos P. J., Smith R. W., Boldt E. A., Holt S. S., & Swank J. H., 1977, ApJL , 211, 63

Sheth R. K., & Tormen G., MNRAS , 308, 119

Smail I. R., & Dickinson M., ApJL , 455, 99

Smail I. R., Hogg D. W., Yan L., Cohen J. G., 1995, ApJL , 449, 105

Smail I. R., Ellis R. S., Dressler A., Couch W. J., Oemler A., Sharples R. M., Butcher H., 1997, ApJ , 479, 70

Smail I. R., Edge A. C., Ellis R. S., Blandford R. D., 1998, MNRAS , 293, 124

Soucail G., Kneib J. P., Jansen A. O., Hjorth J, Hattori M., Yamada T., 2001, A&A , 367, 741

Soneira R. M. & Peebles P. J. E., 1978, AJ , 83, 845

Stanford S. A., Eisenhardt P., Dickinson M., 1998, ApJ , 492, 461

Stanford S. A., Elston R., Eisenhardt P. R., Spinrad H., Stern D., & Dey A., 1997, AJ , 114, 2232

Stanford S. A., Holden B., Rosati P., Tozzi P., Borgani S., Eisenhardt P. R., Spinrad H., 2001, ApJ , 552, 504

Sunyaev R., & Zeldovich Y., 1972, Comments Astrophys. Space Phys., 4, 173

Szalay A. S., Conolly A. J., Szokoly G. P., 1998, AJ , 117, 68

Tonry. J. & Davis.,M.,1979 AJ , 84, 1511

Van Haarlem M. P., Frenk C. S., & White S. D. M., 1997, MNRAS , 287, 817

Vikhlinin A., McNamara B. R., Forman W., & Jones C., 1998, ApJ , 502, 558

Visvanathan N., 1978, A&A , 67, 17

Voges W., 1993, Advances in Space Research, 12, 391

White S. D. M., Efstathiou G., & Frenk C. S., 1993, MNRAS , 262, 1023

White D. A., Jones C., & Forman W., 1997, MNRAS , 292, 419

White R. L., Becker R. H., Helfand D. J., & Gregg M. D., 1997, ApJ , 475, 479

Williams J. P., de Geus E. J., Blitz L., 1994, ApJ , 451, 252

Wittman D., Tyson J. A., Margoniner V. E., Cohen J. G., Dell'Antonio I. P., 2001, astro-ph/0104094

Worthey G., 1994, ApJS , 95, 107

Wu X. P., Xue Y-J., Fang L-Z., 1999, ApJ , 524, 22

Yee H. K. C. & Green R. F., 1987, ApJ , 319, 28

Yee H. K. C. & Lopez-Cruz O., 1999, AJ , 117, 1985

Yee H. K. C., Morris S. L., Lin H., Carlberg R. G., Hall P. B., Sawicki M., Patton D. R., Wirth G. D., Ellingson E., Shepherd C. W., ApJS , 129, 475

York D. G., the SDSS collaboration, 2000, AJ , 120, 1579

Zabludoff A. I, & Mulchaey J. S., 1998, 496, 39

Zaritsky D., Nelson A. E., Dalcanton J. J, & Gonzalez A. H., 1997, ApJL , 480, 91

Zel'Dovich Y., 1970, A&A , 1970, 5, 84